GDAŃSK UNIVERSITY
OF TECHNOLOGY

Faculty of Civil and Environmental Engineering

The author of the PhD dissertation: Beata Zima
Scientific discipline: Civil Engineering

DOCTORAL DISSERTATION

Title of PhD dissertation: Guided waves for nondestructive diagnostics of embedded waveguides

Title of PhD dissertation (in Polish): Fale prowadzone w diagnostyce nieniszczącej prętów osadzonych

Supervisor *signature*	Second supervisor *signature*
dr hab. inż. Magdalena Rucka, prof. nadzw. PG	
Auxiliary supervisor *signature*	Cosupervisor *signature*

Gdańsk, 2018

Page intentionally left blank

GDAŃSK UNIVERSITY
OF TECHNOLOGY

Faculty of Civil and Environmental Engineering

WILiŚ

STATEMENT

The author of the PhD dissertation: Beata Zima

I, the undersigned, agree/~~do not agree~~* that my PhD dissertation entitled:
Guided waves for nondestructive diagnostics of embedded waveguides
may be used for scientific or didactic purposes.[1]

Gdańsk, 20.03.2018 ....
signature of the PhD student

Aware of criminal liability for violations of the Act of 4th February 1994 on Copyright and Related Rights (Journal of Laws 2006, No. 90, item 631) and disciplinary actions set out in the Law on Higher Education (Journal of Laws 2012, item 572 with later amendments),[2] as well as civil liability, I declare, that the submitted PhD dissertation is my own work.

I declare, that the submitted PhD dissertation is my own work performed under and in cooperation with the supervision of Magdalena Rucka.

This submitted PhD dissertation has never before been the basis of an official procedure associated with the awarding of a PhD degree.

All the information contained in the above thesis which is derived from written and electronic sources is documented in a list of relevant literature in accordance with art. 34 of the Copyright and Related Rights Act.

I confirm that this PhD dissertation is identical to the attached electronic version.

Gdańsk, 20.03.2018 ....
signature of the PhD student

I, the undersigned, agree/~~do not agree~~* to include an electronic version of the above PhD dissertation in the open, institutional, digital repository of Gdańsk University of Technology, Pomeranian Digital Library, and for it to be submitted to the processes of verification and protection against misappropriation of authorship.

Gdańsk, 20.03.2018 ....
signature of the PhD student

---

[1] Decree of Rector of Gdansk University of Technology No. 34/2009 of 9th November 2009, TUG archive instruction addendum No. 8.

[2] Act of 27th July 2005, Law on Higher Education: Chapter 7, Criminal responsibility of PhD students, Article 226.

Page intentionally left blank

No! Try not.
Do. Or do not. There is no try.

Master Yoda in Star Wars: Episode V - The Empire Strikes Back

Page intentionally left blank

Abstract

The thesis concentrates on comprehensive theoretical, numerical and experimental analysis of guided wave propagation in bars embedded in concrete or mortar. The investigations are focused on a particular type of objects representing a laboratory model of a ground anchor. Complex description of wave propagation phenomena in partially embedded bars is given and its application in detection of various types of defects is analysed.

The first part of thesis is focused on dispersive relations describing multimode wave propagation in free and multilayered bars of circular cross-section. Analytical solution in the form of dispersion curves is an important element of the analyses presented in the subsequent parts of the work regarding wave propagation in undamaged specimens, specimens with debonding and specimens with localized and surface damages.

Experimental and numerical analysis of wave propagation in undamaged anchors with variable bonding lengths allowed to derive relations enabling estimation of major geometric parameters on the basis of time-domain signals. Next, the influence of debonding length and its location on the wave propagation phenomena was described. The research carried out in the further part of the work proved the possibility of using guided waves for detection of relatively small-size debonding, as well as corrosion and point damage located in both embedded and free parts. The last stage of non-destructive testing concerned the wave propagation in a real drill-hollow bar commonly used for execution of geotechnical facilities. The influence of couplers connecting individual bars on the wave attenuation was analysed. Additionally, drill-hollow bar was used for real small-scale anchor performed in the ground. The possibility of guided wave application in the monitoring of the hardening process of cement mortar forming anchor body was demonstrated. Comparison of the results for anchor placed in the ground and the anchor after excavation allowed to determine the surrounding ground medium impact on the registered time signals.

Finally, the most important conclusions of the conducted research and future plans were pointed out.

Page intentionally left blank

Streszczenie

Praca zawiera analizę teoretyczną, numeryczną oraz eksperymentalną propagacji fal prowadzonych w prętach osadzonych w materiale kompozytowym typu beton lub zaprawa. Głównym obiektem badań był model laboratoryjny kotwy gruntowej. Przedstawiono szczegółowy opis zjawiska propagacji fali w prętach częściowo osadzonych oraz przeanalizowano możliwość jego wykorzystania w detekcji różnych typów uszkodzeń.

W pierwszej części pracy przedstawione zostały rozwiązania dyspersyjne opisujące wielomodową propagację fali w prętach jedno- i wielowarstwowych o kołowym przekroju poprzecznym. Rozwiązanie analityczne w postaci krzywych dyspersji stanowiło ważny element analiz przedstawionych w kolejnych częściach pracy, dotyczących propagacji fali w kotwach nieuszkodzonych, kotwach z uszkodzeniami w postaci rozwarstwienia, a także uszkodzeniami punktowymi i powierzchniowymi.

Badania eksperymentalne oraz obliczenia numeryczne dotyczące propagacji fal prowadzonych w nieuszkodzonych kotwach o zmiennej długości otulenia pozwoliły na opracowanie zależności umożliwiających określenie podstawowych parametrów geometrycznych kotwy na podstawie sygnałów czasowych. Następnie opisano wpływ długości oraz położenia uszkodzenia w postaci rozwarstwienia na zjawisko propagacji fali. Badania przeprowadzone w dalszej części pracy wykazały możliwość wykorzystania fal prowadzonych do wykrywania rozwarstwień o relatywnie niewielkim rozmiarze, a także uszkodzeń korozyjnych oraz punktowych położonych, zarówno w części otulonej jak i swobodnej. Ostatni etap badań nieniszczących dotyczył propagacji fali w rzeczywistej żerdzi powszechnie wykorzystywanej podczas wykonywania obiektów geotechnicznych. Przeanalizowany został wpływ elementów łączących pojedyncze żerdzie na tłumienie fali. Stalowa żerdź posłużyła ponadto do wykonania w gruncie rzeczywistej kotwy w małej skali. Wykazano możliwość wykorzystania fal w monitoringu twardnienia zaprawy cementowej formującej buławę kotwy. Porównanie wyników kotwy umieszczonej w gruncie oraz kotwy po wykopaniu pozwoliło na określenie wpływu obecności ośrodka gruntowego na rejestrowane sygnały czasowe propagującej fali.

W podsumowaniu przedstawiono najważniejsze wnioski z przeprowadzonych badań oraz przyszłe plany dotyczące dalszych prac naukowych.

Page intentionally left blank

Contents

Page intentionally left blank

Figure list

Table list

Page intentionally left blank

List of symbols

A	cross-sectional area
A_n, B_n	unknown amplitudes
$B_{n,r}$	Bessel function differential operator
$\mathbf{C}$	damping matrix
$\mathbf{D}$	material layer matrix
E	modulus of elasticity
$\mathbf{F}$	vector of external forces
F	external force
$\mathbf{H}$	vector field
$H_n^{(1)},\ H_n^{(2)}$	Hankel functions of the first and second kind
$\mathbf{I}$	internal force vector
I	polar moment of inertia
I_n	modified Bessel function of the first kind
$J_n(x)$	Bessel function of the first kind and order *n*
$\mathscr{J}_x$	Onoe’s function
$\mathbf{K}$	stiffness matrix
K	adjustable parameter in Love theory
K_n	modified Bessel function of the second kind
L	rod (anchor) length
L_b	bonding length
L_d	debonding length
L_D	point damage location
L_f	free length
$\mathbf{M}$	mass matrix
N	number of layers
R	reflection coefficient
T	kinetic energy (Chapter 2)
T	transmission coefficient (Chapter 4)
T_w	length of modulation window
U	potential energy
V	work of external forces
W_n	placeholder for a Bessel function of the second kind
Y_n	Bessel function of the second kind
Z	acoustic impedance
Z_n	placeholder for a Bessel function of the first kind
a	radius of a rod or inner radius of a pipe
b	inner radius of the pipe
c_g	group velocity
c_L	velocity of pressure bulk wave
c_S	velocity of shear bulk wave
c_{ph}	phase velocity
d	rod diameter

d_a	diameter of the anchor body
e	Euler number (ln(e)=1)
f	frequency
$f_{\max}$	maximum frequency
$f(r)$	radial behaviour of scalar potential function
$g_i(r)$	radial behaviour of equivoluminal potential function
h	thickness of the cover
i	imaginary unit $\sqrt{-1}$
i	number of increment
k	wavenumber
l_e	element size
l_i	ith layer
n	circumferential order, number of layers
n_w	number of counts in tone burst
p_0	excitation amplitude
q	body force
r	cylindrical coordinate
$\hat{r}$	unit vector in radial direction
t	time
Δt	time step (Chapter 3)
Δt	time interval (Chapter 4, 5 and 6)
Δt_{cr}	critical time step
$\mathbf{u}$	displacement vector
$\dot{\mathbf{u}}$	velocity vector
$\ddot{\mathbf{u}}$	acceleration vector
u	displacement
u_0	longitudinal displacement
$w(t)$	window function
x, y, z	Cartesian coordinates
α	$\sqrt{\omega^2/(c_L)^2 - k^2}$
$\bar{\alpha}$	modul of α
β	$\sqrt{\omega^2/(c_S)^2 - k^2}$
$\bar{\beta}$	modul of β
δ	variation
∂	partial differential operator
ε	strains
ϕ	scalar field
φ_2	function of the axial displacements distribution along the radius of the rod in three- mode theory
κ	stiffness of the layer
λ, μ	Lame constants
$\lambda_1,\ \lambda_2$	parameters to account for difference in plus and minus signs in recurrence relations
$\lambda_{\min}$	shortest wavelength
ν	Poisson’ ratio
π	3.1415926…

θ	circumferential angle
ρ	density
σ	normal stresses
ω	circular frequency
$\omega_{\max}$	maximum eigenfrequency
ψ_1	transverse displacement
∇	vector differential operator
∇^2	Laplace operator

Abbreviations:

GMM	Global Matrix Method
SHM	Structural Health Monitoring
SH	shear horizontal wave
SV	shear vertical wave
STFT	Short Time Fourier Transform
NDT	Nondestructive Testing
NDE	Nondestructive Evaluation
NDE&E	Nondestructive Testing and Evaluation
FEM	Finite Element Modelling
FFT	Fast Fourier Transform
TMM	Transfer Matrix Method
SEM	Spectral Element Modelling
SMM	Stiffness Matrix Method

Page intentionally left blank

CHAPTER 1

Introduction

1.1 Guided waves in diagnostics of engineering structures

Monitoring of structures, assessing their state, early damage detection and predicting the remaining service has become the field of special importance since the uprising of engineering. An increasing number of machines, buildings and vehicles and the need of constant controlling their technical condition have forced the improvement of diagnostic systems. The impressive development of diagnostic techniques has been observed in recent decades. Nondestructive testing (NDT) and nondestructive evaluation (NDE) methods for characterizing defects bring useful information about the current state of the tested elements. Structural health monitoring (SHM) which is an extension of NDT&E systems attempts to develop procedures of damage detection by permanently attached sensors which provide recording, analyzing, localizing damage conditions and making a real-time damage prognosis ([30],[198]).

The SHM is an interdisciplinary research area and nowadays it attracts significant interest of scientists. A variety of methods of NDT&E and SHM gives the opportunity to choose an effective approach with regard to a considered problem or a kind of monitored damage ([55],[88]). Many effective methods have been developed in previous works, e.g. ground penetrating radar ([7],[111],[113]), electrical impedance [148], acoustic emission ([45],[73],[74],[202]), eddy current [123], thermal imaging ([83],[226]), x-rays [191], vibration-based methods ([64],[90],[142],[184],[205],[214],[227]) and wave propagation-based methods [190] including ultrasonics ([41],[105]), impact-echo technique ([59],[66],[89],[122],[185]), or guided waves ([153],[160],[164],[183],[186]).

The SHM systems based on mechanical wave propagation have been successfully applied in diagnostics of civil, naval, and aerospace structures. The main advantage of SHM methods based on wave propagation is a possibility to detect and localize relatively small defects. Despite the fact that the first works on wave propagation appeared several centuries ago, their potential for nondestructive evaluation has not been recognized until 1951, when Firestone and Ling patented the method and means to generate and implement vibrational waves in plates [63]. In 1957 Worlton published a paper on Lamb waves application to inspect plate-like structures [216]. Four years later he also experimentally supported the theory of Horace Lamb formulated in 1916 ([114],[217]). Wortlon in his research excited waves with various frequencies in plates with various thickness – his results confirmed the Lamb theory about vibrations in plate. In 1965 Wortlon also patented a method of generating ultrasonic plane waves at a predetermined frequency [218]. Since that time a large number of works have been devoted to guided wave application in non-destructive testing.

The guided wave propagation in plates has been intensively studied by a number of researchers. The main advantage of wave application in diagnostics of plates is their possibility to monitor large areas during a single measurement. Datta [43] studied dispersive waves in a laminated plate with an arbitrary number of arbitrarily anisotropic laminae. Giurgiutiu et al. [70] used a linear piezoelectric-wafer phased array in monitoring of crack growth in aluminum plates. Ihn and Chang [93] monitored fatigue crack growth in a cracked metallic plate repaired with a bonded composite patch. Kudela et al. [110] proposed a damage detection algorithm for a multilayer composite plate by a clock-like configuration of sensors. Malinowski et al. [138] studied damage detection in an aluminum alloy specimen and implemented a special algorithm to process voltage signals in order to extract features related to defect. Various sensors configurations for damage detection in aluminum plates were investigated by Wandowski et al. [209]. Ambrozinski et al. [11] used self-focusing Lamb waves for SHM of plate structures. Dziendzikowski et al. [58] investigated damage detection in composite plates by two parallel linear arrays. Bayesian system identification theory has been applied for damage detection in plates by Yan [223].

Due to a relatively low energy dissipation guided waves can travel throughout long objects without significant reduction in signal amplitude. This advantage is particularly important in the case of monitoring rods, beams, pipes or rails. A potential application of waves in diagnostics of rods and beams was demonstrated by Palacz et al. [165], who detected an additional mass of the rod. Rucka [181] detected various types of defects in rods by the use of waves. Lucena and Dos Santos [132] proposed a new approach based on the combination of time reversal method and spectral element method to perform damage detection in rodlike structures. Lestari and Qiao [120] measured the traveling time, speed reduction, and wave attenuation parameters of propagating wave and applied them to detect damage in composite laminated beams. Ziaja et al. ([232],[233]) investigated guided wave propagation and possibility of its application for diagnostic purposes in thick-walled cylindrical structures. Defects in rails were detected by the use of waves by Lee et al. [119], who used a hybrid analytical-FEM technique to design the sensor to generate rail boundary conditions by means of a dispersion curve and wave structure analysis. Zumpano and Meo [245] presented a damage detection technique of structural surface damage on rail structures by the use of pressure, shear and Rayleigh waves. Zhang et al. [230] performed a continuous wavelet transform to analyse Lamb wave dispersion and locate damages in switch rails. Mariani et al. [136] investigated rail integrity using a high-speed and noncontact system based on guided waves. They accomplished a prototype which involved ultrasonic air-coupled guided wave signal generation and allowed for air-coupled signal detection. Wave propagation has been successfully applied in damage detection in pipelines by Alleyne and Cawley [10]. They studied $L(0,2)$ mode interaction with features occurring in chemical plant pipework. Lowe et al. [130] detected corrosion damage in insulated pipes by ultrasonic guided waves. Tse and Wang [206] investigated circumferential notches in pipelines and the impact of their depth on collected wave signals. Guided wave behaviour in pipe bends was considered by Sanderson et al. [189].

Guided wave sensitivity to even small defects occurring between particular layers of specimen contributed to the development of methods of nondestructive diagnostics of multilayered composite panels commonly employed in aerospace industry. The potential application of waves in diagnostics of aircraft structures was demonstrated e.g. in [42], [94],[193],[154]. Dalton et al. [42] examined wave propagation across free skin, tapering skin, skin loaded with sealant and paint, double skin joined with either sealant or adhesive and lap and stringer joints which are members of an aircraft fuselage structure. Ihn and Chang [94] detected damages in airbus fuselage panels by a pitch-catch method. Senyurek [193] excited surface waves and estimated the location of defects in wing slats of Boeing 737 aircraft. Monnier [154] presented the results of damage monitoring in carbon/epoxy aeronautical structure using integrated piezoelectric sensors.

Elastic waves are also an attractive alternative for the state assessment of prestressed bolted connections because in contrast to standard visual methods they do not require a direct access to the connection [71]. Wave propagation for diagnostics of bolted lap joints was presented by Amerini and Mao [12], who studied the relationship between the state of bolted specimen and linear and nonlinear acoustic/ultrasound parameters. Wang et al. [212] presented the relationship between wave energy signal and torque level in a bolted connection. Kędra and Rucka [100] proposed a development of damage index based on energy of initial part of a wave signal.

The description above contains only a small part of works that has been devoted to employment of wave propagation phenomena in diagnostics of structural elements however, all reported papers greatly illustrate a potential of SHM systems based on ultrasonic testing.

1.2 Guided wave propagation in condition assessment of embedded waveguides

Any free or embedded metal bar can be perceived as a waveguide to allow for disturbance propagation. Such waveguides can be found in many areas of civil engineering. One of common examples of embedded waveguides are steel rods embedded in concrete. Reinforced concrete is nowadays one of the most frequently and widely used material for civil engineering structures. Steel inserts in the form of bars, wires, strings, cables and nets can be used as a reinforcement in complex structures like bridges, dams, silos or buildings. At best, concrete cover protects metal waveguides from various types of damages. The outer concrete layer protects the steel against mechanical damage, while its alkaline environment prevents from corrosion. However, when the concrete cover is damaged or voids are formed while concrete was pumped, reinforcement is much less protected. Those damage forms are especially dangerous because they develop in the interior of structure without a possibility to be freely observed.

Due to the significant potential of nondestructive methods and the possibility of applying them in diagnostics of common structural elements, wave propagation problems in embedded waveguides have been extensively investigated since 20th century. The first works address theoretical aspects of wave propagation in multilayered bars. The theory of guided waves in multilayered rods can be found in the works of researchers such as Baltrukonis et al. ([17],[18]), McNiven and SackMan [141], Armenàkas ([14],[15]), Whittier and Jones [213], Kelkar [99], Reuter [176], Lai [112] and Thurston

[204]. These papers generally concern analytical solutions for particular wave mode families, the shape of dispersion curves and the procedures to trace them. Their theoretical exploration was a meaningful prerequisite for the implementation of guided waves for many challenging applications like nondestructive testing of embedded bars.

Examples of practical applications of wave propagation cover a wide range of various engineering structures considered as embedded waveguides. The integrity of anchorages of tendons of post-tensioned bridges was investigated by Pavlakovic [171]. He considered analytically and numerically leaky cylindrical systems and then used a developed model for the inspection problem of damage detection of embedded steel tendons. His work proved that nondestructive testing method based on wave propagation can be applied in detection of fracture or mass loss due to corrosion.

The results of applying wave propagation in the diagnostics of rock bolts were presented by Beard et al. ([22],[23],[24]). They investigated mode sensitivity to material parameters and geometry changes of epoxy bonded rock bolts. They also analysed wave attenuation in short lengths of grouted tendons and evaluated mode reflection coefficient from breaks of various geometry. The research team from Dalhousie University investigated the influence of curing time [135], frequency and grouted length [242], grout quality [243], and missing grout [40] on guided wave propagation and proposed a new approach for field monitoring of rock bolts [244]. They also performed simulations of wave attenuation and group velocity [39] and analysed numerically the effects of mesh density and wave excitation frequency on wave propagation signals [229]. Examples of guided ultrasonic waves application in diagnostics of rock bolts can be also found in papers published by Han et al. [81], Ivanović and Neilson [96], Lee et al. [118], Wang et al. [210] and Wu et al. [221].

Guided waves were also used in the detection of most common damage modes of steel reinforcement embedded in concrete. Na et al. ([158],[159]) examined the possibility of guided wave application in a bar-concrete interface testing. Corrosion monitoring was a topic of research presented by Reis et al. [177], Ervin et al. ([60],[61]), Sharma and Mukherjee [194], Li et al. [121], Moustafa et al. [156] and many others. Localized damages in rebar reinforced beams were detected by guided waves, inter alia, by Lu et al. [131] and Moustapha et al. [157].

Guided waves also turned out to be promising tool to assess strains and stresses in embedded waveguides. Stress levels in free seven-wire steel strands and strands anchored in concrete block were monitored with the use of ultrasonic waves by Chaki and Bourse [31]. Akbarov and Guliev [5] applied a three-dimensional linearized theory of wave propagation in an initially stressed body to investigate the influence of finite initial strains in a circular cylinder embedded in elastic medium.

All the papers mentioned above are perfect examples of practical use of the phenomenon of the disturbance propagation in the diagnostics of embedded waveguides. Despite enormous effort of scientists all around the world, many aspects of wave propagation in embedded waveguides remain not recognized yet.

1.3 Ground anchors as embedded waveguides

A structural example to represent an embedded waveguide is a ground anchor. Ground anchors are widely used in mining, tunneling and geotechnical engineering to prevent the movement of rock or ground strata ([80],[195]). They are commonly used, together with rock bolts and soil nails, in slope engineering projects and also for remediation purposes after the loss of slope stability [97]. The major components of ground anchor are steel tendon and anchor body made of mortar (Figure 1.1a). An overall construction process of a ground anchor takes place underground so its state cannot be assessed by standard visual inspection (Figure 1.1b). The most important difference between ground anchors and soil nails or rock bolts playing similar roles is their length. The length of a tendon of ground anchor can be significant because in general the load centre must be located at a maximum distance from the fulcrum edge of the supported structure [86]. Another important difference is the presence of the so-called anchor body of a possible significant diameter compared to the fixed zone of rock bolts.

At the first performance stage of a ground anchor, an oblong hole with a designed inclination is drilled by water-flushing in the ground (Figure 1.1b-II). When the drilling reaches the required depth, it is filled with injected liquid cement-grout. Next a steel tendon is placed in the ground and additional grout is injected (Figure 1.1b-III and IV). The injected grout forms an anchor body which is a retaining structure to transfer shear stresses at the grout/ground interface. After some time secondary grouting (post-grouting) is performed what leads to increase in size of the anchor body. The shapes of anchor bodies and their diameters may vary considerably and generally they depend on the properties of surrounded ground and the application of anchorage system [188].

The ground anchor state assessment usually involves pull-out destructive tests. The pull-out tests are carried out on a few specially prepared anchors. They allow assessing load-carrying capacity of tested specimens and lead to visual inspection of workmanship quality. Destructive tests make it possible to verify the design assumptions regarding the size of the anchor body. However, destructive tests are also expensive, time consuming and provide information on a few chosen specimens only. Limitations of invasive methods forced the need of development of nondestructive techniques which would be faster, more effective and most important, applicable for all anchors.

One of the greatest challenges in the field of diagnostics of ground anchors is their size estimation without violating their integrity. In general, load-carrying capacity of ground anchor greatly depends on the diameter and length of the anchor body. The diameter of the anchor body cannot be determined exactly due to large diversity of soil properties and is only estimated on the basis of soil type and diameter of the drill hole. Forming the anchors with diameters too small threatens the safety of the entire supporting structure, while too big diameters result in injecting too much liquid grout, what is associated with unnecessary, significantly higher costs. The second important parameter is bonding length. The guarantee of good health of the anchor and proper load transfer is a high quality of connection between grout and tendon at the length of the anchor body formation. Furthermore, the thorough cover is an excellent corrosion protection for steel components. Poor bonding quality results not only in lower load-carrying capacity but also in lower durability of an entire anchor. Even after pull-out tests there is no possibility to assess the state of a grout-tendon connection. This kind of quality check would require not only pull-out tests, but also total destruction of the anchor body.

Despite the fact that anchors are relatively simple engineering structures, there are a lot of problems with their proper and effective diagnostics. The desired diagnostic method should be nondestructive, what would let avoid additional costs. It should be easily applied in the state assessment of all investigated anchors, not just a few selected ones. Moreover, it should give the opportunity to estimate the most important geometric parameters like free length, bonding length, the effective length of the steel-grout connection and diameter, without a specimen damage. It should be also suitable for damage detection occurring as a result of corrosive environment or excessive loads. The methods based on a guided wave propagation phenomenon meet all these requirements. The great application potential of waves in diagnostics of different embedded waveguides has been proved by many scientists; however, many aspects of nondestructive inspection of ground anchors are still untouched.

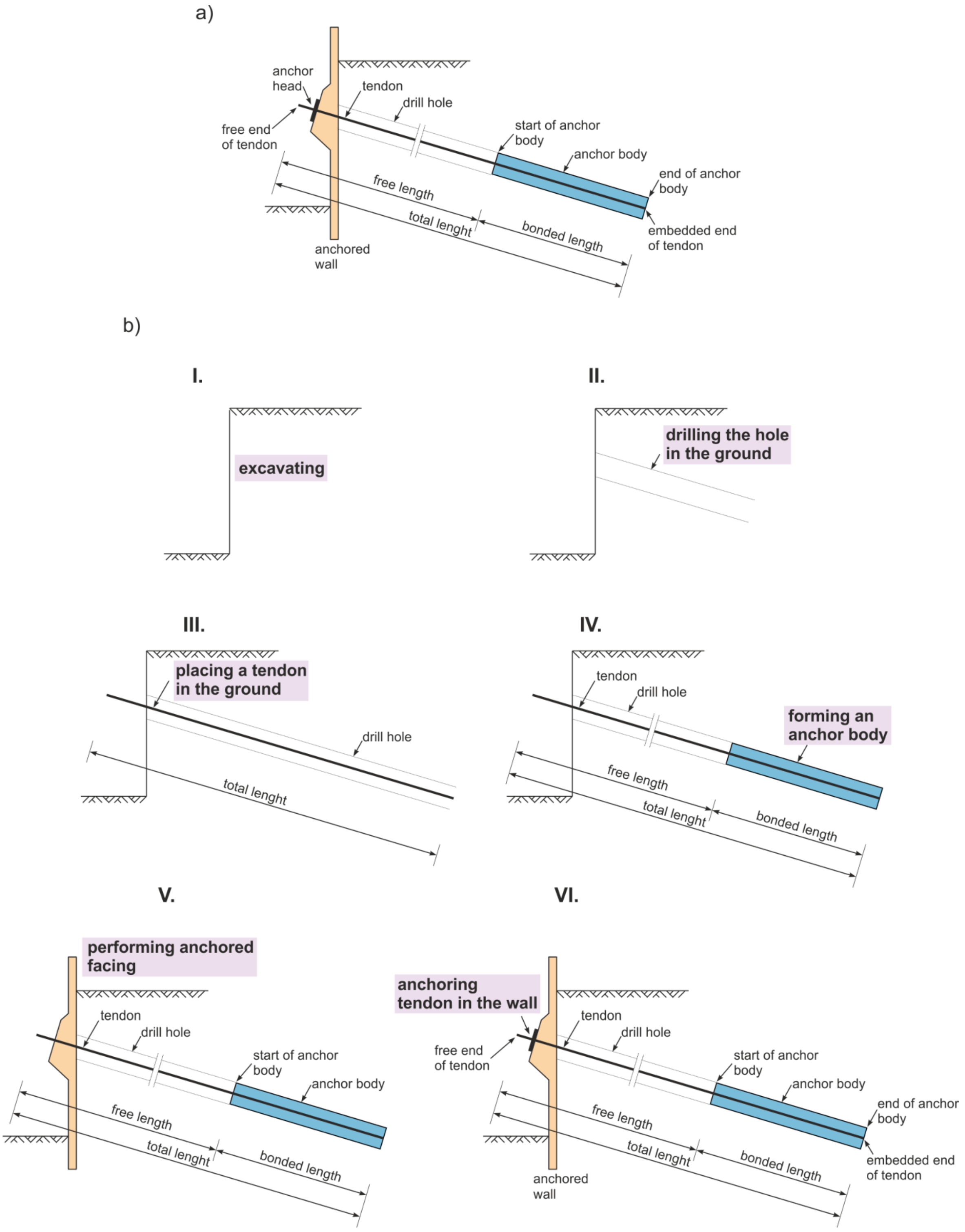

Figure 1.1 a) Ground anchor, b) process of installation of ground anchor

1.4 Aim and scope of study

The main purpose of the conducted research is a complex investigation of specific problems of wave propagation in embedded circular waveguides. The investigations were focused on a particular type of objects representing a laboratory model of a ground anchor. The emphasis of the study is a nondestructive diagnostics of ground anchors including estimation of basic geometric parameters and detection of the most common damage patterns.

The content is organized as follows. **Chapter 1** contains discussion about damage detection in structural elements using guided waves.

Chapter 2 derives an analytical model of longitudinal wave propagation in free and multilayered rods. Basic rod theories bringing approximate solutions for a wave propagation model in a free rod are derived and dispersion curves are presented. Approximate solutions are compared with Pochhammer-Chree theory, whose theory is regarded the most accurate bar theory directed to longitudinal wave propagation. Moreover, because of the fact that steel tendon of the anchor often occurs as hollow-drill bar system, the dispersion equation for hollow cylinders is also presented. In the second part of the chapter three matrix methods (Global Matrix Method, Transfer Matrix Method and Stiffness Matrix Method) commonly used to model wave motion in multilayered systems are presented.

Chapter 3 is devoted to description of numerical and experimental methods applied during the investigations.

Chapter 4 covers theoretical, numerical and experimental investigations of wave propagation in undamaged anchor models. Algorithms dedicated for determining the basic geometric parameters of ground anchors on the basis of wave propagation signals are presented here.

The use of wave propagation phenomenon for debonding detection in ground anchors is presented in **Chapter 5**. Three various locations and variable lengths of debonding are analysed and their influence on the wave propagation phenomenon is investigated.

Chapter 6 describes the use of waves in detecting corrosion - another common damage occurring in anchor systems. Two types of damage (localized damage and uniform corrosion of the rod surface) are investigated. Both free rods and multilayered rods embedded in mortar are considered in the research.

Chapter 7 is focused on experimental investigation of elastic wave propagation in a self-drilling hollow bar system, which is commonly used in geotechnical industry as the element of grouted ground anchors and soil nails. The influence of discontinuities in the form of mounting connections occurring over the tendon length on wave attenuation is analysed. The wave propagation studies are carried out in a small-scale model of the ground anchor performed in the ground with the use of a self-drilling hollow bar system.

The conclusions and future research plans are included in the final **Chapter 8**.

The original elements of the author's scientific work are:

- a detailed description of specific problems of wave propagation in healthy ground anchors with particular emphasis on characteristic features of guided waves propagating in free and embedded parts of the tendon, at the interface between the tendon and the surrounding anchor body as well as waves diffracted on the start of the anchor body,
- explaining the changes in wave velocity for various bonding lengths,
- derivation of formulas by means of which it is possible to determine geometric parameters of the anchor (free length, bonding length, diameter of anchor body),
- theoretical, numerical and experimental investigations of longitudinal guided modes in multilayered cylindrical bars with pre-existing debonding, including the influence of debonding location and its length on the separation of modes, their conversion and diffraction as well as the average wave velocity,
- investigation of influence of pre-existing debonding and its location on the results on destructive pull-out tests,
- investigation of corrosion and point damage detection in free and embedded bars,
- influence analysis of discontinuities in the form of mounting connections occurring over the tendon length on wave attenuation,
- monitoring the process of hardening cement inject on a small-scale real ground anchor,
- comparison of results obtained for underground and excavated anchor to illustrate the influence of surrounding ground on wave propagation signals.

The author conducted theoretical considerations, experimental studies as well as numerical calculations. The results of the research of guided wave propagation in ground anchors were published in papers [235]-[237] and [239]-[241].

Page intentionally left blank

CHAPTER 2

Guided waves in rods

Waves in rodlike structures have been a topic of considerable interest of many investigators over the centuries. A comprehensive review on rod theories can be found in Green [76] and McNiven and McCoy work [140]. Several rod theories varying in basic assumptions have been proposed up till now. Basically, two different approaches to the propagation of longitudinal waves in rods can be distinguished. The first approach is to find the exact theory for the displacements, strains and stresses describing wave motion to satisfy the field equations of isotropic, elastic materials. Due to the fact that the exact solution is characterized by a high degree of complexity and it contains infinite number of possible wave modes, the second approach focuses on formulating approximate theories assuming that the wave motions do not satisfy the field equations of elasticity [140]. Approximate theories are easier to use for engineering applications, however, they allow for obtaining correct relationships between wave velocities and the frequency only in a relatively short range of low frequencies.

The study of mathematical description of longitudinal waves in elastic rods has been already carried out by Bernoulli in 1741 [140]. His investigation concerned vibrations of a column of air, however it led to the same governing equation as for the elementary rod theory presented in paragraph 2.1.1. In 1876 Pochhammer published in his work [174] the exact frequency equation which is still considered the most accurate description of wave propagation in rods of a circular cross-section. Ten years later in 1886 Chree [34], unware of Pochhammer’s investigations, published a paper in which he presented the same frequency equation. It is worth mentioning that many articles include the information that Chree firstly published his frequency equation in his further paper in 1889 [35].

Despite the fact that both Pochhammer and Chree independently proposed the same exact solution of wave propagation problem in cylindrical bars, they also developed the same considerably simpler approximate solution for bars of a small radius. Very similar solution to approximate the Pochhammer-Chree equation but based only on physical reasoning was proposed by Lord Rayleigh in 1894 in [126]. In 1927 Love [127] derived an approximate theory using variational energy equation in which kinetic energy was affected by additional terms resulting from rod contraction due to the Poisson's ratio effect while the rod deforms longitudinally.

Despite the fact that the Pochhammer equation was formulated in 1886, the first attempts to solve it were made in 1941 by Bancroft [19]. Bancroft studied the lowest branch and evaluated the relation between the wavenumber and phase velocity. He indicated that the phase velocity approaches the velocity of the Rayleigh wave as the wavelength becomes smaller. Bancroft's work was then generalized and extended by Hudson [92]. He showed the fundamental branch in general changes with the Poisson's ratio, but also there is one point on the lower branch invariant Poisson's ratio variations. Extensive theoretical and experimental investigations of wave propagation rods using the Hopkinson pressure bar were conducted by Davies [44]. Davies recorded a signal as a time function using a camera and cathode ray oscilloscope, what allowed for performing a detailed image of a propagating pulse. He showed that the shape of the impulse was changing as it travelled along the rod because of the dispersive character of waves. Further studies of the Pochhammer equation conducted by Holden [87] have shown an analogy between the exact Rayleigh-Lamb equation for plates and the Pochhammer equation for rods: each equation can be satisfied by a purely imaginary wavenumber and a real frequency. Moreover, he proposed using bounding curves and intersections which helped tracing the dispersion curves. His idea to construct the frequency spectra by means of bounds was later willingly used by other researchers. The study of the Pochhammer equation was continued by Adem [4], who discovered that the equation can be satisfied by complex wavenumbers. Moreover, he described exponential decay of amplitudes of waves harmonically distributed along the rod axis for complex wavenumbers.

Parallel with the research on the Pochhammer equation, simplified theories were developed. In 1951 Mindlin and Herrmann [143] proposed a new rod theory considering shear strains and the corresponding shearing stresses. Their two-mode theory was a compromise between too complex Pochhammer theory and Love theory which in turn was suitable only for low frequencies. Herrmann [84] analysed the Mindlin-Herrmann dispersion relation but with taking into account free and forced vibrations. The Laplace transform was used by Miklowitz ([145],[146]) to obtain a solution for a semi-infinite rod subjected to axial force. Mindlin-Herrmann dispersion equations were rewritten by Plass and Steyer [173] in another form. They proposed a dispersion relation in the form of five first-order partial differential equations. Volterra [208] proved that the Mindlin-Herrmann equations can be derived directly from the exact Pochhammer-Chree solution. Another rod theory was proposed by Bishop [29] in 1952. The Bishop single mode theory uses assumption of the Love theory on the relation between lateral displacements and axial stresses and additionally takes into account shear stresses associated with rod diameter change due to a passing wave. The Bishop theory additionally takes into account shear stresses which occur as a result of changes of diameter caused by wave motion.

The three-mode approximate theory for longitudinal wave propagation was proposed in 1960 by Mindlin and McNiven [144]. The third mode in this theory was obtained by means of extending the range of the Mindlin-Herrmann theory by expanding the deformations in Taylor series. Simultaneously, Onoe, Mindlin and McNiven conducted studies about the Pochhammer equation and their findings were published in [163]. They presented roots of equation as spectral lines which were plotted using two sets of grid lines. The paper published by Zemanek [228] completed the study on the Pochhammer equation.

Simultaneously, studies on wave propagation in hollow cylinders have been widely conducted. Axially symmetric waves in hollow cylinders have been investigated by McFadden [139], Gosh [72] and Herrman and Mirsky [85]. In 1959 Gazis ([67],[68]) was the first one to consider a three-dimensional wave field in axial, radial and angular directions and presented an analytical foundation of the investigation of harmonic waves. He described a thorough solution for axisymmetric and non-axisymmetric wave modes in a thin-walled hollow cylinder. A comprehensive analysis of guided waves in cylinders is included in works of Achenbach [3], Auld [16], Bird ([27],[28]), Doyle ([51],[52]), Greenspon ([77],[78],[79]), Miklowitz [147], Mirsky ([149],[150]) and Rose [180].

2.1 Waves in free rods

The knowledge and understanding the basic assumptions of particular rod theories is essential in making a conscious choice of approach for the investigations of guided wave propagation in rodlike structures. For this reason, before proceeding to the main problem of dissertation concerning wave propagation in in such a complicated multilayered structure like ground anchors, the author found it appropriate to present a brief introduction in longitudinal wave propagation in rods, hollow cylinders and multilayered rods what is presented in following Chapter. Elementary mechanics is used to present governing equations for rods. At first the simplest elementary rod theory is described and then higher order rod theories (one-mode Love, two-mode Mindlin-Herrman, three-mode Mindlin-McNiven theory and multimode Pochhammer theory) are introduced by appending modifications. The lack in literature for Mindlin-Herrmann and Mindlin-McNiven theories makes the author's decision to present in this Chapter a full derivation for rods with a cylindrical cross-section.

2.1.1 Elementary rod theory

The elementary rod theory considers a long and slender rod carrying only one-dimensional axial stress. Lateral contraction is neglected here. The considered rod is straight, prismatic with constant cross-sectional area *A*, mass density *ρ* and modulus of elasticity *E* (Figure 2.1). This approach presents the simplest available rod model.

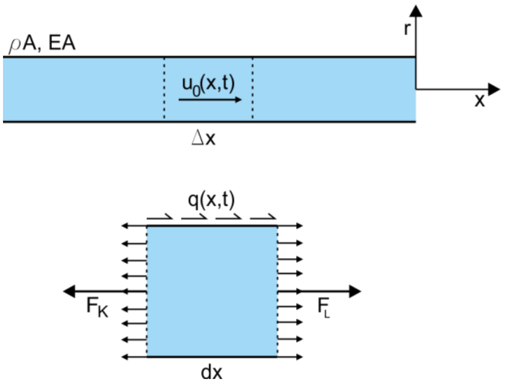

Figure 2.1 Differential element of a rod with loads

The displacement field can be described by an expression:

$$\bar{u}_x(x,r,t)=u_0(x,t)\,, \tag{2.1}$$

where x and t space and time variables, respectively. Displacement field is defined by longitudinal displacement $u_0(x,t)$ only. Derivation of dispersion relation for the elementary rod is made by using the variational Hamilton's principle what must be preceded by calculation of potential, strain and kinetic energies of the rod while the disturbance passes through. The potential strain energy is computed by integrating energy density over the total volume of the rod:

$$U = \frac{1}{2}\int_{\forall}\left[\sigma_{xx}\varepsilon_{xx} + \sigma_{rr}\varepsilon_{rr} + \sigma_{\theta\theta}\varepsilon_{\theta\theta} + \sigma_{xr}\varepsilon_{xr} + \ldots\right]d\forall = \frac{1}{2}\int_{\forall}\{\sigma\}^{T}\{\varepsilon\}\,d\forall\,. \tag{2.2}$$

Assuming linearly elastic material the Hooke's law holds:

$$\sigma_{xx} = E\varepsilon_{xx}\,, \tag{2.3}$$

geometric linearity assumption yields the following axial strain ε_{xx} relation:

$$\varepsilon_{xx} = \frac{\partial u_0}{\partial x}\,. \tag{2.4}$$

Then, according to Eq. (2.2) the potential strain energy due to elementary rod theory is:

$$U = \frac{1}{2}\int_0^L EA\left(\frac{\partial u_0}{\partial x}\right)^2 dx\,, \tag{2.5}$$

and the kinetic energy is:

$$T = \frac{1}{2}\int_0^L \rho A\dot{u}_0^2 dx\,. \tag{2.6}$$

The work made by external potential forces is:

$$V = -\int_0^L q(x,t)dx - (-F_K u_K + F_L u_L) = -\int_0^L q(x,t)dx - Fu_0\Big|_0^L\,. \tag{2.7}$$

The governing equation is obtained substituting strain and kinetic energies and potential into the variational Hamilton's principle:

$$\delta\int_{t_1}^{t_2}\left[T - \left(U + V\right)\right]dt = 0\,. \tag{2.8}$$

After substituting Eqs. (2.5)-(2.7) into Eq. (2.8) and neglecting the action of body forces q the following relation can be obtained:

$$\int_{t_1}^{t_2}\left\{\int_0^L\left[EA\frac{\partial^2 u_0}{\partial x^2}-\rho A\ddot{u}_0\right]\delta u_0 dx-\left[EA\frac{\partial u_0}{\partial x}-F\right]\delta u_0\Big|_0^L\right\}dt=0\,. \tag{2.9}$$

The governing equation of motion for an elementary rod can be formulated comparing the first integrand to zero:

$$EA\frac{\partial^2 u_0}{\partial x^2}-\rho A\frac{\partial^2 u_0}{\partial t^2}=0\,. \tag{2.10}$$

Expressing a harmonic solution in the following exponential form:

$$u_0=\sum U_0 e^{-i(kx-\omega t)}\,, \tag{2.11}$$

the spectrum relation emerges:

$$c_{ph}=\sqrt{\frac{E}{\rho}}=const\,, \tag{2.12}$$

where c_{ph} is phase wave velocity. Phase velocity is a wave speed of individual frequency components and is defined as:

$$c_{ph}=\frac{\omega}{k}\,. \tag{2.13}$$

The velocity of the whole wave packet containing waves with various frequencies is called group velocity. The wave group velocity can be calculated as the derivative of circular frequency with respect to a wavenumber:

$$c_g=\frac{d\omega}{dk}=\sqrt{\frac{E}{\rho}}=c_{ph}\,. \tag{2.14}$$

It can be seen that in case of elementary rod theory group velocity is identical to phase velocity and these wave velocities are constant for all frequencies. As a consequence dispersion effects are not observed in the rod theory domain. Moreover, the group and phase wave velocities in an elementary rod is not affected neither by cross-sectional area, its shape nor inertia moments. For this reason, the elementary rod theory can provide only a crude information about wave velocity for slender rods with an arbitrary cross-section.

2.1.2 Love rod theory

The Love rod theory is an improvement of the elementary rod theory and is derived for rods of cylindrical cross-sections. As in the elementary theory, plane sections remain plane and axial stresses are assumed uniformly distributed over a cross-section. However, the Love theory takes into account rod contraction due to Poisson's ratio effect while rod deforms longitudinally. Thus, each material point is also characterized by transverse velocity. The displacement field can be described by an expression:

$$\overline{u}_x(x,r,t) \approx u_0(x,t) . \tag{2.15}$$

where $u_0(x,t)$ is an average axial displacement in x direction. The additional equation coupling longitudinal and transverse velocities and affecting the rod kinetic energy can be presented as [52]:

$$\dot{u}_r(x,t) = -\nu r \frac{\partial \overline{u}_x}{\partial x} = -\nu r \frac{\partial u_0}{\partial x} . \tag{2.16}$$

As previously, variational Hamilton’s principle is applied to derive dispersion relation for the Love rod. The strain energy for the Love theory:

$$U = \frac{1}{2}\int_0^L EA\left(\frac{\partial u_0}{\partial x}\right)^2 dx , \tag{2.17}$$

is the same as for the elementary rod theory. Thus, the kinetic energy is then affected by additional terms and can be calculated by the expression:

$$T = \frac{1}{2}\int_0^L \left[\rho A \dot{u}_0^2 + \nu^2 \rho I \left(\frac{\partial \dot{u}_0}{\partial x}\right)^2\right] dx , \tag{2.18}$$

where I is the polar moment of inertia for the rod of a circular cross-section with radius a:

$$I = \int_0^{2\pi}\int_0^a r^2 r dr d\theta = \frac{1}{2}\pi a^4 .$$

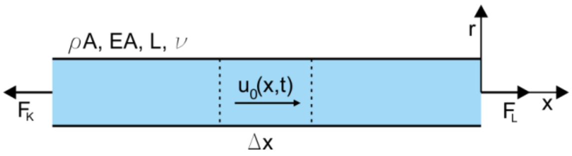

Figure 2.2 Segment of a rod with end loads

According to Figure 2.2 the potential is given as [52]:

$$V=-\int_0^L q(x,t)dx-(-F_K u_K+F_L u_L)=-\int_0^L q(x,t)dx-Fu_0\Big|_0^L . \qquad (2.19)$$

The governing equation can be obtained substituting strain and kinetic energies and potential into the variational Hamilton's principle:

$$\delta\int_{t_1}^{t_2}\left[T-\left(U+V\right)\right]dt=0 . \qquad (2.20)$$

After substitution of Eqs. (2.17), (2.18) and (2.19) into Eq. (2.20), and taking the variations inside and integration by parts, the following equation can be obtained:

$$\int_{t_1}^{t_2}\left\{\int_0^L\left[EA\frac{\partial^2 u_0}{\partial x^2}+\nu^2\rho I\frac{\partial^2 \ddot{u}_0}{\partial x^2}-\rho A\ddot{u}_0\right]\delta u_0 dx-\left[EA\frac{\partial u_0}{\partial x}+\nu^2\rho I\frac{\partial \ddot{u}_0}{\partial x}-F\right]\delta u_0\Big|_0^L\right\}dt=0 . \qquad (2.21)$$

Because of arbitrary space and time limits, the first integrand must be zero and the governing equation of motion for Love rod can be written as:

$$EA\frac{\partial^2 u_0}{\partial x^2}+\nu^2\rho I\frac{\partial^2 \ddot{u}_0}{\partial x^2}-\rho A\frac{\partial^2 u_0}{\partial t^2}=0 . \qquad (2.22)$$

Then, the spectrum relation is given by:

$$k=\pm\omega\sqrt{\frac{\rho A}{EA-\nu^2\rho I\omega^2}} , \qquad (2.23)$$

and the group velocity is:

$$c_g=\sqrt{\frac{E}{\rho}}\left[1-\nu^2\frac{\rho I\omega^2}{EA}\right]^{\frac{3}{2}} . \qquad (2.24)$$

Because of insufficiently accurate approximation for lateral deformation, the correction factor in the form of adjustable parameter *K* can be introduced (cf. [52]). It appears at identical positions as the Poisson's ratio term [52].

2.1.3 Mindlin-Herrmann rod theory

The Mindlin-Herrmann rod theory is the simplest multimode theory considering shear deformation and corresponding shear stresses coupled with transverse displacement. Radial deformations are not dependent of the axial deformations, but the Poisson's ratio relation between axial and radial strains is retained. Similarly to Love theory, plane sections remain plane because of proportion between radial displacements and a radial coordinate. Two additional deformation field components consistent with the axial motion can be presented in following form [247]:

$$\begin{aligned} \bar{u}_x(x,r,t) &\approx u_0(x,t), \\ \bar{u}_r(x,r,t) &\approx \psi_1(x,t)r. \end{aligned} \tag{2.25}$$

The corresponding non-zero strains and stresses can be obtained by applying strain-displacement and stress-displacement relations for axisymmetric problems:

$$\varepsilon_{rr} = \frac{\partial \bar{u}_r}{\partial r} = \psi_1, \tag{2.26}$$

$$\varepsilon_{\theta\theta} = \frac{\bar{u}_r}{r} + \frac{1}{r}\frac{\partial \bar{u}_\theta}{\partial \theta} = \psi_1, \tag{2.27}$$

$$\varepsilon_{xx} = \frac{\partial \bar{u}_x}{\partial x} = \frac{\partial u_0}{\partial x}, \tag{2.28}$$

$$\varepsilon_{rx} = \varepsilon_{xr} = \frac{1}{2}\left(\frac{\partial \bar{u}_r}{\partial x} + \frac{\partial \bar{u}_x}{\partial r}\right) = \frac{1}{2}\left(\frac{\partial \psi_1}{\partial x} r + \frac{\partial u_0}{\partial r}\right), \tag{2.29}$$

$$\sigma_{rr} = 2\mu\frac{\partial \bar{u}_r}{\partial r} + \lambda\left(\frac{\bar{u}_r}{r} + \frac{\partial \bar{u}_r}{\partial r} + \frac{\partial \bar{u}_x}{\partial x}\right) = 2\mu\psi_1 + \lambda\left(2\psi_1 + \frac{\partial u_0}{\partial x}\right), \tag{2.30}$$

$$\sigma_{\theta\theta} = 2\mu\left(\frac{\bar{u}_r}{r} + \frac{1}{r}\frac{\partial \bar{u}_\theta}{\partial \theta}\right) + \lambda\left(\frac{\bar{u}_r}{r} + \frac{\partial \bar{u}_r}{\partial r} + \frac{\partial \bar{u}_x}{\partial x}\right) = 2\mu\psi_1 + \lambda\left(2\psi_1 + \frac{\partial u_0}{\partial x}\right), \tag{2.31}$$

$$\sigma_{xx} = 2\mu\frac{\partial \bar{u}_x}{\partial x} + \lambda\left(\frac{\bar{u}_r}{r} + \frac{\partial \bar{u}_r}{\partial r} + \frac{\partial \bar{u}_x}{\partial x}\right) = 2\mu\frac{\partial u_0}{\partial x} + \lambda\left(2\psi_1 + \frac{\partial u_0}{\partial x}\right), \tag{2.32}$$

$$\sigma_{xr} = \sigma_{rx} = \mu\left(\frac{\partial \bar{u}_r}{\partial x} + \frac{\partial \bar{u}_x}{\partial r}\right) = \mu\left(\frac{\partial \psi_1}{\partial x} r + \frac{\partial u_0}{\partial r}\right). \tag{2.33}$$

The total strain energy according to Eq. (2.2) is given as follows:

$$U=\frac{1}{2}\int_0^L\left[2A\left(\left(2\mu+2\lambda\right)\psi_1^2+\psi_1\lambda\frac{\partial u_0}{\partial x}\right)+A\left(2\mu+\lambda\right)\left(\frac{\partial u_0}{\partial x}\right)^2\right.$$
$$\left.+2\psi_1\lambda\frac{\partial u_0}{\partial x}+\mu I\left(\frac{\partial \psi_1}{\partial x}\right)^2\right]dx. \tag{2.34}$$

The kinetic energy of wave motion in a Mindlin-Herrmann rod is:

$$T=\frac{1}{2}\int_0^L\left[\rho A\dot{u}_0^2+\rho I\dot{\psi}_1^2\right]dx\,. \tag{2.35}$$

The potential of applied surface tractions and loads is given by:

$$V=-\int_0^L q(x)u_0dx-Fu_0\Big|_0^L-Q_1\psi_1\Big|_0^L\,. \tag{2.36}$$

Taking variation inside the integrals above and integrating by parts it reads:

$$\delta\int_{t_1}^{t_2}U=\int_{t_1}^{t_2}\frac{1}{2}\int_0^L\left[8\left(\mu+\lambda\right)A\psi_1\delta\psi_1-4A\lambda\frac{\partial\psi_1}{\partial x}\delta u_0+4A\lambda\frac{\partial u_0}{\partial x}\delta\psi_1+\right.$$
$$\left.-2A\left(2\mu+\lambda\right)\frac{\partial^2 u_0}{\partial x^2}\delta u_0-2\mu I\frac{\partial^2\psi_1}{\partial x^2}\right]dxdt+\int_{t_1}^{t_2}\left[2A\lambda\psi_1\delta\psi_1+\right. \tag{2.37}$$
$$\left.+A\left(2\mu+\lambda\right)\frac{\partial u_0}{\partial x}\delta u_0+2A\lambda\psi_1\delta u_0+\mu I\frac{\partial\psi_1}{\partial x}\delta\psi_1\right]dt,$$

$$\delta\int_{t_1}^{t_2}T=\delta\frac{1}{2}\int_{t_1}^{t_2}\int_0^L\left[\rho A\dot{u}_0^2+\rho I\dot{\psi}_1^2\right]dx=-\int_{t_1}^{t_2}\int_0^L\left[\rho A\ddot{u}_0\delta u_0+\rho I\ddot{\psi}_1\delta\psi_1\right]dxdt\,, \tag{2.38}$$

$$\delta\int_{t_1}^{t_2}V=-\int_{t_1}^{t_2}\int_0^L\left[q(x)\delta u_0dx+F\delta u_0+Q_1\delta\psi_1\right]dxdt\,. \tag{2.39}$$

Applying Hamilton’s principle (Eq. (2.20)) a set of two partial differential equations is formed:

$$\left(2\mu+\lambda\right)A\frac{\partial^2 u_0}{\partial x^2}+2\lambda A\frac{\partial\psi_1}{\partial x}=\rho A\ddot{u}_0-q\,, \tag{2.40}$$

$$\mu I\frac{\partial^2\psi_1}{\partial x^2}-2\lambda A\frac{\partial u_0}{\partial x}-4\left(2\mu+\lambda\right)A\psi_1=\rho I\ddot{\psi}_1\,. \tag{2.41}$$

with associated boundary conditions at both ends of the rod:

$$\begin{aligned} &u_0; \quad F = \left(2\mu+\lambda\right) A \frac{\partial u_0}{\partial x} + 2\lambda A \psi_1, \\ &\psi_1; \quad Q_1 = \mu I \frac{\partial \psi_1}{\partial x} + 2A\lambda \psi_1. \end{aligned} \tag{2.42}$$

In order to obtain the spectrum relation a harmonic solution is expressed in the following form:

$$\begin{aligned} u_0 &= \sum U_0 e^{-i(kx-\omega t)}, \\ \psi_1 &= \sum \Psi_1 e^{-i(kx-\omega t)}. \end{aligned} \tag{2.43}$$

By substituting Eq. (2.43) into Eqs. (2.40) and (2.41), a system of algebraic equations can be written:

$$\begin{bmatrix} -(2\mu+\lambda)Ak^2 + \rho A\omega^2 & -2\lambda Aik \\ 2\lambda Aik & -4(2\mu+\lambda)A - \mu Ik^2 + \rho I\omega^2 \end{bmatrix} \begin{bmatrix} U_0 \\ \Psi_1 \end{bmatrix} = \begin{bmatrix} 0 \\ 0 \end{bmatrix} \tag{2.44}$$

Inserting these expressions into the displacement equations of motion and evaluating the resulting determinant the dispersion relation is obtained:

$$\begin{aligned} &\left[\left(2\mu+\lambda\right)A\mu I\right]k^4 + \left[16\mu\left(\mu+\lambda\right)A^2 - \rho I\omega^2\left(2\mu+\lambda\right)A - \rho A\omega^2\mu I\right]k^2 - \\ &\qquad - \left[4\left(2\mu+\lambda\right)A - \rho I\omega^2\right]\rho A\omega^2 = 0. \end{aligned} \tag{2.45}$$

There are two mode pairs because the equation above is quadratic with respect to k^2. The first mode is real only, but its speed decreases with frequency. In the case of low frequencies it is reduced to the elementary rod theory. The cut-off frequencies ω_{c1} and ω_{c2} for both dispersion curves can be calculated solving Eq. (2.45) when $k = 0$:

$$\omega_{c1} = 0 \quad \text{and} \quad \omega_{c2} = 2\sqrt{\frac{\left(2\mu+\lambda\right)A}{\rho I}}. \tag{2.46}$$

Similarly to the Love rod theory, correction factors may be introduced in the dispersion equation for the Mindlin-Herrmann rod. The correction factors are introduced into the equations for more precise dispersion curve fitting [140]. Hudson [92] proved in his work that generally the fundamental branch varies with the Poisson’s ratio, but also there is one point on the lower branch insensitive to variations in Poisson's ratio. According to Hudson's inquires one of the correction parameters is applied to make the spectral line pass through this point. Second correction parameter may be used to ensure that for small wavelengths the wave velocity approaches the Rayleigh wave velocity.

2.1.4 Three mode theory

Increasing the number of possible deformation modes a more accurate description of wave dispersion can be formulated [13]. The third mode can be obtained extending the range of the Mindlin-Herrmann theory by expanding the deformations in Maclaurin series. The displacements in three-mode theory for axisymmetric cross-sections considered in cylindrical coordinate system are assumed in form [247]:

$$\begin{gathered} \bar{u}_x(x,r,t) \approx u_0(x,t) + \varphi_2(x,t)\left(1-\frac{r^2}{a^2}\right), \\ \bar{u}_r(x,r,t) \approx \psi_1(x,t)r, \end{gathered} \tag{2.47}$$

where a is the radius of the rod, $u_0(x,t)$ is average axial displacement, $\varphi_2(x,t)$ is of a parabolic distribution function of axial displacements along the radius of the rod and $\psi_1(x,t)$ is the transverse displacement ([52],[107]). Non-zero strains and stresses obtained from the presented displacements are:

$$\varepsilon_{rr} = \frac{\partial \bar{u}_r}{\partial r} = \psi_1, \tag{2.48}$$

$$\varepsilon_{\theta\theta} = \frac{\bar{u}_r}{r} + \frac{1}{r}\frac{\partial \bar{u}_\theta}{\partial \theta} = \psi_1, \tag{2.49}$$

$$\varepsilon_{xx} = \frac{\partial \bar{u}_x}{\partial x} = \frac{\partial u_0}{\partial x} + \frac{\partial \varphi_2}{\partial x}\left(1-\frac{r^2}{a^2}\right), \tag{2.50}$$

$$\varepsilon_{rx} = \varepsilon_{xr} = \frac{1}{2}\left(\frac{\partial \bar{u}_r}{\partial x} + \frac{\partial \bar{u}_x}{\partial r}\right) = \frac{1}{2}\left(\frac{\partial \psi_1}{\partial x}r - \varphi_2\frac{2r}{a^2}\right), \tag{2.51}$$

$$\begin{aligned} \sigma_{xx} &= 2\mu\frac{\partial \bar{u}_x}{\partial x} + \lambda\left(\frac{\bar{u}_r}{r} + \frac{\partial \bar{u}_r}{\partial r} + \frac{\partial \bar{u}_x}{\partial x}\right) = 2\mu\left(\frac{\partial u_0}{\partial x} + \frac{\partial \varphi_2}{\partial x}\left[1-\frac{r^2}{a^2}\right]\right) + \\ &+\lambda\left(2\psi_1 + \frac{\partial u_0}{\partial x} + \frac{\partial \varphi_2}{\partial x}\left[1-\frac{r^2}{a^2}\right]\right) = (2\mu+\lambda)\left(\frac{\partial u_0}{\partial x} + \frac{\partial \varphi_2}{\partial x}\left[1-\frac{r^2}{a^2}\right]\right) + 2\mu\psi_1, \end{aligned} \tag{2.52}$$

$$\sigma_{rr} = 2\mu\frac{\partial\bar{u}_r}{\partial r} + \lambda\left(\frac{\bar{u}_r}{r} + \frac{\partial\bar{u}_r}{\partial r} + \frac{\partial\bar{u}_x}{\partial x}\right) = 2\mu\psi_1 + \lambda\left(2\psi_1 + \frac{\partial u_0}{\partial x} + \frac{\partial\varphi_2}{\partial x}\left[1 - \frac{r^2}{a^2}\right]\right), \tag{2.53}$$

$$\sigma_{\theta\theta} = 2\mu\left(\frac{\bar{u}_r}{r} + \frac{1}{r}\frac{\partial\bar{u}_\theta}{\partial\theta}\right) + \lambda\left(\frac{\bar{u}_r}{r} + \frac{\partial\bar{u}_r}{\partial r} + \frac{\partial\bar{u}_x}{\partial x}\right) = 2\mu\psi_1 + \lambda\left(2\psi_1 + \frac{\partial u_0}{\partial x} + \frac{\partial\varphi_2}{\partial x}\left[1 - \frac{r^2}{a^2}\right]\right), \tag{2.54}$$

$$\sigma_{xr} = \sigma_{rx} = \mu\left(\frac{\partial\bar{u}_r}{\partial x} + \frac{\partial\bar{u}_x}{\partial r}\right) = \mu\left(\frac{\partial\psi_1}{\partial x}r - \frac{2}{a^2}\varphi_2\right). \tag{2.55}$$

Total strain and kinetic energy can be calculated as:

$$\begin{aligned} U = \frac{1}{2}\int_0^L \Bigg[& 2\psi_1^2 A\left(2\mu + 2\lambda\right) + 4\psi_1\lambda A\left(\frac{\partial u_0}{\partial x} + \frac{1}{2}\frac{\partial\varphi_2}{\partial x}\right) \\ & + \left(2\mu + \lambda\right)A\left(\left(\frac{\partial u_0}{\partial x}\right)^2 + \frac{\partial u_0}{\partial x}\frac{\partial\varphi_2}{\partial x} + \frac{1}{3}\left(\frac{\partial\varphi_2}{\partial x}\right)^2\right) + \\ & + \mu I\left(\frac{\partial\psi_1}{\partial x}\right)^2 - 2\mu A\frac{\partial\psi_1}{\partial x}\varphi_2 + 2\mu\pi\varphi_2^2\Bigg]dx, \end{aligned} \tag{2.56}$$

$$T = \frac{1}{2}\int_0^L \left[\dot{u}_0^2\rho A + \dot{u}_0\dot{\varphi}_2\rho A + \frac{1}{3}\rho A\dot{\varphi}_2^2 + I\rho\dot{\psi}_1^2\right]dx. \tag{2.57}$$

The potential of applied surface tractions and loads is given by:

$$V = -\int_0^L q(x)u_0 dx - Fu_0\Big|_0^L - Q_1\psi_1\Big|_0^L - Q_2\varphi_2\Big|_0^L. \tag{2.58}$$

Similarly to the previous case, the use of Hammilton’s principle requires the variations of potential strain and kinetic energies. Taking variation inside the above integrals and integrating by parts one can obtain:

$$\begin{aligned} \delta\int_{t_1}^{t_2} U = \int_{t_1}^{t_2}\int_0^L \Bigg[& 4A\left(\mu + \lambda\right)\psi_1\delta\psi_1 - 2\lambda A\left(\frac{\partial\psi_1}{\partial x}\delta u_0 - \frac{\partial u_0}{\partial x}\delta\psi_1\right) + \\ & - \lambda A\left(\frac{\partial\psi_1}{\partial x}\delta\varphi_2 - \frac{\partial\varphi_2}{\partial x}\delta\psi_1\right) - \left(2\mu + \lambda\right)A\left(\frac{\partial^2 u_0}{\partial x^2}\delta u_0 + \frac{1}{2}\frac{\partial^2\varphi_2}{\partial x^2}\delta u_0 + \right. \\ & \left. + \frac{1}{2}\frac{\partial^2 u_0}{\partial x^2}\delta\varphi_2 + \frac{1}{3}\frac{\partial^2\varphi_2}{\partial x^2}\delta\varphi_2\right) - \mu I\frac{\partial^2\psi_1}{\partial x^2}\delta\psi_1 + \\ & + \mu A\left(\frac{\partial\varphi_2}{\partial x}\delta\psi_1 - \frac{\partial\psi_1}{\partial x}\delta\varphi_2\right) + 2\mu\pi\varphi_2\delta\varphi_2\Bigg]dxdt + \end{aligned} \tag{2.59}$$

$$+\int_{t_1}^{t_2}\Big[2\lambda A\psi_1\delta u_0+\lambda A\psi_1\delta\varphi_2+$$

$$+\left(2\mu+\lambda\right)A\left(\frac{\partial u_0}{\partial x}\delta u_0+\frac{1}{2}\frac{\partial\varphi_2}{\partial x}\delta u_0+\frac{1}{2}\frac{\partial u_0}{\partial x}\delta\varphi_2+\frac{1}{3}\frac{\partial\varphi_2}{\partial x}\delta\varphi_2\right)+$$

$$-\mu A\varphi_2\delta\psi_1+A\left(2\mu+\lambda\right)\frac{\partial u_0}{\partial x}\delta u_0+2A\lambda\psi_1\delta u_0+\mu I\frac{\partial\psi_1}{\partial x}\delta\psi_1\Bigg]dt,$$

$$\begin{gathered}\delta\int_{t_1}^{t_2}T=\delta\frac{1}{2}\int_{t_1}^{t_2}\int_0^L\left[\dot{u}_0^2\rho A+\dot{u}_0\dot{\varphi}_2\rho A+\frac{1}{3}\rho A\dot{\varphi}_2^2+I\rho\dot{\psi}_1^2\right]dx=\\ -\int_{t_1}^{t_2}\int_0^L\left[\rho A\ddot{u}_0\delta u_0+I\rho\ddot{\psi}_1\delta\psi_1+\frac{1}{3}\rho A\ddot{\varphi}_2\delta\varphi_2+\frac{1}{2}\rho A\ddot{\varphi}_2\delta u_0+\frac{1}{2}\rho A\ddot{u}_0\delta\varphi_2\right]dxdt,\end{gathered}\tag{2.60}$$

$$\delta\int_{t_1}^{t_2}V=-\int_{t_1}^{t_2}\int_0^L\left[q(x)\delta u_0dx+F\delta u_0+Q_1\delta\psi_1+Q_2\delta\varphi_2\right]dxdt\,.\tag{2.61}$$

The differential governing equations can be obtained substituting these energy components into Hamilton’s principle (Eq. (2.20)):

$$-2\lambda A\frac{\partial\psi_1}{\partial x}-\left(2\mu+\lambda\right)A\frac{\partial^2u_0}{\partial x^2}-\frac{1}{2}\left(2\mu+\lambda\right)A\frac{\partial^2\varphi_2}{\partial x^2}=\rho A\ddot{u}_0+\frac{1}{2}\rho A\ddot{\varphi}_2-q\,,\tag{2.62}$$

$$4A\left(\mu+\lambda\right)\psi_1+2\lambda A\frac{\partial u_0}{\partial x}+\lambda A\frac{\partial\varphi_2}{\partial x}-\mu I\frac{\partial^2\psi_1}{\partial x^2}+\mu A\frac{\partial\varphi_2}{\partial x}=I\rho\ddot{\psi}_1,\tag{2.63}$$

$$-\lambda A\frac{\partial\psi_1}{\partial x}-\left(2\mu+\lambda\right)A\left(\frac{1}{2}\frac{\partial^2u_0}{\partial x^2}+\frac{1}{3}\frac{\partial^2\varphi_2}{\partial x^2}\right)-\mu A\frac{\partial\psi_1}{\partial x}+2\mu\pi\varphi_2=\frac{1}{3}\rho A\ddot{\varphi}_2+\frac{1}{2}\rho A\ddot{u}_0\,.\tag{2.64}$$

The associated boundary conditions at both ends of the rod are defined as:

$$\begin{aligned}&u_0; && F=\left(2\mu+\lambda\right)A\left[\frac{\partial u_0}{\partial x}+\frac{1}{2}\frac{\partial\varphi_2}{\partial x}\right]+2\lambda A\psi_1,\\ &\psi_1; && Q_1=\mu I\left[\frac{\partial\psi_1}{\partial x}-\frac{2\varphi_2}{a^2}\right],\\ &\varphi_2; && Q_2=\left(2\mu+\lambda\right)A\left[\frac{1}{2}\frac{\partial u_0}{\partial x}+\frac{1}{3}\frac{\partial\varphi_2}{\partial x}\right].\end{aligned}\tag{2.65}$$

Assume the solution for three dependent variables u_0, ψ_1, φ_2 in the form:

$$\begin{aligned} u_0 &= U_0 e^{-i(kx-\omega t)}, \\ \psi_1 &= \Psi_1 e^{-i(kx-\omega t)}, \\ \varphi_2 &= \Phi_2 e^{-i(kx-\omega t)}. \end{aligned} \tag{2.66}$$

Substituting (2.66) into (2.62)-(2.64) leads to the system of algebraic equations:

$$\begin{bmatrix} (2\mu+\lambda)Ak^2+\rho A\omega^2 & 2\lambda Aik & \frac{1}{2}(2\mu+\lambda)Ak^2+\frac{1}{2}\rho A\omega^2 \\ -2\lambda Aik & 4A(\mu+\lambda)+\mu Ik^2+I\rho\omega^2 & -\lambda Aik-\mu Aik \\ \frac{1}{2}(2\mu+\lambda)Ak^2+\frac{1}{2}\rho A\omega^2 & \lambda Aik+\mu Aik & \frac{1}{3}(2\mu+\lambda)Ak^2+2\mu\pi+\frac{1}{3}\rho A\omega^2 \end{bmatrix} \begin{bmatrix} U_0 \\ \Psi_1 \\ \Phi_2 \end{bmatrix} = \begin{bmatrix} 0 \\ 0 \\ 0 \end{bmatrix}. \tag{2.67}$$

and the determinant on expansion is:

$$a_3k^6+a_2k^4+a_1k^2+a_0=0, \tag{2.68}$$

where:

$$\begin{aligned} a_3 &= \frac{1}{12}\left[(2\mu+\lambda)^2 A^2 I\mu\right], \\ a_2 &= \frac{A}{12}\left[4A^2\left(\lambda^3+\mu\lambda^2+4\mu^3\right)+IA\lambda\rho\omega^2\left(\lambda+6\mu+8\mu^2\right)+24\pi I\mu^2\left(2\mu+\lambda\right)\right], \\ a_1 &= A\left[\rho A\omega^2\left(\frac{2}{3}A(\mu+\lambda)^2+I\rho\omega^2\left(\frac{\lambda}{6}+\frac{5\mu}{12}\right)\right)+\right. \\ &\qquad\left. +8\pi\mu A(\mu+\lambda)^2+2\pi I\mu\rho\omega^2(\mu+\lambda)\right], \\ a_0 &= \rho A\omega^2\left[(\mu+\lambda)\left(\frac{A^2\rho\omega^2}{3}+8\pi A\mu\right)+\rho\omega^2\left(\frac{IA\rho\omega^2}{12}+2\pi I\mu\right)\right]. \end{aligned} \tag{2.69}$$

The equation above is cubic with respect k^2 and therefore there are three-mode pairs. As previously, correction factors for a precise curve fitting may be applied. An example of dispersion equations for a three-mode theory introducing the correction parameters may be found in [140].

More accurate higher-mode theories can be obtained increasing the number of possible deformation modes ([13],[247]). In general, displacement components can be expanded into a Maclaurin series and the number of unknown functions defining a displacement field taken into account determines the number of modes which can be obtained as a result of solving the dispersion equation. The form of displacement field for various rod theories and higher order rod theories can be found in [247].

2.1.5 Pochhammer theory

The rod theories presented in the preceding sections are not exact and they are suitable for describing wave dispersion relations for relatively long and thin rods only. The exact dispersion relation, which represents a nonlinear model of longitudinal wave propagation in elastic, thick rods has been derived by Pochhammer [174] and Chree [34]. Wave propagation characteristics in a cylindrical coordinate system (Figure 2.3) were derived by Gazis [67]. Pavlakovic [171] adapted his work for multilayered systems including material damping and slightly corrected Gazis paper. The derivation of wave propagation characteristics presented in following section is greatly based on their works.

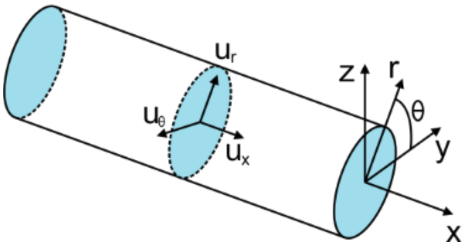

Figure 2.3 Structural element of a rod with circular cross-section

The displacement field must satisfy Navier's displacement equation of motion for elastic isotropic media:

$$\mu\nabla^2\mathbf{u}+(\lambda+\mu)\nabla\nabla\mathbf{u}=\rho\ddot{\mathbf{u}}\,. \tag{2.70}$$

According to the Helmholtz decomposition, the displacement field vector $\mathbf{u}$ can be expressed as the sum of irrotational vector field u_ϕ and the solenoidal vector field u_r [164]. It assumes that the displacement field vector can be decomposed as the sum of scalar field called scalar potential ϕ and vector field called vector potential $\mathbf{H}=(H_x,H_r,H_\theta)$:

$$\mathbf{u}=\nabla\phi+\nabla\times\mathbf{H}\,, \tag{2.71}$$

with

$$\nabla\cdot\mathbf{H}=F(r,\theta,x,t)\,. \tag{2.72}$$

Function $F(r,\theta,x,t)$ can be chosen arbitrary for gauge invariance ([67], [75], [171]). In the case of simple rods F equals zero. Substituting Eq. (2.71) into a displacement equation of motion (2.70) results in wave equations given by the following expressions:

$$\nabla^2\phi=\frac{1}{\left(c_L\right)^2}\ddot{\phi}\,, \tag{2.73}$$

$$\nabla^2\mathbf{H}=\frac{1}{\left(c_S\right)^2}\frac{\partial^2\mathbf{H}}{\partial t^2}\,. \tag{2.74}$$

where c_L and c_S are velocities of longitudinal and shear waves in infinite medium, respectively:

$$c_L=\sqrt{\frac{\lambda+2\mu}{\rho}}\,, \tag{2.75}$$

$$c_S=\sqrt{\frac{\mu}{\rho}}\,. \tag{2.76}$$

The solution of wave equations can be assumed as follows:

$$\phi=f(r)\cos n\theta e^{i(kx-\omega t)}\,, \tag{2.77}$$

$$H_x=g_3(r)\sin n\theta e^{i(kx-\omega t)}\,, \tag{2.78}$$

$$H_\theta=g_\theta(r)\cos n\theta e^{i(kx-\omega t)}\,, \tag{2.79}$$

$$H_r=g_r(r)\sin n\theta e^{i(kx-\omega t)}\,, \tag{2.80}$$

where $f\left(r\right)$, $g_3\left(r\right)$, $g_\theta\left(r\right)$, $g_r\left(r\right)$ are potential functions of radial coordinate r and n is a circumferential order number representing the static wave pattern in a circumferential direction.

Substituting equations (2.77)-(2.80) into (2.73) yields:

$$\frac{d^2f}{dr^2}+\frac{1}{r}\frac{df}{dr}-\left(\frac{n^2}{r^2}-\left(\frac{\omega^2}{\left(c_L\right)^2}-k^2\right)\right)f=0\,. \tag{2.81}$$

Substituting vector potential $\mathbf{H}$ from (2.78)-(2.80) into (2.74) results in coupled scalar equations:

$$c_S^2\nabla^2\mathbf{H} = \nabla\left(\nabla\cdot\mathbf{H}\right) - \nabla\times\left(\nabla\times\mathbf{H}\right) = \frac{\partial^2\mathbf{H}}{\partial t^2} = \\ = \hat{r}\left(\nabla^2 H_r - \frac{H_r}{r^2} - \frac{2}{r^2}\frac{\partial H_\theta}{\partial\theta}\right) + \hat{\theta}\left(\nabla^2 H_\theta - \frac{H_\theta}{r^2} - \frac{2}{r^2}\frac{\partial H_r}{\partial\theta}\right) + \hat{x}\left(\nabla^2 H_x\right), \tag{2.82}$$

where $\hat{r}$, $\hat{\theta}$ and $\hat{x}$ denote unit vectors in appropriate directions and the Laplacian is defined as:

$$\nabla^2 = \frac{\partial^2}{\partial r^2} + \frac{1}{r}\frac{\partial}{\partial r} + \frac{1}{r^2}\frac{\partial^2}{\partial\theta^2} + \frac{\partial^2}{\partial x^2}\,. \tag{2.83}$$

The separated equation (2.82) can be presented in the form:

$$\frac{d^2 g_3}{dr^2} + \frac{1}{r}\frac{dg_3}{dr} - \left(\frac{n^2}{r^2} - \left(\frac{\omega^2}{\left(c_S\right)^2} - k^2\right)\right) g_3 = 0\,, \tag{2.84}$$

$$\frac{d^2 g_r}{dr^2} + \frac{1}{r}\frac{dg_r}{dr} + \frac{1}{r^2}\left(-n^2 g_r + 2ng_\theta - g_r\right) - k^2 g_r + \frac{\omega^2}{\left(c_S\right)^2} g_\theta = 0\,, \tag{2.85}$$

$$\frac{d^2 g_\theta}{dr^2} + \frac{1}{r}\frac{dg_\theta}{dr} + \frac{1}{r^2}\left(-n^2 g_\theta + 2ng_r - g_\theta\right) - k^2 g_\theta + \frac{\omega^2}{c_S^2} g_r = 0\,. \tag{2.86}$$

Using the Bessel differential operator defined as:

$$B_{n,r} = \left(\frac{\partial^2}{\partial r^2} + \frac{1}{r}\frac{\partial}{\partial r} - \left(\frac{n^2}{r^2} - 1\right)\right), \tag{2.87}$$

equations (2.81) and (2.84)-(2.86) can be rewritten as Bessel-type equations:

$$B_{n,\alpha r}\left[f\right] = 0\,, \tag{2.88}$$

$$B_{n,\beta r}\left[g_3\right] = 0\,, \tag{2.89}$$

$$B_{n+1,\beta r}\left[g_r - g_\theta\right] = 0\,, \tag{2.90}$$

$$B_{n-1,\beta r}\left[g_r + g_\theta\right] = 0\,, \tag{2.91}$$

where:

$$.\alpha^2 = \frac{\omega^2}{\left(c_L\right)^2} - k^2, \tag{2.92}$$

$$\beta^2 = \frac{\omega^2}{\left(c_S\right)^2} - k^2. \tag{2.93}$$

The unknown functions $f(r)$, $g_3(r)$, $g_\theta(r)$, $g_r(r)$ can be expressed as the solution of Bessel equations in (2.88)-(2.91):

$$f = A_0 Z_n\left(\bar{\alpha} r\right) + B_0 W_n\left(\bar{\alpha} r\right), \tag{2.94}$$

$$g_3 = A_3 Z_n\left(\bar{\beta}\, r\right) + B_3 W_n\left(\bar{\beta}\, r\right), \tag{2.95}$$

$$2g_1 = \left(g_r - g_\theta\right) = 2A_1 Z_{n+1}\left(\bar{\beta} r\right) + 2B_1 W_{n+1}\left(\bar{\beta} r\right), \tag{2.96}$$

$$2g_2 = \left(g_r + g_\theta\right) = 2A_2 Z_{n-1}\left(\bar{\beta} r\right) + 2B_2 W_{n-1}\left(\bar{\beta} r\right). \tag{2.97}$$

where $\bar{\alpha}$ and $\bar{\beta}$ are moduli of α and β. In order to satisfy the operator the pair of linearly independent Bessel functions is required. However, several combinations of Bessel functions may satisfy the differential operator and their choice depends on the real or imaginary character of α and β. The choice of pair of function affects the solution stability, too.

The first pair of functions to satisfy the differential operator are Bessel function of the first kind J_n and Bessel function of the second kind Y_n, also called Weber or Naumann function. The graphs of Bessel functions look like oscillating sine or cosine function decaying proportionally to $1/\sqrt{x}$ and they represent standing waves. The second pair are modified or hyperbolic Bessel functions of the first and second kind I_n and K_n. These functions are characterized by exponential growth or decay, respectively. A third valid combination includes Hankel functions of the first and second kind $H_n^{(1)}$ and $H_n^{(2)}$, also called Bessel functions of the third kind. Hankel functions represent oscillating waves outward- and inward-propagating from the origin. Several factors affected the choice of Bessel functions combination were described in [67] and [171] and are given in Table 2.1.

Table 2.1 Criteria of choice of Bessel functions and parameters values

$c_{ph} > c_L$	$c_L > c_{ph} > c_S$	$c_L > c_S > c_{ph}$
$\alpha = \sqrt{\alpha^2}$ $\beta = \sqrt{\beta^2}$ $\lambda_1 = 1$ $\lambda_2 = 1$ $Z_n(\alpha r) = J_n(\alpha r)$ $W_n(\alpha r) = Y_n(\alpha r)$ $Z_n(\beta r) = J_n(\beta r)$ $W_n(\beta r) = Y_n(\beta r)$	$\alpha = \sqrt{-\alpha^2}$ $\beta = \sqrt{\beta^2}$ $\lambda_1 = -1$ $\lambda_2 = 1$ $Z_n(\alpha r) = I_n(\alpha r)$ $W_n(\alpha r) = K_n(\alpha r)$ $Z_n(\beta r) = J_n(\beta r)$ $W_n(\beta r) = Y_n(\beta r)$	$\alpha = \sqrt{-\alpha^2}$ $\beta = \sqrt{-\beta^2}$ $\lambda_1 = -1$ $\lambda_2 = -1$ $Z_n(\alpha r) = I_n(\alpha r)$ $W_n(\alpha r) = K_n(\alpha r)$ $Z_n(\beta r) = I_n(\beta r)$ $W_n(\beta r) = K_n(\beta r)$

Following Graff [75], in the analyzed case of the Pochhammer rod the second solution Y_n in Eqs. (2.94)-(2.97) can be neglected, because of its singular behaviour at the origin. The forms of equations which allow to determine the displacements in the analysed medium are:

$$u_x = \frac{\partial \phi}{\partial x} + \frac{\partial H_\theta}{\partial r} - \frac{1}{r}\frac{\partial H_r}{\partial \theta}, \tag{2.98}$$

$$u_r = \frac{\partial \phi}{\partial r} + \frac{1}{r}\frac{\partial H_x}{\partial \theta} - \frac{\partial H_\theta}{\partial x}, \tag{2.99}$$

$$u_\theta = \frac{1}{r}\frac{\partial \phi}{\partial \theta} + \frac{\partial H_r}{\partial x} - \frac{\partial H_x}{\partial r}. \tag{2.100}$$

The displacement field in terms of potential functions can be obtained by substituting Eqs. (2.94)-(2.97) and (2.77)-(2.80) into Eqs. (2.98)-(2.100). The gauge invariance property can be used to eliminate two unknown integration constants from the Eqs. (2.94)-(2.97). The relationship between the components of $\mathbf{H}$ is constituted by Eq. (2.71). For this reason, only three of each set of four potentials ϕ, H_x, H_r, H_θ are independent and consequently, one of the potentials g_1, g_2 or g_3 can be set to zero without the loss of solution generality. This implies that a combination of two equivoluminal potentials of Eqs. (2.94)-(2.97) can be used to define the displacement field corresponding to another equivoluminal potential g_j.

Setting $g_2 = 0$ one obtains:

$$g_r = -g_\theta = g_1 \,, \tag{2.101}$$

hence the displacement components can be expressed as:

$$u_x = \left[-kf - \frac{\partial g_1}{\partial r} - \left(1+n\right)\frac{g_r}{r} \right] \cos n\theta e^{i\left(kx-\omega t\right)} = U_x\left(r\right) \cos n\theta e^{i\left(kx-\omega t\right)} \,, \tag{2.102}$$

$$u_r = \left[\frac{\partial f}{\partial r} + \frac{n}{r} g_3 + kg_1 \right] \cos n\theta e^{i\left(kx-\omega t\right)} = U_r\left(r\right) \cos n\theta e^{i\left(kx-\omega t\right)} \,, \tag{2.103}$$

$$u_\theta = \left[-n\frac{f}{r} + kg_1 - \frac{\partial g_3}{\partial r} \right] \sin n\theta e^{i\left(kx-\omega t\right)} = U_\theta\left(r\right) \sin n\theta e^{i\left(kx-\omega t\right)} \,. \tag{2.104}$$

The strains-displacement relations:

$$\varepsilon_{rr} = \frac{\partial u_r}{\partial r} \,, \tag{2.105}$$

$$\varepsilon_{rx} = \frac{1}{2}\left(\frac{\partial u_r}{\partial x} + \frac{\partial u_x}{\partial r} \right), \tag{2.106}$$

$$\varepsilon_{r\theta} = \frac{1}{2}\left[r\frac{\partial}{\partial r}\left(\frac{u_\theta}{r} \right) + \frac{1}{r}\frac{\partial u_r}{\partial \theta} \right], \tag{2.107}$$

and stress-displacement relations of the linear theory of elasticity:

$$\sigma_x = 2\mu\frac{\partial u_x}{\partial x} + \lambda\left(\frac{u_r}{r} + \frac{\partial u_r}{\partial r} + \frac{\partial u_x}{\partial x} \right), \tag{2.108}$$

$$\sigma_r = 2\mu\frac{\partial u_r}{\partial r} + \lambda\left(\frac{u_r}{r} + \frac{\partial u_r}{\partial r} + \frac{\partial u_x}{\partial x} \right), \tag{2.109}$$

$$\tau_{xr} = \mu\left(\frac{\partial u_r}{\partial x} + \frac{\partial u_x}{\partial r} \right), \tag{2.110}$$

may be incorporated to express the stress components in terms of potentials f, g_1 and g_3:

$$\sigma_{rr} = \left\{ -\lambda\left(\alpha^2 + k^2\right) f + 2\mu\left(-\frac{f}{r} + \left[\frac{n^2 - \left(\alpha r\right)^2}{r^2} \right] f + \frac{n}{r}\left(\left(g_3\right)' - \frac{g_3}{r} \right) + k\left(g_1\right)' \right) \right\} \times \\ \times \cos n\theta e^{i\left(kx-\omega t\right)}, \tag{2.111}$$

$$\sigma_{r\theta} = \mu\left\{-\frac{2n}{r}\left(f' - \frac{f}{r}\right) + \frac{2g_3}{r} - \left(\frac{2n^2}{r^2} - \beta^2\right)g_3 + k\left[g_1 - \left(\frac{n+1}{r}\right)g_1\right]\right\}\times \\ \times \sin n\theta e^{i(kx-\omega t)}, \tag{2.112}$$

$$\sigma_{rx} = \mu\left[-2kf' - \frac{kn}{r}g_3 - \left(g_1\right)'\left(\frac{n^2+n}{r^2} - \beta^2 + k^2\right)\right]\times \cos n\theta e^{i(kx-\omega t)}. \tag{2.113}$$

Applying boundary conditions of zero tractions on the external rod surface:

$$\sigma_{rr}\Big|_{r=a} = \sigma_{r\theta}\Big|_{r=a} = \sigma_{rx}\Big|_{r=a} = 0, \tag{2.114}$$

and after substituting Eqs. (2.111)-(2.113) into Eqs. (2.114) the characteristic equation formed by determinant of the coefficients of the amplitudes reads:

$$\left|\mathbf{c}_{ij}\right| = 0 \qquad (i, j = 1,2,3), \tag{2.115}$$

where:

$$\begin{aligned}
c_{11} &= \left[\frac{\lambda\left(\alpha^2+k^2\right)\left(\alpha a\right)^2}{2\mu\alpha^2} + \left(\alpha a\right)^2 - n^2\right]J_n\left(\alpha a\right) + \alpha a J_n'\left(\alpha a\right),\\
c_{12} &= \left[n^2 - \left(\beta a\right)^2\right]J_n\left(\beta a\right) - \beta a J_n'\left(\beta a\right),\\
c_{13} &= 2n\left[\beta a J_n'\left(\beta a\right) - J_n\left(\beta a\right)\right],\\
c_{21} &= n\left[\alpha a J_n'\left(\alpha a\right) - J_n\left(\alpha a\right)\right],\\
c_{22} &= -n\left[\beta a J_n'\left(\beta a\right) - J_n\left(\beta a\right)\right],\\
c_{23} &= -\left[2n^2 - \left(\beta a\right)^2\right]J_n\left(\beta a\right) + 2\beta a J_n'\left(\beta a\right),\\
c_{31} &= -\alpha a J_n'\left(\alpha a\right),\\
c_{32} &= -\frac{\beta^2 - k^2}{2k^2}\beta a J_n'\left(\beta a\right),\\
c_{33} &= nJ_n\left(\beta a\right).
\end{aligned} \tag{2.116}$$

The Eq. (2.115) is a general dispersion equation for circular cross-section rods. While longitudinal modes are considered only and a circumferential order number n is equal to zero, the frequency equation can be expressed by a cofactor of a matrix. The direct consequence of symmetry in the case of longitudinal wave is that the potential vector $\mathbf{H}$ includes only one nonzero component H_θ, thus in general the considered displacements can be simplified. The following equations present axial and radial displacements, respectively:

$$u_x = \frac{\partial \phi}{\partial x} + \frac{1}{r}\frac{\partial\left(rH_\theta\right)}{\partial r}, \tag{2.117}$$

$$u_r = \frac{\partial \phi}{\partial r} - \frac{\partial H_\theta}{\partial x}. \tag{2.118}$$

The solutions for ϕ and $\mathbf{H}$ given by Eqs. (2.77)-(2.80) now can be rewritten as:

$$\phi = A_0 J_0\left(\alpha r\right) e^{i\left(kx-\omega t\right)}, \tag{2.119}$$

$$H_\theta = -A_1 J_1\left(\beta r\right) e^{i\left(kx-\omega t\right)}. \tag{2.120}$$

Applying boundary conditions of zero tractions at the external rod surface:

$$\sigma_{rr}\Big|_{r=a} = \sigma_{rx}\Big|_{r=a} = 0, \tag{2.121}$$

nontrivial solution can be obtained assuming a zero determinant of amplitude coefficients. It leads to nonlinear equation known as the Pochhammer-Chree dispersion equation describing longitudinal mode propagation in rods of a circular cross-section:

$$\begin{gathered}\frac{2\alpha}{a}\left(\beta^2 + k^2\right) J_1\left(\alpha a\right) J_1\left(\beta a\right) - \left(\beta^2 - k^2\right)^2 J_0\left(\alpha a\right) J_0\left(\beta a\right) + \\ -4k^2 \alpha\beta J_1\left(\alpha a\right) J_1\left(\beta a\right) = 0.\end{gathered} \tag{2.122}$$

It is worth mentioning that the presented derivation is not restricted to axial waves only. In order to obtain dispersion equations for flexural and torsional modes it is required to introduce appropriate boundary conditions. In the case of flexural waves all displacement components exist what makes the derivation of dispersion relation much more complex than for the longitudinal waves. The resulting form of dispersion equation can be find in Pao's and Mindlin's work [168]:

$$J_1\left(\tilde{\alpha}\right) J_1^2\left(\tilde{\beta}\right)\left[f_1 \mathcal{J}_{\tilde{\beta}}^2 + f_2 \mathcal{J}_{\tilde{\alpha}} \mathcal{J}_{\tilde{\beta}} + f_3 \mathcal{J}_{\tilde{\beta}} + f_4 \mathcal{J}_{\tilde{\alpha}} + f_5 \right] = 0, \tag{2.123}$$

where:

$$\begin{aligned}
f_1 &= 2\left(\tilde{\beta}^2 - \tilde{k}^2\right)^2, \\
f_2 &= 2\tilde{\beta}^2\left(5\tilde{k}^2 + \tilde{\beta}^2\right), \\
f_3 &= \tilde{\beta}^6 - 10\tilde{\beta}^4 - 2\tilde{\beta}^4\tilde{k}^2 + 2\tilde{\beta}^2\tilde{k}^2 + \tilde{\beta}^2\tilde{k}^4 - 4\tilde{k}^4, \\
f_4 &= 2\tilde{\beta}^2\left(2\tilde{\beta}^2\tilde{k}^2 - \tilde{\beta}^2 - 9\tilde{k}^2\right), \\
f_5 &= \tilde{\beta}^2\left(-\tilde{\beta}^4 + 8\tilde{\beta}^2 - 2\tilde{\beta}^2\tilde{k}^2 + 8\tilde{k}^2 - \tilde{k}^4\right),
\end{aligned} \tag{2.124}$$

and $\tilde{\alpha}$, $\tilde{\beta}$ and $\tilde{k}$ are defined as dimensionless wave numbers:

$$\tilde{\alpha} = \alpha a\,, \tag{2.125}$$

$$\tilde{\beta} = \beta a\,, \tag{2.126}$$

$$\tilde{k} = ka\,. \tag{2.127}$$

Function $\mathscr{J}_x$ occurring in Eq. (2.123) is Onoe's function of the first kind and order unity ([162],[168]):

$$\mathscr{J}_x = \mathscr{J}_1(x) = x\frac{J_0(x)}{J_1(x)}\,. \tag{2.128}$$

2.1.6 Longitudinal wave propagation in hollow cylinders

In the case of hollow cylinders, boundary conditions are defined at the outer and inner surfaces of the cylinder (Figure 2.4):

$$\sigma_{rr}\Big|_{r=a} = \sigma_{r\theta}\Big|_{r=a} = \sigma_{rx}\Big|_{r=a} = \sigma_{rr}\Big|_{r=b} = \sigma_{r\theta}\Big|_{r=b} = \sigma_{rx}\Big|_{r=b} = 0\,. \tag{2.129}$$

The governing equations (2.71)-(2.74), (2.82), (2.98)-(2.100) derived for a rod are still valid for a hollow cylinder, however Gazis [67] proposed slightly different form of Eqs. (2.77)-(2.80) :

$$\phi = f(r)\cos n\theta\cos\left(\omega t + kx\right), \tag{2.130}$$

$$H_x = g_3(r)\sin n\theta\cos\left(\omega t + kx\right), \tag{2.131}$$

$$H_\theta = g_\theta(r)\cos n\theta\sin\left(\omega t + kx\right), \tag{2.132}$$

$$H_r = g_r(r)\sin n\theta\sin\left(\omega t + kx\right). \tag{2.133}$$

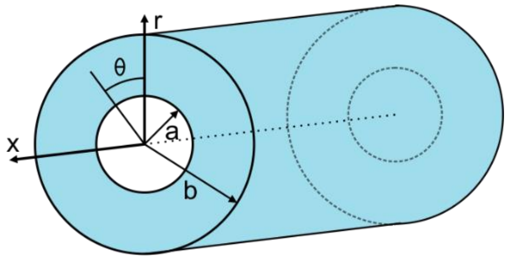

Figure 2.4 Hollow cylinder with reference to coordinate system

Next, exponential function $e^{i(kx-\omega t)}$ in the equations for displacement components (2.102)-(2.104) and stresses (2.111)-(2.113) is replaced by a sine of cosine function:

$$u_x = \left[-kf - \frac{\partial g_1}{\partial r} - (1+n)\frac{g_r}{r} \right] \cos n\theta e^{i(kx-\omega t)} = U_x(r) \cos n\theta \sin(\omega t + kx), \quad (2.134)$$

$$u_r = \left[\frac{\partial f}{\partial r} + \frac{n}{r} g_3 + kg_1 \right] \cos n\theta e^{i(kx-\omega t)} = U_r(r) \cos n\theta \cos(\omega t + kx), \quad (2.135)$$

$$u_\theta = \left[-n\frac{f}{r} + kg_1 - \frac{\partial g_3}{\partial r} \right] \sin n\theta e^{i(kx-\omega t)} = U_\theta(r) \sin n\theta \cos(\omega t + kx), \quad (2.136)$$

$$\sigma_{rr} = \left\{ -\lambda\left(\alpha^2 + k^2\right) f + 2\mu\left(-\frac{f}{r} + \left[\frac{n^2 - (\alpha r)^2}{r^2} \right] f + \frac{n}{r}\left(\left(g_3\right)' - \frac{g_3}{r} \right) + k\left(g_1\right)' \right) \right\} \times \\ \times \cos n\theta \cos(\omega t + kx), \quad (2.137)$$

$$\sigma_{r\theta} = \mu\left\{ -\frac{2n}{r}\left(f' - \frac{f}{r} \right) + \frac{2g_3}{r} - \left(\frac{2n^2}{r^2} - \beta^2 \right) g_3 + k\left[g_1 - \left(\frac{n+1}{r} \right) g_1 \right] \right\} \times \\ \times \sin n\theta \cos(\omega t + kx), \quad (2.138)$$

$$\sigma_{rx} = \mu\left[-2kf' - \frac{kn}{r} g_3 - \left(g_1\right)' \left(\frac{n^2 + n}{r^2} - \beta^2 + k^2 \right) \right] \times \cos n\theta \sin(\omega t + kx). \quad (2.139)$$

The dispersion equation is a result of substituting (2.137)-(2.139) into boundary conditions. There are six unknown constants A_0, B_0, A_1, B_1, A_3 and B_3 (compare Eqs. (2.94)-(2.97) and (2.101)) and six boundary conditions. The dispersion equation can be written in the form:

$$\left| \mathbf{c}_{ij} \right| = 0 \quad (i, j = 1 \text{ to } 6), \quad (2.140)$$

where the elements of the first three rows of the determinant are:

$$
\begin{aligned}
c_{11} &= \left[2n\left(n-1\right)-\left(\bar{\beta}^2-k^2\right)a^2\right]Z_n\left(\bar{\alpha}a\right)+2\lambda_1\bar{\alpha}aZ_{n+1}\left(\bar{\alpha}a\right),\\
c_{12} &= 2k\bar{\beta}a^2Z_n\left(\bar{\beta}a\right)-2ka\left(n+1\right)Z_{n+1}\left(\bar{\beta}a\right),\\
c_{13} &= -2n\left(n-1\right)Z_n\left(\bar{\beta}a\right)+2\lambda_2n\bar{\beta}aZ_{n+1}\left(\bar{\beta}a\right),\\
c_{14} &= \left[2n\left(n-1\right)-\left(\bar{\beta}^2-k^2\right)a^2\right]W_n\left(\bar{\alpha}a\right)+2\lambda_1\bar{\alpha}aW_{n+1}\left(\bar{\alpha}a\right),\\
c_{15} &= 2\lambda_2k\bar{\beta}a^2W_n\left(\bar{\beta}a\right)-2\left(n+1\right)kaW_{n+1}\left(\bar{\beta}a\right),\\
c_{16} &= -2n\left(n+1\right)W_n\left(\bar{\beta}a\right)+2n\bar{\beta}aW_{n+1}\left(\bar{\beta}a\right),\\
c_{21} &= 2n\left(n-1\right)Z_n\left(\bar{\alpha}a\right)-2\lambda_1n\bar{\alpha}aZ_{n+1}\left(\bar{\alpha}a\right),\\
c_{22} &= -k\bar{\beta}a^2Z_n\left(\bar{\beta}a\right)+2ka\left(n+1\right)Z_{n+1}\left(\bar{\beta}a\right),\\
c_{23} &= -\left[2n\left(n-1\right)-\bar{\beta}^2a^2\right]Z_n\left(\bar{\beta}a\right)-2\lambda_2\bar{\beta}aZ_{n+1}\left(\bar{\beta}a\right),\\
c_{24} &= 2n\left(n-1\right)W_n\left(\bar{\alpha}a\right)-2n\bar{\alpha}aW_{n+1}\left(\bar{\alpha}a\right),\\
c_{25} &= -\lambda_2k\bar{\beta}a^2W_n\left(\bar{\beta}a\right)+2ka\left(n+1\right)W_{n+1}\left(\bar{\beta}a\right),\\
c_{26} &= -\left[2n\left(n-1\right)-\bar{\beta}^2a^2\right]W_n\left(\bar{\beta}a\right)-2\bar{\beta}aW_{n+1}\left(\bar{\beta}a\right),\\
c_{31} &= 2nk\bar{\alpha}Z_n\left(\bar{\alpha}a\right)-2\lambda_1k\bar{\alpha}a^2Z_{n+1}\left(\bar{\alpha}a\right),\\
c_{32} &= n\bar{\beta}aZ_n\left(\bar{\beta}a\right)-\left(\bar{\beta}^2-k^2\right)a^2Z_{n+1}\left(\bar{\beta}a\right),\\
c_{33} &= -nkaZ_n\left(\bar{\beta}a\right),\\
c_{34} &= 2nkaW_n\left(\bar{\alpha}a\right)-2k\bar{\alpha}a^2W_{n+1}\left(\bar{\alpha}a\right),\\
c_{35} &= \lambda_2n\bar{\beta}aW_n\left(\bar{\beta}a\right)-\left(\bar{\beta}^2-k^2\right)a^2W_{n+1}\left(\bar{\beta}a\right),\\
c_{36} &= -nkaW_n\left(\bar{\beta}a\right).
\end{aligned}
\tag{2.141}
$$

The remaining three rows can be obtained from the expressions for first three rows while *b* is substituted for *a*. Functions Z_x and W_x are appropriate Bessel functions (J_n and Y_n or I_n and K_n) and criteria for functions and parameters λ_1 and λ_2 are given in Table 2.1. Dispersions equation for particular modes can be obtained comparing an appropriate subdeterminant of the matrix to zero.

In the case of longitudinal waves involving displacements u_r and u_x the dispersion equation takes the following form:

$$D_L = 0, \tag{2.142}$$

where:

$$D_L = \begin{vmatrix} c_{11} & c_{12} & c_{14} & c_{15} \\ c_{31} & c_{32} & c_{34} & c_{35} \\ c_{41} & c_{42} & c_{44} & c_{45} \\ c_{51} & c_{52} & c_{54} & c_{65} \end{vmatrix}. \qquad (2.143)$$

2.1.7 Dispersion curves

Dispersion curves for all presented rod theories described in paragraphs 2.1.1-2.1.6 have been plotted using MATLAB software. For solutions of Love, Mindlin-Herrmann and three-mode Mindlin-McNiven theories correction factors were neglected. The results are presented in Figure 2.5. The format of the modes names used in the thesis was proposed by Silk and Baintion [196]. The dispersion curves were plotted for variable diameters of a steel rod ($\rho =$ 7850 kg/m^3, $E =$ 210 GPa, $\nu =$ 0.3).

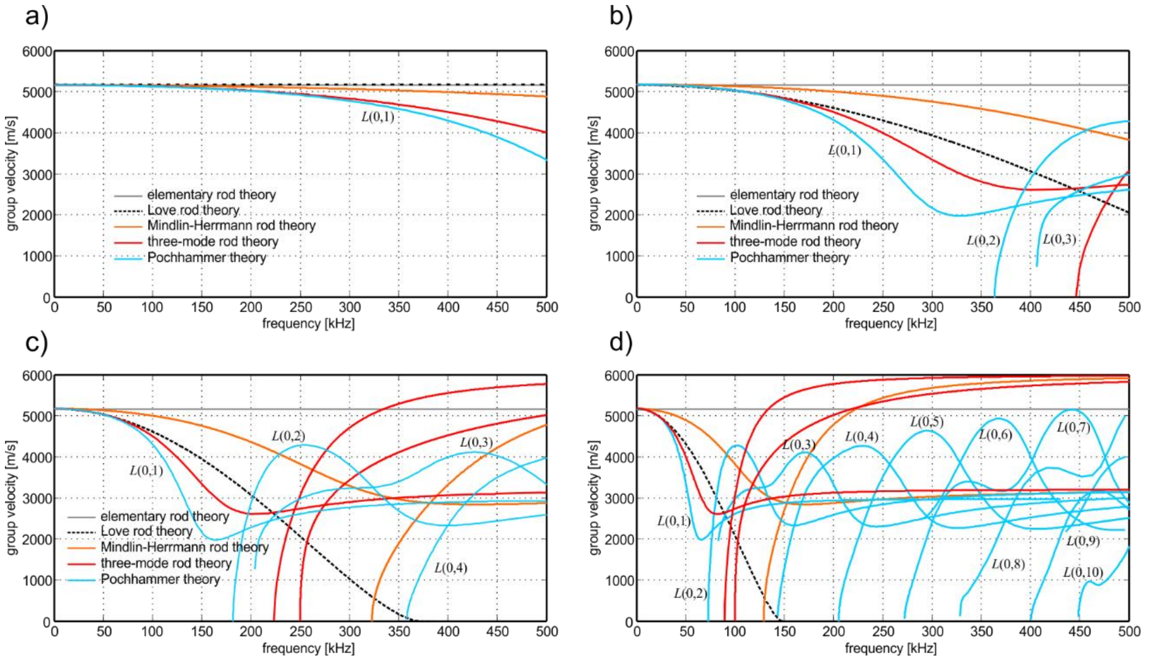

Figure 2.5 Dispersion curves for steel rod ($\rho = 7850$ kg/m^3, $E = 210$ GPa, $\nu = 0.3$) and diameter of a) 1 mm, b) 5 mm, c) 10 mm and d) 20 mm

While the diameter is relatively small dispersion curves obtained on the basis of five considered theories have similar shapes and overlap for a low frequency range (0 to about 150 kHz). The smaller diameter, the greater compatibility of dispersion curves: while the diameter equals 10 mm and more results obtained for various theories significantly differ from the exact Pochhammer solution. The main differences are the shape of dispersion curves, the cut-off frequencies and the number of possible modes for a particular frequency. It can be concluded that approximate theories can be applied only for rods with small diameters and relatively low frequency excitations. In the case of rods with large diameters application of the exact Pochhammer theory is the only one to bring correct results.

Figure 2.6 presents results in the form of dispersion curves for steel pipes with constant outer diameter size but variable inner diameter size obtained by using PCDISP [192]. The first graph presents curves for a pipe with a zero inner diameter (solid bar). With an increase of size of inner diameter the number of dispersion curves in the analysed frequency range (0-500 kHz) decreases.

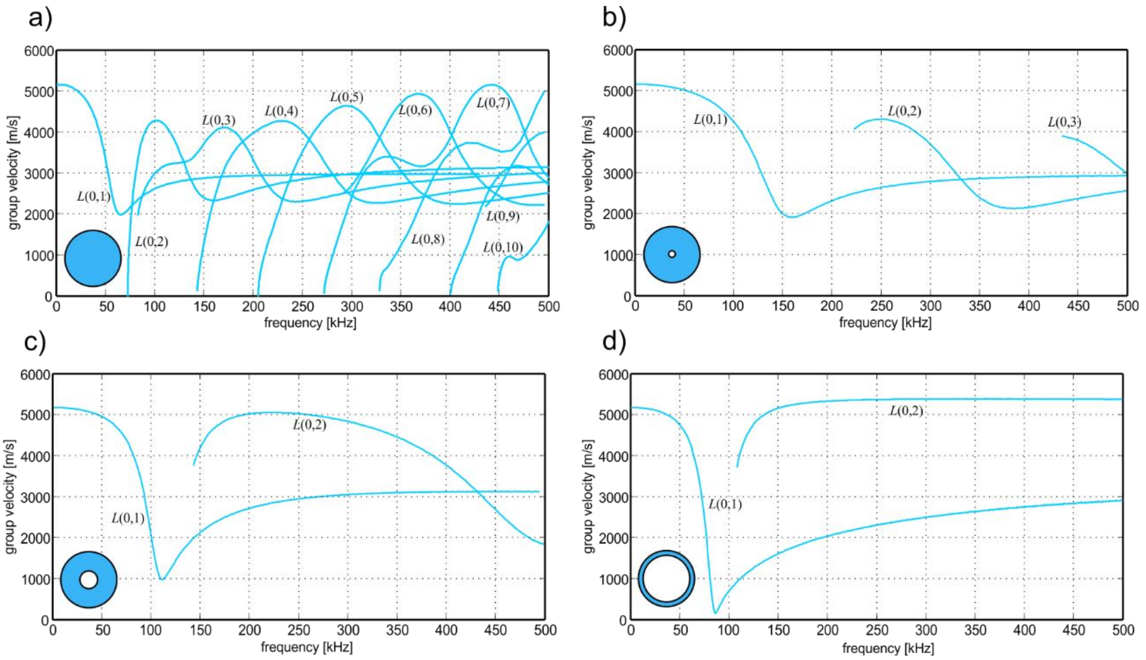

Figure 2.6 Dispersion curves for steel pipe ($\rho =$ 7850 kg/m^3, $E =$ 210 GPa, $\nu =$ 0.3) with outer diameter of 20 mm inner diameter of a) 0 mm, b) 2 mm, c) 10 mm and d) 18 mm

2.2 Guided waves in multilayered rods

Wave propagation in layered media is considerably a much more complicated task than analysed in single layer systems and it has been a topic of significant interest of scientists. A detailed historical background of studies about wave mechanics in multilayered media has been presented by Lowe in 1995 [129]. The first attempts to describe wave propagation in multilayered media were made by Lord Rayleigh in 1885 [125]. His work concerned propagation of elastic waves along a free surface of a semi-infinite elastic half-space. Further investigations of wave propagation in layered media were conducted by Lamb [114], Stoneley [200] and Love [128]. In 1917 Lamb published his description and analysis of waves propagating in thin plates. Stoneley's paper concerned boundary waves propagating at the interface of two adjacent media. Love proved that the existence of transverse modes is possible in a finite thickness layer.

The need to analyse the seismic surface waves in stratified media resulted in developing the theories dedicated to seismological applications. Several modelling methods dedicated to multilayered media with arbitrary numbers of layers variable in thickness and material parameters have been created. The first derivation of dispersion equations for a multilayered system was proposed by Thompson in 1950 [203]. He introduced a transfer matrix which assured the displacement continuity and stress equilibrium at the interface between particular layers. His method has been developed by Haskell [82] who also proved that this method is useful in search of the modal solutions for surface waves. Their method is called Transfer Matrix Method (TMM) or Thompson-Haskell method. The method was later developed allowing complex wavenumbers or the frequencies. This modification made TMM useful for modelling of leaky wave modes. The main advantage of TMM is its formulation simplicity, however unfortunately, TMM turned out to be unstable for waves with high frequencies propagating along layers of large thickness, what is known as large *fd* problem (*f* is the frequency and *d* is the layer thickness) [57]. Imperfection of this method brought the necessity of its modification, what was proposed by several investigators. Described modifications caused that TMM lost it initial simplicity what ultimately created the need of formulating alternative methods.

The second primary method used in multilayered media modelling is Global Matrix Method (GMM) developed by Knopoff [103] and Randall [175]. In Global Matrix Method the equations for all layers of the system are assembled in one large matrix called a global matrix. In the case of GMM no solution instability problem occurs, however for large number of layers the size of global matrix slows the computation down.

The last method considered here is Stiffness Matrix Method (SMM) proposed by Kausel [102] and developed by Wang and Rokhlin ([211],[178],[179]). A stiffness transfer matrix relates displacements and stresses at the top and bottom of a layer. The main advantage of SMM is that is its unconditional stability. A brief description of all mentioned methods (Transfer Matrix Method, Global Matrix Method and Stiffness Matrix Method) has been described by Giurgiutiu [69].

All mentioned methods and their modifications significantly improved the works on propagation in waveguides. They allowed to identify particular wave modes and to more effectively apply of disturbance propagation in diagnostics. Special attention was paid to wave propagation in multilayered cylindrical systems, which are common elements of machines or engineering structures. The study of wave propagation in composite cylinders were conducted among others by Baltrukonis et al. ([17],[18]), McNiven and SackMan [141], Armenàkas ([14],[15]), Whittier and Jones [213], Kelkar [99], Reuter [176], Achenbach [2], Lai [112] and Thurston [204]. Plane-strain transverse vibrations and axial shear vibrations in an infinitely long hollow cylinder were studied by Baltrukonis et al. ([17],[18]). McNiven and SackMan [141] conducted the study of axisymmetric longitudinal waves in a rod embedded in solid. They presented a numerical approach to dispersion equation for a two-material rod. Axisymmetric longitudinal waves in two-layer hollow cylinder were investigated by Whittier and Jones [213]. The same but more general solution was given by Armenàkas [14]. Moreover, Armenàkas solution also deals with flexural modes propagation. Kelkar [99] presented natural frequencies and mode shapes for a composite hollow cylinder. He incorporated the theory of elasticity and the theory of thin shells, while torsional solution of Achenbach [2] involves a single displacement component only. Flexural waves in a circular bimaterial cylinder were studied by Reuter [176]. He presented the first branch dispersion curves for the first flexural wave modes. Lai [112] showed that the frequency equations for axisymmetric waves and infinite axial wavelength can be reduced from the general dispersion equation. Thurston [204] presented a reasonably complete description of wave modes in clad rods, paying special attention to correspondences with appropriate limit cases.

The knowledge on wave characteristics in multilayered cylindrical specimens was practically used in a wide scale. Pavlakovic [171] investigated imbedded bars with the aim to develop the technique of diagnostics of tendons of post-tensioned bridges. Beard and Lowe [24] used guided wave propagation to assess the integrity of rock bolts. They were modelled as rods with a circular cross-section, surrounded by a layer of epoxy and embedded in limestone. Simmons et al. [197] and Drescher-Krasicka [54] investigated leaky and nonleaky axisymmetric modes for metal-metal and metal-ceramic interface studies. Wave propagation in pipelines covered by protecting coatings was the topic of study conducted by Barshinger and Rose [20], Kirby et al. [101], Marzani et al. [137], Hua and Rose [91] and others. One can see that the studies have been carried out in a variety of directions what proves the great potential of wave propagation method in diagnostics various engineering structures.

2.2.1 Assumptions and limitations of the model

A cylindrical wave propagation model derived in the following Chapter must be preceded by description of certain assumptions which are crucial in establishing the limits of the scope of the system.

The main assumption says that the model is infinitely long and axisymmetric. Material parameters may vary only in radial direction. Moreover, within a particular discrete layer the material is homogeneous and changes in parameters may occur only as instantaneous changes at the boundaries of these layers [129]. Perfect bonding between layers is assumed, so the derived model does not capture some phenomena like delamination.

The materials of particular layers are assumed isotropic. In general, isotropic materials may be modelled as elastic or material damping can be introduced in model. However, examples presented in the thesis are limited to the case of elastic materials.

The last group of assumptions concerns wave motion in a considered cylindrical system. The waves are assumed as continuous and the frequency real. These assumptions exclude the possibility of incorporating transient effects into the model. Moreover, the waves in a model show finite energy so any energy cannot be added to the system from external sources, but total energy of the system may decrease due to damping and wave leakage into the surrounding medium. The wave is excited at one end of the system continually and allowed to propagate [171].

2.2.2 Material Layer Matrix

Displacements and stresses are expressed by six equations (2.102)-(2.104) and (2.111) -(2.113) in terms of potential functions. The stress and displacement field can be easily calculated when solutions for these potentials are known (compare Eqs. (2.88)-(2.91)). Substituting the solutions of potentials into equations involving displacements and stresses leads to six equations with six unknowns, which are partial-wave participation factors. Three equations present partial wave amplitudes of outgoing waves and three stand for incoming waves and they correspond to coefficients of Bessel functions used in Eqs. (2.94)-(2.97). The partial waves in each layer of a five-layer cylindrical system are given in Figure.2.7. The longitudinal waves L correspond to the solution of $f(r)$, the shear vertical waves (*SV*) to the solution of g_1 and the shear horizontal waves (*SH*) to the solution of g_3.

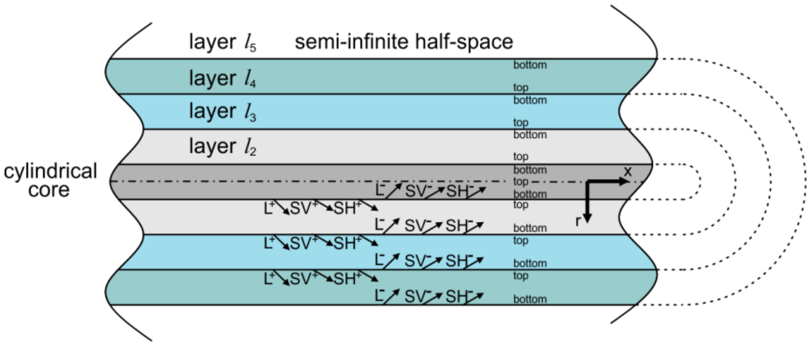

Figure.2.7 Five layered cylindrical system with partial waves in each layer

The displacements and stresses at any location in a particular layer are result of summing of contribution of six partial waves in the layer. Six equations (2.102)-(2.104) and (2.111)-(2.113) can be expressed in a matrix form:

$$\begin{Bmatrix} u_r \\ u_\theta \\ u_x \\ \sigma_{rr} \\ \sigma_{r\theta} \\ \sigma_{rx} \end{Bmatrix} = [\mathbf{D}] \begin{Bmatrix} A_{(L_+)} \\ A_{(L_-)} \\ A_{(SV_+)} \\ A_{(SV_-)} \\ A_{(SH_+)} \\ A_{(SH_-)} \end{Bmatrix}, \tag{2.144}$$

where $\mathbf{D}$ is called the material layer matrix. The graphical form of matrix $\mathbf{D}$ is presented in Figure 2.8.

$$\begin{array}{ccccccc}
 & A_{(L_+)} & A_{(L_-)} & A_{(SV_+)} & A_{(SV_-)} & A_{(SH_+)} & A_{(SH_+)} \\
u_r & \mathbf{D}(1,1) & \mathbf{D}(1,2) & \mathbf{D}(1,3) & \cdots & \ldots & \mathbf{D}(1,6) \\
u_\theta & \mathbf{D}(2,1) & \ddots & & & & \\
u_x & & & & & & \\
\sigma_{rr} & \vdots & & & & & \\
\sigma_{r\theta} & & & & & \ddots & \\
\sigma_{rx} & \mathbf{D}(6,1) & & & & & \mathbf{D}(6,6)
\end{array}$$

Figure 2.8 Graphical form of material matrix layer

Particular columns of the material layer matrix include consecutively outward propagating waves f, inward propagating waves f, outward propagating waves g_1, inward propagating waves g_1, outward propagating waves g_3 and inward propagating waves g_3. The rows contain normal displacements u_r, shear displacements u_θ, in-plane displacements u_x, normal stresses σ_{rr}, shear stresses perpendicular to the propagation direction of propagation $\sigma_{r\theta}$ and shear stresses in the propagation direction σ_{rx}, respectively.

$$\mathbf{D}(1,1) = kr^2 W_n(\alpha r) \qquad \mathbf{D}(4,1) = \left((k^2-\beta^2)r^2 + 2n(n-1)\right) W_n(\alpha r) + 2\alpha r W_{n+1}(\alpha r)$$

$$\mathbf{D}(1,2) = kr^2 Z_n(\alpha r) \qquad \mathbf{D}(4,2) = \left((k^2-\beta^2)r^2 + 2n(n-1)\right) Z_n(\alpha r) + 2\lambda_1 \alpha r Z_{n+1}(\alpha r)$$

$$\mathbf{D}(1,3) = \lambda_2 \beta r^2 W_n(\beta r) \qquad \mathbf{D}(4,3) = 2\lambda_2 k\beta r^2 W_n(\beta r) - 2(n+1)krW_{n+1}(\beta r)$$

$$\mathbf{D}(1,4) = \beta r^2 Z_n(\beta r) \qquad \mathbf{D}(4,4) = 2k\beta r^2 Z_n(\beta r) - 2kr(n+1)Z_{n+1}(\beta r)$$

$$\mathbf{D}(1,5) = 0 \qquad \mathbf{D}(4,5) = 2n(n-1)W_n(\beta r) - 2n\beta r W_{n+1}(\beta r)$$

$$\mathbf{D}(1,6) = 0 \qquad \mathbf{D}(4,6) = 2n(n-1)Z_n(\beta r) - 2\lambda_2 n\beta r Z_{n+1}(\beta r)$$

$$\mathbf{D}(2,1) = nrW_n(\alpha r) - \alpha r^2 W_{n+1}(\alpha r) \qquad \mathbf{D}(5,1) = 2nkrW_n(\alpha r) - 2k\alpha r^2 W_{n+1}(\alpha r)$$

$$\mathbf{D}(2,2) = nrZ_n(\alpha r) - \lambda_1 \alpha r^2 Z_{n+1}(\alpha r) \qquad \mathbf{D}(5,2) = 2nkrW_n(\alpha r) - 2\lambda_1 k\alpha r^2 Z_{n+1}(\alpha r)$$

$$\mathbf{D}(2,3) = kr^2 W_{n+1}(\beta r) \qquad \mathbf{D}(5,3) = \lambda_2 n\beta r W_n(\beta r) + (k^2-\beta^2)r^2 W_{n+1}(\beta r)$$

$$\mathbf{D}(2,4) = kr^2 Z_{n+1}(\beta r) \qquad \mathbf{D}(5,4) = n\beta r Z_n(\beta r) + (k^2-\beta^2)r^2 Z_{n+1}(\beta r)$$

$$\mathbf{D}(2,5) = nrW_n(\beta r) \qquad \mathbf{D}(5,5) = nkrW_n(\beta r)$$

$$\mathbf{D}(2,6) = nrZ_n(\beta r) \qquad \mathbf{D}(5,6) = nkrZ_n(\beta r)$$

$$\mathbf{D}(3,1) = nrW_n(\alpha r) \qquad \mathbf{D}(6,1) = 2n(n-1)W_n(\alpha r) - 2n\alpha r W_{n+1}(\alpha r)$$

$$\mathbf{D}(3,2) = nrZ_n(\alpha r) \qquad \mathbf{D}(6,2) = 2n(n-1)Z_n(\alpha r) - 2\lambda_1 n\alpha r Z_{n+1}(\alpha r)$$

$$\mathbf{D}(3,3) = -kr^2 W_{n+1}(\beta r) \qquad \mathbf{D}(6,3) = -k\lambda_2 \beta r^2 W_n(\beta r) + 2kr(n+1)W_{n+1}(\beta r)$$

$$\mathbf{D}(3,4) = -kr^2 Z_{n+1}(\beta r) \qquad \mathbf{D}(6,4) = -k\beta r^2 Z_n(\beta r) + 2kr(n+1)Z_{n+1}(\beta r)$$

$$\mathbf{D}(3,5) = nrW_n(\beta r) - \beta r^2 W_{n+1}(\beta r) \qquad \mathbf{D}(6,5) = \left(2n(n-1) - \beta^2 r^2\right) W_n(\beta r) + 2\beta r W_{n+1}(\beta r)$$

$$\mathbf{D}(3,6) = nrZ_n(\beta r) - \lambda_2 \beta r^2 Z_{n+1}(\beta r) \qquad \mathbf{D}(6,6) = \left(2n(n-1) - \beta^2 r^2\right) Z_n(\beta r) + 2\lambda_2 \beta r Z_{n+1}(\beta r)$$

(2.145)

Functions Z_x and W_x are relevant Bessel functions (J_n and Y_n or I_n and K_n) representing incoming and outgoing waves, respectively. The criteria for functions and values of parameters λ_1 and λ_2 are given in Table 2.1.

2.2.3 Transfer Matrix Method

When the stresses and displacements at the first interface i_1 are assumed known, the amplitudes of the six waves can be determined inverting the matrix $\mathbf{D}$:

$$\begin{Bmatrix} A_{(L_+)} \\ A_{(L_-)} \\ A_{(SV_+)} \\ A_{(SV_-)} \\ A_{(SH_+)} \\ A_{(SH_-)} \end{Bmatrix}_{l_2} = \mathbf{D}_{l_2,top}^{-1} \begin{Bmatrix} u_r \\ u_\theta \\ u_x \\ \sigma_{rr} \\ \sigma_{r\theta} \\ \sigma_{rx} \end{Bmatrix}_{l_2,top} . \tag{2.146}$$

While the amplitudes in layer l_1 are known the displacements and stresses at the bottom of the layer l_1 can be calculated:

$$\begin{Bmatrix} u_r \\ u_\theta \\ u_x \\ \sigma_{rr} \\ \sigma_{r\theta} \\ \sigma_{rx} \end{Bmatrix}_{l_1,bottom} = \mathbf{D}_{l_2,bottom}\mathbf{D}_{l_2,top}^{-1} \begin{Bmatrix} u_r \\ u_\theta \\ u_x \\ \sigma_{rr} \\ \sigma_{r\theta} \\ \sigma_{rx} \end{Bmatrix}_{l_1,top} . \tag{2.147}$$

The above equation relates displacements and stresses at the top and bottom of a single layer l_2. The Equation (2.147) can be simplified introducing a layer transfer matrix $\mathbf{L}$:

$$\mathbf{L}_{l_1} = \mathbf{D}_{l_1,bottom}\mathbf{D}_{l_1,top}^{-1} . \tag{2.148}$$

Due to the displacements and stresses continuity across an interface between two layers it can be written that:

$$\begin{Bmatrix} u_r \\ u_\theta \\ u_x \\ \sigma_{rr} \\ \sigma_{r\theta} \\ \sigma_{rx} \end{Bmatrix}_{l_2,top} = \begin{Bmatrix} u_r \\ u_\theta \\ u_x \\ \sigma_{rr} \\ \sigma_{r\theta} \\ \sigma_{rx} \end{Bmatrix}_{l_1,bottom} = \mathbf{L}_{l_2} \begin{Bmatrix} u_r \\ u_\theta \\ u_x \\ \sigma_{rr} \\ \sigma_{r\theta} \\ \sigma_{rx} \end{Bmatrix}_{l_1,top} . \tag{2.149}$$

Using the similar process for each layer of the system the equation is obtained:

$$\begin{Bmatrix} u_r \\ u_\theta \\ u_x \\ \sigma_{rr} \\ \sigma_{r\theta} \\ \sigma_{rx} \end{Bmatrix}_{l_n,bottom} = \mathbf{S} \begin{Bmatrix} u_r \\ u_\theta \\ u_x \\ \sigma_{rr} \\ \sigma_{r\theta} \\ \sigma_{rx} \end{Bmatrix}_{l_1,top} , \tag{2.150}$$

where n is the number of the last layer and $\mathbf{S}$ is a matrix obtained by multiplying individual transfer matrices for each layer as:

$$\mathbf{S} = \mathbf{L}_{l2}\mathbf{L}_{l3}\cdots\mathbf{L}_{n} . \tag{2.151}$$

Equation (2.150) can be then written as:

$$\begin{Bmatrix} u_r \\ u_\theta \\ u_x \\ \sigma_{rr} \\ \sigma_{r\theta} \\ \sigma_{rx} \end{Bmatrix}_{l_n,bottom} = \begin{bmatrix} S_{11} & S_{12} & S_{13} & S_{14} & S_{15} & S_{16} \\ S_{21} & S_{22} & S_{23} & S_{24} & S_{25} & S_{26} \\ S_{31} & S_{32} & S_{33} & S_{34} & S_{35} & S_{36} \\ S_{41} & S_{42} & S_{43} & S_{44} & S_{45} & S_{46} \\ S_{51} & S_{52} & S_{53} & S_{54} & S_{55} & S_{56} \\ S_{61} & S_{62} & S_{63} & S_{64} & S_{65} & S_{66} \end{bmatrix} \begin{Bmatrix} u_r \\ u_\theta \\ u_x \\ \sigma_{rr} \\ \sigma_{r\theta} \\ \sigma_{rx} \end{Bmatrix}_{l_1,top} . \tag{2.152}$$

For particular modes, stress-free boundary conditions to simplify the Eq. (2.152) can be applied. Because the system contains six equations, six boundary conditions need to be introduced. For free motion stresses at the bottom surface n in each case are equal to zero. In the case of analysed longitudinal modes additionally stresses $\sigma_{r\theta}$ and displacements u_θ vanish in the entire volume of the rod. Thus, Eq. (2.152) can be rewritten as:

$$\begin{Bmatrix} 0 \\ 0 \\ 0 \\ 0 \end{Bmatrix} = \begin{bmatrix} S_{21} & S_{23} & S_{24} & S_{26} \\ S_{41} & S_{43} & S_{44} & S_{46} \\ S_{51} & S_{53} & S_{54} & S_{56} \\ S_{61} & S_{63} & S_{64} & S_{66} \end{bmatrix} \begin{Bmatrix} u_r \\ u_x \\ \sigma_{rr} \\ \sigma_{rx} \end{Bmatrix}_{l_1,top} . \tag{2.153}$$

Non-trivial solution of the Eq. (2.153) exists in the case of a singular $\mathbf{S}$ matrix:

$$\begin{vmatrix} S_{21} & S_{23} & S_{24} & S_{26} \\ S_{41} & S_{43} & S_{44} & S_{46} \\ S_{51} & S_{53} & S_{54} & S_{56} \\ S_{61} & S_{63} & S_{64} & S_{66} \end{vmatrix} = 0 . \tag{2.154}$$

Dispersion curves for longitudinal modes can be determined solving Eq. (2.154). In the case of torsional and flexural modes appropriate boundary conditions concerning stresses and displacements are required in Eq. (2.153).

2.2.4 Global Matrix Method

The second matrix method commonly used for the modelling of multilayered systems is Global Matrix Method. As stated in paragraph 2.2.3 the displacements and stresses at any interface can be expressed as a function of the wave amplitudes at the top or bottom of two adjacent layers according to Figure.2.7:

$$\mathbf{D}_{l_1,bottom} \begin{Bmatrix} A_{(L_+)} \\ A_{(L_-)} \\ A_{(SV_+)} \\ A_{(SV_-)} \\ A_{(SH_+)} \\ A_{(SH_-)} \end{Bmatrix}_{l_1} = \mathbf{D}_{l_2,top} \begin{Bmatrix} A_{(L_+)} \\ A_{(L_-)} \\ A_{(SV_+)} \\ A_{(SV_-)} \\ A_{(SH_+)} \\ A_{(SH_-)} \end{Bmatrix}_{l_2} . \tag{2.155}$$

The Equation (2.155) can be presented in a single-matrix form:

$$\begin{bmatrix} \mathbf{D}_{l_1,bottom} & -\mathbf{D}_{l_2,top} \end{bmatrix} \begin{Bmatrix} \mathbf{A}_1 \\ \mathbf{A}_2 \end{Bmatrix} = \mathbf{0} , \tag{2.156}$$

where $\mathbf{A}_1$ and $\mathbf{A}_2$ are layer wave vectors containing amplitudes in layer 1 and 2, respectively. A similar equation to Eq. (2.155) can be created for interface 3 and added to matrix Eq. (2.156). Creating a unified matrix for every layer results in $6(n-1)$

equations and $6n$ unknowns for six partial waves. In the case presented in Figure.2.7 the global matrix can be assembled as:

$$\begin{bmatrix} \left[\mathbf{D}_{l_1,bottom}\right] & \left[-\mathbf{D}_{l_2,top}\right] & [0] & [0] & [0] \\ [0] & \left[\mathbf{D}_{l_2,bottom}\right] & \left[-\mathbf{D}_{l_3,top}\right] & [0] & [0] \\ [0] & [0] & \left[\mathbf{D}_{l_3,bottom}\right] & \left[-\mathbf{D}_{l_4,top}\right] & [0] \\ [0] & [0] & [0] & \left[\mathbf{D}_{l_4,bottom}\right] & \left[-\mathbf{D}_{l_5,top}\right] \end{bmatrix} \begin{Bmatrix} \{\mathbf{A}_1\} \\ \{\mathbf{A}_2\} \\ \{\mathbf{A}_3\} \\ \{\mathbf{A}_4\} \\ \{\mathbf{A}_5\} \end{Bmatrix} = \{0\}. \qquad (2.157)$$

The incoming waves in the two half-spaces ($\mathbf{A}_1^+$ and $\mathbf{A}_5^-$) are assumed known. As a result the first three and the last three columns can be removed from global matrix, resulting in:

$$\begin{bmatrix} \left[\mathbf{D}^-_{l_1,bottom}\right] & \left[-\mathbf{D}_{l_2,top}\right] & [0] & [0] & [0] \\ [0] & \left[\mathbf{D}_{l_2,bottom}\right] & \left[-\mathbf{D}_{l_3,top}\right] & [0] & [0] \\ [0] & [0] & \left[\mathbf{D}_{l_3,bottom}\right] & \left[-\mathbf{D}_{l_4,top}\right] & [0] \\ [0] & [0] & [0] & \left[\mathbf{D}_{l_4,bottom}\right] & \left[-\mathbf{D}^+_{l_5,top}\right] \end{bmatrix} \begin{Bmatrix} \{\mathbf{A}_1^-\} \\ \{\mathbf{A}_2\} \\ \{\mathbf{A}_3\} \\ \{\mathbf{A}_4\} \\ \{\mathbf{A}_5^+\} \end{Bmatrix} = \{0\}, \qquad (2.158)$$

where the subscripts + and – denote inward and outward propagating waves, respectively. This equation is satisfied when the determinant of global matrix is equal to zero.

2.2.5 Stiffness Matrix Method

Recall Eqs. (2.144) and (2.146) describing displacements and stresses at the top and bottom of a particular layer:

$$\begin{aligned} \begin{Bmatrix} u_{top} \\ \sigma_{top} \end{Bmatrix} &= \mathbf{D}_{top}\mathbf{A}, \\ \begin{Bmatrix} u_{bottom} \\ \sigma_{bottom} \end{Bmatrix} &= \mathbf{D}_{bottom}\mathbf{A}. \end{aligned} \qquad (2.159)$$

According to Figure 2.8 the matrix $\mathbf{D}$ can be divided into two parts: the first one contains coefficients related with displacements and the second with stresses:

$$\mathbf{D} = \begin{bmatrix} \mathbf{D}^u \\ \mathbf{D}^\sigma \end{bmatrix}. \qquad (2.160)$$

Then, Eqs. (2.159) can be expanded:

$$u_{top} = \mathbf{D}^{u}_{top}\mathbf{A}, \tag{2.161}$$

$$\sigma_{top} = \mathbf{D}^{\sigma}_{top}\mathbf{A}, \tag{2.162}$$

$$u_{bottom} = \mathbf{D}^{u}_{bottom}\mathbf{A}, \tag{2.163}$$

$$\sigma_{bottom} = \mathbf{D}^{\sigma}_{bottom}\mathbf{A}. \tag{2.164}$$

Eliminating $\mathbf{A}$ from Eqs. (2.161) and (2.162) stresses can be expressed by displacements for the top of the layer:

$$\sigma_{top} = \mathbf{D}^{\sigma}_{top}\left[\mathbf{D}^{u}_{top}\right]^{-1} u_{top}. \tag{2.165}$$

The same procedure can be used to obtaining stress-displacement relations for a bottom layer:

$$\sigma_{bottom} = \mathbf{D}^{\sigma}_{bottom}\left[\mathbf{D}^{u}_{bottom}\right]^{-1} u_{bottom}. \tag{2.166}$$

Combining Eqs. (2.165) and (2.166) leads to expression in form:

$$\begin{Bmatrix} \sigma_{top} \\ \sigma_{bottom} \end{Bmatrix} = \kappa \begin{Bmatrix} u_{top} \\ u_{bottom} \end{Bmatrix}, \tag{2.167}$$

where:

$$\kappa = \begin{bmatrix} \mathbf{D}^{\sigma}_{top} \\ \mathbf{D}^{\sigma}_{bottom} \end{bmatrix} \begin{bmatrix} \mathbf{D}^{u}_{top} \\ \mathbf{D}^{u}_{bottom} \end{bmatrix}^{-1}, \tag{2.168}$$

is the stiffness of the layer. For further derivations indexes t and b, which are abbreviations from the of ‘top’ and ‘bottom’ are introduced to ensure clarity of the presented equations. For a layer number n stiffness matrix takes the form:

$$\kappa_{l_n} = \begin{bmatrix} \kappa_{l_n,tt} & \kappa_{l_n,tb} \\ \kappa_{l_n,bt} & \kappa_{l_n,bb} \end{bmatrix}. \tag{2.169}$$

Important element of the presented Stiffness Matrix Method is creating the stiffness matrix of the global system from stiffness matrices obtained for individual layers. Global stiffness matrix for a system containing n layers is denoted as $\mathbf{K}_{l_n}$. It is obtained by means of a recursive process using stiffness matrix of system of $n-1$ layers $\mathbf{K}_{l_{n-1}}$ and stiffness for the *n*-layer κ_{l_n}.

For system of $n-1$ layers the stress-displacement relation is given as:

$$\begin{Bmatrix} \sigma_{l_1,t} \\ \sigma_{l_{n-1},b} \end{Bmatrix} = \mathbf{K}_{l_{n-1}} \begin{Bmatrix} u_{l_1,t} \\ u_{l_n,b} \end{Bmatrix} = \begin{bmatrix} \mathbf{K}_{l_{n-1},tt} & \mathbf{K}_{l_{n-1},tb} \\ \mathbf{K}_{l_{n-1},bt} & \mathbf{K}_{l_{n-1},bb} \end{bmatrix} \begin{Bmatrix} u_{l_1,t} \\ u_{l_{n-1},b} \end{Bmatrix}. \tag{2.170}$$

For the n-th layer the expression (2.167) can be then rewritten as:

$$\begin{Bmatrix} \sigma_{l_n,t} \\ \sigma_{l_n,b} \end{Bmatrix} = \kappa_{l_n} \begin{Bmatrix} u_{l_n,t} \\ u_{l_n,b} \end{Bmatrix} = \begin{bmatrix} \kappa_{l_n,tt} & \kappa_{l_n,tb} \\ \kappa_{l_n,bt} & \kappa_{l_n,bb} \end{bmatrix} \begin{Bmatrix} u_{l_n,t} \\ u_{l_n,b} \end{Bmatrix}. \tag{2.171}$$

After the expansion, Eqs. (2.170) and (2.171) take the form:

$$\sigma_{l_1,t} = \mathbf{K}_{l_{n-1},tt} u_{l_1,t} + \mathbf{K}_{l_{n-1},tb} u_{l_{n-1},b}\,, \tag{2.172}$$

$$\sigma_{l_{n-1},b} = \mathbf{K}_{l_{n-1},bt} u_{l_1,t} + \mathbf{K}_{l_{n-1},bb} u_{l_{n-1},b}\,, \tag{2.173}$$

$$\sigma_{l_n,t} = \kappa_{l_n,tt} u_{l_n,t} + \kappa_{l_n,tb} u_{l_n,b}\,, \tag{2.174}$$

$$\sigma_{l_n,b} = \kappa_{l_n,bt} u_{l_n,t} + \kappa_{l_n,bb} u_{l_n,b}\,. \tag{2.175}$$

Boundary conditions between layers *n*-1 and *n* assume the continuity of stresses and displacements:

$$u_{l_n,t} = u_{l_{n-1},b}\,, \tag{2.176}$$

$$\sigma_{l_n,t} = \sigma_{l_{n-1},b}\,. \tag{2.177}$$

After substituting (2.176) and (2.177) into (2.172) and (2.173) it holds:

$$\sigma_{l_1,t} = \mathbf{K}_{l_{n-1},tt} u_{l_1,t} + \mathbf{K}_{l_{n-1},tb} u_{l_n,t}\,, \tag{2.178}$$

$$\sigma_{l_n,t} = \mathbf{K}_{l_{n-1},bt} u_{l_1,t} + \mathbf{K}_{l_{n-1},bb} u_{l_n,t}\,. \tag{2.179}$$

Eliminating $\sigma_{l_n,t}$ between (2.174) and (2.179) leads to:

$$\kappa_{l_n,tt} u_{l_n,t} + \kappa_{l_n,tb} u_{l_n,b} = \mathbf{K}_{l_{n-1},bt} u_{l_1,t} + \mathbf{K}_{l_{n-1},bb} u_{l_n,t}\,. \tag{2.180}$$

Equation (2.180) can be solved to obtain displacements at the top of *n*-th layer:

$$u_{l_n,t} = \left(\kappa_{l_n,tt} - \mathbf{K}_{l_{n-1},bb}\right)^{-1} \mathbf{K}_{l_{n-1},bt} u_{l_1,t} - \left(\kappa_{l_n,tt} - \mathbf{K}_{l_{n-1},bb}\right)^{-1} \kappa_{l_n,tb} u_{l_n,b} . \tag{2.181}$$

The rearranged Eq. (2.181) can be substituted into (2.175) and (2.178):

$$\begin{aligned} \sigma_{l_n,b} = {} & \kappa_{l_n,bt} \left(\kappa_{l_n,tt} - \mathbf{K}_{l_{n-1},bb}\right)^{-1} \mathbf{K}_{l_{n-1},bt} u_{l_1,t} + \\ & + \left[\kappa_{l_n,bb} - \kappa_{l_n,bt} \left(\kappa_{l_n,tt} - \mathbf{K}_{l_{n-1},bb}\right)^{-1} \kappa_{l_n,tb}\right] u_{l_n,b}, \end{aligned} \tag{2.182}$$

$$\begin{aligned} \sigma_{l_1,t} = {} & \left[\mathbf{K}_{l_{n-1},tt} u_{l_1,t} + \mathbf{K}_{l_{n-1},tb} \left(\kappa_{l_n,tt} - \mathbf{K}_{l_{n-1},bb}\right)^{-1} \mathbf{K}_{l_{n-1},bt}\right] u_{l_1,t} - \\ & - \mathbf{K}_{l_{n-1},tb} \left(\kappa_{l_n,tt} - \mathbf{K}_{l_{n-1},bb}\right)^{-1} \kappa_{l_n,tb} u_{l_n,b}. \end{aligned} \tag{2.183}$$

Equations (2.182) and (2.183) in the matrix form can be rewritten as:

$$\begin{Bmatrix} \sigma_{l_1,t} \\ \sigma_{l_n,b} \end{Bmatrix} = \begin{bmatrix} \mathbf{K}_{l_{n-1},tt} + \mathbf{K}_{l_{n-1},tb} \left(\kappa_{l_n,tt} - \mathbf{K}_{l_{n-1},bb}\right)^{-1} \mathbf{K}_{l_{n-1},bt} & -\mathbf{K}_{l_{n-1},tb} \left(\kappa_{l_n,tt} - \mathbf{K}_{l_{n-1},bb}\right)^{-1} \kappa_{l_n,tb} \\ \kappa_{l_n,bt} \left(\kappa_{l_n,tt} - \mathbf{K}_{l_{n-1},bb}\right)^{-1} \mathbf{K}_{l_{n-1},bt} & \kappa_{l_n,bb} - \kappa_{l_n,bt} \left(\kappa_{l_n,tt} - \mathbf{K}_{l_{n-1},bb}\right)^{-1} \kappa_{l_n,tb} \end{bmatrix} \begin{Bmatrix} u_{l_1,t} \\ u_{l_n,b} \end{Bmatrix} \tag{2.184}$$

The right-hand side matrix is a stiffness matrix $\mathbf{K}_{l_n}$ of the system of *n*-layers and the above equation shows a recursive procedure of its calculation. The overall stiffness matrix can be written as:

$$\mathbf{K}_{l_n} = \begin{bmatrix} \mathbf{K}_{l_n,tt} & \mathbf{K}_{l_n,tb} \\ \mathbf{K}_{l_n,bt} & \mathbf{K}_{l_n,bb} \end{bmatrix}, \tag{2.185}$$

and then Eq. (2.184) can be rewritten in simpler form:

$$\begin{Bmatrix} \sigma_{l_1,t} \\ \sigma_{l_n,b} \end{Bmatrix} = \begin{bmatrix} \mathbf{K}_{l_n,tt} & \mathbf{K}_{l_n,tb} \\ \mathbf{K}_{l_n,bt} & \mathbf{K}_{l_n,bb} \end{bmatrix} \begin{Bmatrix} u_{l_1,t} \\ u_{l_n,b} \end{Bmatrix}. \tag{2.186}$$

As previously mentioned stresses at the bottom on the *n*-th layer $\sigma_{l_n,b}$ are equal to zero:

$$\begin{bmatrix} \mathbf{K}_{l_n,tt} & \mathbf{K}_{l_n,tb} \\ \mathbf{K}_{l_n,bt} & \mathbf{K}_{l_n,bb} \end{bmatrix} \begin{Bmatrix} u_{l_1,t} \\ u_{l_n,b} \end{Bmatrix} = \begin{Bmatrix} \sigma_{l_1,t} \\ 0 \end{Bmatrix}. \tag{2.187}$$

In order to solve Eq. (2.186) additional boundary conditions related with longitudinal, flexural or torsional wave motion need to be considered, which were mentioned in the paragraph 2.2.3. Applying of boundary conditions related with stresses and displacements at the top and bottom of extreme layers simplifies the Eq. (2.186). A non-trivial solution of a homogeneous algebraic system can be obtained when the system determinant is equal to zero.

With the aim to track dispersion curves for multilayered specimen presented in further parts of the thesis software PCDISP [192] was used.

Page intentionally left blank

CHAPTER 3

Experimental investigations and finite element modelling of wave propagation

This Chapter contains the essential information about experimental and numerical methods used in investigations presented in further parts of the thesis. The Chapter is divided into two parts. The first part is focused on describing a strategy of finite element method (FEM) program ABAQUS to solve the wave propagation problems. A typical numerical model of a ground anchor has also been described. Experimental investigations are presented next. Experimental setup, criteria influencing on the choice of excitation frequency, the number of cycles and windowing functions are discussed.

3.1 Modelling of wave propagation

In general two different approaches of modelling of guided wave propagation phenomenon can be distinguished. The first approach presented in Chapter 2 assumes investigating an analytical solution of governing motion equations for analyzed type of structure. The main advantage of modal models is they exact character. They allow predicting number of modes which can propagate for a chosen excitation frequency and establish their propagation velocity or assess the intensity of wave leakage into surrounding medium in case of multilayered structures. A prior knowledge on wave structure or wave field distribution is essential for choosing an appropriate mode for diagnostics purposes what can significantly reduce the complexity of wave propagation phenomenon. The programs capable to analyse wave propagation problems in continuous uniform and infinitely long structures are DISPERSE ([129],[170]), or PCDISP [192].

Analytical solutions, despite of important advantages, can be used in a limited range of engineering problems only. Dispersion curves can be obtained only for objects with simple geometry for which dispersion equation can be formulated, while majority of engineering structures are complex-shaped. In each structure an infinite number of wave modes can be excited and additionally, various interactions between them can occur. Interactions with complex structural features including multiple-cracks, irregular geometry or corrosion in layered, anisotropic materials often cannot be effectively described by means of analytical approach only.

The second approach is based on numerical simulations of wave motion what allows to recognize the cases which cannot be analyzed analytically or experimentally. Numerous of different computational techniques can be applied in wave propagation modelling, such as finite difference method (FDM) ([199],[201]), finite element method (FEM) ([21],[56],[106],[234]), finite strip elements (FSE) ([32],[124]), boundary element methods (BEM) ([33],[231]), mass-spring lattice model (MSLM) ([50],[224]), local interaction simulation approach (LISA) ([46],[47],[48],[49],[116],[117]), time-domain spectral element method (SEM) ([36],[108],[109],[167],[172],[182],[187],[215],[246],[248]) or FFT-based spectral element method ([51],[165]).

Nowadays, the finite element method is the most common one. The main advantage of FEM is a variety of commercial ready-made codes which do not have to be modified or developed by the user. In general a finite element mesh can be easily generated and quality of the output can be improved by mesh refinement. The FEM allows modelling wave motions in complex structures and visualizing results what was successfully applied in a wide range of wave propagation problems ([8],[238]). The FEM provides information on complicated cases such as interaction with local changes like various discontinuities ([9],[56],[207]). Analysis of wave motion may be conducted without any special knowledge about the behaviour of particular mode however, the most important and real advantages of FEM application come from combining computational techniques with analytical investigations. Analytical solutions can be applied to determine the cut-off frequencies of particular wave modes, calculate their velocities and chose the most appropriate modes for the conducted investigation, while FEM allows verifying the mode choice and simulating the disturbance propagation.

In this work a two-dimensional finite element method of structural dynamics is employed to recognize and visualize phenomena occurring during wave propagation in embedded bars. A commercial software ABAQUS was firstly introduced and then used in the modelling of multilayered cylinders. Prior to results presentation of numerical studies in the next chapters, a short introduction on ABAQUS strategy of solving dynamics problems, meshing and infinite boundary conditions is presented.

3.2 ABAQUS strategy

In general, dynamics problems can be divided into two groups. The first group is addresses to analysis in the case of relatively low frequencies of an applied load and slower vibrations, like seismic problems. The second group relates the cases of higher frequency range, like wave propagation problems. The response history of dynamic problems can be generally obtained by a modal method, implicit direct integration or explicit direct integration. The modal method and implicit direct integration are suitable for the problems of structural dynamics, while explicit direct integration is usually used to solve wave propagation problems. However, it is possible to use both explicit and implicit integration to solve time-domain wave propagation problems, but the explicit direct integration is far more efficient and is characterized by lower computational cost. In this work, time-domain models are solved with the help of ABAQUS/Explicit package [1], based on explicit integration rules.

3.2.1 ABAQUS Explicit method

Regarding dynamic problems, the applied load is time function and consequently the response of a structure is time-variant, too. The equation of dynamic equilibrium is:

$$\mathbf{M}\ddot{\mathbf{u}}+\mathbf{C}\dot{\mathbf{u}}+\mathbf{K}\mathbf{u}=\mathbf{F}, \tag{3.1}$$

where $\ddot{\mathbf{u}}$, $\dot{\mathbf{u}}$ and $\mathbf{u}$ are nodal acceleration, velocity and displacement, respectively. The matrix $\mathbf{M}$ is a diagonal lumped mass matrix, $\mathbf{C}$ is a viscous damping matrix and $\mathbf{K}$ is a static stiffness matrix involving elastic modulus and Poisson's ratio of the material. The vector $\mathbf{F}$ covers the external load. Dynamic analysis assumes that the acceleration-dependent inertia forces and the velocity-dependent damping forces are both taken into consideration. Because inertia forces, damping forces and elastic forces are all time-dependent, there is a need to satisfy Eq. (3.1) not at any time t but at discrete time intervals Δt separately [21]. Next, the Eq. (3.1) can be rewritten with respect to *i*th time step:

$$\mathbf{M}\ddot{\mathbf{u}}^{i} + \mathbf{C}\dot{\mathbf{u}}^{i} + \mathbf{K}\mathbf{u}^{i} = \mathbf{F}^{i}\,. \tag{3.2}$$

Direct integration conducts a numerical step-by-step procedure to integrate the equations. Direct integration assumes that the integrated equations are not transformed into a differential equation form [21]. When the solution is required from 0 to time *T*, the considered time is divided into *n* equal time intervals Δt and then the approximate solution is investigated at time instants 0, Δt, $2\Delta t$, $3\Delta t$, $\ldots, t, \ldots, T$. One of effective ways to solve equations of motion for certain time steps is the Central Difference Method which is utilized in ABAQUS software and it is based on the following assumptions:

$$\dot{\mathbf{u}}^{(i+\frac{1}{2})} = \dot{\mathbf{u}}^{(i-\frac{1}{2})} + \frac{\Delta t^{(i+1)} + \Delta t^{(i)}}{2}\ddot{\mathbf{u}}^{(i)} \tag{3.3}$$

$$\mathbf{u}^{(i+1)} = \mathbf{u}^{(i)} + \Delta t^{(i+1)}\dot{\mathbf{u}}^{(i+\frac{1}{2})} \tag{3.4}$$

The superscripts $i+\frac{1}{2}$ and $i-\frac{1}{2}$ refer to mid-increment values. Explicit integration is applied in the ABAQUS code, what means that the results for a current step are obtained using historical results. While the values $\dot{\mathbf{u}}^{(i-\frac{1}{2})}$ and $\ddot{\mathbf{u}}^{(i)}$ are known, the current kinematic state can be determined:

$$\mathbf{u}^{(i+1)} = f\left\{\mathbf{u}^{(i)}, \dot{\mathbf{u}}^{(i)}, \ddot{\mathbf{u}}^{(i)}, \mathbf{u}^{(i-1)}, \ldots\right\} \tag{3.5}$$

The explicit procedure is computationally efficient because the global mass matrix is not necessary to be assembled and inverted. The mass matrix $\mathbf{M}$ is diagonal, so when accelerations are calculated:

$$\ddot{\mathbf{u}}^{(i)} = \mathbf{M}^{-1}(\mathbf{F}^{(i)} - \mathbf{I}^{(i)}) \tag{3.6}$$

The matrix $\mathbf{M}^{-1}$ can be easily obtained. The vector $\mathbf{F}$ is applied load vector and $\mathbf{I}$ is the internal force vector.

In general, explicit methods are conditionally stable only. The time step size Δt is intended to be smaller than the critical time step Δt_{cr} in order to satisfy stability limit [166]:

$$\Delta t \le \Delta t_{cr} = \frac{2}{\omega_{\max}}\,. \tag{3.7}$$

The critical time step Δt_{cr} is a limit value to assure stability of undamped linear systems. The stability limit depends on maximum eigenfrequency $\omega_{\max}$. In problems of wave propagation in solids the critical time step is approximately equal to a time for the longitudinal elastic wave to run through the smallest element of the model mesh with velocity c_L ([25],[104]):

$$\Delta t \leq \Delta t_{cr} = \frac{\Delta L}{c_L}, \tag{3.8}$$

where ΔL is the smallest element size (Figure 3.1). The relationship between the stability limit and the transit time for information between two adjacent nodes is known as the Courant-Fredricks-Lewy condition (*CFL* condition) [38]. The ratio between the actual time step used in the model and a critical time step is called a Courant number:

$$CLF = \frac{\Delta t}{\Delta t_{cr}}. \tag{3.9}$$

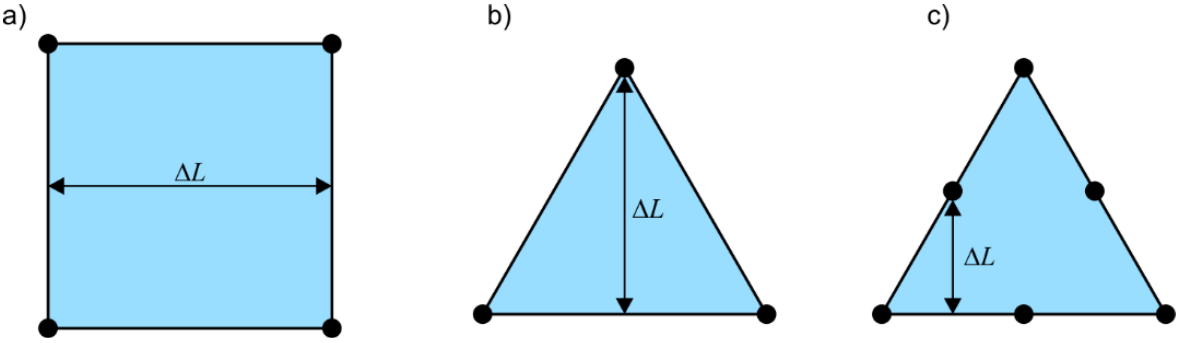

Figure 3.1 Smallest element size ΔL for a) linear square element, b) linear triangle element and c) quadratic triangle element

Substituting Eq. (3.8) into (3.9), the time increment formula can be rewritten in the following form:

$$\Delta t = CFL \Delta t_{cr} = CFL \frac{\Delta L}{c_L}. \tag{3.10}$$

The increment length must satisfy the stability condition, but also there are some recommendations related with the wave time period. An efficient procedure is to use an amount of minimum 20 points per cycle at the highest frequency [155]:

$$\Delta t = \frac{1}{20 f_{\max}} \tag{3.11}$$

Longer time increments may lead to divergences in high-frequency resolving components. A shorter time increment may bring the waste of computation time. The amount of 20 points is recommended as a compromise between both accuracy and speed criteria.

The second important factor influenced by wave frequency and in consequence its velocity is the finite element size. The level of discretization is determined by the condition, which says that per the shortest wavelength of interest at least 20 nodes must be introduced in a model. The condition can be written as:

$$l_e = \frac{\lambda_{\min}}{20} \tag{3.12}$$

where l_e is element size and $\lambda_{\min}$ is the shortest wavelength of interest.

3.2.2 Description of typical FEM model

All rods investigated in this thesis had a circular cross-section and were embedded in mortar block with a circular cross-section, too. A typical anchor model is therefore axisymmetric. The axisymmetric model allows to shorten the time of calculations, however axisymmetry implies some restrictions. The main drawback of the use of the axisymmetric model is the threat of no mode conversion between wave modes with different circumferential order, so the flexural modes would not propagate. In order to allow the propagation of any mode, a three-dimensional specimen model is necessary to naturally involve a longer calculation time.

The axisymmetric FEM models of ground anchors were developed applying 4-node bilinear axisymmetric quadrilateral elements with reduced integration (CAX4R). The dimensions of all elements were 1 mm × 1 mm. In order to choose an appropriate element size, the mesh convergence study has been performed. The transient wave propagation problem was solved with the integration time step $\Delta t = 10^{-7}$ s. In every investigated case a narrow range of relatively low frequencies was assumed (60-100 kHz), thus, all performed models were characterized by the same element size and the same length of the integration time step.

The wave excitation performance was conducted applying a concentrated force at a chosen node. The load was applied as a sine function modulated by the Hanning window. Material parameters and geometry of the model as well as parameters of excitation load (number of cycles of sine, frequency) were introduced in ABAQUS on the basis of experimental data. Material damping effects in anchor models were neglected here.

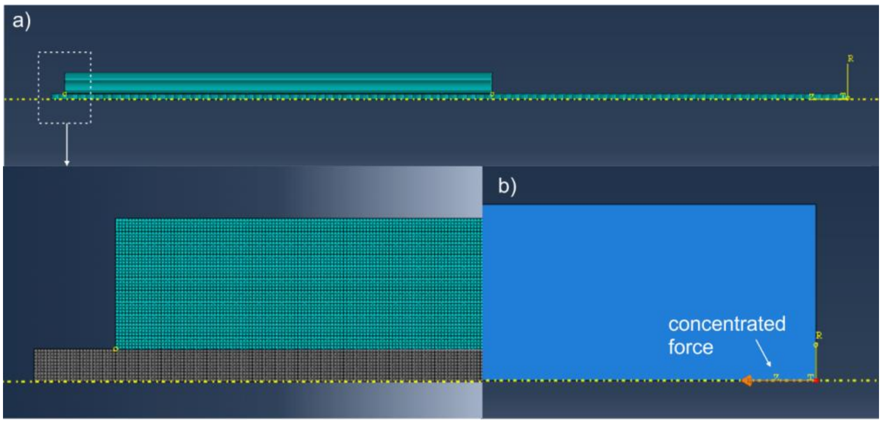

Figure 3.2 Ground anchor model: a) geometry and b) applied concentrated force

The models of ground anchors were validated comparing the shape and the amplitude of experimental and numerical signals. The numerical models were created taking into account geometry and material parameters of experimental models. Next, numerical models were divided into two groups A and B: one group (A) was used to calibrate numerical parameters, which could not be determined experimentally. The calibration was performed comparing the shapes and amplitudes of numerical and experimental signals. The identified, calibrated parameters were introduced in models in the group B. The numerical results of group B were then compared with the experimental results.

The connection between the rod and the cover was assumed rigid and modelled as a tie constraint. In case of modelling the debonding between the mortar cover and the steel rod (see Chapter 5), the connection between steel and mortar was not defined on a certain length. Exemplary acceleration map of the anchor with debonding located in the middle of the specimen is presented in Figure 3.3.

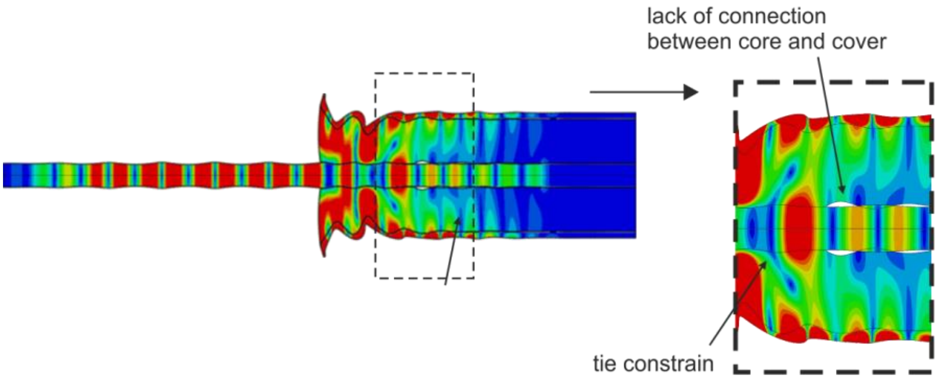

Figure 3.3 Model of ground anchor with debonding between core and cover

3.2.3 Infinite elements

In order to consider the case of ground anchor with large diameter of the anchor body or to include high energy dissipation at the border of mortar and soil, infinite elements have been introduced in several anchor models. Infinite elements are generally applied to model the surrounding medium whose size is large compared to the region of interest by conjunction with standard finite elements.

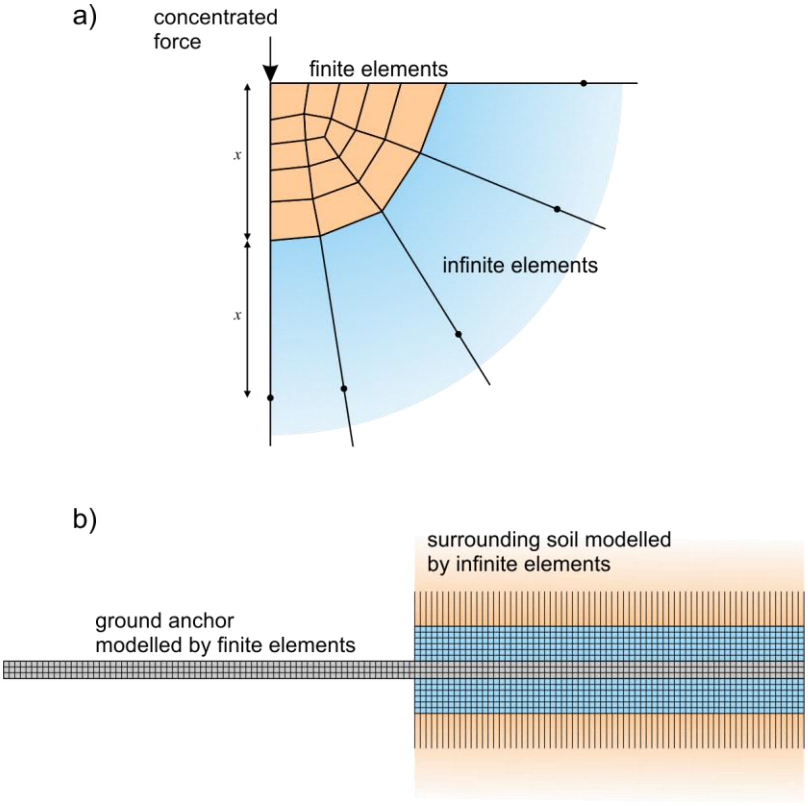

Figure 3.4 Application examples of infinite elements: a) point load on elastic half space [1] and b) ground anchor surrounded by the soil

The region of interest should be modelled by standard finite elements while infinite elements should be used to model the far-field behaviour (Figure 3.4). According to [1] infinite elements are characterized by a linear behaviour and are applied while there is a need to consider boundary value problems defined in unbounded domains. In the case of dynamic analysis they provide “quiet” boundaries. In conducted analyzes presented in Chapter 4, 4-node, one-way infinite axisymmetric solid continuum elements (CINAX4) with two degrees of freedom in each node were used.

3.3 Experimental investigations

3.3.1 Experimental setup

The instruments used in experimental tests include the PAQ 16000D device for generation and registration of wave signals and the plate piezo actuators Noliac NAC2011 used for both actuation and sensing of guided waves. The PAQ 16000D device allows to investigate wave propagation in structural elements collecting signals which contain information about object response (Figure 3.5a). The wave excitation was performed using piezo elements located at one end of the tested specimen (Figure 3.5b).

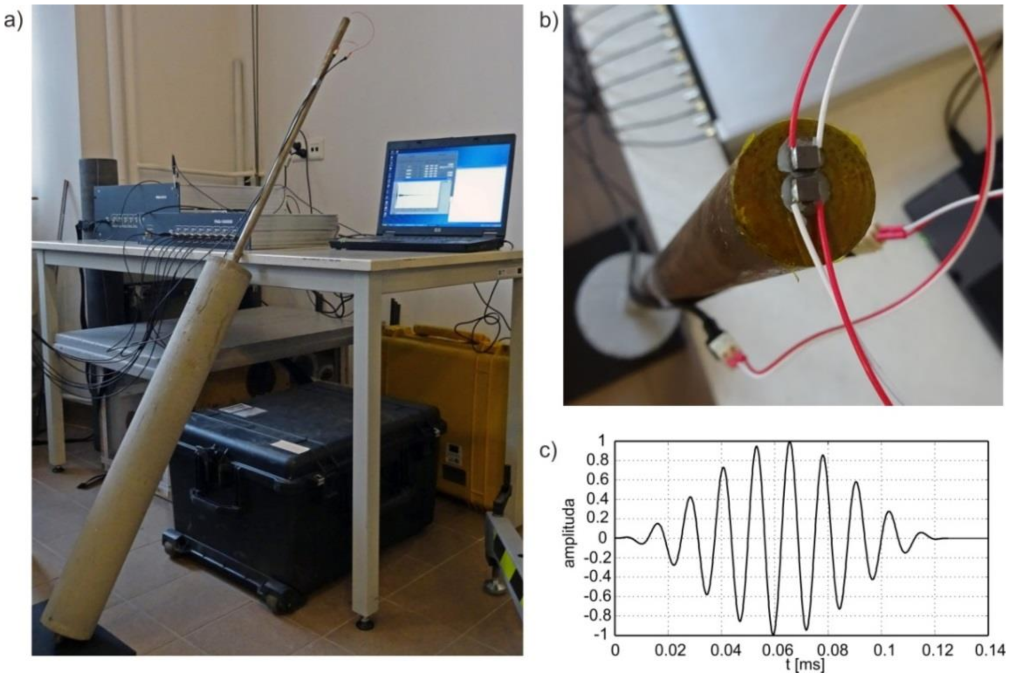

Figure 3.5 Experimental setup: a) laboratory model of ground anchor, b) actuator and sensor attached to the free end of the specimen, c) excitation signal [235]

It is well known that an effective monitoring system and reliable damage detection requires an appropriate location of transducers. Their position is usually determined by location of critical areas which need to be monitored. Location of the actuator determines a type of an excited wave mode. In the case of unfavorable actuator location, the wave can be damped fast what is especially disadvantageous while structures detect a significant wave attenuation level (i.e. concrete structures). Also, the large distance between actuator and the sensors results in a poor signal-to-noise ratio and the spread of signal due to dispersion. Despite the fact that many methods dedicated to optimize the sensor and actuator location have been proposed, they cannot be easily used in anchors monitoring due to practical aspects. As mentioned in Chapter 1, the anchor is mostly located underground and there is access to any of its part. For practical reasons, actuator can be located at the free end of the anchor tendon. The free end of a tendon is only part above the ground after making the anchor. It can be assumed that while performing a ground anchor it is possible to install additional transducers in any location of the anchor, however, the most practical solution is to attach them on the free end of a specimen. For this reason in the majority of the presented research the actuator was located at the free end of the anchor.

The piezo elements are widely used as versatile components of SHM systems due to their advantages like duration, relatively low cost and small size. They can be used in a wide frequency range from 10 to 500 kHz what allows frequency adjustment to the monitored object or type of detected damage. The piezo elements use piezoelectric effect to measure changes in strains converting them to electric charge. They can be attached to the object by means of wax adhesive.

3.3.2 Excitation signal

3.3.2.1 Shape of excitation signal

The excitation signals used in experiments were applied in the form of sine functions modulated by Hanning window (Figure 3.6). The function of excitation load can be expressed as:

$$p(t) = \begin{cases} p_0 \sin(2\pi ft) \cdot w(t) & t \in [0, T_w] \\ 0 & t \geq T_w \end{cases} \tag{3.13}$$

where f is excitation frequency, p_0 is signal excitation amplitude, T_w is the length of a modulating window. The modulation window is described by a function $w(t)$:

$$w(t) = 0.5\left(1 - \cos(2\pi ft / n_w)\right), \quad t \in [0, T_w] \tag{3.14}$$

and n_w is the number of counts in the tone burst. A possible excitation function is presented in Figure 3.7. The modulation of sine function is a technique minimizing frequency leakage and decreasing amplitude of sidelobes in signal frequency representation. Windowing involves forcing the amplitude of input signal at the beginning and at the end of input signal interval to run smoothly towards a single common amplitude value [133]. Figure 3.8 presents the Fast Fourier Transform (FFT) spectra of 10-cycle sine function modulated by various window functions. The most significant reduction of sidelobes leakage is provided using Hanning window so it was applied in the investigations.

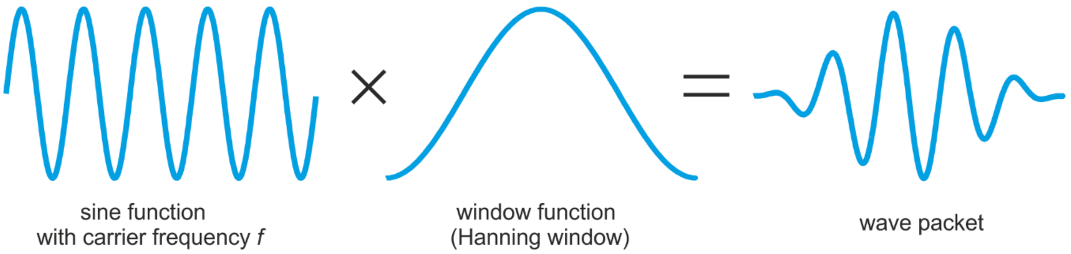

Figure 3.6 Modulation of wave excitation signal used in experimental investigations

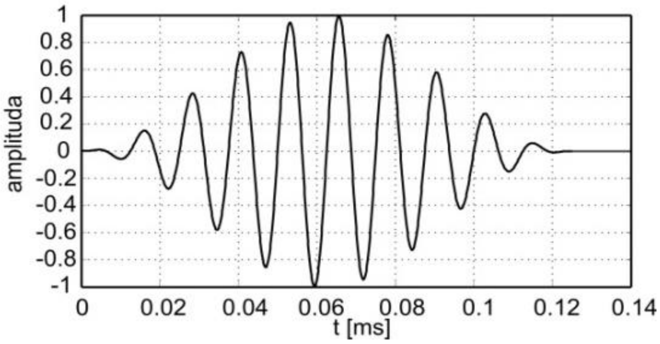

Figure 3.7 Exemplary excitation function: ten-cycle sine with carrier frequency of 80 kHz modulated by Hanning window

The second important parameter of the excitation signal is the number of cycles. Let’s consider examples of signals and their FFT spectra. As previously, the sine function

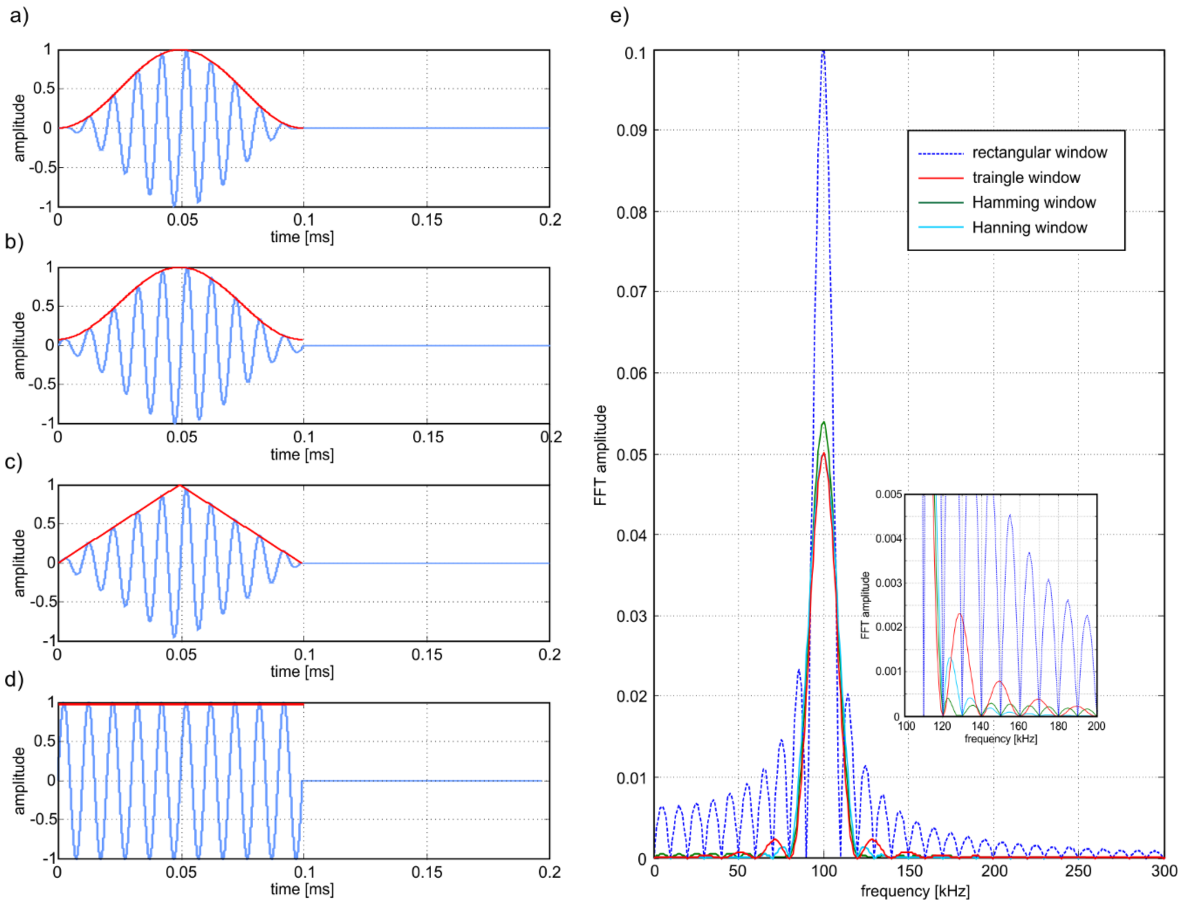

Figure 3.8 Sine excitation signals modulated by a) Hanning, b) Hamming, c) triangle, d) rectangle window and e) their Fast Fourier Transforms spectra

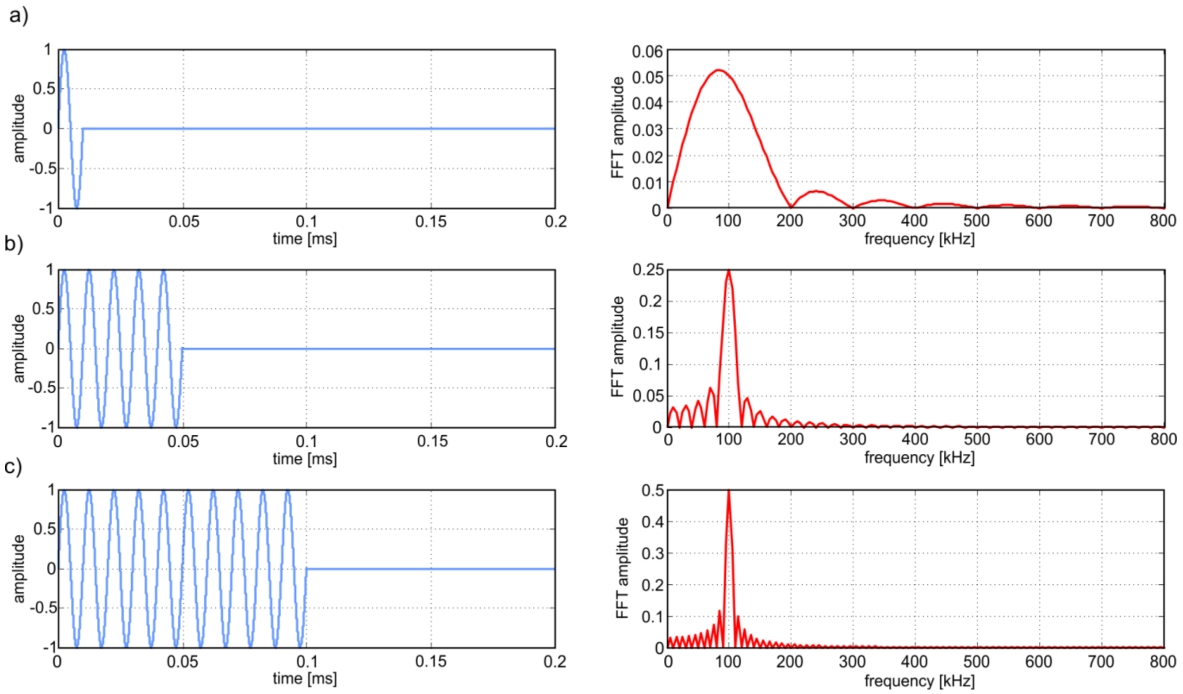

Figure 3.9 Sine excitation signals and their Fast Fourier Transforms spectra: a) signal with one cycle, b) signal with five cycles and c) signal with ten cycles

is considered however, only a rectangular window is applied. Figure 3.9 presents three sine function examples with the same frequency of 100 kHz and a unit amplitude but with variable number of cycles. The first sine shows one cycle, the second one shows five cycles and the last one detects ten cycles. It can be seen that in the case of five and ten-cycle sine the main lobe peak value in FFT corresponds to the excitation frequency of 100 kHz (Figure 3.9b and c). For a one-cycle sine the main lobe peak value in FFT corresponds to a lower frequency what is incompatible with the input data. The most visible influence concerns the number of cycles on main lobe parameters. The main lobe width decreases and an amplitude increases with an increasing number of cycles. This effect especially concerns the cases of desirable narrow frequency range excitation. However, according to Heisenberg uncertainty principle the “spread” of an input function and its Fourier transform are inversely proportional. A single peak in the spectrum of FFT requires an infinitely excitation time. The main drawback of a significant number of cycles of an excitation signal is the time duration of an excitation. In the case of long excitation particular reflections are possibly registered in the signal even during the excitation, what significantly hinders the signal interpretation. It should also be mentioned that despite narrowing of the main lobe by increasing number of cycles of excitation, in each FFT some side lobes are visible. The presence of side lobes in FFT spectrum indicates frequency leakage what is minimized by windowing (compare Figure 3.8).

3.3.2.2 Frequency selection criteria

Guided waves are dispersive waves and for this reason excitation frequency determines propagation velocity but also number of possible modes to be excited. The higher frequency, the larger number of possible wave modes. A large number of propagating modes may lead to difficulties in inspection. On the other hand, high frequency provides short time of an excitation packet. A short packet with a large number of cycles results in a narrow bandwidth of excitation. Moreover, short packets provide good temporal separation of. incident and reflected waves. There is a need to find a compromise between number of modes and signal legibility. Moreover, wave attenuation is affected by frequency. The signals registered for various excitation frequencies are characterized by different amplitudes.

The frequency used in experiments was chosen of the basis of a tunning test. The tunning test was based on comparison of signal amplitudes collected after excitations of various frequencies in the investigated specimens. The choice of the carrier frequency

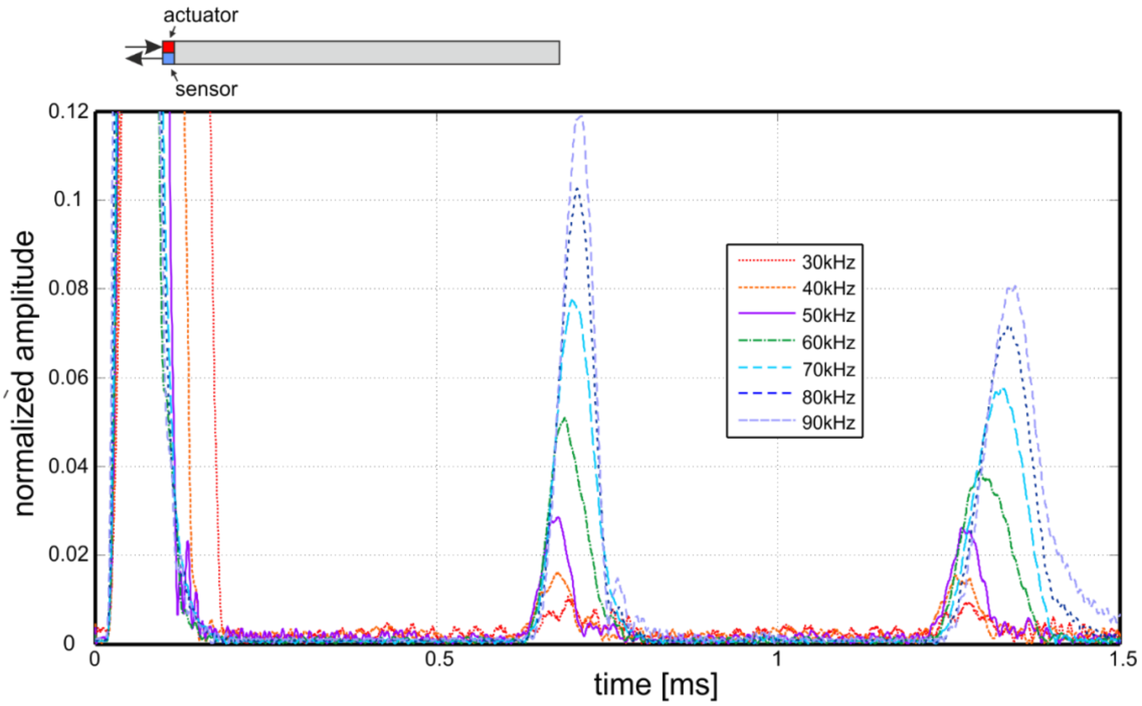

Figure 3.10 Set of wave propagation signals (in the form of signal envelopes) collected during experiments for different carrier frequency of excitation for the free rod

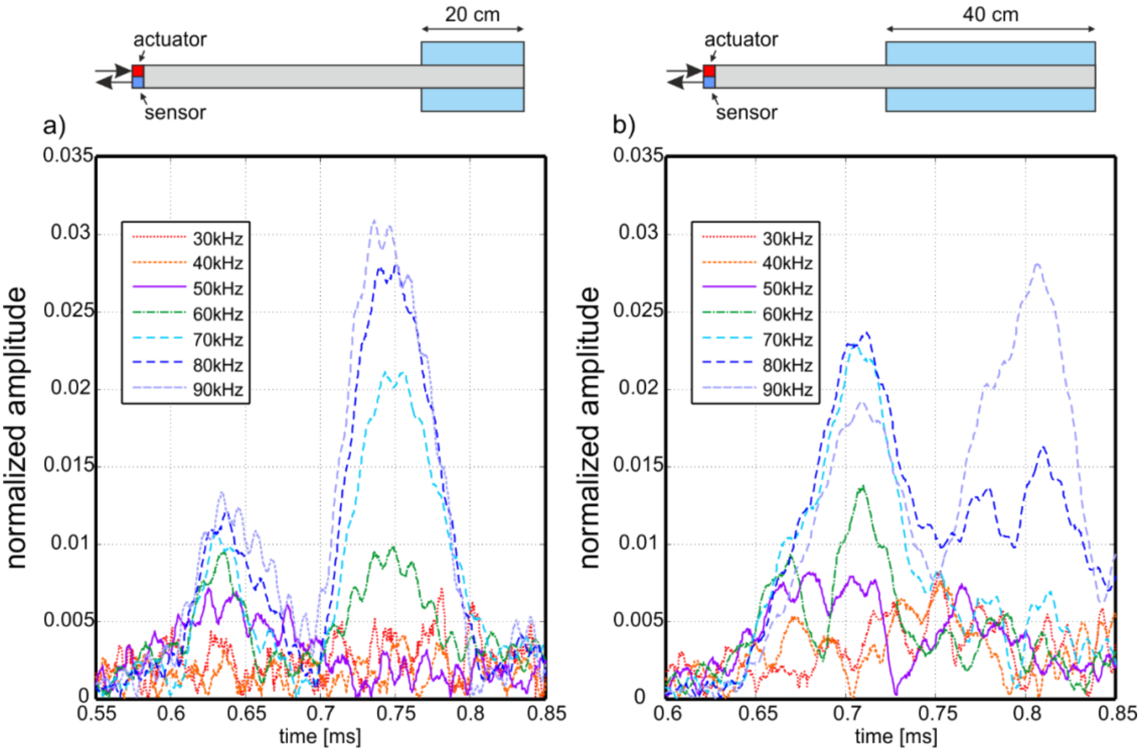

Figure 3.11 Set of reflections from anchorage collected during experiments for different carrier frequency of excitation for anchor with bonding length equal to: a) 20 cm, b) 40 cm

was influenced by the amplitude of the characteristic peaks values, the number of possible modes which can be excited in specimen and legibility of a signal. Exemplary tunning test is described in [236]. During investigations different excitation frequencies have been tested with the aim to select the most sensitive frequency for detection of border of media. In Figure 3.10 and Figure 3.11 envelopes of signals obtained for a free rod and for two anchors with different bonding lengths are presented. Envelopes of wave propagation signals created using the Hilbert transform.

The envelopes of the vibration velocity signals were normalized with respect to the input wave amplitude by the following formula:

$$\hat{v}_n(t) = \frac{\hat{v}(t)}{\max\left(\hat{v}(t)\right)} \tag{3.15}$$

where $\hat{v}(t)$ is the spectrum of the Hilbert transform of velocity signal $v(t)$. It can be observed that the amplitude of the first and second reflections from the end of the rod varies with the change of frequency of an incident wave. Even though reflections for all considered frequencies are clear, a significant difference between amplitude values for different carrier frequencies can be observed. With the increase of the excitation frequency, the increase of the first and second reflection can be observed. The maximum value was archived for the frequency of 90 kHz, while some frequencies (compare results registered for 30 and 40 kHz) brought the reflections from the end of the rod (Figure 3.10) or from the anchorage (Figure 3.11) are almost invisible.

Page intentionally left blank

CHAPTER 4

Wave propagation in undamaged ground anchors

4.1 Introduction

As mentioned in Chapter 1 rock bolts and ground anchors are widely used in mining, tunnelling and geotechnical engineering to prevent the movement of rock or ground strata. They are subjected to continuous state deterioration due to the exposure to corrosive environments or excessive loads ([65],[98]), thus the real problems of such permanent structural elements concerns their durability. Since visual inspection of anchors is not possible and the conventional pull-out tests are destructive, expensive and time consuming, various non-invasive testing methods and monitoring techniques have been recently developed ([151],[152]).

As mentioned in paragraph 1.2 ground anchors are structures especially threatened by damages caused by corrosive environment or excessive loads. However, even a healthy undamaged ground anchor brings a significant threat for the safety and durability of a whole supporting structure if the anchor was performed out of design assumptions or its dimensions differ from the design anchor dimensions. The main issue for the geotechnicians is the inability to verify real fulfilment of design assumptions and the anchor dimensions consistency check with the project. The quality of manufacturing can be tested during the pull-out tests, however, due to many drawbacks of this destructive method, there is a need to develop less invasive techniques which would be employed in the diagnostics of all performed anchors, not just a few selected ones.

Two major groups of nondestructive testing methods of anchor structures include vibration methods (e.g. [96],[161]) and wave propagation methods (e.g. [24],[39],[40],[118],[210],[221],[229],[242],[243],[244]). The design and dynamic analysis of an impulse generating device for the condition assessment of ground anchors have been developed by Neilson et al. [161]. Both impulse and sine excitations to estimate a total bolt length were investigated by Ivanović and Neilson [96]. Beard and Lowe [24] applied guided waves to determine a bolt length and to identify major defects in rock bolts. Zhang et al. [229] analysed numerically the characteristics of guided waves in free and grouted rock bolts as well as the effect of mesh density and wave frequency on the obtained results. Numerical simulations of wave attenuation and group velocity in rock bolts were conducted by Cui and Zou [39]. They proposed a method to determine boundary effects on the attenuation at the bolt ends. The behaviour of guided waves in free and grouted rock bolts was also studied by Zou et al. [242]. In the paper, attenuation and group velocity of guided waves were tested experimentally, with respect to frequency and the grouted length. Experimental and numerical investigations of wave propagation in rock bolts for different frequencies of excitation were conducted by Wang et al. [210]. They also presented results for grouted rock bolts at various curing times and investigated the formation of the interface wave. Zou et al. [243] investigated the correlation between the group velocity and the attenuation of captured signals and the grout quality, in particular the air content in the grout and the grout compressive strength. Zou and Cui [244] proposed a field test method of installing a receiving transducer on the grout surface of the bolt. The application of Fourier and wavelet transforms for the evaluation of rock bolt integrity was performed by Lee et al. [118]. Wu et al. [221] described and experimentally tested nondestructive determination of bolt length, anchoring length and body forces by means of stress waves. Cui and Zou [39] conducted numerical simulations and laboratory tests of wave attenuation and the group velocity in fully grouted rock bolts and bolts with grout voids or insufficient rebar length.

The previous studies indicate a large potential of the use of guided wave propagation techniques in diagnostic applications of anchored systems. However, most of the above reported works deal with the diagnostics of rock bolts. This Chapter is focused on nondestructive inspection of ground anchors, much more complex than the rock bolts, despite many similarities. The main difference is the presence of the so-called anchor body of a possible significant diameter compared to the fixed zone of rock bolts.

The Chapter describes wave propagation phenomena in a healthy ground anchor. Particular attention is paid to the characteristic features of guided waves propagating in free and embedded parts of the tendon, at the interface between the tendon and the surrounding anchor body as well as waves diffracted on the start of the anchor body.

The anchors with variable length and diameter of the anchor body and the anchors with non-reflecting boundary conditions are analyzed numerically. Experimental measurements are conducted on ground anchors variable in the fixed length. The study shows that the detailed recognition of the phenomenon of the transfer of wave energy between the tendon and the anchor body is crucial for the appropriate application of guided wave propagation method for nondestructive inspection of ground anchors.

Both, experimental and numerical results clearly indicate that three decisive geometric parameters (anchor body length, free length of steel tendon and diameter of the anchor body) can be successfully determined on the basis of the registered signals. The results presented in this Chapter were published in [239].

4.2 Theoretical background of wave propagation in healthy ground anchor

4.2.1 Multimode propagation in free and embedded bar

A ground anchor consists of three parts: an anchor head, a tendon and an anchor body ([86],[222]). A schematic sketch of components of the ground anchor is given in Figure 4.1. The tendon can be made of a steel bar, a multi-wire strand, drill-hollow systems or a cable. The total length of the tendon can be divided into the free length and the bond length. The anchor body is formed in the subsoil by cement grout injection. The wave excited at the free end of the tendon, propagates along its free length and next, along the fixed length. At the interface between the tendon and the anchor body the wave leakage occurs. Moreover, at the starting point of the tendon fixing in the anchor body, wave diffraction takes place. In this section, characteristic features of waves propagating in ground anchors are investigated.

As mentioned above wave excited at the free end of the tendon propagates along single-layer steel bar. Due to grout surrounding the steel core along a fixed length the problem of wave propagation becomes more complicated and there is a need to consider wave propagation in multilayered rods.

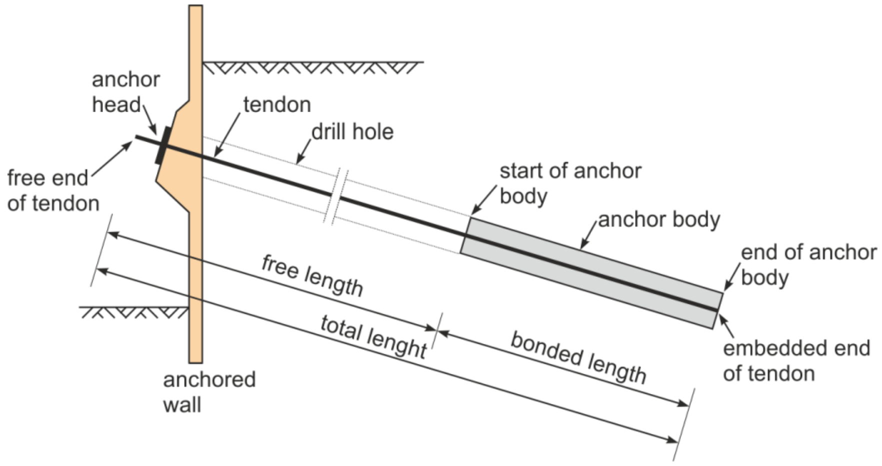

Figure 4.1. Schematic sketch of ground anchor components

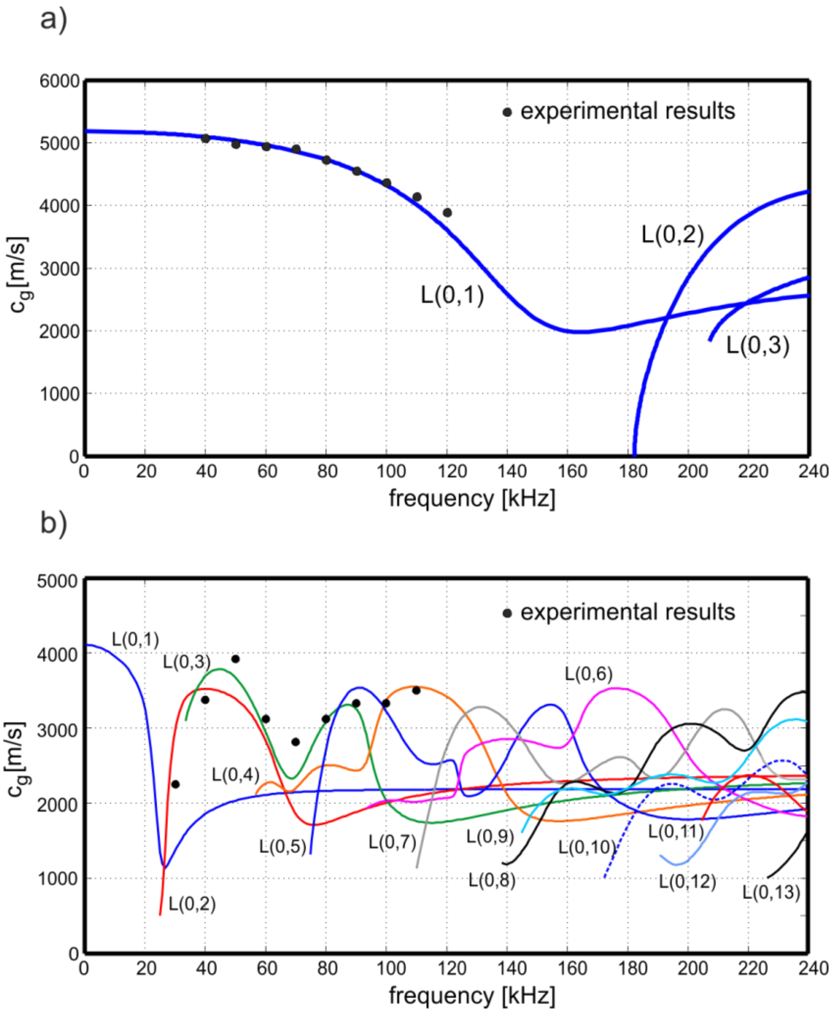

Figure 4.2 Group velocity dispersion curves of a) 2 cm diameter steel bar (*E* = 210 GPa, *ν* = 0.2, ρ = 7820 kg/m^3) and b) for a steel 2 cm diameter bar (*E* = 210 GPa, *ν* = 0.3, *ρ* = 7820 kg/m^3) embedded in 4 cm thickness cover (*E* = 26 GPa, *ν* = 0.2, *ρ* = 2084 kg/m^3)

Figure 4.2a illustrates the group velocity dispersion curves for a bar of a circular cross-section with a 2 cm diameter which is considered in the next part of the Chapter. In the presented frequency range 0–240 kHz three longitudinal modes propagate, i.e. the fundamental mode $L(0,1)$ and two higher $L(0,2)$ and $L(0,3)$ modes appearing above their cut-off frequencies. The dispersion curves calculated by solving the Pochhammer equation (2.122) are compared with the experimental data in the range 40–120 kHz.

In the case of a bar embedded in the material of different physical properties, it is necessary to calculate the dispersion relations for a multilayered elastic solid cylinder. The ground anchor can be considered a two-layer axially symmetric system consisting of a layer of steel and a layer of the cement grout.

It can be seen in Figure 4.2b that the presence of additional 4 cm layer of the grout causes a significant increase of the number of propagating modes and thus the increase in the complexity of the occurring phenomena. The cut-off frequencies of higher-order modes have lower values than for the free bar, thus in the considered frequency range the number of propagating modes significantly increases. Moreover, the velocity of the fastest $L(0,1)$ mode in the free bar is significantly higher than the velocity of $L(0,1)$ mode in the bar with the cover. Experimental results are marked in Figure 4.2b by dots. They were determined in the frequency range 30–110 kHz, exhibiting multimode propagation. Calculation of the wave velocity was based on the time-of-flight (Figure 4.3). In the measured signal the first reflection from the end of the specimen has been identified and the wave velocity was determined on the basis of time-of-flight registered for this wave packet. This approach brings about the velocity of the fastest mode for a given frequency only. The other slower wave modes were not identified.

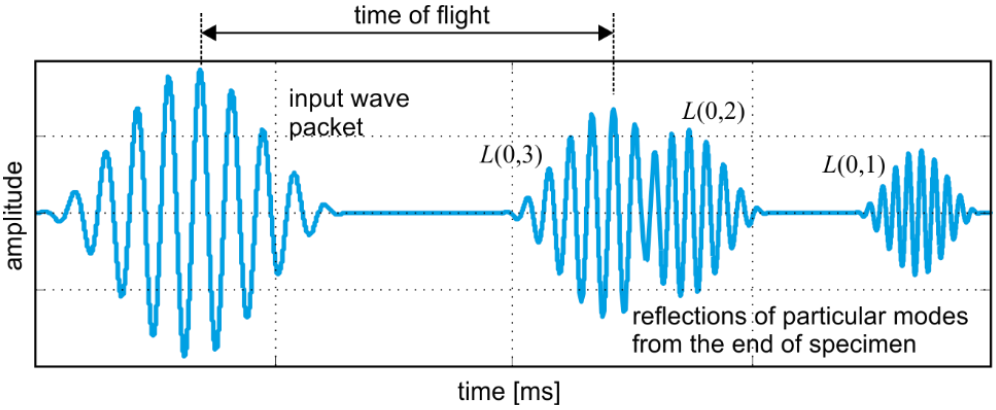

Figure 4.3 Scheme of the signal and time-of-flight determining

4.2.2 Wave propagation at the bar/anchor body and the anchor body/ground interface

Considering a wave that passes through the interface between media with different physical properties (i.e. mass density ρ and modulus of elasticity E), two phenomena may occur, i.e. reflection from the interface or transmission into the second medium. The intensity of reflection and transmission occurring at the media boundary depends on the acoustic impedance Z, which is an inherent property of a medium [71]:

$$Z = \rho c_P = \sqrt{\rho E}\,. \tag{4.1}$$

The reflection coefficient R and the transmission coefficient T can be defined on the basis of acoustic impedances [180]:

$$R = \frac{Z^{(2)} - Z^{(1)}}{Z^{(1)} + Z^{(2)}} = \frac{\rho_2 c_2 - \rho_1 c_1}{\rho_1 c_1 + \rho_2 c_2} \tag{4.2}$$

$$T = \frac{2Z^{(2)}}{Z^{(1)} + Z^{(2)}} = \frac{2\rho_2 c_2}{\rho_1 c_1 + \rho_2 c_2} \tag{4.3}$$

The transmission and reflection coefficients are parameters describing the extend of wave energy reflected from the media boundary and the extend of energy transferred into the second medium. When the acoustic impedances of both media are equal, the transmitted wave is identical to the incident wave and the presence of the interface does not affect the incoming wave.

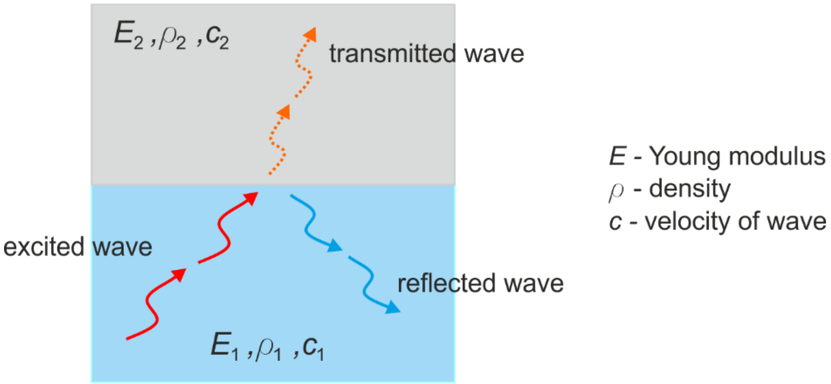

Figure 4.4 Wave reflecting and passing through the boundary between media

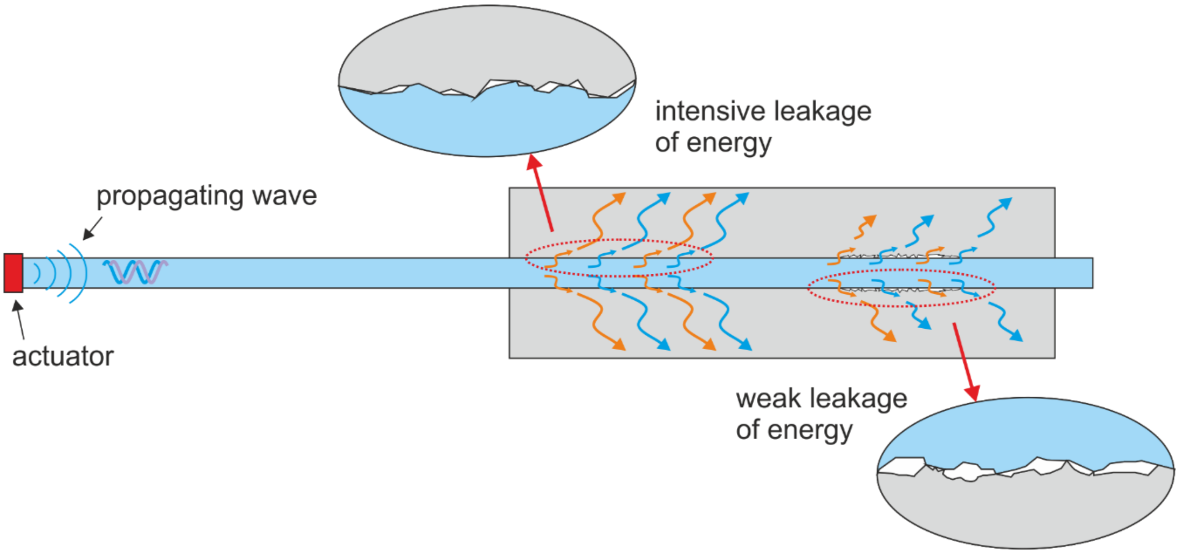

Figure 4.5. Wave leakage at the interface between steel bar and surrounding anchor body

In the case of two media with different values of the acoustic impedance only the part of the wave energy passes into the second medium, while the remaining part is reflected. For $Z^{(2)} \gg Z^{(1)}$, the reflected wave is much weaker than the transmitted wave. While $Z^{(2)} \ll Z^{(1)}$ the reflected wave is much stronger than the transmitted wave. The acoustic impedance of the second medium close to zero results in a complete wave reflection.

Ground anchors consist of two layers made of different materials: a steel bar and a surrounding anchor body. The longitudinal guided wave excited in the bar propagates along its length. In the fixed part, the wave transmitted along the bar leaks into the anchor body (Figure 4.5). The intensity of the leakage of the wave energy depends not only on the material parameters of two media but also on the quality of the bond between the bar and the anchor body. If the bonding quality is high, the energy transfer from the bar to the surrounding medium is strong, producing a large wave leakage. In the case of weak bonding the wave leakage is less effective.

The ground anchor bodies are manufactured in a pre-drilled hole in the ground by grouting. Due to the parameters of the surrounding ground and the connection between the grout and the ground, two phenomena can occur. When the impedances of the soil and the grout are similar or the anchor body strongly interact with the surrounding ground in a large area, the wave reaching the media boundary is transferred into the ground where is damped rapidly. On the other side, when the anchor body borders with the soil of considerably different material parameters from the injected grout or the connection between the anchor body and the ground is weak, a significant amount of wave energy is reflected at anchor body/ground interface, so the anchor can be considered a two-layer system.

4.2.3 Wave diffraction on the start of the anchor body

Injected grout tends to cause expansion, triggering pressure to the surrounding ground. Thus the anchor diameter largely depends on material parameters of the ground. Soil parameters are determined solely on the basis of several sample parameters from an area where anchors are often not performed. The designer estimates the diameter of the anchor based on the diameter of the borehole and soil parameters, while the actual diameter may differ materially from the design assumptions. In extreme cases infiltration of liquid inject into the ground can be so intense that the diameter of the anchor grows to an immense size, much larger than the designed one. Due to significant differences in the size of the anchor bodies, two cases need to be considered: the model of anchor with infinite and definite diameter.

The character of the wave propagation in the anchor body depends on its size. When the anchor body is relatively large in thickness compared to the wavelength, the description of the wave propagation phenomenon will be analogous to the wave propagation in the bar embedded in the semi-infinite medium. The wave excited at the free end of the bar propagates along its length, diffracting at the start of the anchor body (Figure 4.6a). After diffraction and mode conversion, the surface wave, the antisymmetric mode and the symmetric mode propagate in the semi-infinite medium. Part of the wave energy not leaking into the surrounding medium propagates in the fixed length of the steel bar in the form of particular modes. The number of propagating modes depends on the excitation frequency. As a result, in a signal registered at the free end of the bar, the diffracted wave and possible reflections of subsequent modes from the embedded end of the bar may be registered.

If the anchor body has the thickness comparable to the wavelength of the excited guided wave, the occurring diffraction phenomenon is more complicated (Figure 4.6b). The excited wave propagates to the start of the anchor body and then it diffracts in accordance with the Huygens principle (phase I in Figure 4.6b). The diffracted wave (phase II in Figure 4.6b) propagates back to the free end of the bar and it also transmits into the anchor body. As it reaches the outer surface of the anchor body, it diffracts again and propagates to the bar (phase III in Figure 4.6b). The reflection from the start of the anchor body after the first wave diffraction displays a relatively small amplitude, so in the case of small diameters of the anchor body it interferes with the reflection from the outer surface of the anchor body.

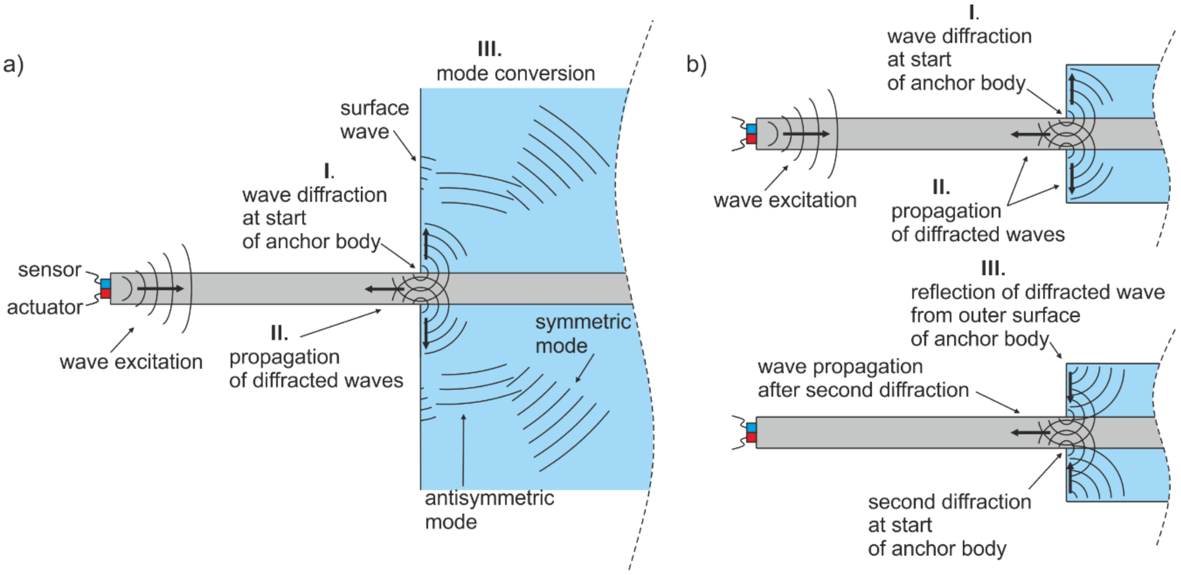

Figure 4.6. Wave diffraction at start of anchor body: a) anchor body thickness much smaller than the excited wavelength; b) anchor body thickness comparable with the excited wavelength

4.3 Experimental and numerical investigations of wave propagation in undamaged ground anchors

4.3.1 Description of specimens

Wave propagation investigations were carried out on laboratory models of ground anchors. The specimens were made of a steel circular bars of a diameter $d = 2$ cm and a length 150 cm embedded centrally in a cylindrical block with an outer diameter of $d_a = 10$ cm, constituting a concrete cover with a thickness of $h = 4$ cm. The material parameters of steel were: $E = 210$ GPa; $\nu = 0{,}3$; $\rho = 7820$ kg/m^3. The anchor body was made of C30/37 concrete of the following material parameters: $E = 26$ GPa; $\nu = 0{,}2$; $\rho = 2084$ kg/m^3. The test specimens included a free bar and eight anchors of a variable bond length. The anchor length L consists of the free length L_f and the bond length L_b (the length of the concrete cover). The length L_x results from technological aspects of preparing specimens. The geometry of a typical specimen is presented in Figure 4.7 and the dimensions of individual ground anchors are specified in Table 4.1.

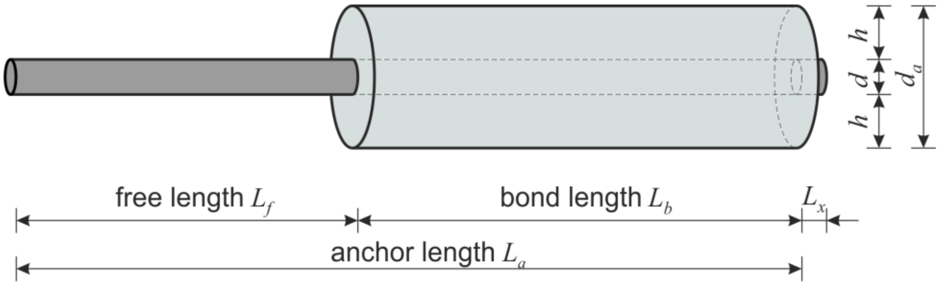

Figure 4.7. Geometry of the laboratory model of ground anchor

Table 4.1. Dimensions of ground anchor specimens with different bond lengths

Specimen	Length [cm] L_f [cm]	 L_b [cm]	 L_x [cm]
Free bar	150	-	-
Anchor #1	137	10.5	2.5
Anchor #2	127	20.5	2.5
Anchor #3	117.5	30	2.5
Anchor #4	107	40.5	2.5
Anchor #5	98.5	50	1.5
Anchor #6	87	60.5	2.5
Anchor #7	67	80.5	2.5
Anchor #8	47.5	100	2.5

4.3.2 Experimental procedure

Figure 4.8a presents the set-up for wave propagation experiment in laboratory models of ground anchors. A wave packet consisting of a ten-cycle sine function with a carrier frequency of 80 kHz modulated by the Hanning window was applied as the excitation signal. According to Figure 4.2 this excitation frequency allows for single mode propagation in the steel bar and a multimode propagation in the two-layer cylinder. Due to multimode propagation, the observation of separation of modes travelling with different velocities and mode conversion was possible.

The configuration of measurement points is illustrated in Figure 4.8b. The piezo actuator (denoted as *A* in Figure 4.8b) was attached to the free end of the steel bar in order to induce guided waves along the bar length. Two sensors (sensor 1 and sensor 2) were positioned on both free and embedded ends of the bar to measure longitudinal waves. The additional sensors (sensor 3 and sensor 4) were attached to the bar at the start and at the end of the anchor body.

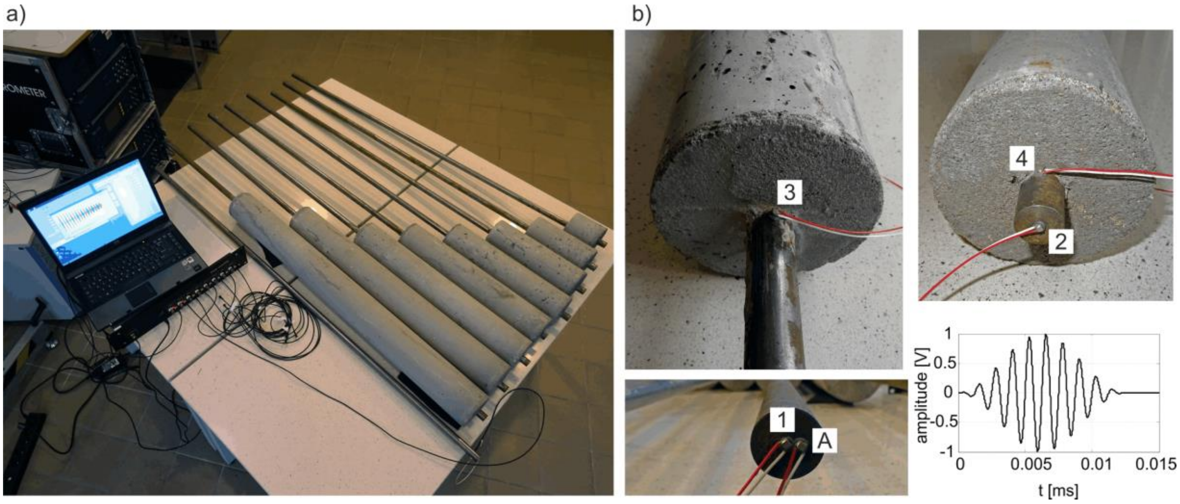

Figure 4.8. Experimental set-up: a) equipment and laboratory models of ground anchors with different bond lengths; b) distribution of measurement points and excitation signal

4.3.3 Parameters of FEM analysis

Several cases of ground anchors were analysed numerically. The first group of numerical models included anchors with a variable anchor body length L_b from 0 cm to 100 cm with a 1 cm step. The second group was made of anchors with a fixed length of the anchor body L_b = 80.5 cm (the length of the anchor#7) but with a variable cover thickness from 0 cm to 100 cm with a 1 cm step. The third group included models with identical geometry to the experimental specimens. In this case, additional analysis was conducted, taking into consideration the presence of the medium surrounding the anchor body by means of infinite elements. In these numerical models a layer of 4-node axisymmetric infinite finite elements (CINAX4) with a thickness of 4 cm was introduced.

4.4 Results

4.4.1 Analysis of wave propagation in ground anchors

Figure 4.9a presents numerical results for ground anchor #4 (cf. Table 4.1), with the bonding length equal to 40.5 cm. The snapshots at selected time instants illustrate the magnitude of acceleration and the deformation of the specimen. At the beginning, only a longitudinal mode $L(0,1)$ propagates along the bar as a single wave packet (Figure 4.9a, t = 0.15 ms and t = 0.19 ms). When the wave packet reaches the start of the anchor body (t = 0.27 ms), it diffracts. Part of the wave energy propagates back along the free bar, while the remaining part propagates in the bar embedded in concrete. In the case of considered frequency of excitation equal to 80 kHz, five longitudinal modes can propagate in the part of the bar with the concrete cover (cf. Figure 4.2b). At the beginning of propagation in the two-layer specimen, a single wave packet containing all modes is visible only. However, due to different group velocities of particular modes, they separate during propagation in the anchored length of the specimen. The longer the multilayered part, the longer time interval between particular modes can be achieved and more clear separation can be observed. At t = 0.36 ms, two wave packets can be distinguished only. Particular wave packets reflecting from the end of the specimen propagate back to reach the free part of the bar. Next, they are converted into modes, bound to propagate for a given frequency in the free bar. In the presented example of anchor #3 two separated wave packets are converted into $L(0,1)$ mode which travels in the form of two single wave packets (t = 0.70 ms).

Similar maps are given for anchor #7 with a longer bonding length equal to 80.5 cm (Figure 4.9b). In this case the wave diffraction at the start of the anchor body can be observed earlier, at t = 0.19 ms. The distance showing five modes propagate in a two-layer specimen is longer, therefore separation of modes into three wave packets is visible at t = 0.70 ms.

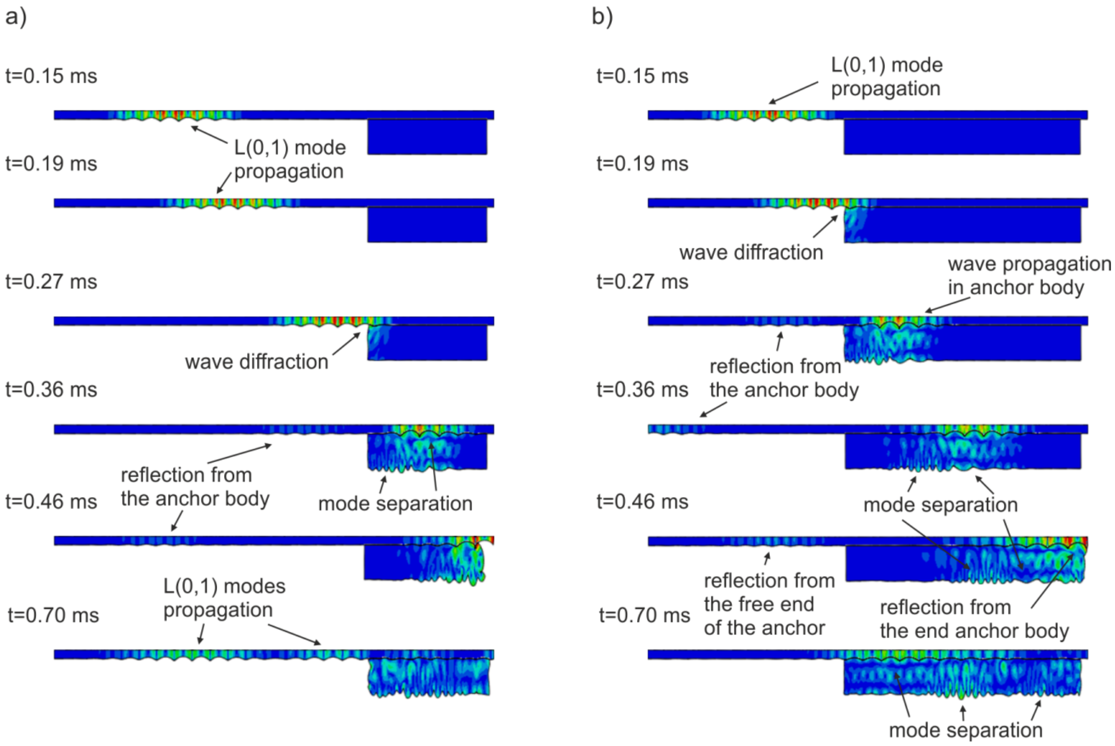

Figure 4.9. Snapshots of propagating waves (magnitude of acceleration) in anchor #4 at selected time instants: a) t =0.15 ms; b) t =0.19 ms ; c) t =0.27 ms; d) t = 0.36 ms; e) t = 0.46 ms; f) t = 0.70 ms

Figure 4.10 shows wave propagation signals registered at the free end and the embedded end of the bar in the form of 3D surface charts. The time responses, in the form of the envelopes of the magnitude of acceleration, were calculated for the anchor with variable anchor body length varying from 0 cm to 100 cm with a step equal to 1 cm. Thus, each chart presents 101 numerical signals. In both charts, some characteristic wave packets were identified. The input wave packet (scaled by a factor 0.02 for better visibility) can be observed in the initial part of signals registered at point #1 situated at the free end of the rod (Figure 4.10a). Next, the wave diffracted at the start of the anchor body is visible. Its amplitude is relatively small and for small length of a concrete cover it interferes with the reflection from the embedded end of the bar making it impossible to identify of particular wave packets. Near the reflection from the end of the specimen, the separation of additional $L(0,1)$ mode propagating in the free part of bar is very clearly visible. The increase of the anchor body length causes the increase of time interval between propagating $L(0,1)$ modes.

In the signals registered at an embedded end of the bar (point #2), the reflections from the end of the anchor can be indicated (Figure 4.10b). The time interval between the beginning of propagation and the first reflection increases proportionally to the anchor body length. While the bond length increases, the first reflection containing all five modes propagating in the part of the bar embedded in concrete, splits into two additional wave packets containing separated modes. It is clearly visible that the amplitude of the reflection from the end of the anchor changes periodically and it is characterized by numerous local maxima and minima for different bonding lengths L_b, but in general trend of amplitude-anchor body length function is characterized by a low tendency to decline with the increasing length of the concrete cover. The same effect is observed for the reflection from the end of the bar registered at point#1 (Figure 4.10a), but these variations in amplitude values are not as regular as in the previous case. Two effects are visible here: the decreasing trend in the amplitude is caused by the wave energy leakage (wave damping). Local maxima and minima of the amplitude may be caused by constructive and destructive interferences of several types of waves and their reflections propagating in the anchor body. Thus, it can be concluded that the decrease in amplitude is not only a result of wave leakage but is also affected by wave interference. For this reason a frequent conclusion saying that the longer boning length, the greater amplitude decrease (e.g. [229],[242],[210]), is not always true, especially in the case of small variations in bonding length.

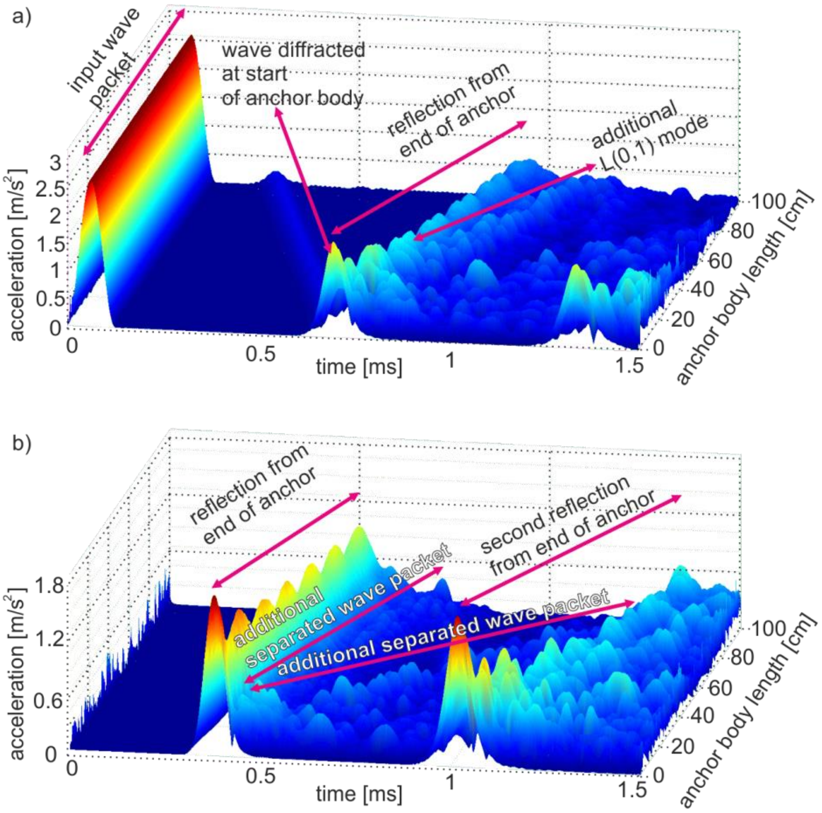

Figure 4.10. Time response of propagating waves (magnitude of acceleration) depending on the anchor body length: a) signal registered at free end of the bar (point #1); b) signal registered at embedded end of the bar (point #2)

4.4.2 Influence of anchor body diameter

While for rock bolts the thickness of the grouting layer between steel bar and the embedding rock is usually small and it amounts to a few millimeters, the size of the body of ground anchors can achieve a significant size. Thus the character of wave propagation in these two types of supporting systems is different. The thickness of the anchor body acts greatly upon on the phenomena of multimode propagation in the cover part of the ground anchor. Figure 4.11 presents dispersion curves for longitudinal modes to be excited in the anchor body with variable thickness of the grout cover.

It should be noted that the number of dispersion curves and their shapes are very sensitive to variations in cladding thickness. With an increase of cover thickness the number of possible modes increases, too. It means that interpretation of signal registered for anchor of large size could be hindered by mode separations and numerous conversions.

It can be observed that the velocity for low frequencies of the first mode decreases with the increase of the cover thickness. The dispersion curve for an anchor with 1 cm cover thickness indicates that in the 0 kHz case the group velocity is equal to above 4500 m/s. For a 5 cm thickness cover the group velocity in the 0 kHz case is equal to about 3700 m/s, while for thickness of 20 cm and 50 cm the difference is almost invisible and the velocity in the 0 kHz case is about 3500 m/s. While the diameter of an anchor body is large, the velocity of the fastest mode for a particular frequency tends to the velocity of the first mode in the 0 kHz case. It can be concluded that for large-size specimens group velocity for any frequency can be easily estimated on the basis of the starting point of the first curve.

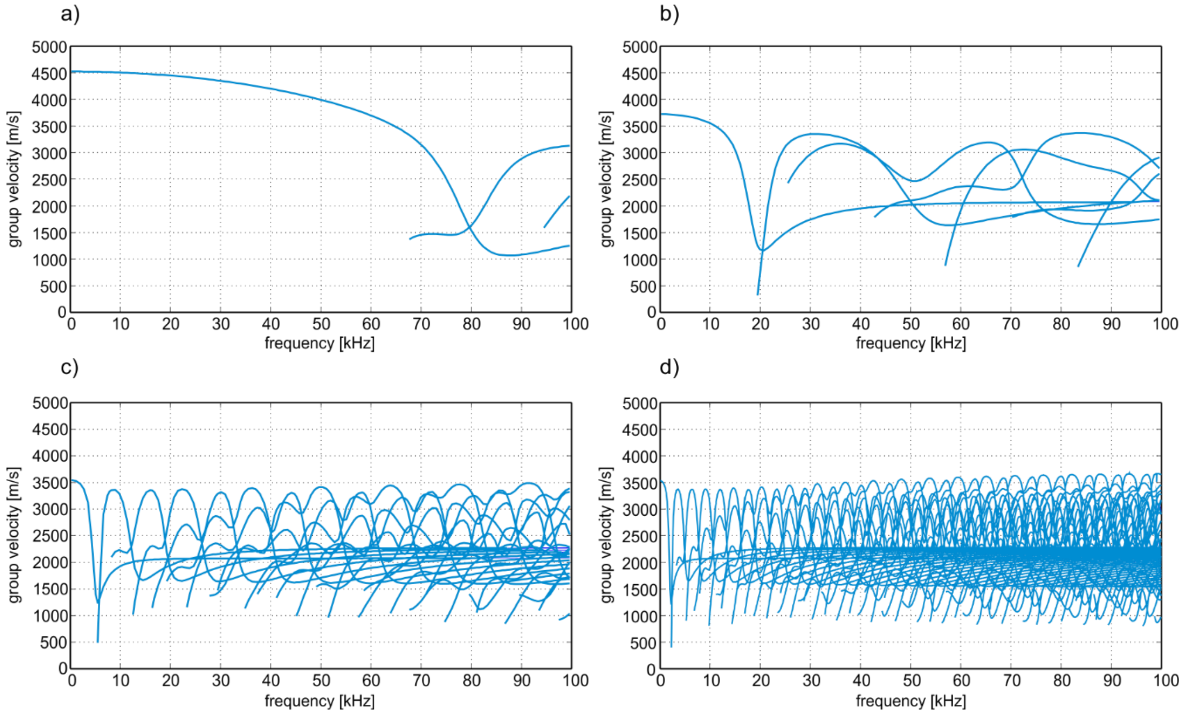

Figure 4.11 Dispersion curves for longitudinal modes for steel rod with diameter of 2 cm embedded in concrete cover with thickness of a) 1 cm, b) 5 cm, c) 20 cm and d) 50 cm

In order to observe propagation of particular waves in the ground anchor body, the specimen with the bond length equal to 80.5 cm and the cover thickness equal to 80 cm were analysed numerically. A large size of the anchor body allows to observe occurring

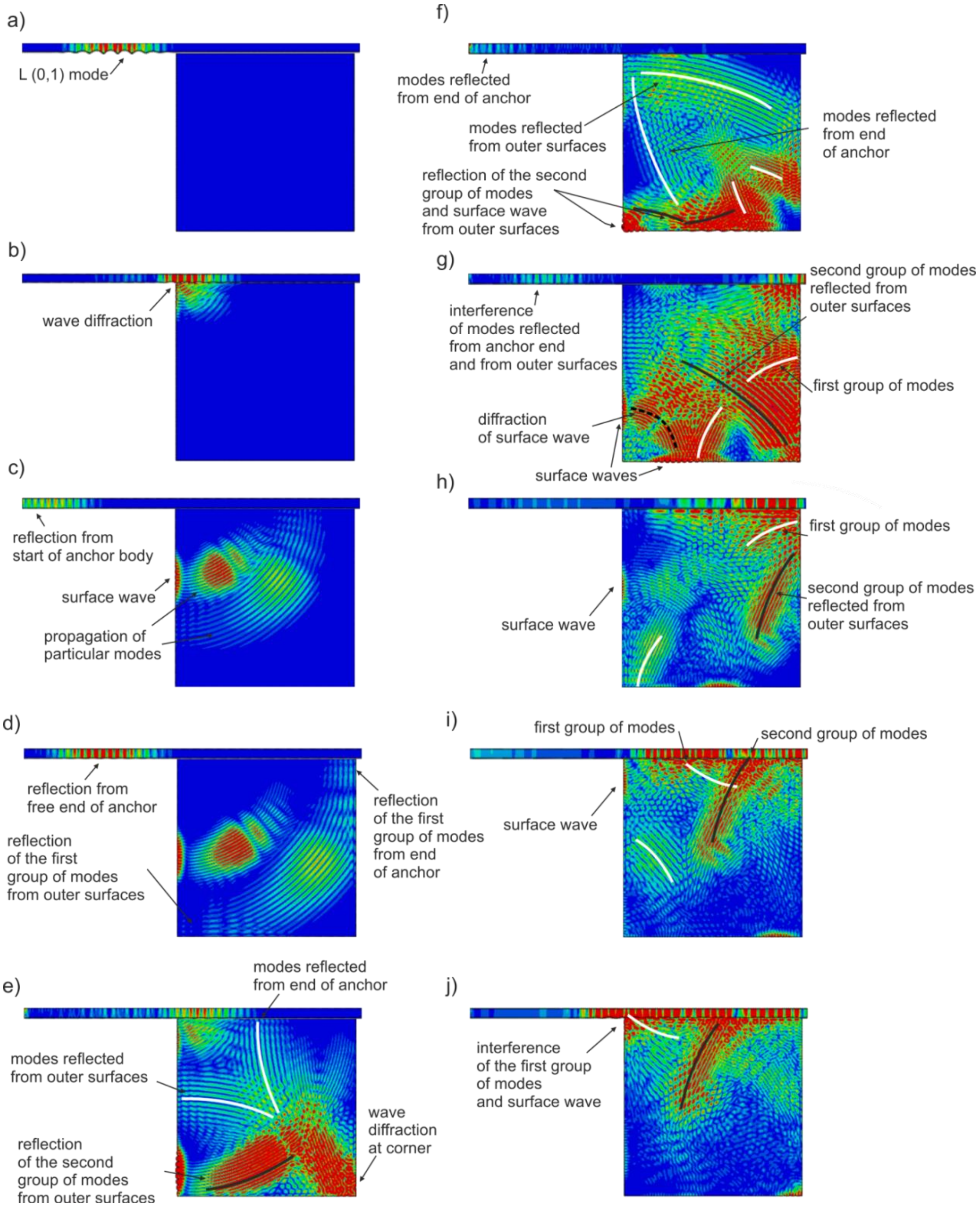

Figure 4.12. Snapshots of propagating waves (magnitude of acceleration) in ground anchor with 80 cm cover thickness at selected time instants: a) *t* =0.15 ms ; b) *t* =0.24 ms ; c) *t* =0.36 ms ; d) *t* =0.42 ms; e) *t* = 0.54 ms; f) *t* = 0.60 ms; g) *t* = 0.70 ms; h) *t* = 0.81 ms; i) *t* = 0.93 ms; j) *t* =0.98 ms

phenomena in detail. The snapshots of the acceleration magnitude and the specimen deformations at selected time instants are presented in Figure 4.12. Initially, longitudinal *L*(0,1) mode propagates along the free length of the bar (Figure 4.12a).

After wave diffraction, in the anchor body two groups of modes and the surface wave start propagating (Figure 4.12b). The diffracted wave propagates back along the steel bar

(Figure 4.12c), next it is reflected from the free end of the bar (Figure 4.12d). The first group of modes propagating in the anchor body is reflected from the outer surface of the anchor body and from the end of the specimen (Figure 4.12d and e). In the presented example these reflections occur simultaneously due to similar length and thickness of the anchor body. Part of the energy of these waves is reflected from the border of the steel and concrete cover (Figure 4.12f) while another part propagates as the interference wave along the steel bar (Figure 4.12g). At the same time multiple reflections of the second group of modes from the boundaries are observed (Figure 4.12e-h). After reflection from the end of the specimen (Figure 4.12h) both group of modes propagate back in the direction of the start of the anchor body (Figure 4.12i and j). The reflection and diffraction of the surface wave are visible in Figure 4.12f and Figure 4.12g. The reflected surface wave propagates perpendicularly to the anchor axis and at the end it transmits into the steel bar. Moreover, in the presented example, the surface wave interferes with the subsequent reflection of the first group of modes from the end of the specimen (Figure 4.12j).

In order to determine the influence of the variable anchor body size on wave patterns, several numerical models with a bond length equal to 80.5 cm and variable-thickness concrete cover have been performed. Acceleration signals were registered at the free end of the bar. The results are presented in Figure 4.13 as a 3D surface chart. The signals were calculated for the anchor with an anchor body thickness varying from 0 cm to 100 cm with a 1 cm step (globally 101 numerical signals). Accordingly to Figure 4.6 and Figure 4.12, when the incident wave reaches the part embedded in concrete, it reflects from the start of the anchor body and from its outer surfaces. Those reflections were identified and indicated in Figure 4.13. In each case of anchor body thickness, the diffracted wave occurs at the same time and its amplitude is constant due to a constant anchor body length. The reflection time of the surface wave from the outer surface of the anchor body is proportional to the cover thickness. The reflection from the end of the anchor is easy to identify only for a relatively small thickness of the anchor body, not exceeding 5 cm. For a 5-45 cm thickness range reflections are characterized by very low amplitudes and their identification is difficult. Next, the amplitude is greatly increased for a thickness exceeding 45 cm. The explanation may be the occurrence of constructive interferences, which appear when the cover thickness is comparable with the bond length (cf. Figure 4.12i and j). It should be noted that even though some reflections can be observed in snapshots in Figure 4.12 – e.g. the wave raised after the second diffraction at the start of the anchor body (Figure 4.12e) or the wave travelling after interference of modes reflected from boundaries (Figure 4.12g) – they are difficult to recognize in the registered wave propagation time histories. Moreover, as the cover thickness increases, a gradual decrease in the amplitude of the reflected waves from the end of the anchor is observable. This results from the increasing intensity of the energy leakage into the cover, but also from wave propagation over increasingly longer distances, which causes spreading of the input wave packet and the decrease of the signal amplitude.

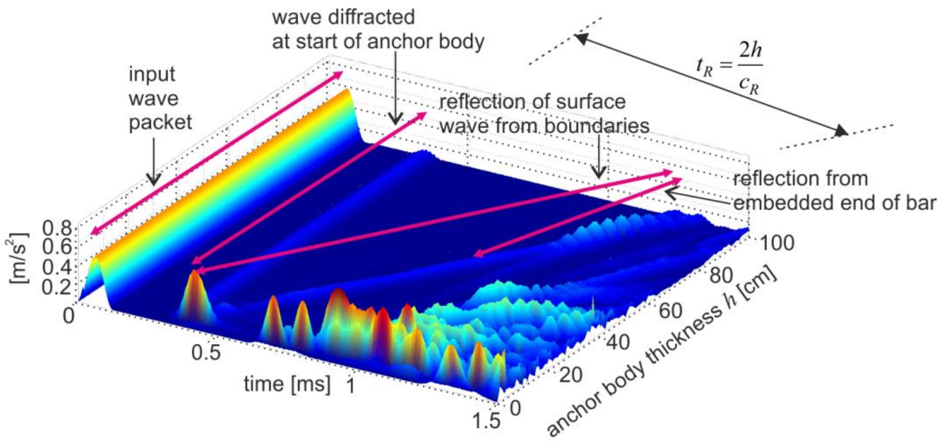

Figure 4.13. Time response of propagating waves (magnitude of acceleration) depending on the anchor body thickness (signal registered at free end of the bar)

4.4.3 Influence of infinite boundary conditions

As mentioned in paragraph 4.2.3 the ground anchor bodies are manufactured in soil by means of grout pressurized injection. Injected grout tends to cause expansion, which applies pressure to the surrounding ground, so the anchor body interacts with the surrounding ground medium. Part of the inject penetrates into ground so as a consequence at the border of media grout and soil can be mixed with one another. Irregular shape of ground anchor body and slurred border of media may act significantly on the intensity of the energy leakage and the energy dissipation, which greatly hinders the acquisition and interpretation of wave propagation signals. Moreover, due to the infiltration of inject into the surrounding ground, the shape of the anchor body is often irregular and it varies in thickness throughout its length. Wave reflection from irregular boundaries results in a much more intensive energy dissipation. In order to simulate the interaction of the anchor body with a surrounding medium and the shape irregularity, the non-reflecting boundary conditions are assumed in numerical models by means of introducing infinite finite elements along the outer surface of the anchor body.

The evolution of wave propagation through the anchor with L_b = 80.5 cm and non-reflecting boundary conditions is presented in Figure 4.14. The introduction of infinite conditions along the boundaries of the anchor body results in the lack of reflections of the surface wave from the boundaries (Figure 4.14b). Additionally, in the infinite elements area no disturbance is observed. As a consequence, after the wave diffraction at the start of the anchor body, part of the energy propagates back (Figure 4.14c and Figure 4.14d) and the other part propagates along the anchor, to be rapidly dissipated. In Figure 4.14e the wave after reflection from the free end of the anchor is diffracted again. Wave motion is observable only in a free steel rod, while in the remaining volume of the anchor no wave motion is recorded. Subsequent wave diffractions at the start of the anchor body and reflections from the free end of the anchor can be observed until the entire wave energy is dissipated. Analysing time histories for anchors with different bonding lengths (Figure 4.15), in all registered signals, the wave packets are visible corresponding to the wave diffracted at the start point of the anchor body. However, due to infinite boundary conditions, the wave is attenuated so fast, that no reflections from the embedded end of the bar can be observed, even in the case of a relatively short bond length.

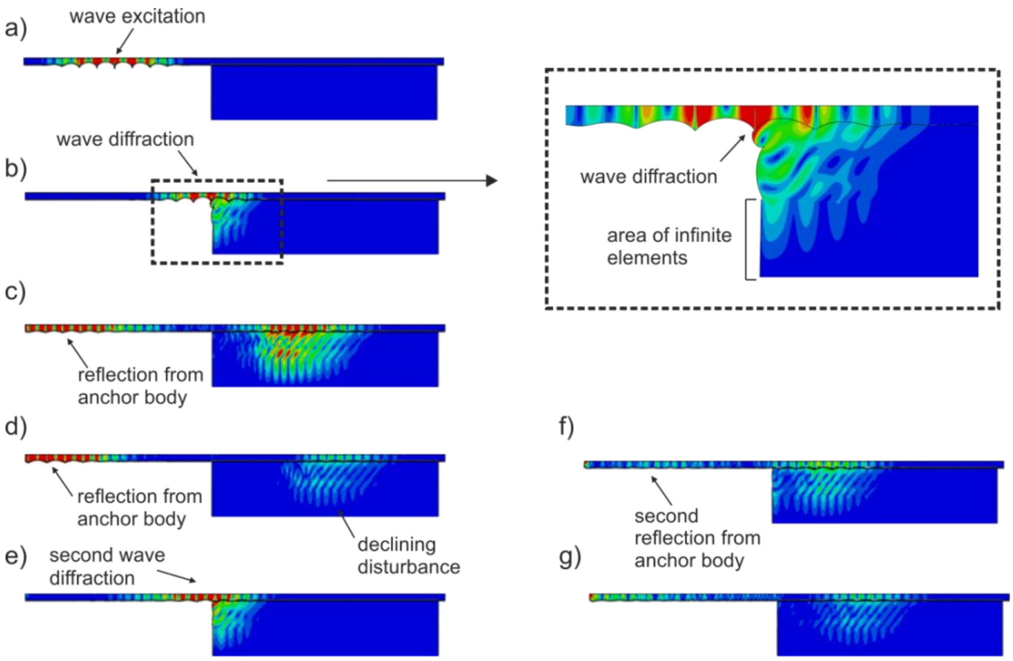

Figure 4.14. Snapshots of propagating waves (magnitude of acceleration) in ground anchor with non-reflecting boundary conditions at selected time instants a) t =0.13 ms ; b) t =0.21 ms ; c) t =0.32 ms ; d) t =0.37 ms ; e) t =0.50 ms ; f) t =0.58 ms ; g) t =0.62 ms

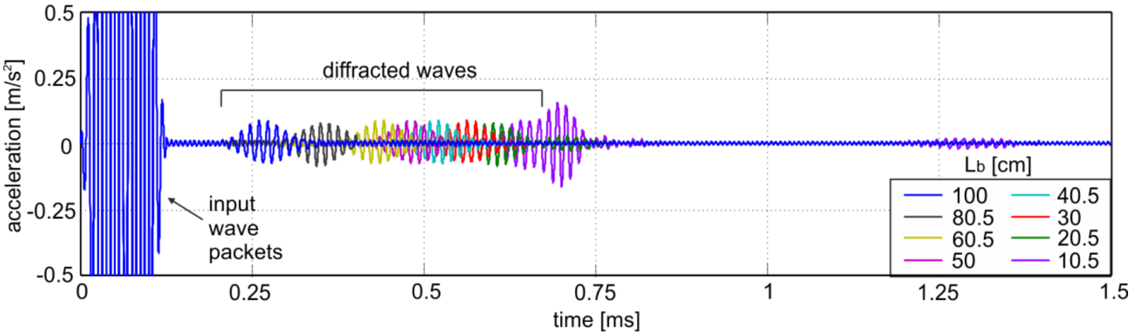

Figure 4.15 Acceleration signals registered at the free end of the anchors with infinite boundary conditions

4.4.4 Analysis of wave travel time

Based on experimental and numerical wave propagation signals for anchors with variable anchor body length L_b, group velocity for the free part of the anchor (v_f), group velocity for the embedded part of the anchor (v_b) and the average group velocity for the whole ground anchor (v_a) was estimated.

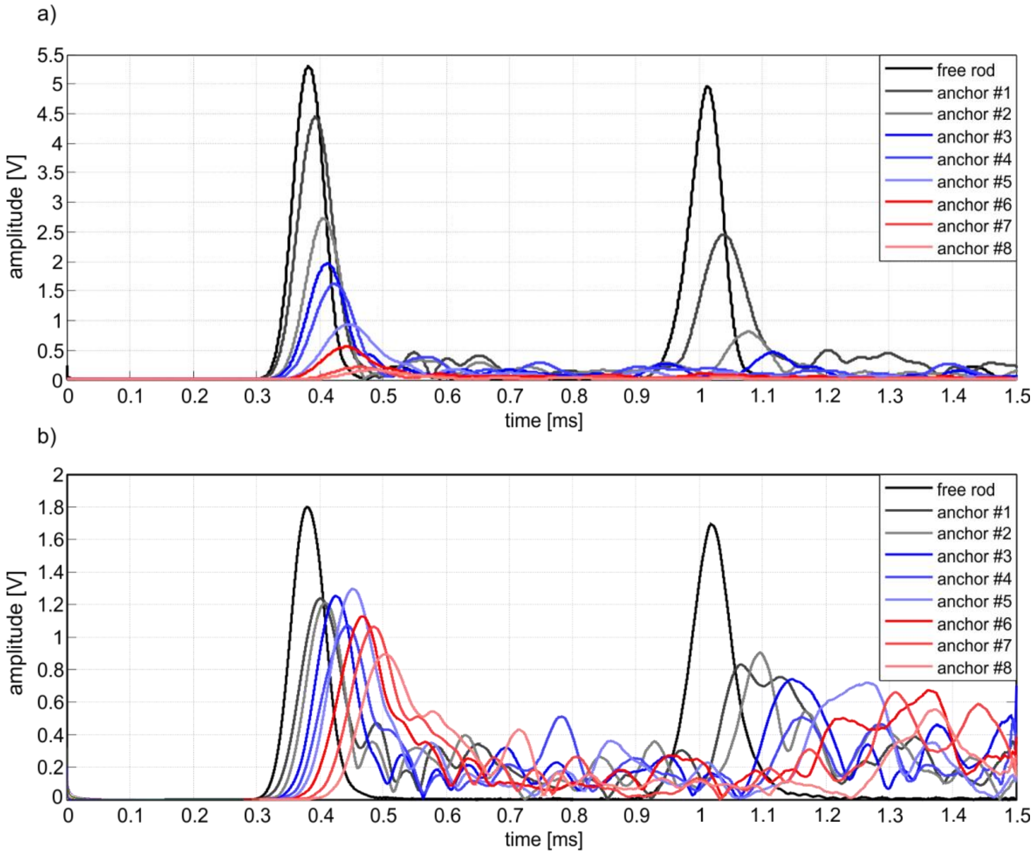

Figure 4.16. Envelopes of a) experimental wave propagation signals registered by sensor #2, b) numerical wave propagation signals registered at point #2

The wave velocity in the free part was determined using signals registered by sensors #1 and #3, while the velocity in the embedded part by sensors #3 and #4 (see Figure 4.8b). In order to identify the velocity for the entire ground anchor, signals registered by sensors #1 and #2 were used. Examples of numerical and experimental signals registered by sensor #2 are presented in Figure 4.16. In the case of signals registered close to bonded end of the anchor (sensors #2 and #4) the first registered wave packet included more than a single mode, therefore the identified velocity is the velocity of the fastest group of modes.

Figure 4.17 illustrates the group velocities of waves propagated in particular parts of the ground anchor, for experimental specimens and their numerical models and for numerical models with infinite elements, depending on the bond length. The velocities of waves propagating in the free and bonded parts are constant independently of their length (Figure 4.17a and b). The mean velocity value in the free part of the bar was identified as: 4751 m/s (experimental), 4721 m/s (numerical), 4721 m/s (numerical with infinite elements) and 4729.3 m/s (analytical). In the bonded length the determined velocities were: 2946 m/s (experimental), 2738 m/s (numerical), 3576 m/s (numerical with infinite elements) and 3141 m/s (analytical for the fastest mode). The velocity for the model with infinite elements is greater than the velocity for the model corresponding to experimental specimens.

While the group velocities in particular parts of the ground anchor are known, the relationship between the average group velocity v_a in a function of the anchor body length L_b or a ratio L_b / L_f can be written as:

$$c_a\left(L_b\right) = \frac{L_a c_b c_f}{L_a c_b + L_b\left(v_f - c_b\right)}, \tag{4.4}$$

$$c_a\left(\frac{L_b}{L_f}\right) = \frac{\left(1+\dfrac{L_b}{L_f}\right)c_b c_f}{\dfrac{L_b}{L_f}c_f + c_b}. \tag{4.5}$$

In Figure 4.17c the relationship given by Eq. (4.4) is plotted by a dashed line. Experimental and numerical results were marked at particular points corresponding to bond lengths. It can be seen that the average group velocity v_a decreases with the increase of the bond length.

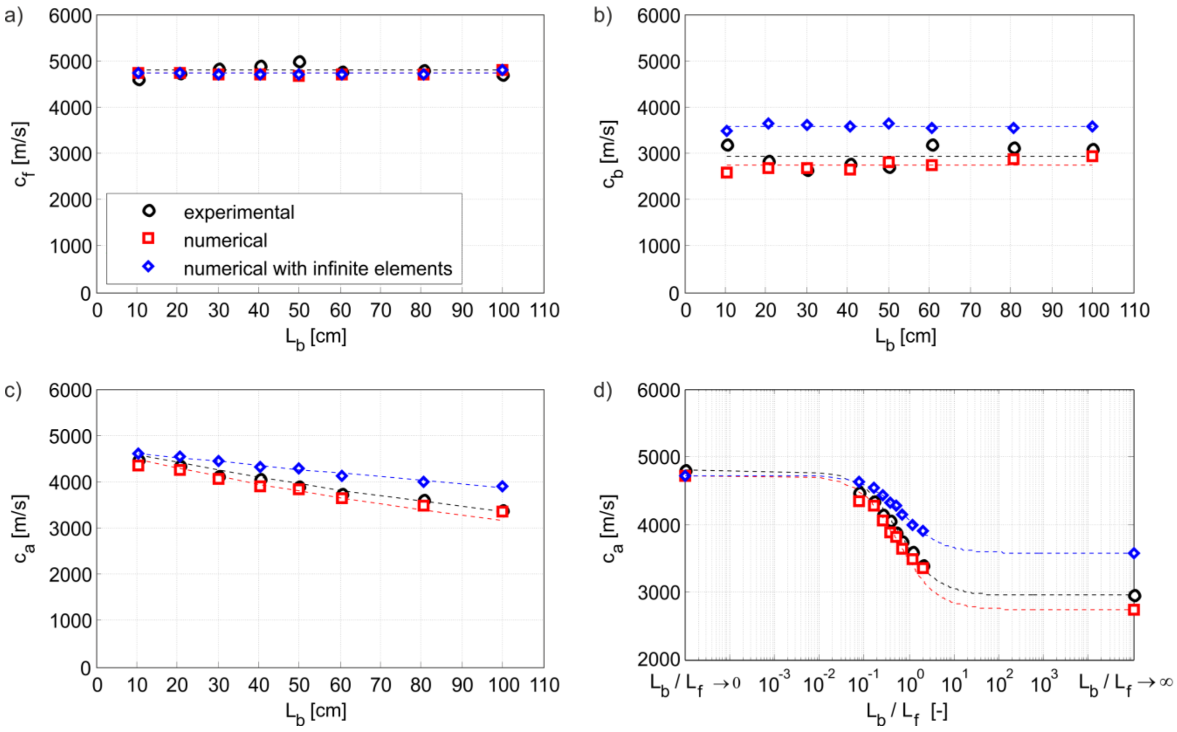

Figure 4.17. Relationships of wave velocities: a) velocity of wave propagated through free length L_f ; b) velocity of wave propagated through bonded length L_b , c) velocity of wave propagated through anchor length L_a in a function of L_b ; d) velocity of wave propagated through anchor length L_a in a function of L_b / L_f

Figure 4.17d presents the relationship, given by Eq. (4.5), between the average group velocity at the total length of the anchor L_a and different ratios of the free length to the embedded length (L_b / L_f). In the case of a fully grouted anchor ($L_b / L_f \to \infty$), the average velocity c_a is close to the velocity c_b, while for a fully delaminated specimen ($L_b / L_f \to 0$), the average velocity c_a approaches the velocity for a free bar c_f. The obtained results indicate that the average velocity for the entire anchor can be used to determine the anchor body length.

4.4.5 Identification of geometric parameters of ground anchors

Practical assessment of conditions or the identification of geometrical parameters in real engineering facilities allows a sole use of signals measured at the free end of the tendon. Figure 4.18 presents a set of experimental wave propagation signals together with the envelopes of numerical signals registered at the free end of the bar for all considered ground anchors. Characteristic reflections from the start of the anchor body and from the end of the anchor have been identified and highlighted. The straight lines crossing the marked reflections additionally illustrate direct proportionality between the registration time of particular wave packets and the bond length. Furthermore, the inclination of the lines points to the difference in the wave velocities in the free and multilayered parts. The line passing through the wave packets propagating after diffraction is characterized by higher inclination because of a higher wave velocity in the free part of the steel bar (cf. Figure 4.17).

Both numerical and experimental wave propagation histories involve waves diffracted at the start of the anchor body. The wave diffracted at the start of the anchor body is registered even in the case of intensive energy dissipation. For this reason, the free length of the tendon can always be identified. The identification of a free length of the examined ground anchors was performed on the basis of a known group velocity in the free part of steel bar c_f and the determined time-of-flight (TOF) between the input wave packet and the diffracted wave t_f :

$$L_f^{TOF} = \frac{c_f t_f}{2} \tag{4.6}$$

The results obtained for experimental specimens and for numerical models are summarized in Table 4.2.

Table 4.2. Identification of free length based on Eq. (4.6)

Specimen	L_f [cm]	experimental		numerical		numerical with infinite elements	
		L_f^{TOF} [cm]	$\Delta L_f = \left\lvert L_f^{TOF} - L_f \right\rvert$ [cm]	L_f^{TOF} [cm]	$\Delta L_f = \left\lvert L_f^{TOF} - L_f \right\rvert$ [cm]	L_f^{TOF} [cm]	$\Delta L_f = \left\lvert L_f^{TOF} - L_f \right\rvert$ [cm]
Free bar	150	150.2	0.2	150.9	0.9	-	-
Anchor #1	137	153.0	16.0	141.2	4.2	138.1	1.1
Anchor #2	127	135.2	8.2	132.2	5.2	128.4	1.4
Anchor #3	117.5	128.0	10.5	122.3	4.8	118.9	1.4
Anchor #4	107	117.9	10.9	112.8	5.8	108.4	1.4
Anchor #5	98.5	103.1	4.6	104.6	6.1	99.9	1.4
Anchor #6	87	91.7	4.7	93.0	6.0	88.4	1.4
Anchor #7	67	73.4	6.4	71.5	4.5	68.4	1.4
Anchor #8	47.5	55.6	8.1	53.8	6.3	48.9	1.4

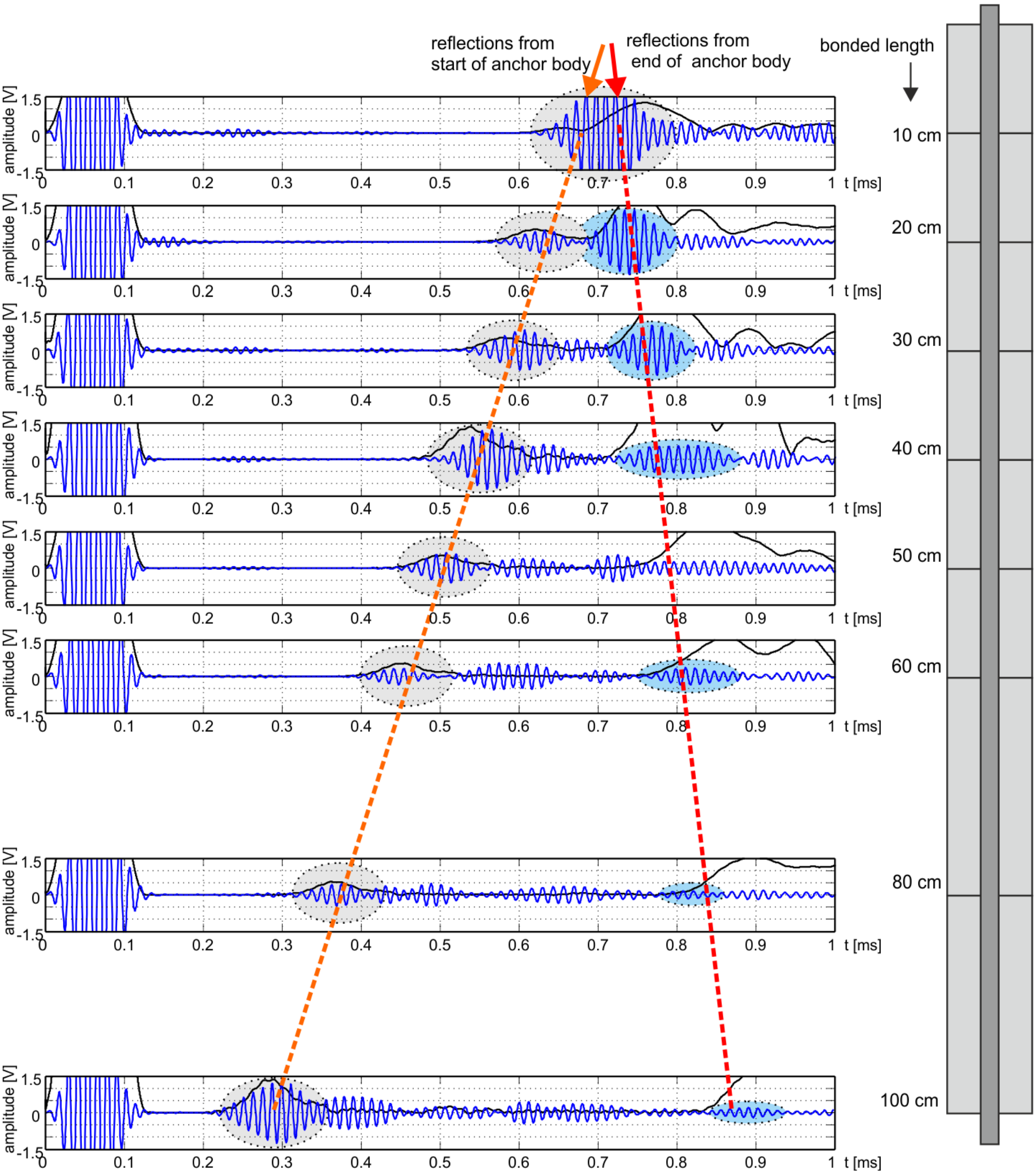

Figure 4.18. Set of experimental signals and envelopes of numerical signals for ground anchors with different bond lengths

The discrepancies between the real free lengths L_f and the lengths calculated on the basis of the time-of-flight L_f^{TOF} ranged from 4.6 cm to 16 cm for experimental signals and from 4.2 cm to 6.3 cm for numerical signals. In all cases the identified length based on the time-of-flight is longer than the real length. The main reason for this discrepancy is the interference of the diffracted wave and the wave reflected from the boundaries. Figure 4.13 shows that in the case of relatively small thickness of the cover, the diffracted wave and the wave reflected from the boundaries of the anchor body overlap, making it difficult to calculate the time-of-flight. This explanation is additionally confirmed by the results obtained for numerical models with non-reflecting boundary conditions. The absolute error in the estimation of free lengths is close for all considered anchors and its value is about 1 cm. Infinite boundary conditions inhibit the reflection of the surface wave from the anchor body boundaries and as a consequence only diffracted waves are registered in signals.

In general, the thickness of the anchor body can be precisely determined only for anchors with relatively large cover thickness, making the diffracted wave not overlap with the surface wave reflected from the boundaries of the anchor body. The anchor body thickness can be calculated based on a prior-known velocity of the surface wave c_R (Rayleigh wave velocity) and the time-of-flight between t_R the diffracted wave and the reflection from the outer surface of the anchor body (cf. Figure 4.13 and Figure 4.14):

$$h = \frac{c_R t_R}{2} \tag{4.7}$$

where

$$c_R = c_S \left(\frac{0,87 + 1,12\nu}{1+\nu} \right) \tag{4.8}$$

In this thesis, experimental investigations were performed for anchors of a relatively small thickness of the cover, making the diffracted wave and the wave reflected from the boundaries of the anchor body overlap, thus making it difficult to calculate the time-of-flight (cf. Figure 4.13). This situation makes it impossible to perform a direct identification of the cover thickness. However, the obtained results include information about the cover thickness is included in the difference between the free length identified using the time-of flight and the real free length ΔL_f . The cover thickness can be roughly estimated as:

$$h \approx \Delta L_f \frac{c_R}{c_f} \tag{4.9}$$

Table 4.3 Identification of cover thickness based on Eq. (4.9)

Specimen	experimental	numerical
	h [cm]	h [cm]
Anchor #1	7.0	1.8
Anchor #2	3.6	2.3
Anchor #3	4.6	2.1
Anchor #4	4.8	2.6
Anchor #5	2.0	2.7
Anchor #6	2.1	2.6
Anchor #7	2.8	2.0
Anchor #8	3.5	2.8

The identified values of the cover thickness are presented in Table 4.3 The bonding length can be determined on the basis of a known group velocity in the fixed length c_b and the identified time-of-flight between the diffracted wave and the reflection from the end of the anchor t_b :

$$L_b^{TOF} = \frac{c_b t_b}{2} \tag{4.10}$$

The identified bond length values obtained for experimental and numerical anchors are given in Table 4.4. The discrepancies between the real bond lengths L_b and the lengths calculated on the basis of time-of-flight L_b^{TOF} ranged from 0.1 cm to 10.5 cm for experimental signals and from 2.1 cm to 9.7 cm for numerical signals. As in the case of the free length identification, this discrepancy is mainly caused by overlapping of the diffracted wave and the wave reflected from the boundaries of the anchor body.

Table 4.4. Identification of bonding length based on Eq. (4.10)

Specimen	L_b [cm]	experimental		numerical	
		L_b^{TOF} [cm]	$\Delta L_b = \left\| L_b^{TOF} - L_b \right\|$ [cm]	L_b^{TOF} [cm]	$\Delta L_b = \left\| L_b^{TOF} - L_b \right\|$ [cm]
Anchor #1	10.5	0	10.5	13.7	3.2
Anchor #2	20.5	15.5	5.0	17.5	3.0
Anchor #3	30	24.3	5.7	27.9	2.1
Anchor #4	40.5	34.5	4.0	34.8	5.7
Anchor #5	50	50.1	0.1	45.0	5.0
Anchor #6	60.5	62.0	1.5	55.9	4.7
Anchor #7	80.5	77.3	3.2	73.2	7.3
Anchor #8	100	103.1	3.1	90.4	9.7

As a new approach, the bond length can be identified based on the relation describing the average velocity for an entire anchor (derived in paragraph 4.4.4).

$$L_b^{TOF} = \frac{c_b(t_a c_f - 2L_a)}{2(c_f - c_b)} \tag{4.11}$$

The feature of this approach is the fact, that the identification is based on the time-of-flight t_a not involving the time-of-flight t_f and t_b, so all the most important geometric parameters of the anchor can be determined on the basis of signal registered on the free length of the anchor only. The identified bond length values obtained for experimental and numerical anchors are given in Table 4.5. The discrepancies between the real bond lengths L_b and the lengths calculated on the basis of time-of-flight L_b^{TOF} ranged from 1.9 cm to 17.3 cm for experimental signals and from 1.9 cm to 17.7 cm for numerical signals.

Table 4.5. Identification of bonding length based on Eq. (4.11)

Specimen	L_b [cm]	experimental		numerical	
		L_b^{TOF} [cm]	$\Delta L_b = \left\|L_b^{TOF} - L_b\right\|$ [cm]	$L_b^{\Delta t}$ [cm]	$\Delta L_b = \left\|L_b^{TOF} - L_b\right\|$ [cm]
Anchor #1	10.5	4.9	5.6	20.4	9.9
Anchor #2	20.5	16.5	4.0	17.1	3.4
Anchor #3	30	28.1	1.9	28.2	1.8
Anchor #4	40.5	43.6	3.1	31.5	9.0
Anchor #5	50	55.3	5.3	44.5	5.5
Anchor #6	60.5	68.1	7.6	54.3	6.2
Anchor #7	80.5	78.5	2.0	66.0	14.5
Anchor #8	100	117.3	17.3	82.3	17.7

4.5 Summary and conclusions

In this Chapter numerical and experimental investigations of guided wave propagation in ground anchors were carried out. Anchors with variable length and diameter of the anchor body, as well as anchors with non-reflecting boundary conditions were analysed here. The study was focused on the recognition of the phenomenon of wave energy transfer between a steel tendon and a anchor body, because this aspect is crucial for the development of monitoring systems based on guided wave propagation. The presence of the anchor body affects the average group velocity of waves propagating in the anchor, the amplitude of vibrations in the registered signals and additionally, in the case of multimode propagation, on the separation of particular wave modes and the mode conversion. The results of numerical simulations allowed to observe mode separation along the anchor body length. The wave separation increased with the increase of anchor body length and with the increase of difference between velocities of particular modes. Wave conversion was observable due to two distinct anchor parts (free part and two-layer part), displaying various propagation wave modes. The modes in free bar were converted into modes in two-layer part, and conversely, modes in two-layer part were converted into modes propagating in free bar. These two phenomena, the mode separation and the mode conversion, are indispensable elements of wave propagation in ground anchors and they greatly complicate the interpretation of wave propagation signals.

The presented investigations indicated both potentials and limitations of a guided wave propagation technique in the diagnostics of ground anchors. It was observed that the three most important geometric parameters, i.e. the free length of the tendon, the anchor body length and the thickness of the anchor body, can be determined on the basis of wave propagation signals recorded at the free end of the anchor. Both numerical and experimental wave propagation histories include waves diffracted in the regions of variable geometry. The wave diffracted at the start of the anchor body was registered even in the case of intensive energy dissipation. For this reason, the free length of the tendon can be always identified on the basis of a known group velocity in the tendon and the determined time-of-flight between the input wave packet and the diffracted wave. However, in the case of anchors with relatively small diameter of the anchor body the identified free length are slightly variable due to the interference of the diffracted wave and the wave reflected from the boundaries of the anchor body.

The anchor body thickness can be determined on the basis of a known velocity of the surface wave and the time-of-flight between the diffracted wave and the reflection from the outer surface of the anchor body. In the case of anchors with relatively large thickness of the cover these wave packets propagate separately and they are easy to identify. However, for a relatively small diameter of the anchor body the diffracted wave and the wave reflected from the boundaries of the anchor body overlap making the identification of the cover thickness impossible.

The bonding length was determined in two ways. At first, the bond length was calculated on the basis of a known group velocity in the fixed length and the identified time-of-flight between the diffracted wave and the reflection from the end of the anchor. As a new approach, the bonding length was identified based on the relation describing the average velocity for an entire anchor. In both approaches identification of the bond length in the anchor with a relatively small diameter of the anchor body led to slight discrepancies between the real bond length and the length calculated on the basis of the time-of-flight due to overlapping of the diffracted wave and the wave reflected from the boundaries of the anchor body. On the other hand, in the case of a large-diameter anchor body or the anchor body strongly interacting with the surrounding ground, the identification of the reflection from the end of the anchor may be difficult or even impossible. It was shown that due to infinite boundary conditions assumed around the anchor body in numerical models, the wave was attenuated so fast, that reflection from the embedded end of the bar was observable only in the case of the anchor with the shortest bond lengths.

Page intentionally left blank

CHAPTER 5

Wave propagation in ground anchors with debonding

5.1 Introduction

In general ground anchors works as active support systems. It means that after performing the anchor, it is additionally pre-stressed. They are adapted to transmit significant tensile and shear forces from the bar through the bar/grout interface to the surrounding ground. Thus the bond between a tendon and grout is a critical aspect of the anchor load-carrying capacity and a proper load transferring. Moreover, the grout cover additionally provides corrosion protection of a steel tendon. Inaccurate cover may be the cause of corrosion spot and in consequence may lead to serious damage to the anchor and entire supporting system. Since interface damage can be a potential threat to proper operation, the analysis of effects of debonding between the bar and grout has been investigated to improve the reliability and safety of ground anchors. Benmokrane et al. [26] presented a study of the behaviour of cement-grouted ground anchors subjected to tensile loading. Strains were measured by vibrating-wire gauges welded at certain intervals to the surface of a steel bar. Next, three types of tests including loading and unloading test, creep test and long-term test were conducted and the load distribution along the anchor length was monitored. An analytical model of rock bolts subjected to tensile load was presented by Ma et al [134]. They presented derivations for load-displacement curves, shear stress distribution at the interface between bolt and grout and axial load distribution in the bolt in pull-out tests. Ivanović and Neilson [95] proposed a model to capture static and dynamic effects of debonding in terms of static load distribution and dynamic response to transient loading. The influence of pre-existing debonding in ground anchors on the load carrying capacity was examined by means of pull-out tests by Akisanya and Ivanović [6].

In recent years, a growing interest has arisen in the use of nondestructive testing methods for condition assessment of ground anchors. The previous works indicate a large potential of the use of guided waves in diagnostics of ground anchors, especially to assess the effects of insufficient rebar and missing grout ([40],[225]), the identification of a free length of an anchor [236] and the evaluation of grout quality ([243],[210]). However, the number of studies on the application of guided waves for the detection of debonding between steel and concrete is limited. Na et al. [159] considered a steel bar embedded in a rectangular block of concrete with 0%, 25%, 50% and 75% delaminated interface situated at one end of the bar. Lamb wave measurements were performed by a pitch-catch method using a transmitter and a receiver located at both ends of the bar or the concrete block. Concrete beams with a steel reinforcing bar embedded in the middle of the beam were investigated by Wu and Chang ([219],[220]). Debonding of different lengths was introduced at the centre part of the beam. Eight PZT actuators and sensors were mounted to the bar surface, then variations in signal amplitude and time of arrival were monitored. It was experimentally observed, that the amplitude of wave propagation signals increases with the increased debond length however, there were no significant changes in the time of signal arrival [219], this fact was confirmed later by FEM simulations [220]. Zima and Rucka [237] applied guided waves for the assessment of adhesive bonding in double-layer cylindrical specimens made of a steel bar embedded in concrete. They investigated numerically the impact of a bonding length on the excitation of multiple modes of longitudinal guided waves.

This Chapter deals with guided wave propagation in steel bars partially embedded in grout. The first part of the study concerns theoretical and numerical investigations of longitudinal guided modes in multilayered cylindrical bars with pre-existing debonding, including the influence of debonding location and its length on the separation of modes, their conversion and diffraction as well as the average wave velocity. The second part of the Chapter presents experimental results of both nondestructive testing using guided waves and destructive pull-out tests conducted on laboratory models of ground anchors with variable debonding length and location. Three locations of debonding and five levels of the debonding length are considered. In the previous experimental research debonding between the core and cladding was simulated using a section of a PVC pipe around a bar what completely separated the bar and concrete (e.g. [159],[219]). However, real debonding may show a significantly smaller size, especially in the case of progressive deterioration of the bond. Therefore, in this study debonding is performed by means of wrapping the bar in a cellophane film of a very small thickness (about $60\,\mu\text{m}$). The presented approach provides indirect contact between steel and grout, but significantly reduces grout adhesion to steel and consequently, there is no continuity of stresses and displacements on the contact layer, which is the basic assumption in the model of wave propagation in multilayered specimens (compare paragraph 2.2.1). Despite of such small thickness of debonding, guided waves appear extremely sensitive in detection of defects in adhesive bonding. High sensitivity of guided waves for debonding detection was confirmed by the results of pull-out tests for fully debonded specimens. The obtained results show that guided waves application may be an effective method for detection of adhesive debonding in the early stages of its development.

A novel element of the conducted investigation is a complex description of the nature of the wave phenomena occurring in a debonded element with special emphasis on the influence of the damage location on wave conversion and diffraction. The study includes the derivation of relationships between average velocities of particular modes and the debonding length (Section 5.2.2 and 5.2.3). Moreover, a short background for the longitudinal wave propagation in a single waveguide and a multilayered waveguide is recalled in paragraph 5.2.

The results presented in this Chapter were published in [241].

5.2 Theoretical background of wave propagation in free and embedded bar

The conducted investigations are focused on guided wave propagation in a steel bar partially embedded in grout (Figure 5.1c) with particular emphasis on the debonding between steel and grout. The wave excited along a free bar results in propagation of particular number of longitudinal modes in a single waveguide. When the wave reaches the part embedded in grout, propagation in a multilayered waveguide occurs.

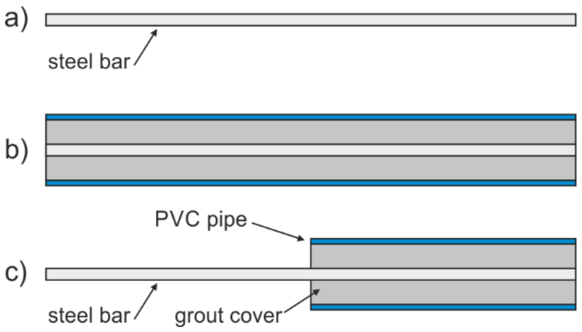

Figure 5.1. Schematic diagram of cylindrical waveguides: a) free bar; b) fully embedded bar; c) partially embedded bar

The inquiry presented in this section is related to the case of dispersion curves for a 1 cm steel bar embedded in grout with a thickness of 17.5 mm formed in a PVC pipe with a thickness of 2.5 mm, however in general they are valid for any case. The excitation frequency is 60 kHz to induce multimode propagation and to make observation of the mode conversion possible. For a selected frequency value, a single mode can propagate in the free bar and two modes with different velocities can propagate in the three-layer part of the specimen. Beside considerations based on dispersion curves, the results of finite element method (FEM) simulations performed in Abaqus/Explicit programme are presented here. Numerical results are presented in the form of snapshots illustrating the magnitude of acceleration and the deformation of the specimen at selected time instants

5.2.1 Wave propagation in free and multilayered bar

Dispersion curves for a multilayered waveguide are an important prerequisite for the implementation of the guided wave method for nondestructive testing. Figure 5.2 presents dispersion curves for a single 1 cm steel bar (Figure 5.1a) for a 1 cm steel bar embedded in grout with a thickness of 17.5 mm formed in a PVC pipe with a thickness of 2.5 mm, (Figure 5.1b). The excitation frequency used in the investigation is 60 kHz. According to dispersion curves given in Figure 5.2 for the selected value of frequency, a single mode can propagate in the free bar and two modes with different velocities can propagate in the three-layer part of the specimen. Thus, multimode excitation makes it possible to observe mode conversion. Longitudinal modes excited in multilayered part are denoted as standard: $L(0,1)$, $L(0,2)$, $L(0,3)$ etc. while modes in free part are indicated by upper index: $L^{bar}(0,1)$, $L^{bar}(0,2)$, $L^{bar}(0,3)$ etc.

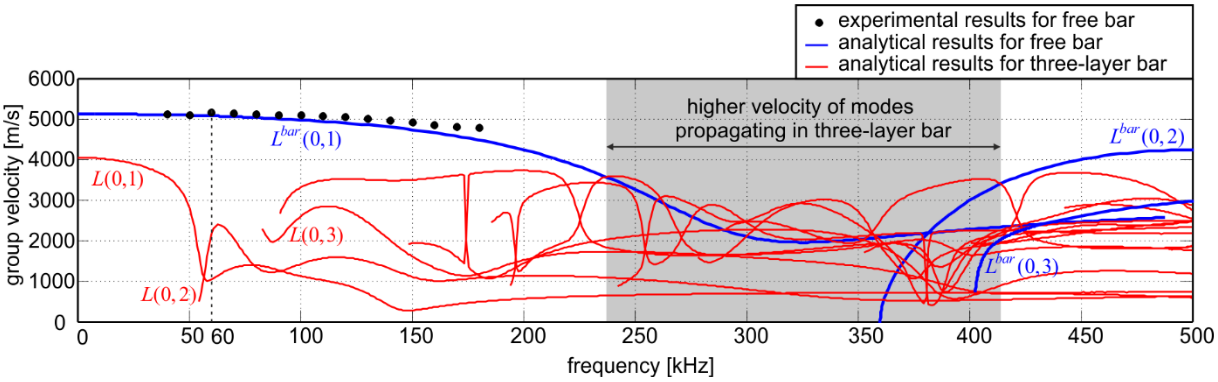

Figure 5.2. Group velocity dispersion curves of 1 cm diameter steel bar (E = 207 GPa, ν = 0.3, ρ = 7894 kg/m^3) and dispersion curves of 1 cm diameter steel bar embedded in grout with thickness of 17.5 mm (E = 33 GPa, ν = 0.2, ρ = 2067 kg/m^3) formed in PVC pipe with thickness of 2.5 mm (E = 1.5 GPa, ν = 0.4, ρ = 900 kg/m^3)

The velocity of the first $L(0,1)$ mode is smaller than the velocity of the first mode $L^{bar}(0,1)$ for a free bar. The cut-off frequencies of higher-order modes show lower values than for the free bar, thus the number of wave modes excited in the three-layer waveguide is much larger than for the free bar. It can be also observed that there is a frequency interval (from 237 kHz to 413.74 kHz) wherein the wave in the multilayered part propagates faster than in the free core.

In the further part of the Chapter, the phenomenon of the wave mode conversion is described. In order to systematize the names of modes, the following way of naming is adopted. The waves in the free bar are called $L^{bar}(0,1)$, $L^{bar}(0,2)$ etc. Waves in the multilayered bar are called $L(0,1)$, $L(0,2)$ etc. Waves in the tube are called $L^{tube}(0,1)$, $L^{tube}(0,2)$ etc. If a mode is converted, a low subscript is added and then for example label $\left\{L^{bar}(0,1)\right\}_{L(0,1)}$ means that the mode in the free bar $L^{bar}(0,1)$ was converted from the mode of the multilayered bar $L(0,1)$.

5.2.2 Wave propagation in partially embedded bars with perfect bonding

As the wave travels through the free length L_f of the bar, only the $L^{bar}(0,1)$ mode may propagate (Figure 5.3a), with the group velocity c_g^{bar} equal to 5071.9 m/s (cf. Figure 5.2). After the wave diffraction at the proximal end of the embedded part (i.e. at the anchorage), this mode propagates back to be recognized as the diffracted wave in the signal registered by sensor A (Figure 5.3b). Identification of this wave packet and assessment of its registration time t_d^A allows to determine the length of the uncoated bar:

$$L_f = \frac{c_g^{bar} t_d^A}{2}. \tag{5.1}$$

The diffracted wave is reflected from the free end of the bar and can be diffracted again at the proximal end of the embedded part. This multiple diffraction can be visible in the signal until its energy is dissipated. The second diffraction is marked in the signal from sensor A by dashed line (Figure 5.3d). The time interval between the input wave packet and the diffracted wave is the same as the time interval between subsequent diffractions.

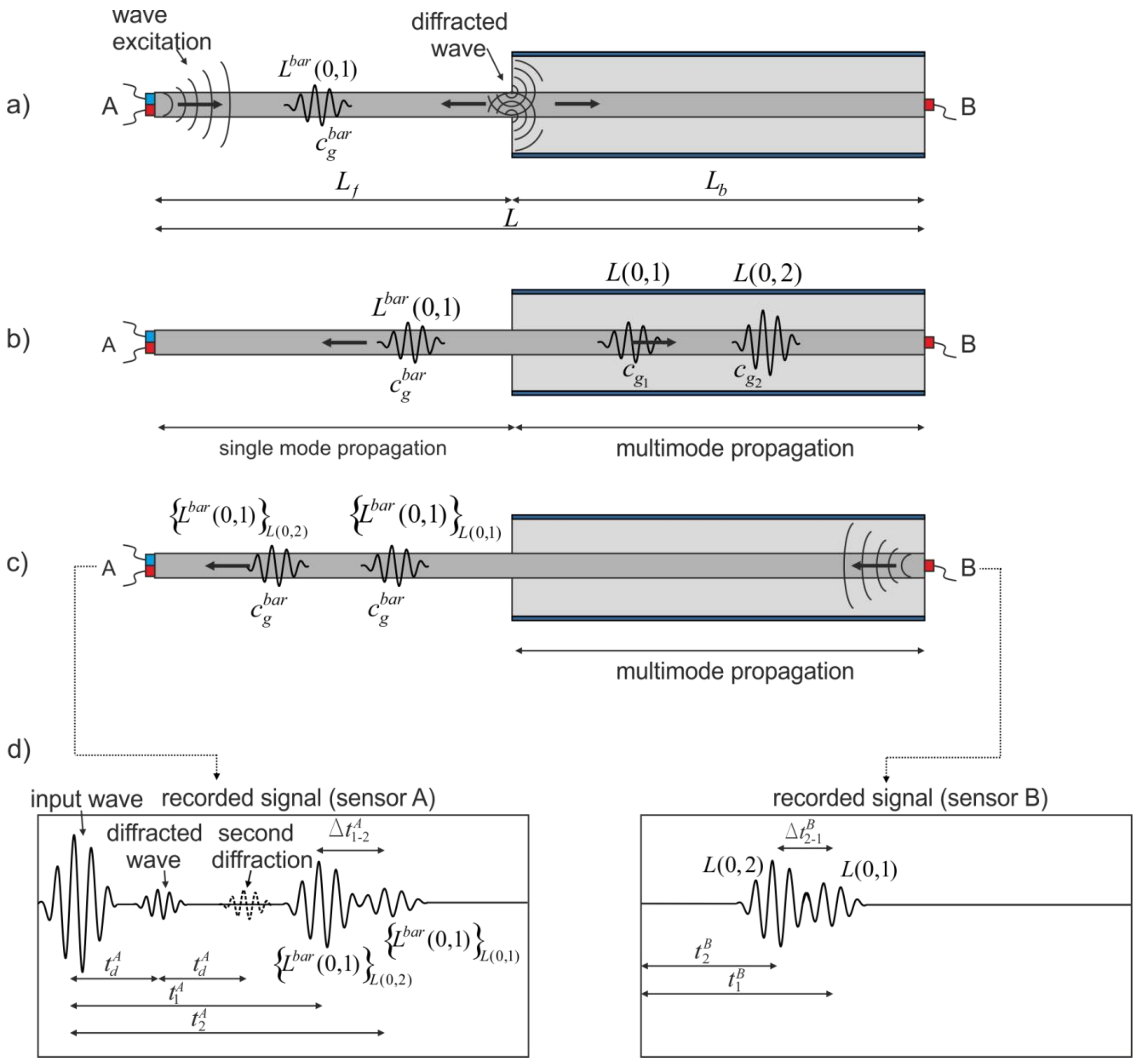

Figure 5.3. Wave propagation in a partially embedded bar, perfectly bonded with grout cover: a) wave diffraction at the proximal end of the embedded part, b) multimode propagation and mode separation at embedded part of bar, c) mode conversion at free part of bar, d) schemes of signals registered at both ends of the specimen

As the wave travels through the embedded part of the bar L_b, its energy is separated into particular modes which may propagate in the multilayered waveguide with different group velocities c_{g_i}. In the considered case the faster mode $L(0,2)$ propagates with the group velocity c_{g_2} = 2132.2 m/s, and the slower mode $L(0,1)$ propagates with the group velocity c_{g_1} = 1031.2 m/s (Figure 5.2 and Figure 5.3b). Particular wave packets corresponding to modes $L(0,1)$ and $L(0,2)$ can be registered by a sensor B when they reflect from the distal end of the embedded part of the specimen. Because of the difference in the group velocities, the mode $L(0,2)$ is registered earlier than $L(0,1)$ mode. The registration times of individual wave packets registered by a sensor B after passing the distance equal to the length of the specimen $L = L_f + L_b$ are:

$$t_i^B = \frac{L_f}{c_g^{bar}} + \frac{L_b}{c_{g_i}}. \tag{5.2}$$

The time interval between registration times of particular modes *i* and *j* in the signal registered by sensor B can be expressed by the formula:

$$\Delta t_{i-j}^B = \frac{L_b(c_{g_j} - c_{g_i})}{c_{g_i} c_{g_j}}. \tag{5.3}$$

The reflected modes propagate back along the coated bar. At the proximal end of the multilayered bar, after a repeated diffraction, they are subsequently converted into two $L^{bar}(0,1)$ modes existing in the free bar (Figure 5.3c). As the first $L(0,2)$ mode is converted into $\left\{L^{bar}(0,1)\right\}_{L(0,2)}$ mode and then $L(0,1)$ into $\left\{L^{bar}(0,1)\right\}_{L(0,1)}$. The velocities of modes $\left\{L^{bar}(0,1)\right\}_{L(0,2)}$ and $\left\{L^{bar}(0,1)\right\}_{L(0,1)}$ are identical and they are equal to c_g^{bar}. The registration times of individual wave packets, to be identified in the signal registered by sensor A after passing the double length of the specimen $2L$ are:

$$t_i^A = \frac{2L_f}{c_g^{bar}} + \frac{2L_b}{c_{g_i}} \tag{5.4}$$

the interval between their registration times is equal to:

$$\Delta t_{i-j}^A = \frac{2L_b(c_{g_j} - c_{g_i})}{c_{g_i} c_{g_j}}. \tag{5.5}$$

The average velocity of wave modes passing the double length of the specimen can be then calculated as:

$$c_{g_i}^{av} = \frac{2l}{t_i^A} = \frac{2(c_{g_i} l_f + c_g^{bar} l_b)}{c_g^{bar} c_{g_i}}. \tag{5.6}$$

Formulae (5.3) and (5.5) allow to conclude that with the increase of the bonded length L_b and the difference between velocities c_{g_i} of particular modes, the time interval Δt_{i-j}^A and Δt_{i-j}^B between modes increases, too. Thus, for a relatively short specimen, the mode separation may not be observed and the only mark of multimode propagation may be a spread of the input wave packet. Moreover, one can see that dispersion curves for a free core and a multilayered waveguide given in Figure 5.2 are an important prerequisite for the implementation of guided waves for nondestructive testing of embedded bars, because depending on the value of excitation frequency, the average velocity of the guided wave propagating through the total anchor length with debonding can be smaller, grater or the same as the average velocity of the guided wave propagated through the healthy anchor. Theoretical considerations have been confirmed by numerical calculations results. Figure 5.4 presents FEM results for the partially embedded bar with perfect bonding.

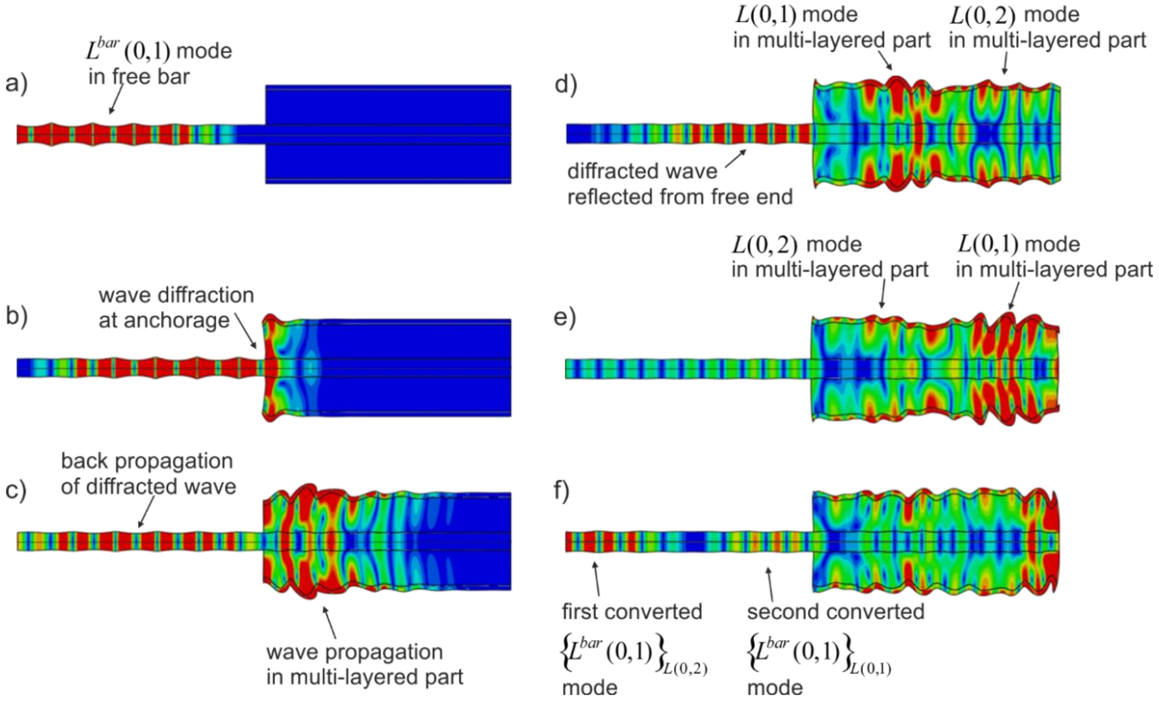

Figure 5.4. FEM results of wave propagation in the partially embedded specimen with perfect bonding: a) 0.1 ms; b) 0.16 ms; c) 0.25 ms; d) 0.38 ms; e) 0.59 ms; f) 0.73 ms

The magnitude of acceleration and the deformation of the specimen are illustrated in the snapshots at selected time instants. At the beginning, only longitudinal mode $L^{bar}(0,1)$ propagates along the bar as a single wave packet (Figure 5.4a). The wave diffraction at the proximal end of the embedded part is visible at t = 0.16 ms (Figure 5.4b). After diffraction, the wave is separated into two waves travelling in opposite directions (Figure 5.4c). The wave packet travelling along the steel bar contains the $L^{bar}(0,1)$ mode only, while in the part of the grouted bar two longitudinal modes can propagate. At the beginning of propagation in the three-layer specimen, a single wave packet containing both modes is visible solely (Figure 5.4c). However, due to different group velocities of particular modes, they separate during propagation in the anchored length of the specimen. At t = 0.38 ms, two wave packets can be distinguished (Figure 5.4d), namely $L(0,1)$ and $L(0,2)$. Next, these wave packets are reflected from the end of the specimen to reach the free part of the bar. Next, they are converted into two $\left\{L^{bar}(0,1)\right\}_{L(0,2)}$ and $\left\{L^{bar}(0,1)\right\}_{L(0,1)}$ modes, which propagate with the same velocity (Figure 5.4f).

5.2.3 Wave propagation in partially embedded bars with debonding

In this section three damage scenarios differing in debonding locations (i.e. debonding at the beginning, at the middle and at the end of the embedded part of the three-layer specimen) are analysed. The influence of the location of debonding on a registered wave propagation signals is investigated here.

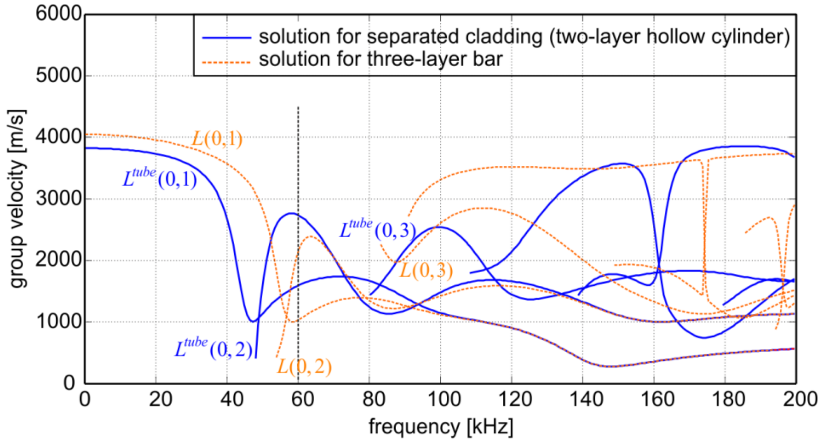

Figure 5.5. Group velocity dispersion curves of 1 cm diameter steel bar (E = 207 GPa, ν = 0.3, ρ = 7894 kg/m^3) embedded in grout with thickness of 17.5 mm (E = 33 GPa, ν = 0.2, ρ = 2067 kg/m^3) formed in PVC pipe with thickness of 2.5 mm (E = 1.5 GPa, ν = 0.4, ρ = 900 kg/m^3) and dispersion curves of two-layer grout-PVC hollow cylinder with removed steel core

With the development of debonding between the steel core and the grout cover, the debonded cladding becomes actually a two-layer hollow cylinder and the steel core inside can be considered as the free element. The velocity of wave propagating in separated grout-PVC system is determined from the dispersion relations corresponding to the multilayered hollow cylindrical waveguide. Dispersion curves for the tube consisting of grout and PVC mould are given in Figure 5.5. Additionally, modes for perfectly bonded three-layer system are traced by dashed lines.

It can be seen that removing the steel core acts on velocities of particular modes at some frequency ranges. For the considered excitation frequency equal to 60 kHz, both tube modes $L^{tube}(0,1)$ and $L^{tube}(0,2)$ propagate faster in a debonded grout/pipe system than the three-layer bar modes $L(0,1)$ and $L(0,2)$.

5.2.3.1 Debonding at the beginning of the embedded part

The first damage scenario concerns debonding located at the beginning of the embedded part. The phenomenon of wave propagation resembles the case of a specimen without debonding. After wave excitation, at the debonded part of length L_d a single mode $L^{bar}(0,1)$ can propagate solely. As the wave reaches the location of where the bar embedded in grout, it diffracts (Figure 5.6a). The part of the wave energy propagates back along the free bar and it is registered as the diffracted wave and the other part propagates in the separated cladding as $L^{tube}(0,1)$ and $L^{tube}(0,2)$ modes as well as in the three-layer composite part as $L(0,1)$ and $L(0,2)$ modes (Figure 5.6b). While the uncovered part of the bar L_f is longer than in the case of perfect bonding, the wave diffracted at the anchorage is registered later. Accordingly to Eq. (5.4) the shortening of the multilayered part L_b causes that modes separation is poorly visible.

The schemes of signals registered at both ends of the bar are presented in Figure 5.6c. Additionally, the signals for fully bonded specimen are imposed to illustrate shifting of characteristic wave packets. The first reflection from the end of the specimen is registered at a point A after the time interval t_i^A described by Eq. (5.4). In the presented case, the group velocity of the first mode in the free bar c_g^{bar} is higher than the velocity of the fastest mode in the coated bar $c_{g,\max}$. The increase of the length of the free part, resulting from the debonding occurrence, causes that the reflection from the end of the specimen is recorded faster than for the healthy specimen.

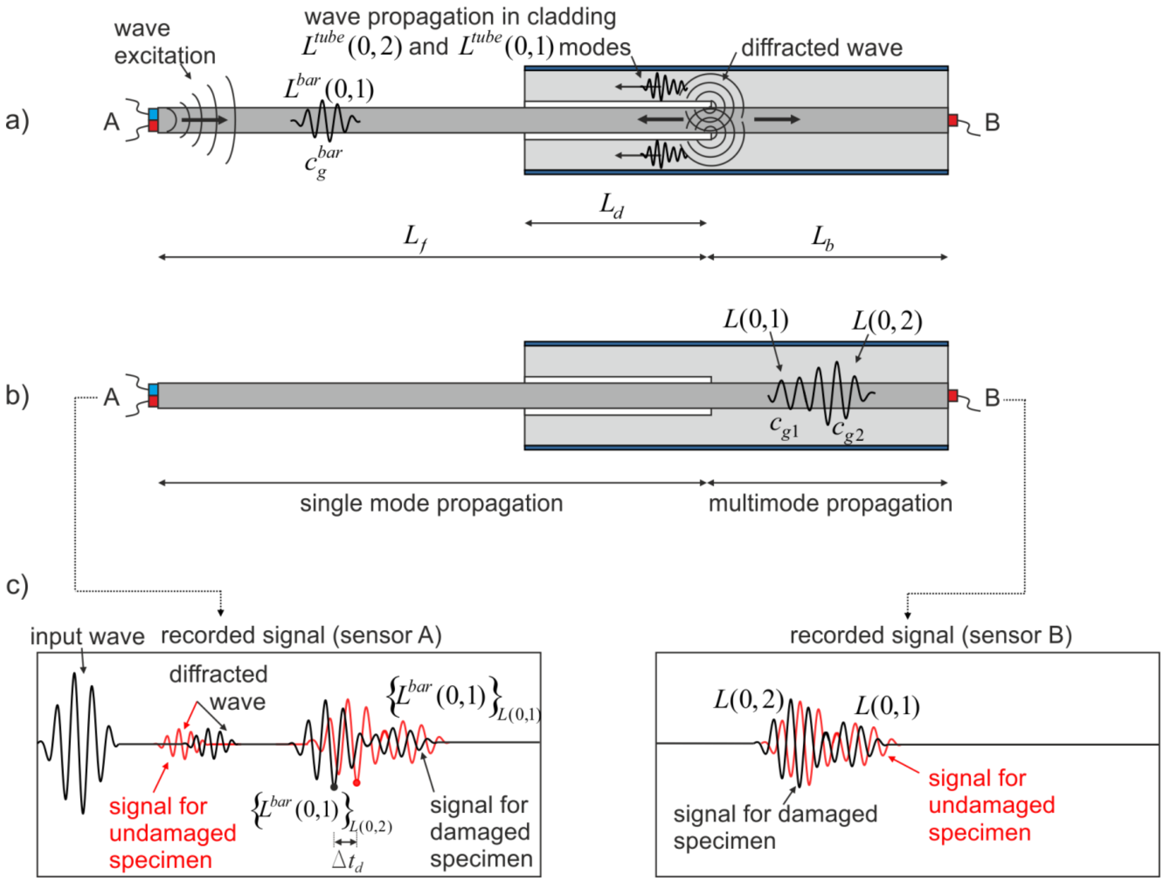

Figure 5.6. Wave propagation in the partially embedded bar with debonding at the beginning of the embedded part: a) wave diffraction at the debonding end; b) multimode propagation in coated part; c) schemes of signals registered at both ends of the specimen

The difference in the time of registration between the damaged specimen with debonding of length L_d and the healthy specimen equals:

$$\Delta t_d = \frac{2L_d\left(c_g^{bar} - c_{g,\max}\right)}{c_g^{bar} c_{g,\max}}. \tag{5.7}$$

The increase in the length of the defective connection shortens the time-of-flight (Δt_d is positive). This relationship is valid only when free bar modes propagate faster than multilayered bar modes ($c_g^{bar} > c_{g,\max}$, c.f. Figure 5.2). In the case of frequency ranges corresponding to the fastest multilayered bar mode propagates faster than free bar modes ($c_g^{bar} < c_{g,\max}$), the damaged bonding causes the increase of registration time of the first reflection from the end of the anchor (Δt_d is negative). When the fastest multilayered bar mode propagates with the same group velocity as the free bar modes ($c_g^{bar} = c_{g,\max}$), the increase of bonding length does not change the time-of-flight of reflection from the end of the anchor (Δt_d is equal to zero). The length of debonding can be estimated on the basis of the average wave velocity of reflections from the end provided known dispersion curves for the free core and for the cladding. The selection of appropriate excitation frequency affects the effectiveness of the assessment of the debonding length. The greater the difference between the fastest mode propagating in the free bar and the fastest mode in the coated bar, the greater the variation of the average wave velocity due to the debonding occurrence.

The results of FEM calculations for the specimen with debonding of length of 20 cm at the beginning of the embedded part are illustrated in Figure 5.7. Initially, the wave propagates in the uncovered bar (Figure 5.7a, b).

After being diffracted, part of the energy is transmitted into a separated grout part (Figure 5.7c) and it propagates back. Due to a shorter multilayered part comparing with the undamaged specimen (Figure 5.4), particular longitudinal modes $L(0,1)$ and $L(0,2)$ cannot be distinguished, thus they are visible as a single wave packet containing both longitudinal forms.

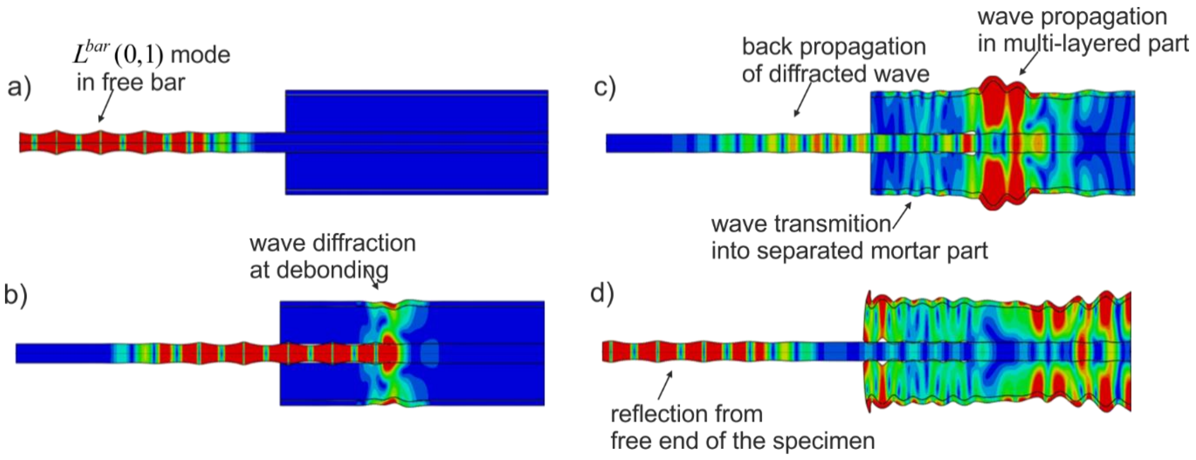

Figure 5.7. FEM results of wave propagation in a partially embedded specimen with debonding at the beginning of the embedded part: a) 0.1 ms, b) 0.19 ms, c) 0.27 ms, d) 0.46 ms

Figure 5.8 shows numerical acceleration signals registered at four nodes (s1 to s4): at the beginning of the specimen (Figure 5.8a), at the end of the free length Figure 5.8b), in the middle of the anchor body (Figure 5.8c) and at the end of the specimen (Figure 5.8d). Vibrations accelerations of were registered along the bar in longitudinal direction. The shape of numerically obtained signals corresponds to theoretical signal schemes shown in Figure 5.6c.

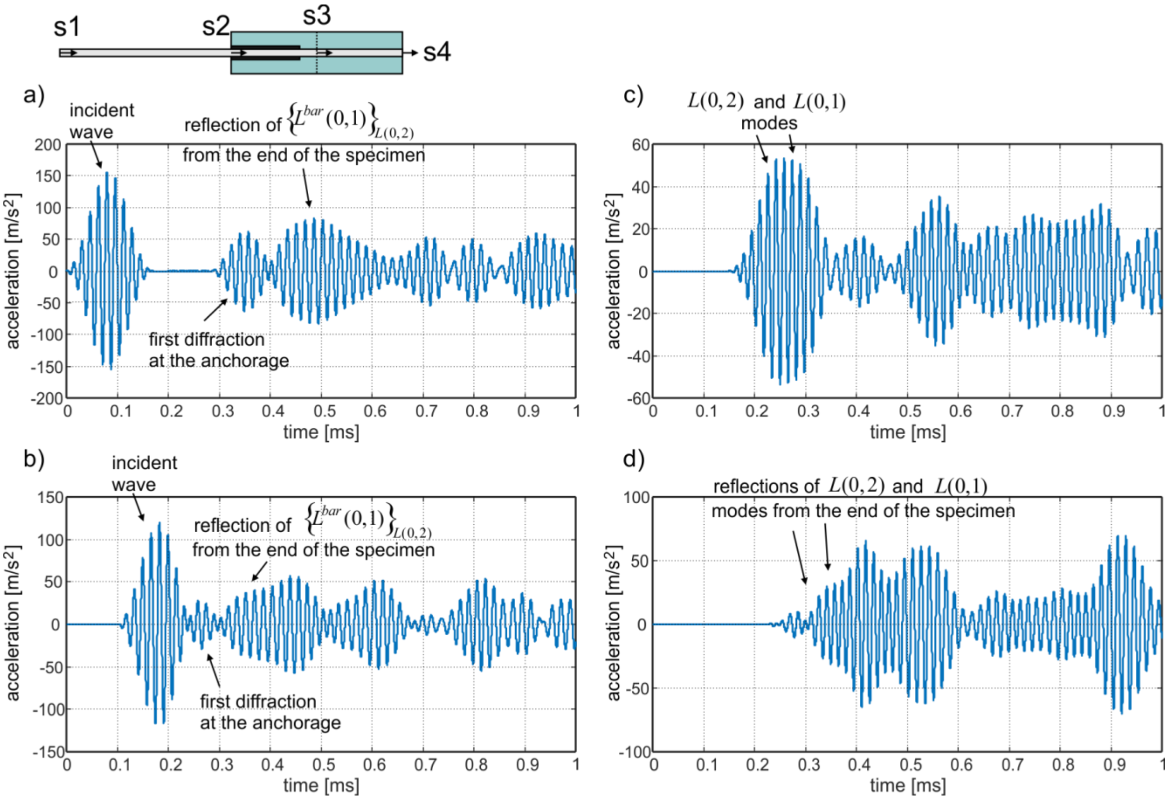

Figure 5.8. FEM results of wave propagation in a partially embedded specimen with 20 cm debonding at the beginning of the embedded part in the form of time-domain signals registered at nodes: a) s1; b) s2; c) s3 and d) s4

5.2.3.2 Debonding in the middle of the embedded part

The second damage scenario concerns debonding located in the middle of the embedded part of the specimen (Figure 5.9). After wave excitation and diffraction at the proximal end of the embedded part, two modes propagate along the bonded length L_{b_1} (a). When the wave reaches the start of debonding, it diffracts. Along the free part L_f the first mode existing in the free bar $L^{bar}(0,1)$ may propagate solely. Moreover, a part of energy propagates in the separated cladding as wave packets containing four modes $\{L^{tube}(0,1)\}_{L(0,1)}$, $\{L^{tube}(0,2)\}_{L(0,1)}$, $\{L^{tube}(0,1)\}_{L(0,2)}$ and $\{L^{tube}(0,2)\}_{L(0,2)}$ (Figure 5.9b). In the debonded steel core two modes exist: $\{L^{bar}(0,1)\}_{L(0,2)}$ and $\{L^{bar}(0,1)\}_{L(0,1)}$. Four modes travelling in the separated cladding and two modes travelling in the debonded steel core reach the end of debonding and there they are again diffracted (Figure 5.9c)

After the diffraction each mode is converted into two modes propagating along the bonded length L_{b_2}. As a consequence along L_{b_2} at least twelve modes start travelling. Four modes $\{L(0,1)\}_{L^{bar}(0,1)}$, $\{L(0,1)\}_{L^{bar}(0,2)}$, $\{L(0,2)\}_{L^{bar}(0,1)}$ and $\{L(0,2)\}_{L^{bar}(0,2)}$ were excited after diffraction of $\{L^{bar}(0,1)\}_{L(0,2)}$ and $\{L^{bar}(0,1)\}_{L(0,1)}$ while next eight modes

$\left\{L(0,1)\right\}_{\left\{L^{tube}(0,1)\right\}_{L(0,1)}}$, $\left\{L(0,2)\right\}_{\left\{L^{tube}(0,1)\right\}_{L(0,1)}}$, $\left\{L(0,1)\right\}_{\left\{L^{tube}(0,1)\right\}_{L(0,2)}}$, $\left\{L(0,2)\right\}_{\left\{L^{tube}(0,1)\right\}_{L(0,2)}}$, $\left\{L(0,1)\right\}_{\left\{L^{tube}(0,2)\right\}_{L(0,1)}}$, $\left\{L(0,2)\right\}_{\left\{L^{tube}(0,2)\right\}_{L(0,1)}}$, $\left\{L(0,1)\right\}_{\left\{L^{tube}(0,2)\right\}_{L(0,2)}}$, $\left\{L(0,2)\right\}_{\left\{L^{tube}(0,2)\right\}_{L(0,2)}}$ were excited after the diffraction of modes travelling in the separated cladding. According to dispersion curves given in Figure 5.2 and Figure 5.5, the converted bar modes travel faster than the converted tube modes.

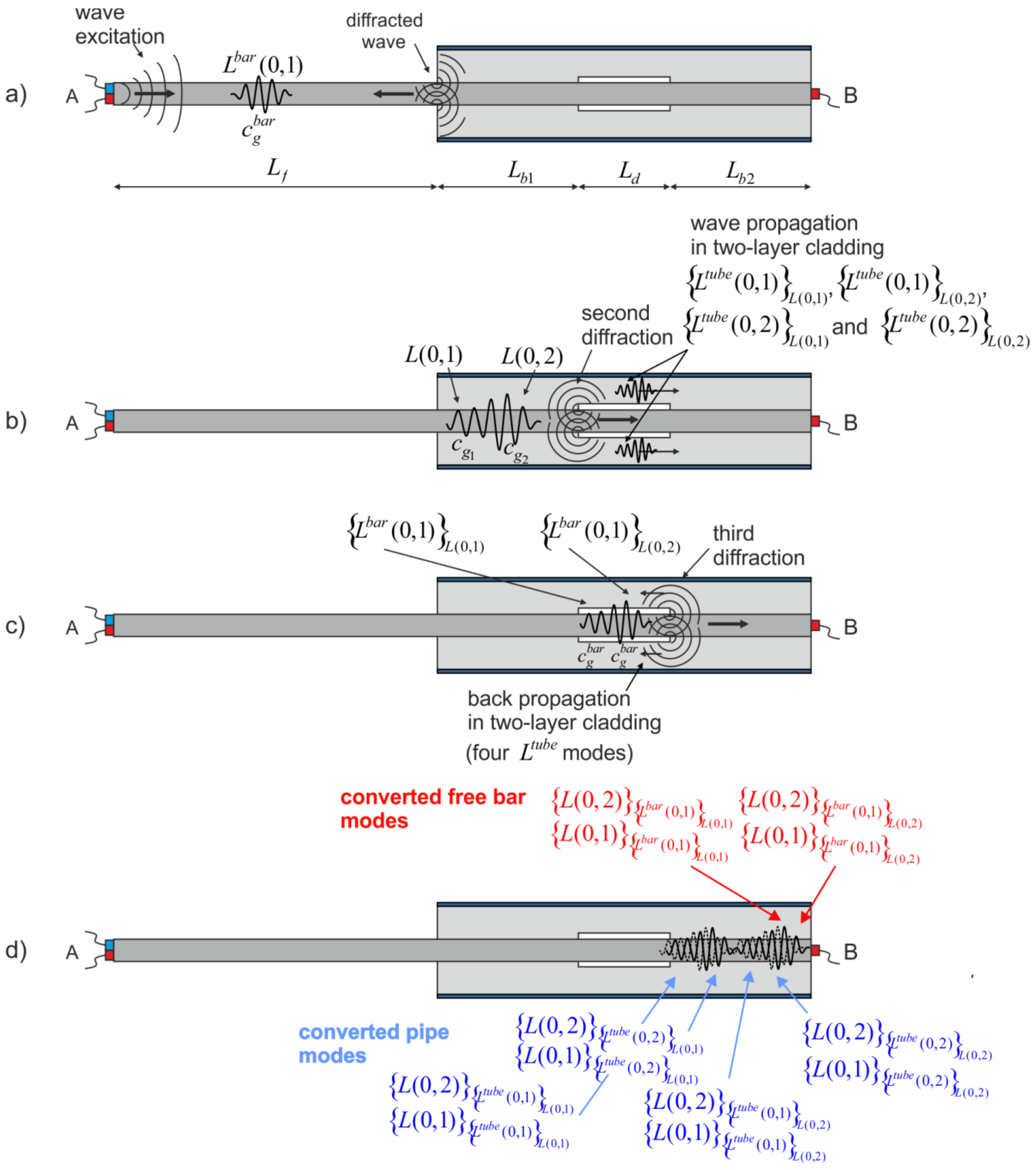

Figure 5.9. Wave propagation in a partially embedded bar with debonding at the middle of the embedded part: a) wave diffraction at the proximal end of the embedded part, b) multimode propagation in coated part, second diffraction at the beginning of debonding, c) mode conversion in separated free rod and third diffraction at the end of debonding, d) mode conversion and multimode propagation in coated part

The converted free bar modes are represented in Figure 5.9d by a solid line, while converted tube modes by a dashed line.

The results of FEM analysis are presented in Figure 5.10 and Figure 5.11. Figure 5.10 presents graphical visualization of wave propagation while time-domain signals are given in Figure 5.11. The travelling wave (Figure 5.10a) diffracts at the anchorage (Figure 5.10b) and again at the start of debonding (Figure 5.10c).

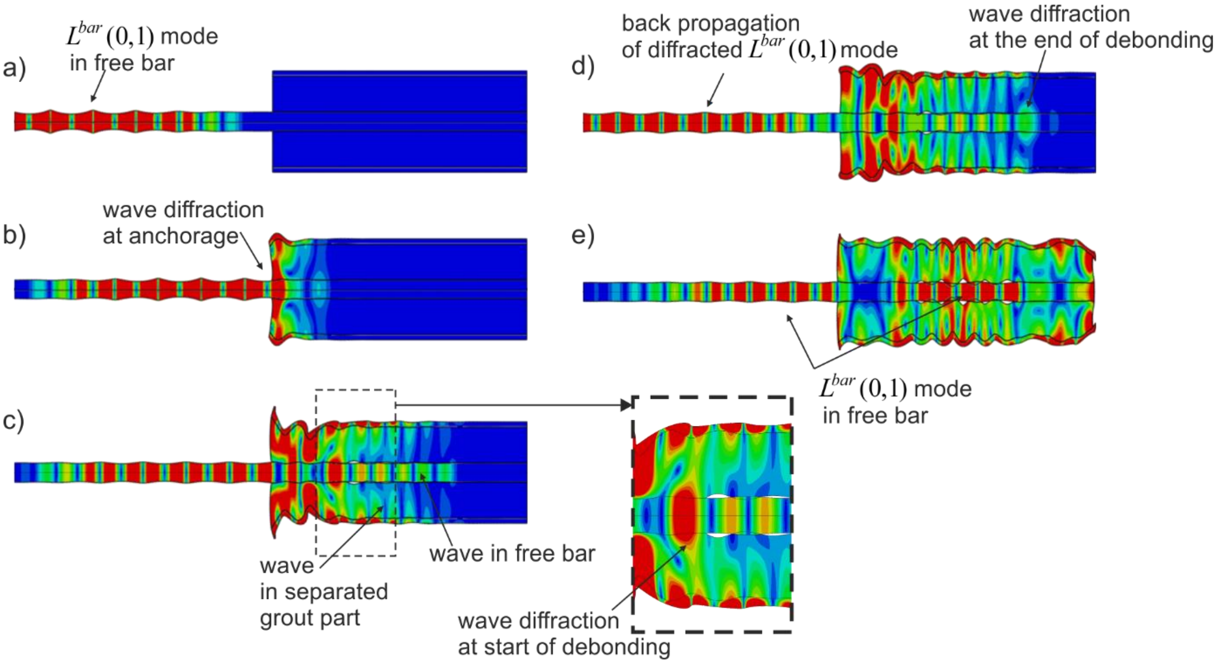

Figure 5.10. FEM results of wave propagation in a partially embedded specimen with debonding at the middle of the embedded part: a) 0.1 ms, b) 0.16 ms, c) 0.24 ms, d) 0.26 ms, e) 0.38 ms

The visualization in Figure 5.10c clearly indicates that after diffraction the wave energy is divided into $L^{bar}(0,1)$ mode propagating in the free bar and waves travelling in the separated grout part. Group velocities of these wave modes differ. As a consequence, the wave which propagates in the free bar reaches the end of debonding first, where is diffracted again (Figure 5.10d). The next wave diffraction at the debonding end causes that in the middle part of the separated cover both forward and backward waves interfere with each other. The complexity of the phenomena greatly hinders the interpretation and recognition of individual wave modes.

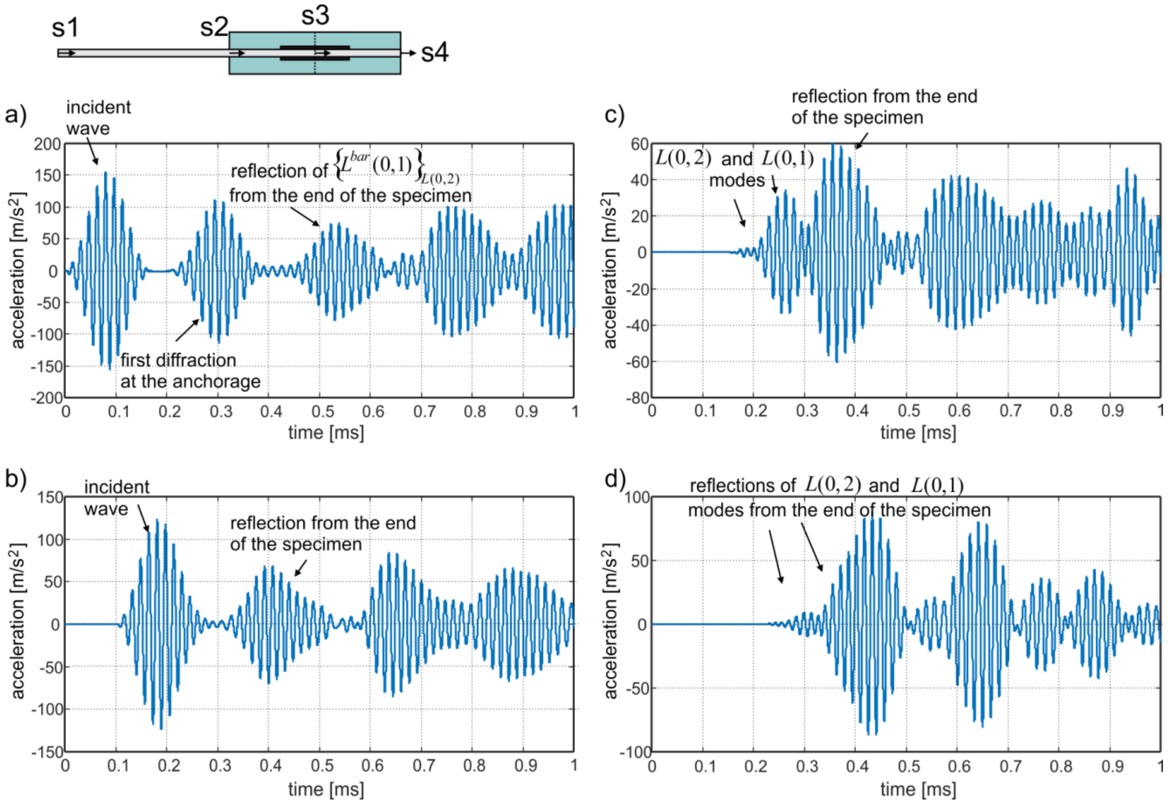

Figure 5.11. FEM results of wave propagation in a partially embedded specimen with 20 cm debonding in the middle of the embedded part in the form of time-domain signals registered at nodes: a) s1; b) s2; c) s3 and d) s4

5.2.3.3 Debonding at the end of embedded bar

The last damage scenario refers to the case of a debonding occurring at the end of the three-layer composite bar. The single mode $L^{bar}(0,1)$ propagates along the free bar (Figure 5.12a). In the three-layer part of length L_{b_1} two longitudinal modes propagate and after diffraction they are converted into $\left\{L^{bar}(0,1)\right\}_{L(0,2)}$ and $\left\{L^{bar}(0,1)\right\}_{L(0,1)}$ modes propagating in the free bar and into modes propagated in the two-layer separated cladding $\left\{L^{tube}(0,1)\right\}_{L(0,1)}$, $\left\{L^{tube}(0,2)\right\}_{L(0,1)}$, $\left\{L^{tube}(0,1)\right\}_{L(0,2)}$ and $\left\{L^{tube}(0,2)\right\}_{L(0,2)}$ (Figure 5.12b and c). Waves are reflected from the end of the specimen and during propagation along bonded part are converted into twelve longitudinal modes (Figure 5.12d): six $L(0,1)$ and six $L(0,2)$ (Figure 5.12d).

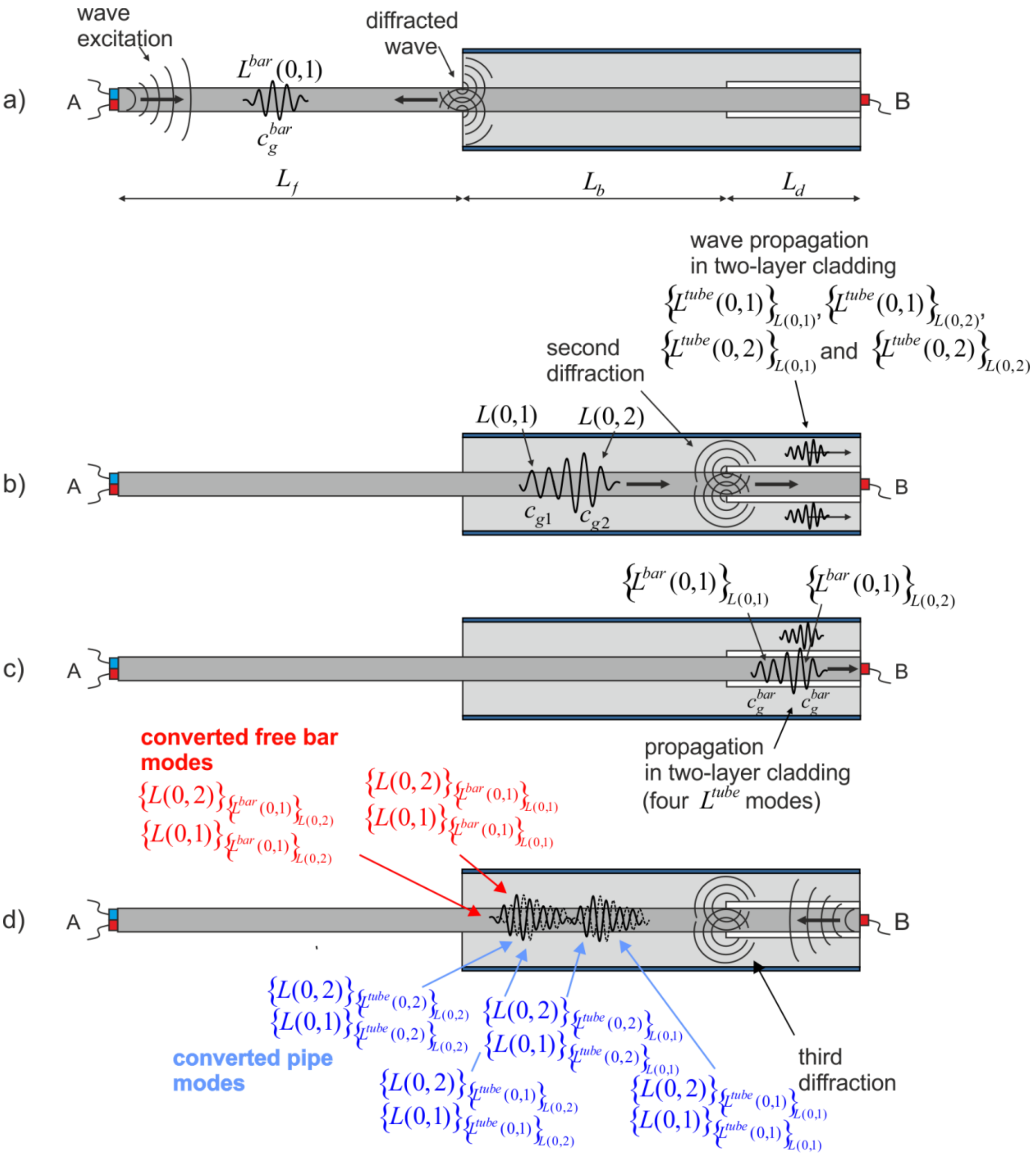

Figure 5.12. Wave propagation in a partially embedded bar, with debonding at the end of the grout part: a) wave diffraction at the distal end of the embedded part, b) multimode propagation in coated part, second diffraction at the start of debonding, c) mode conversion in separated free rod and third diffraction at the end of debonding, d) reflection from the end of the anchor, third diffraction at the start of debonding, mode conversion and multimode propagation in coated part

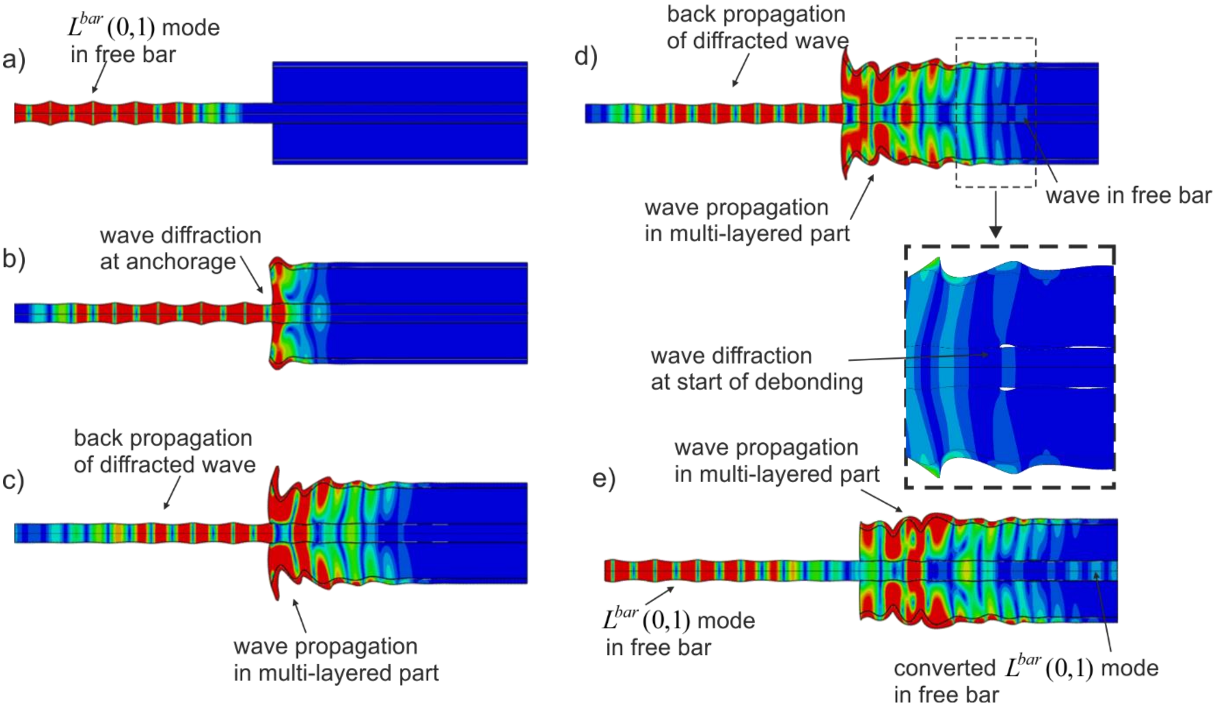

Figure 5.13. FEM results of wave propagation in the in the partially embedded specimen with debonding at the distal end of the embedded part: a) 0.1 ms, b) 0.16 ms, c) 0.22 ms, d) 0.24 ms and e) 0.27 ms

Figure 5.13 shows the results of FEM analysis. The excited wave is diffracted both at the proximal end of the embedded part and at the start of debonding. Before the second diffraction it propagates in the covered rod with perfect bonding between layers. The length of the multilayered part of perfect inter-layer bonding is equal to 30 cm and it is too short to allow for separation of $L(0,1)$ and $L(0,2)$ modes. Thus, only one wave packet is initially visible. After $t = 0.24$ ms the diffracted wave is transmitted into grout and into the steel bar (Figure 5.13c). The wave in the steel core propagates faster than the wave in the two-layer separated tube and reaches the end of the specimen after t = 0.27 ms. The wave travelling in grout is reflected from the distal end of the specimen and it propagates back. Numerical signals registered at four nodes along the anchor FEM model are given in Figure 5.14.

The theoretical consideration presented in above paragraphs 5.2.3.1-5.2.3.3 indicates that the presence of debonding affects the wave propagation in a multilayered specimen, inter alia, the number of travelling modes, their velocities, conversions and diffractions. In order to consider the phenomenon of wave propagation in bars partially embedded in grout with debonding at steel/grout interface, dispersion curves for multilayered bars, hollow cylinders and free bars need additional inquiry.

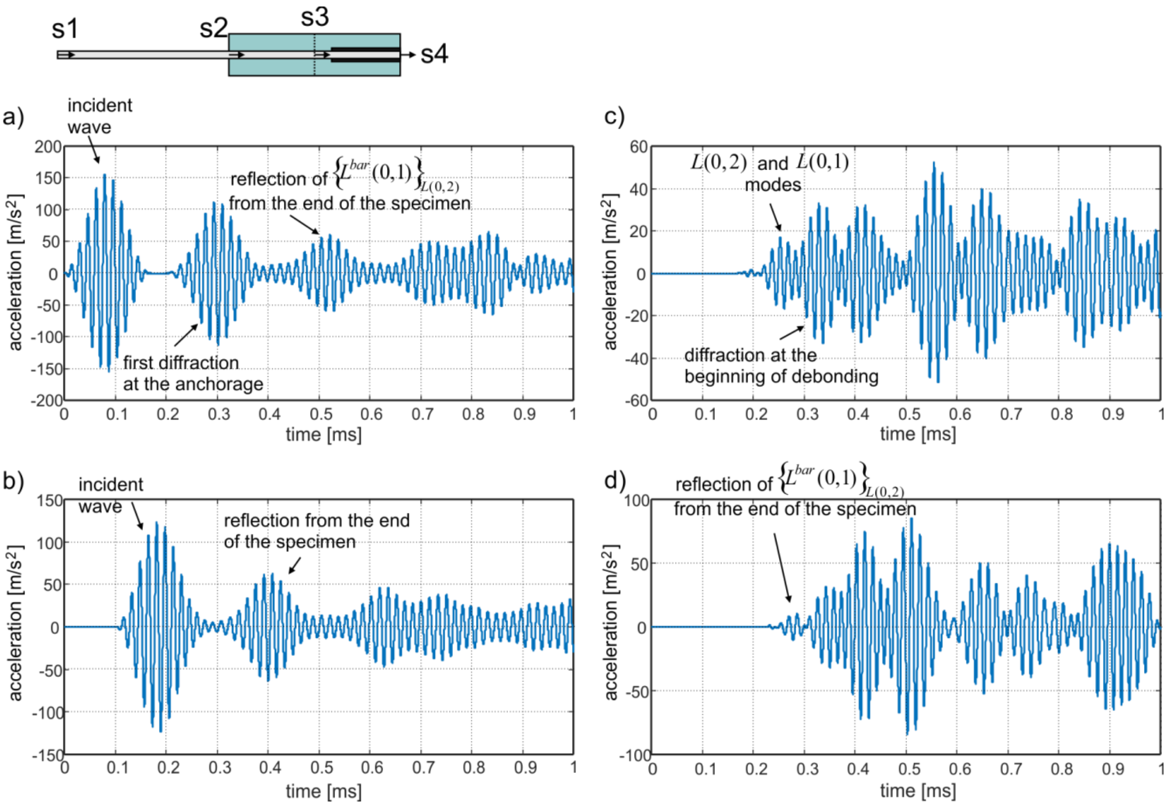

Figure 5.14. FEM results of wave propagation in a partially embedded specimen with 20 cm debonding at the end of the embedded part in the form of time-domain signals registered at point: a) s1; b) s2; c) s3 and d) s4

5.3 Experimental investigations on partially embedded bars with pre-existing debonding

5.3.1 Description of specimens

Experimental investigations were carried out on laboratory models of ground anchors. The specimens were made of a steel circular bar with a diameter of d = 1 cm and a length of 100 cm, embedded in a cylindrical grout block performed in a PVC mould having an outer diameter of d_a = 5 cm. The thickness of the mould wall was 2.5 mm. The material parameters are: E = 207 GPa; ν = 0,3; ρ = 7894 kg/m^3 (steel), E = 33 GPa, ν = 0.2, ρ = 2067 kg/m^3 (grout), E = 1.5 GPa; ν = 0,4; ρ = 900 kg/m^3 (PVC). Prior to experimental tests the specimens were left to cure in order to obtain the full grout strength.

The test specimens included one pristine anchor and thirteen anchors with various damage scenarios, collected into five groups (from #A to #E), as shown in Figure 5.15. Groups #A, #B, and #C contain specimens with debonding located at the beginning, in the middle and at the end of the multilayered part of the anchor. Within each of groups #A–C four different specimens were prepared of different length of the debonded part (L_d = 10, 20, 30 and 40 cm). Additionally, one fully debonded (#D) and one fully bonded (#E) specimens were performed. The defect in the form of debonding was introduced using a cellophane film with a thickness of about 30 micrometers. Two layers of the film were attached to the bar only at its edge and tightly wrapped around the bar.

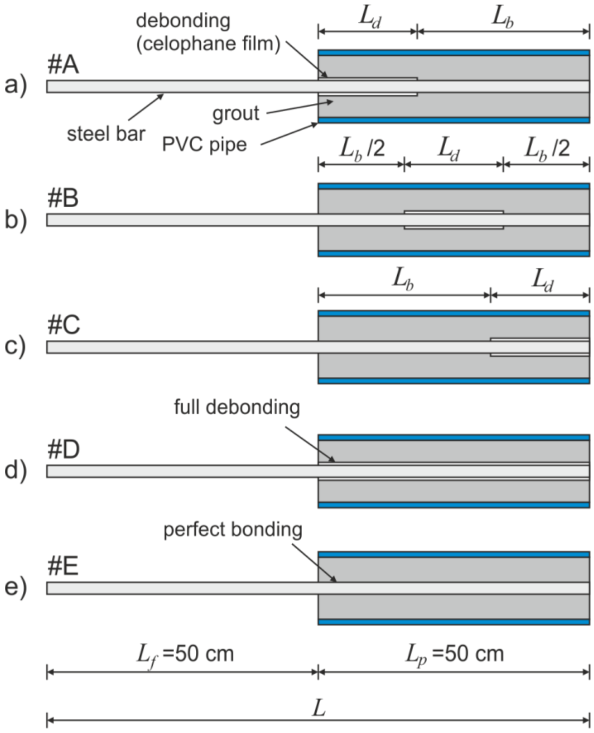

Figure 5.15. Schemes of investigated specimens: a) group #A with debonding at the beginning of the embedded part; b) group #B with debonding in the middle of the embedded part; c) group #C with debonding at the end of the embedded part; d) fully debonded anchor #D; e) fully bonded anchor #E

5.3.2 Experimental procedure

The prepared specimens were subjected to both nondestructive and destructive tests. In the first stage, ultrasonic guided waves were generated and propagated though the anchors. The experimental set-up for wave propagation measurements is presented in Figure 5.16a. Three plate piezo transducers Noliac NAC2011 used for both actuation and sensing of guided waves. Two transducers were attached to the free end of the bar, i.e. the actuator and sensor A while one transducer (sensor B) was attached to the fixed end of the bar. The excitation signal was a wave packet represented by a ten-cycle sine function with a carrier frequency of 60 kHz modulated by the Hanning window.

In the second stage, all specimens were subjected to destructive tests (Figure 5.16b) in order to investigate the influence of pre-existing debonding on the load capacity of the connection between steel and grout. The specimen was inserted in the steel frame to ensure that the tensile load is applied axially. The pull-out tests were carried out in a testing machine Zwick/Roell Z400 using displacement control with the cross-head speed equal 3 mm/min.

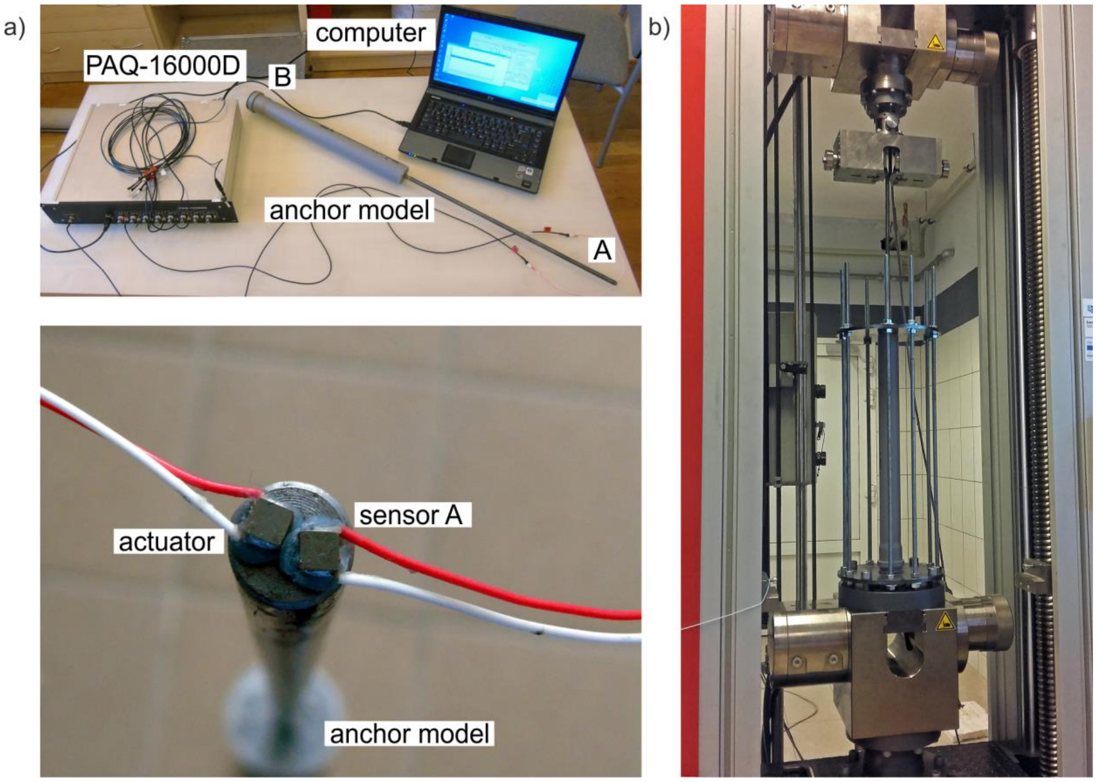

Figure 5.16. Experimental set-up: a) equipment for guided wave propagation and the tested specimen with a detail of actuator and sensor attached to the free end of the bar; b) pulled-out specimen mounted on the testing machine

5.4 Results

5.4.1 Results of guided wave propagation

Experimental wave propagation signals acquired for anchors with a variable length of a defect are presented in Figures 5.17 to 5.19 for specimens showing debonding part at the start, in the middle and at the other end of the embedded part, respectively. All measured signals were normalized to achieve the maximum amplitude value equal 1. The characteristic reflections have been identified and described. Moreover, straight dashed lines led through the highlighted wave packets indicate a linear relationship between the time-of-flight of particular reflections and the debonding length.

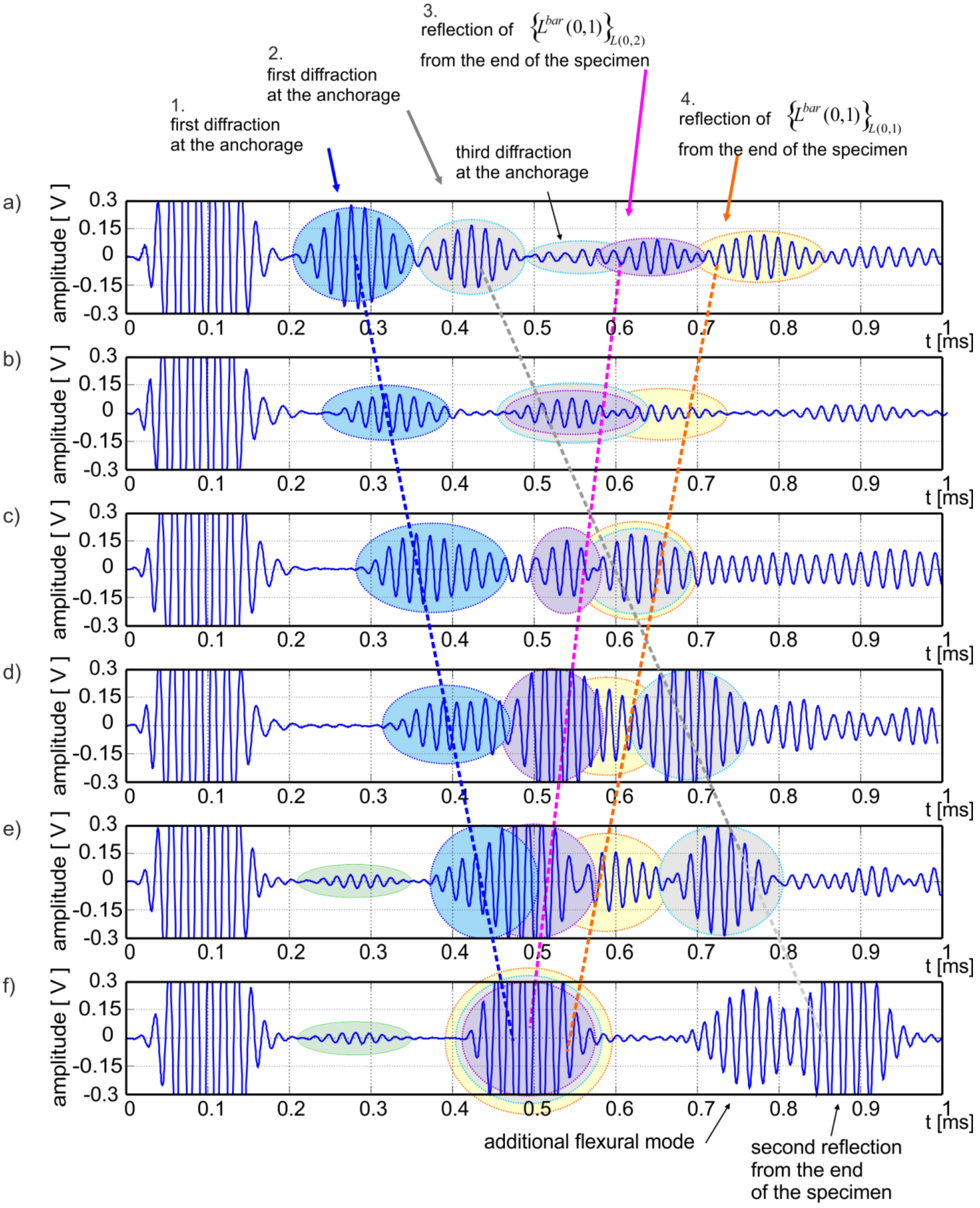

Figure 5.17. Experimental wave propagation signals registered at the free end of the bar with debonding at the beginning of the embedded part: a) fully bonded specimen #E, specimen #A with debonding of length of b) 10 cm, c) 20 cm, d) 30 cm, e) 40 cm and f) fully debonded specimen #D

Figure 5.17 presents signals for the case of specimen with debonding at the start of the embedded part. Line no. 1 passes through highlighted wave packets diffracted at the anchorage and line no. 2 crosses the wave packets corresponding to the second diffraction. Additionally, in the signal for the fully bonded specimen case, a third diffraction can be observed. This is the case of the shortest distance between the excitation point and the anchorage and the energy dissipation intensity is low. In other specimens the third diffraction cannot be identified due to its interference with other wave packets. For each signal the distance between the lines no. 1 and no. 2 is the same as the distance between the line no. 1 and the input wave. Another group of identified wave packets comes from the reflections from the end of the specimen. Due to specimens with a relatively long fully bonded part two modes can be clearly indicated. The line no. 3 indicates a mode propagating in a free bar $\left\{L^{bar}(0,1)\right\}_{L(0,2)}$ originated from the reflection of $L(0,2)$ mode at the end of the specimen. Similarly, line no. 4 indicates a $\left\{L^{bar}(0,1)\right\}_{L(0,1)}$ mode. While the debonding length is not larger than 30 cm these two modes are registered as a single wave packet and they are difficult to identify in registered signals. The time-of-flight of reflections from the anchorage increases with the debonding length until it coincides with the reflection from the end of the specimen registered for a fully debonded anchor #D. The registration time of reflections from the end of the specimen decreases proportionally to the increase of debonding length damage according to Eq. (5.3). The difference in the angle of inclination for the lines no. 3 and 4, passing through the wave packets reflected from the end of the specimen is caused by difference in wave velocity of particular modes, i.e. $L(0,2)$ mode is characterized by a higher group velocity than $L(0,1)$ mode and consequently, the line connecting subsequent reflections of $L(0,2)$ has the higher angle of inclination. Figure 5.18 shows results for the specimens with debonding in the middle of the embedded part. Because deboning is located within the three-layer part, in each signal the diffracted wave is observed at the same time independently of the debonding length. Therefore, lines no. 1 and no. 2 are vertical. In general, only the first diffraction is easy to identify. The second diffraction is clearly visible only in the signal gained for anchor #A. The lines no. 3 and no. 4 indicate reflections of $\left\{L^{bar}(0,1)\right\}_{L(0,2)}$ and $\left\{L^{bar}(0,1)\right\}_{L(0,1)}$ modes, respectively. An additional line no. 5 connects reflections from the start of the debonding. This reflection interferes with the second diffraction for shorter debonding lengths L_d. In the case of longer debonding lengths the distance L_{b_1} between the proximal end of the embedded part and the start of debonding shortens and reflections from the beginning of debonding interfere with the first diffraction.

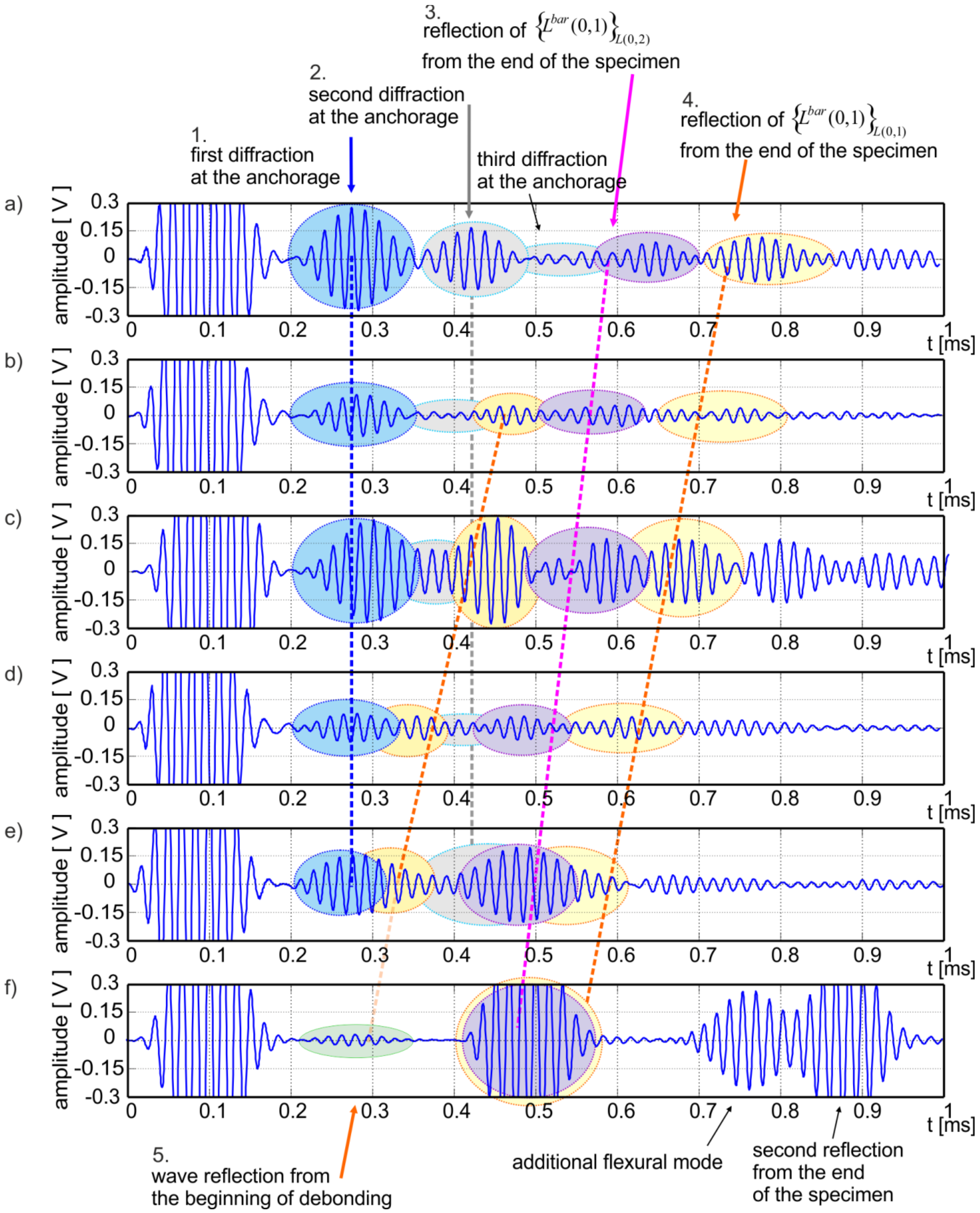

Figure 5.18. Experimental wave propagation signals registered at the free end of the bar with debonding at the middle of the embedded part: a) fully bonded specimen #E, specimen #A with debonding of length of b) 10 cm, c) 20 cm, d) 30 cm, e) 40 cm and f) fully debonded specimen #D

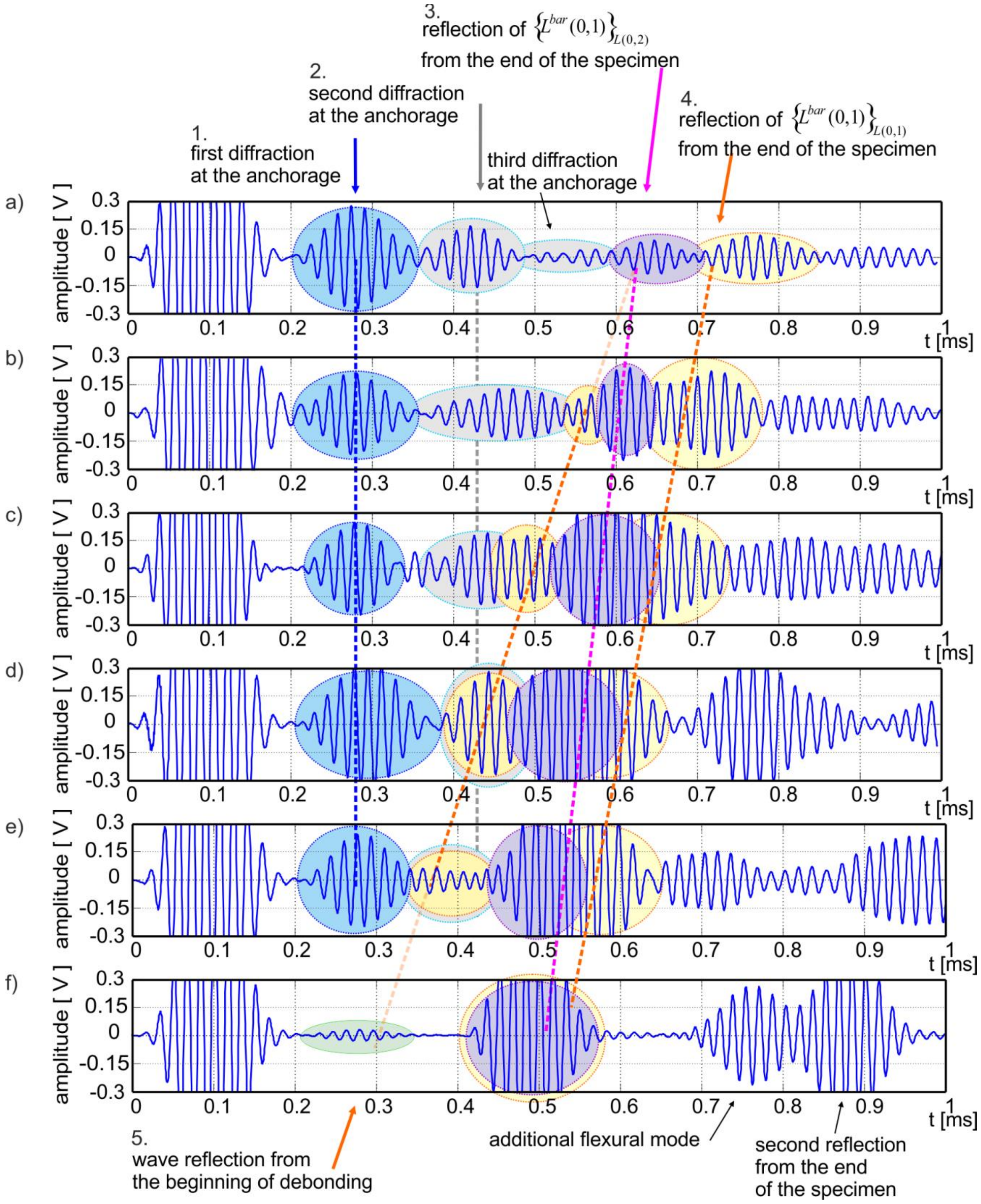

Figure 5.19. Experimental wave propagation signals registered at the free end of the bar with debonding at the end of the embedded part: a) fully bonded specimen #E, specimen #A with debonding of length of b) 10 cm, c) 20 cm, d) 30 cm, e) 40 cm and f) fully debonded specimen #D

Figure 5.19 presents results for specimens with debonding at the end of the embedded part. As previously, reflections from the anchorage are registered at the same time and they are indicated by a vertical line no. 1. Reflections from the beginning of debonding are visible (line no. 5), but for shorter debonding length they interfere with reflections of $\left\{L^{bar}(0,1)\right\}_{L(0,2)}$ mode from the end of the specimen and for longer debonding lengths they interfere with the second (line no. 2) or the first diffraction (line no. 1).

The debonding length L_d is incremented with a step of 10 cm for specimens from groups #A, #B and #C. Accordingly, the times of flight of reflections from the end of specimens decrease by the same time step in each group. Thus, straight lines no. 4 and no. 5 passing through reflections of $\left\{L^{bar}(0,1)\right\}_{L(0,2)}$ and $\left\{L^{bar}(0,1)\right\}_{L(0,1)}$ are characterized by the same angle of inclination in each of the three cases. The difference between the angle of inclination can be observed for the lines connecting reflections from the beginning of debonding (lines no. 5 in Figure 5.18 and Figure 5.19). In particular anchors of the group #B the difference in the distance between the PZT sensor and the beginning of debonding ($L_f + L_{b_1}$) is equal to 5 cm, while for anchors in group #C for the same distance ($L_f + L_b$) the difference is equal to 10 cm. For this reason, the line connecting reflections from debonding in group #C is more inclined.

Figure 5.20 shows signals registered by sensor B plotted in the form of envelopes with normalized amplitudes. It can be seen that also in the case of signals registered at the fixed end, the time shifting of the first reflection is visible for various lengths of debonding. Between the first and second reflections of $L(0,2)$ mode from the end of the specimen, separated $L(0,1)$ modes, converted tube modes and flexural modes excited as a result of the non-perfect central position of the actuator were registered.

Figures 5.17 to 5.19 show that the location of debonding does not affect the average velocity of a guided wave propagating throughout the anchor, however, it acts strongly on the complexity of wave propagation signals and the number of modes excited during wave propagation. Debonding located at the beginning of the bonded part of the anchor is the easiest to identify because only one diffraction occurs in this case. Debonding located in the middle and at the end of the specimen result in numerous diffractions and modes conversions what considerably impede signal interpretation.

Figure 5.21 compares the signals registered in the free bar and in the fully debonded specimen. Particular reflections from both bar ends were registered at the same time for both specimens. Thus the wave velocity in the fully debonded anchor identical to the wave velocity in the free bar clearly indicates no cooperation between the core and cladding.

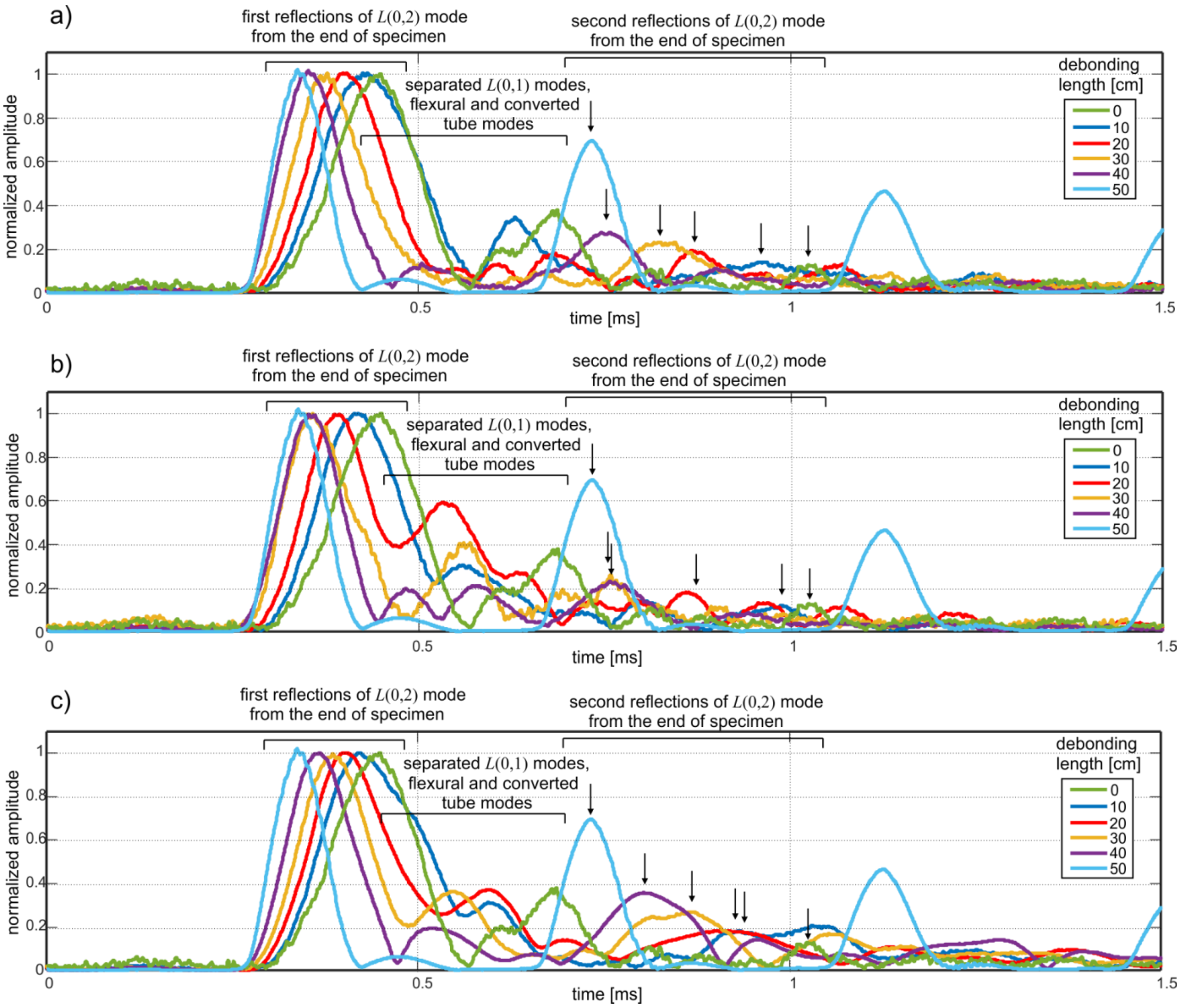

Figure 5.20. Envelopes of experimental wave propagation signals registered at the fixed end of the bar with variable length of debonding located at a) the beginning, b) in the middle and c) at the end of specimen

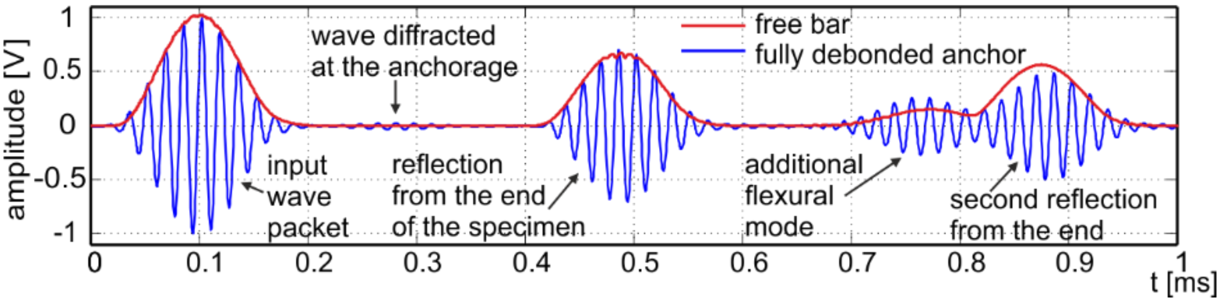

Figure 5.21. Comparison of experimental signals recorded for the free rod and the fully debonded specimen

The only difference between signals is the wave diffracted at the anchorage which was recorded for a fully debonded specimen case. The same diffracted wave is visible in the signal for specimen #A with 40 cm debonding at the beginning (Figure 5.17e). It is characterized by very low amplitude and it can be hardly identified. This locally diffracted wave results from imperfections in specimen manufacturing.

In order to compare results for anchors with variable debonding locations, amplitude values of the first reflection from the end of the specimen have been determined and listed in Table 5.1. Amplitudes are given as the percentage of the value of the input amplitude. In each column the amplitude with the lowest value has been marked. Despite a small number of samples one can observe a tendency. In three of four cases the amplitude registered for the anchor with middle-located debonding has the lowest value. In the case of debonding with a length of 20 cm the difference between the lowest value and the value registered for middle located debonding is insignificant. Not a single reflection only, but all the signals for the middle debonding location are characterized by relatively low amplitudes what can be observed while Figure 5.18 is compared with Figure 5.17 and Figure 5.19. In general, the amplitude decrease is caused by wave damping and energy transferring into surrounding cladding, being a possible result of multiple diffractions or mode separation. As presented in Section 2.3, the damage in the middle of the specimen results in multiple wave diffractions, division of energy on modes propagating in the free part, which are converted into modes travelling in perfectly bonded part and tube modes in a separate cladding. A multitude of phenomena in such damaged elements and a high degree of their complexity result in the most intensive energy dissipation.

Table 5.1. Amplitude values of reflections from the end of the specimen for various debonding length and position

Debonding position	Debonding length [cm]					
	0	10	20	30	40	50
beginning	8.73	7.93	14.37	46.21	40.71	70.69
middle		5.68	17.28	6.28	19.56	
end		13.82	42.52	57.36	72.02	

5.4.2 Results of the pull-out test

In this case the failure mechanism is the same for all specimens, involving damage of the connection on the grout/bar interface. The photo of the damaged specimen is given in Figure 5.22. The presence of initial debonding introduced in the form of the cellophane film at the bar/grout interface act strongly on the load-displacement responses.

Figure 5.22. Failure mode of the anchor after pull-out procedure

Figure 5.23 shows the force-displacement curves for all tested specimens with variable debonding lengths. Additionally, load-displacement reference responses for fully bonded and fully debonded anchors were plotted. The output force-displacement curves obtained for the specimens with the same length of debonding, regardless of its position, reveal similar features (Figure 5.23). The failure of anchors is accompanied by a sudden load drop (Figure 5.23a). For some specimens with a debonding length of 20 cm and 30 cm, the load-displacement curves cease to be smooth after reaching the maximum applied load, while the bars do not eject uniformly from mortar cover. This manifests by numerous local load maxima, but none of them exceeds the value of the first occurring peak (Figure 5.23b and c). For anchors with 40 cm debonding at least two distinct peaks were recorded. Importantly, in two cases, the global maximum was reached after amplification after the first load drop (Figure 5.23d). The same effect can be observed for a fully debonded anchor. In this case damage of adhesive bonding between the core and cladding already occurred after the first load drop. The increase of the load while continuing pull-out test was caused by friction forces between steel and grout.

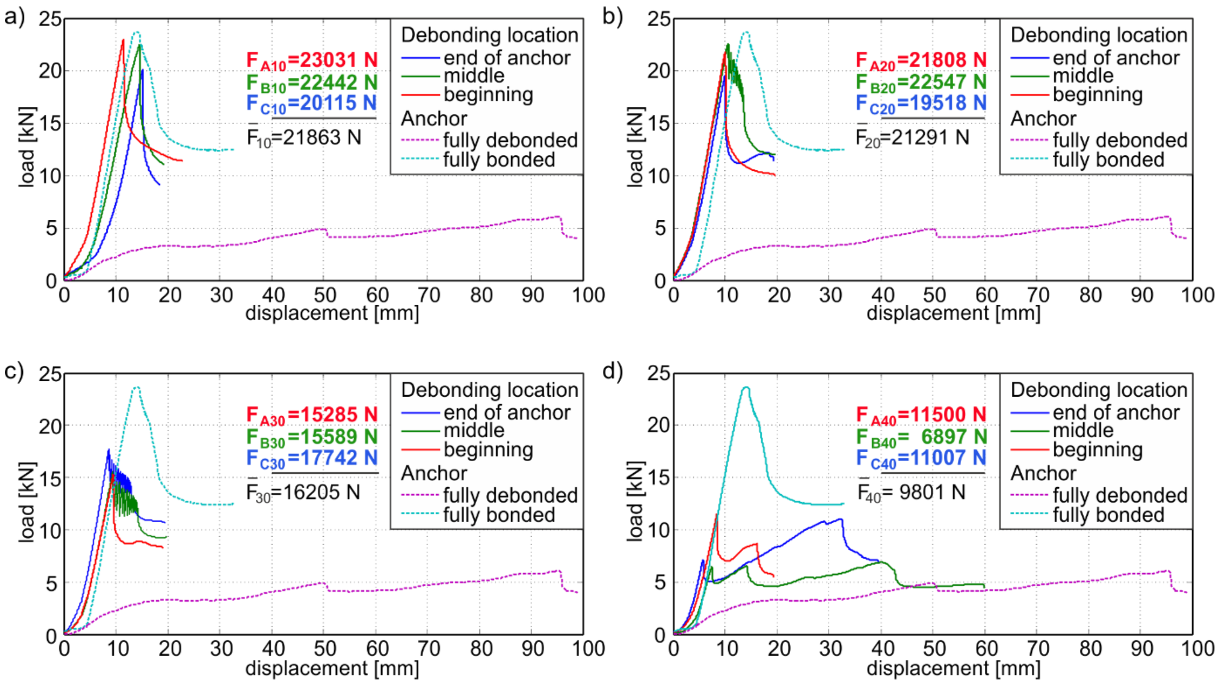

Figure 5.23. Load-displacement curves for anchors with pre-existing debonding with length equal to: a) 10 cm; b) 20 cm; c) 30 cm; d) 40 cm

Figure 5.23 presents the load capacities of anchors listed and the average load capacity of the anchors with the same debonding length determined. The plot of the average load capacity of bar/grout connection for anchors with the same debonding length is given in Figure 5.24. It is clearly visible that the load capacity decreases with the increase of bonding length.

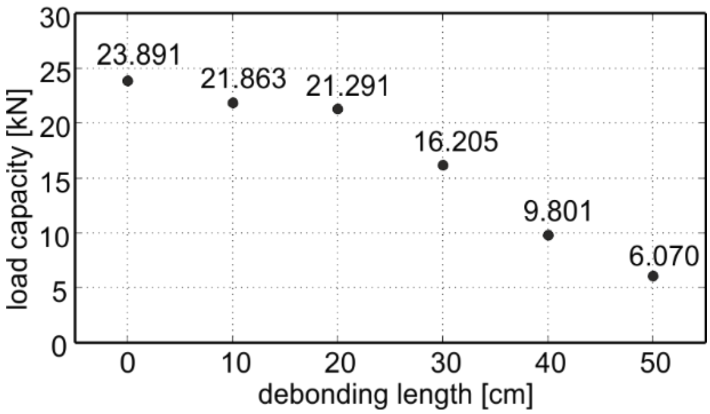

Figure 5.24. Average load capacity of anchors with variable debonding length

The most important observation from destructive tests concerns a fully debonded specimen. The maximum load carried by the fully debonded anchor was equal to 6.07 kN, which represents more than 25% of load-carrying capacity of a fully bonded anchor, while the wave propagation signal registered for this specimen revealed a complete inability to carry shear stresses. It can be therefore concluded that guided waves are characterized by high sensitivity to debonding detection.

5.5 Summary and conclusions

In this Chapter theoretical, numerical and experimental investigations of guided wave propagation in a steel bar partially embedded in grout with pre-existing debonding were carried out. Anchors with variable length and location of debonding were analyzed. The study brings a comprehensive description of the nature of wave phenomena occurring in a debonded element pointing out the damage location impact on wave conversion and diffraction.

The following concluding remarks can be drawn from the theoretical description of guided wave propagation in partially embedded bars with debonding supported by the FEM analysis:

- The phenomenon of wave propagation in bars partially embedded in grout with debonding at steel/grout interface requires the regard of dispersion curves for multilayered bars, hollow cylinders and free bars, guided wave propagation due to different velocities of guided wave propagation through the free length of the anchor, the bonded length of the anchor and the separated cover.
- The presence of debonding affects the wave propagation in a multilayered specimen, inter alia, the number of travelling modes, their velocities, conversion and diffraction.
- Dispersion curves for a free core and a multilayered waveguide form an important prerequisite for the implementation of guided waves for nondestructive testing of partially embedded bars, because depending on the value of the excitation frequency, the average velocity of the guided wave propagating through the total anchor length with debonding can be smaller, grater or the same as the average velocity of the guided wave propagated through the healthy anchor.
- The debonding length can be estimated on the basis of the average wave velocity of the reflections from the end provided that the dispersion curves for the free core and for the cladding are known. The selection of appropriate excitation frequency

affects the effectiveness of the assessment of the debonding length. The greater the difference between the fastest mode propagating in the free bar and the fastest mode in the coated bar, the greater variation of the average wave velocity triggered by the deboning occurrence.

- The average velocity in the anchor may be a meaningful indicator of the bonding quality only in the case of partially embedded bars while geometry is known. In the case of partially embedded bars for which the geometry of the bonded part is not precisely known (e.g. real ground anchors or soil nails), guided waves with lower frequency should be used, showing the velocity of the first $L(0,1)$ mode in the free bar is higher than do the modes in the covered bar. Next, it is possible to assume that the anchor deterioration is associated with the increase in the average velocity. In addition, a low frequency range ensures the smallest possible number of excited modes, which may facilitate interpretation of the results. The choice of high frequency range without the knowledge of the shape of dispersion curves for the free and multilayered bar may be decisive for the average velocity of the first reflection from the end of the anchor in the case of its state deterioration to increase, decrease or remain unchanged.
- The debonding location does not affect average velocity of a guided wave propagating through the anchor, however it has a great influence on the complexity of wave propagation signals and the number of modes excited during wave propagation. Debonding located at the beginning of the bonded part of the anchor is the easiest to identify because only one diffraction occurs in this case. Debonding located at the middle and at the end of the specimen results in numerous diffractions and modes conversions to considerably impede signal interpretation.

The experimental investigations of guided wave propagation and pull-out tests conducted for partially embedded bars with pre-existed debonding support the following conclusions:

- A wave propagation signal measured at the free end of the bar contains bar modes diffracted at the anchorage or defect beginning/end as well as bar modes originated from the reflection of multilayered modes from the end of the specimen. Detection of debonding based on a signal registered during single measurement can be difficult due to the multimode propagation, a plurality of diffractions and therefore, considerable difficulties in the identification of registered wave packets. However, the application of guided wave based monitoring system turns out to be an effective and promising method to observe of debonding evolution in anchors. Experimental signals acquired for specimens of debonding lengths increasing from 0% to 100% with a step of 20% of the bonded length, led to identification of debonding. The differences between signals for different debonding lengths were clearly visible is all analysed cases of damage location.

- The relative value of the amplitude of the wave reflected from the end of the anchor does not only depend on the intensity of wave energy leakage into surrounding medium but also on the kind of phenomena during wave propagation. In general, the greatest decrease of the amplitude was observed for anchors with debonding in the middle of the fixed length. For this defect location the most intensive energy dissipation occurs due to multiple wave diffractions, mode conversions and division of energy on modes propagating in the free and coated parts. Therefore, it can be concluded, that even is the case of the same length of the damaged connection between the core and cladding, debonding within the anchor body causes the increase of complexity level of registered wave propagation signals.
- In laboratory models of anchors, debonding was introduced using a cellophane film with a total thickness about 60 micrometers. Despite of such small thickness of debonding, guided waves appeared extremely sensitive in the detection of defects in adhesive bonding and any stress discontinuity at the interface of two layers. The wave velocity identified for a fully debonded specimen was equal to the velocity for the free bar, so it can be concluded that there was no cooperation between steel and the cover.
- The pull-out tests revealed that the force-displacement curves obtained for the specimens with the same length of debonding, regardless of its position, showed similar features, including similar load-carrying capacity. High sensitivity of guided waves to the detection of debonding was confirmed by pull-out test results for a fully debonded specimen. The maximum load carried by a fully debonded anchor was equal 6.07 kN, which represents more than 25% of the load-carrying capacity of the fully bonded anchor, while the wave propagation signal registered for this specimen revealed its complete inability to carry shear stresses.

It can be therefore concluded that guided waves may be used as an effective method to detect adhesive debonding in early stages of its development.

CHAPTER 6

Damage detection in ground anchor tendon

6.1 Introduction

Ground anchors are intended to in the ground so they are constantly exposed to aggressive environment. For this reason one of the most common anchor failure mode is corrosion. In extreme cases the localized damage is necking caused by tension deformation or corrosion pit.

A significant potential of the use of guided waves in diagnostics of free and embedded bars with localized damage has been presented by many scientists. Research of monitoring and defect detection by guided stress wave method in wire strands was conducted by Lanza et al. [115]. Experimental and numerical research of detection of additional mass in an aluminium bar has been described by Palacz et al. [165]. Rucka [181] investigated an influence of different types of discontinuities, namely a notch, an additional mass and a weld on wave propagation in steel bars. Lu et al. [131] presented the results of experimental works on damage detection in the form of partial material removal in a rebar embedded in a concrete beam. A study concerning wave scattering from discontinuities of variable length and depth in waveguides were conducted by Pau et al. [169]. Lucena and Dos Santos [132] applied a new approach based on the time reversal method for damage detection in cracked bars.

A second group of common damage patterns in bars are uniform defects resulting from corrosion of an element surface. Corrosion process takes a long time and usually the early corrosion stage is usually not dangerous for a structure. However, in order to avoid serious consequences, e.g. replacement of entire structural elements regular inspections and continuous updates of the condition assessment are required. Moreover, in the case of reinforced concrete structures corrosion process occurring inside the concrete cover cannot be observed directly. Attempts to develop a wireless embedded sensor system to monitor and assess corrosion damage in reinforced concrete were taken by Reis et al. [177]. Ervin and Reis [60] tested both low and high frequency ranges of ultrasonic waves for the monitoring of corrosion damage in reinforced mortar specimens. Longitudinal waves of high frequencies were used by Ervin et al [61] to monitor reinforced mortar specimens undergoing accelerated uniform and localized corrosion. Two ultrasonic techniques of pulse transmission and pulse echo were used to monitor the healthy and damaged reinforcing bar in concrete by Sharma and Mukherjee [194]. Fractal analysis of guided ultrasonic waves to evaluate the corrosion level in post-tensioned systems was proposed by Moustafa et al. [156]. Farhidzadeh and Salamone [62] used dispersion curves, continuous wavelet transform and wave velocity measurement in the quantification of corrosion damage of multiwire prestressing steel strands.

All the reported papers greatly illustrate the diversity of works to develop nondestructive techniques for damage and corrosion detection in free and embedded bars. Despite significant achievements and improvements in the field of structural diagnostics there is still a need of constant improvement of existing methods and directing them into monitoring of particular types of structures. A fast and effective method of defect detection is especially important in the case of structural objects like ground anchors (Figure 6.1) which cannot be inspected by standard visual inspection approach. In general both, localized and surface damage may develop in any part of the anchor so there is a need to create methods allowing to identify any type of damage. In the case of tendons cracks and necking are possible failure modes. Moreover, corrosion damage may develop along the free part of the tendon or may occur along embedded part as a result of poor manufacturing and debonding between the tendon and the anchor body.

The following Chapter deals with the experimental investigation of point damage and corrosion detection in bars by means of guided wave propagation method. Experiments are conducted for steel free bars and covered bars embedded in grout, which can be treated as laboratory models of a ground anchors. Point defect in the form of notch and variable levels of corrosion damage of steel core are investigated. Particular attention is paid to influence of damage occurrence on wave propagation phenomena which varies with the type of damage and the presence of the additional layer of the grout. Moreover, two types of excitation signals were analysed: a broad-band excitation with the use of a pulse and a single frequency excitation with the use of a wave packet. The results are presented in the form of spectrograms of pulse induced waves and time-domain signals of wave packet induced waves.

The aim of the investigation is to compare the effectiveness of various wave excitations and signal processing procedures in point and corrosion damage detection in free and embedded bars. The main elements are detailed description of wave mode conversion and separation in multilayered bar with point damage, deriving a formula for localizing point damages in multilayered bar on the basis of time-of-flight and velocities of the fastest wave modes, performing analytical spectrograms for free and multilayered bar with point damage and the comparison of analytical and experimental time-frequency representations for bars with point and surface damage.

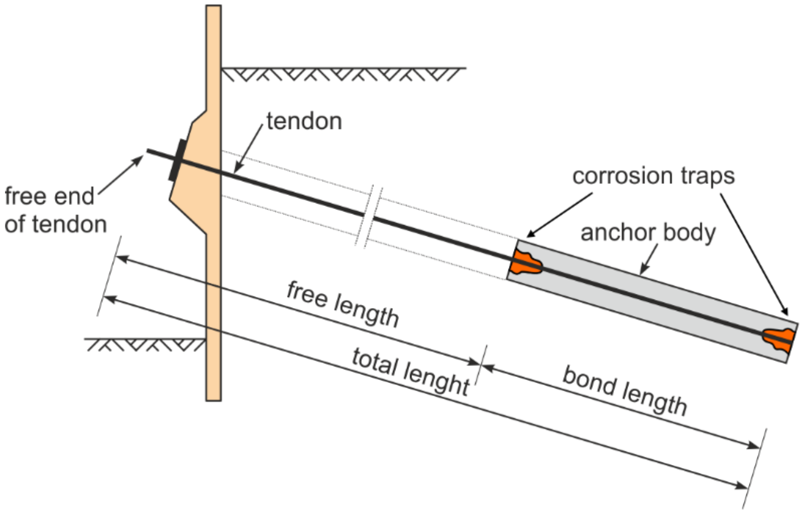

Figure 6.1 Schematic sketch of ground anchor with indicated corrosion traps

6.2 Theoretical background

6.2.1 Identification of localized damage

In this section, the interaction of guided waves with crack-type damage is investigated, in both free and partially embedded bars. The inquiry presented here is related to the case of dispersion curves for free and embedded bar given in Figure 6.2, however in general, it is universal. The excitation frequency used in the further part of this Chapter was chosen on the basis of tunning test and was equal to 60 kHz for free rod and 70 kHz for multilayered rod. The excitation of 60 kHz allows inducing a single longitudinal mode in a single-layer bar, while the excitation of 70 kHz results in propagation of two longitudinal modes in multilayered bar. In the presented frequency range up to 500 kHz, three longitudinal modes $L^{bar}(0,1)$, $L^{bar}(0,2)$, $L^{bar}(0,3)$ and three flexural modes $F^{bar}(1,1)$, $F^{bar}(1,2)$ and $F^{bar}(1,3)$ can be excited in a free bar. Compared to these curves (given by dashed black lines in Figure 6.2), the number of both longitudinal and flexural modes increases significantly while the bar is covered by additional layers. It can be also observed, that in the plot for longitudinal modes there is a frequency interval (from about 250 kHz to 395 kHz) to make the wave in the multilayered bar propagates faster than in the free bar. In the case of flexural modes, the velocity of any mode does not exceed the velocity of the first mode for the free bar $F^{bar}(1,1)$.

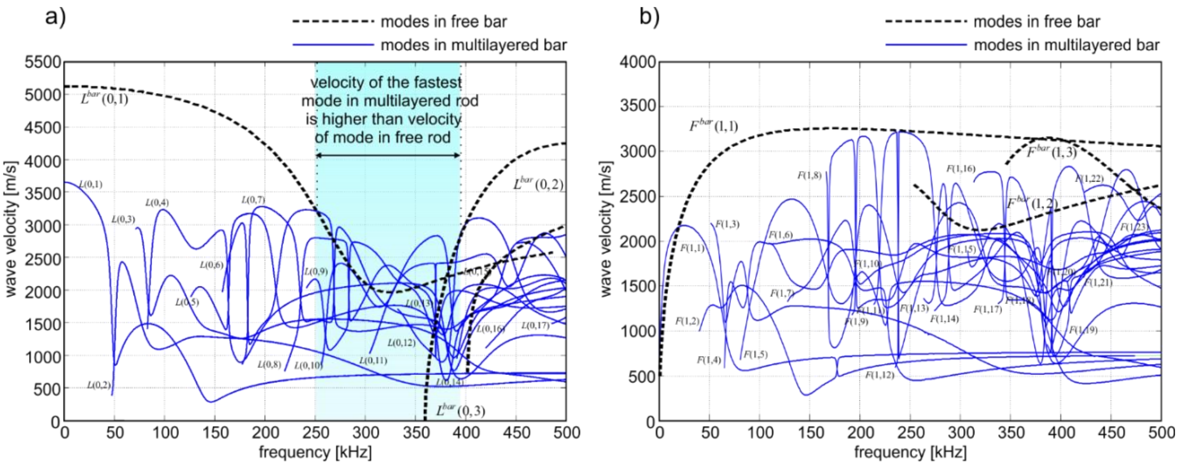

Figure 6.2. Group velocity dispersion curves of 1 cm diameter steel bar (*E* = 207 GPa, *v* = 0.3, *ρ* = 7894 kg/m^3) embedded in mortar with thickness of 17.5 mm (*E* = 23.68 GPa, *v* = 0.2, *ρ* = 2067 kg/m^3) formed in PVC pipe with thickness of 2.5 mm (E = 1.5 GPa, *v* = 0.4, *ρ* = 900 kg/m3): a) longitudinal modes, b) flexural modes

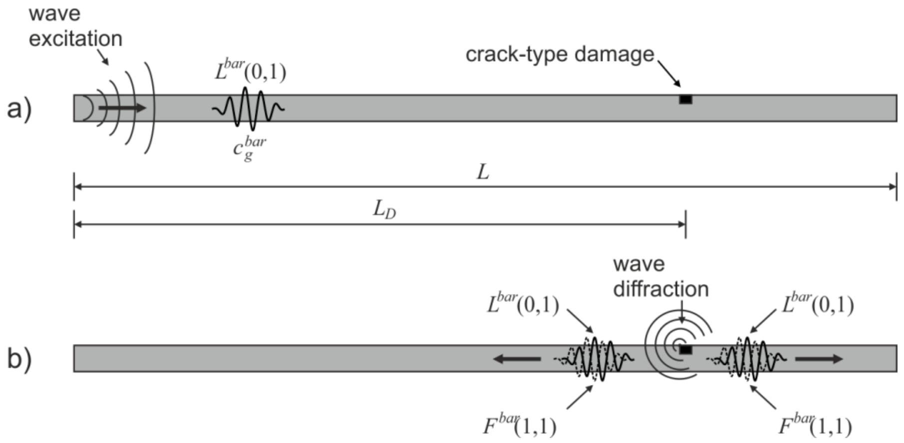

Figure 6.3. Wave propagation in the free bar by guided wave propagation: a) excitation of wave, single mode propagation; b) conversion of modes after wave diffraction by crack

Figure 6.3 illustrates interaction of waves with the crack in the free bar. Initially, the excited $L^{bar}(0,1)$ mode propagates along the bar. Next, the wave is diffracted and transmitted past the crack. Moreover, due to non-symmetrical defect, mode conversion is possible resulting in the appearance of the $F^{bar}(1,1)$ mode.

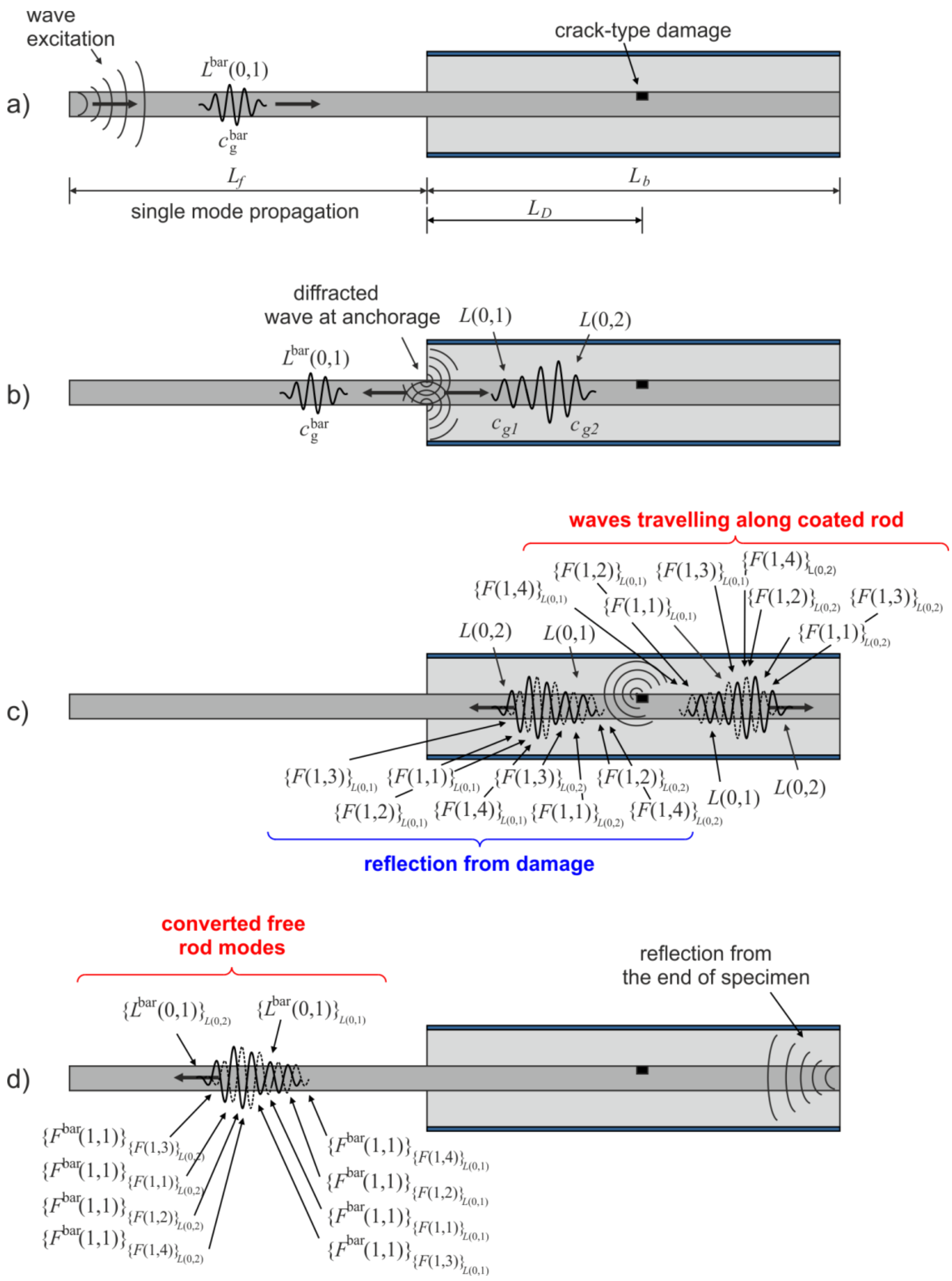

Figure 6.4. Wave propagation in a partially embedded bar with crack-type damage: a) excitation of wave, single mode propagation in the free bar; b) wave diffraction at the anchorage, multimode propagation and mode separation at embedded part of bar, c) conversion of modes after wave diffraction by crack; d) multimode propagation in the free bar

Figure 6.4 shows the case, when the crack-type damage is located within the coated part of a multilayered cylindrical system. The excited $L^{bar}(0,1)$ mode propagates along the free part of the bar (Figure 6.3a). After the wave diffraction at the anchorage (Figure 6.4b), part of the wave energy in the form of a longitudinal mode $L^{bar}(0,1)$ travels back along the bar. The remaining wave energy is transferred into the multilayered part (Figure 6.4b) and after conversion it still travels forward in the form of two longitudinal modes $L(0,1)$ and $L(0,2)$. Due to the difference in their velocities they separate and according to considered dispersion curves (Figure 6.2), the mode $L(0,2)$ propagates faster. Next, both longitudinal modes are diffracted by damage (Figure 6.4c). Similarly to the free bar case, the crack occurrence may lead to the mode conversion and as a consequence each diffracted longitudinal mode can be converted into four modes, which can propagate in a multilayered system: four flexural modes $F(1,1)$, $F(1,2)$, $F(1,3)$, $F(1,4)$ and longitudinal modes $L(0,1)$ and $L(0,2)$. In Figure 5.3c the flexural modes converted from $L(0,1)$ mode are denoted as $\{F(1,1)\}_{L(0,1)}$, $\{F(1,2)\}_{L(0,1)}$,$\{F(1,3)\}_{L(0,1)}$ and $\{F(1,4)\}_{L(0,1)}$ while modes converted from $L(0,2)$ mode are $\{F(1,1)\}_{L(0,2)}$, $\{F(1,2)\}_{L(0,2)}$, $\{F(1,3)\}_{L(0,2)}$ and $\{F(1,4)\}_{L(0,2)}$. Therefore, after interaction with damage, one wave packet with ten converted modes propagates back and another wave packet with eight modes propagate along the coated bar, subsequently reflecting from the end of the specimen (Figure 6.4d). As the wave packet propagating back reaches the free part of the bar, the eight modes are converted into two longitudinal modes $\{L^{bar}(0,1)\}_{L(0,2)}$, $\{L^{bar}(0,1)\}_{L(0,1)}$ and eight flexural modes $\{F^{bar}(1,1)\}_{\{F(1,3)\}_{L(0,2)}}$, $\{F^{bar}(1,1)\}_{\{F(1,1)\}_{L(0,2)}}$, $\{F^{bar}(1,1)\}_{\{F(1,2)\}_{L(0,2)}}$, $\{F^{bar}(1,1)\}_{\{F(1,4)\}_{L(0,2)}}$ $\{F^{bar}(1,1)\}_{\{F(1,3)\}_{L(0,1)}}$, $\{F^{bar}(1,1)\}_{\{F(1,1)\}_{L(0,1)}}$, $\{F^{bar}(1,1)\}_{\{F(1,2)\}_{L(0,1)}}$, $\{F^{bar}(1,1)\}_{\{F(1,4)\}_{L(0,1)}}$ which may exist in the uncoated bar according to dispersion solution presented in Figure 6.2. Damage localization can be identified on the basis of the signal registered by sensor A, located at left end of the bar (compare Figure 6.4). The schemes of wave propagation signals for free and partially embedded bars are given in Figure 6.5. As a result of the interaction of the wave with crack-type damage in the free bar, an additional wave packet occurs (Figure 6.5a). Location of the defect can be easily determined on the basis of the time-of-flight (ToF) $t_{oF}^{D,bar}$:

$$L_D = \frac{c_g^{bar} t_{oF}^{D,bar}}{2} \tag{6.1}$$

where c_g^{bar} is the group velocity of the registered wave packet.

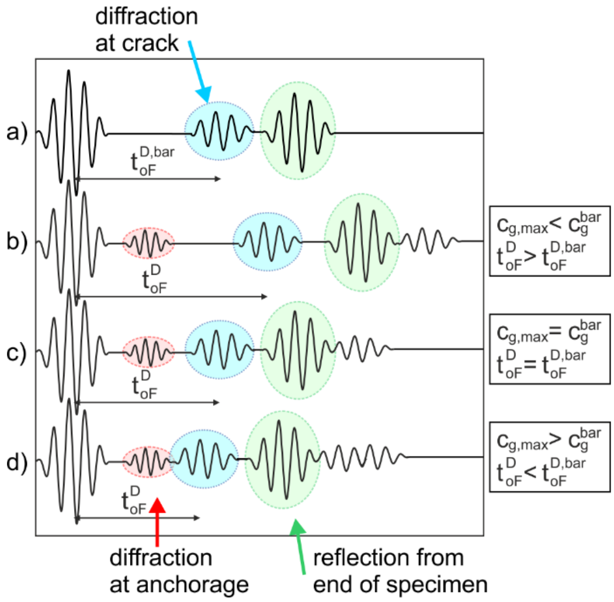

Figure 6.5. Schemes of wave propagation signals registered for a) free bar and for partially embedded bar with different relations of group velocity b) $c_{g,\max} < c_g^{bar}$; c) $c_{g,\max} = c_g^{bar}$ and d) $c_{g,\max} > c_g^{bar}$

The signal recorded in the multilayered bar contains at least three wave packets: the diffraction at the anchorage containing one longitudinal mode $L^{bar}(0,1)$, the diffraction at the crack containing eight modes and reflection from the end of the specimen. Damage position L_D can be determined on the basis of the time-of-flight t_{oF}^{D} between the incident wave and the diffraction by the crack. For the considered specimen partially embedded in mortar, the longitudinal mode in the free bar travels with velocity c_g^{bar} while longitudinal modes in the multilayered part travel with velocities $c_{g_j}^{L}$ (*j* denotes the number of modes, so the first mode travels with velocity $c_{g_1}^{L}$ and the second mode with velocity $c_{g_2}^{L}$) and flexural modes travel with velocity $c_{g_j}^{F}$ ($c_{g_1}^{F}, c_{g_2}^{F}$ and $c_{g_3}^{F}$). The fastest mode travels double length of the free part L_f and double distance to damage in the embedded part L_D before it is registered by the sensor. The time-of-flight of the diffracted wave can be calculated as:

$$t_{oF}^{D} = \frac{2L_f}{c_g^{bar}} + \frac{2L_D}{c_{g,\max}}, \tag{6.2}$$

where $c_{g,\max}$ is group velocity of the fastest mode in the multilayered part and in the presented case $L(0,2)$ mode is the fastest. Because modes in the free bar are characterized by different velocities than the modes in the covered part, there are some differences in registration time of reflections from damage located at the same place for the free and covered bar. The difference in times-of-flight between the free and covered bar is:

$$\Delta t_{oF}^{D} = \frac{2L_f}{c_g^{bar}} + \frac{2L_D}{c_{g,\max}} - \frac{2(L_f + L_D)}{c_g^{bar}} = \frac{2L_D(c_g^{bar} - c_{g,\max})}{c_g^{bar} c_{g,\max}} . \qquad (6.3)$$

If the velocity of the fastest mode in the free bar is higher than the velocity of the fastest mode in the covered bar, the reflection from damage is registered later. Otherwise, the reflection is registered earlier. The signals recorded in the multilayered bar for different relations between group velocities c_g^{bar} and $c_{g,\max}$ are presented in Figure 6.5b-d. In order to determine the damage position for the covered bar reformulated Eq. (6.3) may be applied:

$$L_D = \frac{t_{oF}^{D} c_g^{bar} c_{g,\max} - 2L_F c_{g,\max}}{2c_g^{bar}} \qquad (6.4)$$

6.2.2 Identification of uniform corrosion damage

This section addresses guided wave propagation in a uniformly corroded bar. The main effects of such corrosion are reduction of the bar diameter and appearance of irregularities on the bar surface in the form of wide-spread pitting.

The reduction in bar diameter acts upon on the velocity of a guided wave. Figure 6.6a shows dispersion curves of the first longitudinal mode for a steel bar with different diameters: 1 mm, 5 mm, 10 mm and 40 mm. It can be observed that in the considered frequency range 0–1700 kHz the number of modes decreases with the decrease of the bar diameter. Moreover, for the established frequency the wave velocity of particular modes changes with the variation of the bar diameter. Considering the first longitudinal mode $L(0,1)$ it can be seen that the frequency corresponding to the minimum value of the group velocity increases with the decrease of the bar diameter (Figure 6.6a). The plot of the derivative of the group velocity of the first mode $L(0,1)$ with respect to the bar diameter dc_g / dD (Figure 6.6b) indicates the frequency range which is the most sensitive to changes in the bar diameter. Exemplary, for bars with relatively small diameters (1-10 mm) mode $L(0,1)$ detects high sensitivity to changes in the bar diameter for a wide frequency range. With the increase of the bar diameter, the width of the zone sensitive to bar diameter variation is significantly reduced.

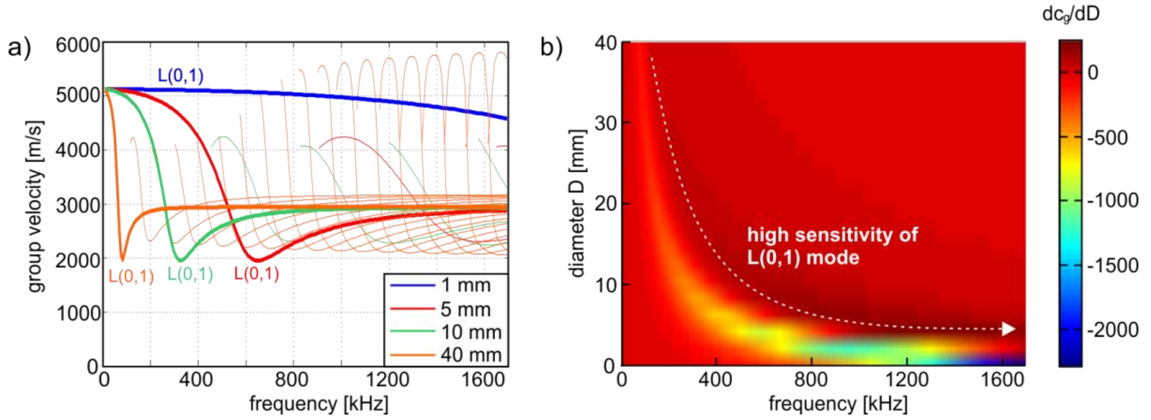

Figure 6.6. (a) Group velocity dispersion curves for steel bar (E = 207 GPa, ν = 0.3, ρ = 7894 kg/m^3) with different diameters; (b) derivative of the group velocity with respect to the bar diameter for $L(0,1)$ mode

Corrosion is an oxidation-reduction process leading to structural steel deterioration, converting main component of steel, iron *Fe*, into ferrous hydroxide species. With the corrosion development, in the bar corrosion pits occur, which locally change the structure of a bar surface and cause mass reduction of the bar. The Huygens principle states that each point in a wave is a source of secondary waves of the same frequency and wavelength, thus in a corroded bar including irregularities multiple diffractions may be observed (Figure 6.7). Irregularities of bar surface also lead to mode conversions and thereby, to increase of the complexity of the governing phenomena. Another important consequence of a rough surface is a higher wave damping. Due to the number of diffractions and conversions, the wave energy dissipation is more intense here than in the undamaged bar.

In the case of uniform corrosion of the bar embedded in mortar, corrosion products tend to cause expansion, which in consequence apply a pressure to the surrounding mortar. This expansion pressure induces tensile stresses in the mortar around the reinforced bar consequently leading to cover cracking.

Additionally, expansion of corrosion products may cause debonding between steel and mortar. Due to corrosion, a multilayered perfectly bonded bar may act as a steel core with irregular surface and separate cladding, resulting in a faster wave damping, the occurrence of reflection from corrosion pits or even change in the wave group velocity.

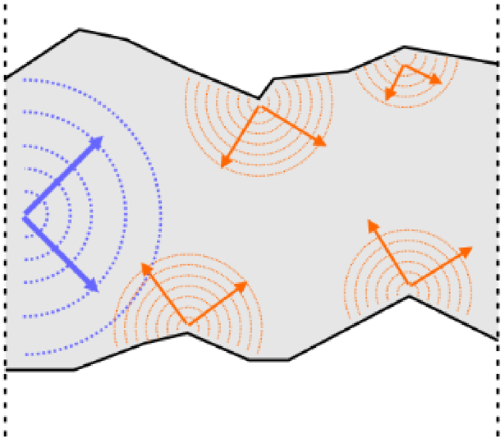

Figure 6.7. Wave diffractions in corroded bar

6.3 Experimental investigations

6.3.1 Description of specimens

Two types of specimens were investigated in this study, namely a free bar and a multilayered bar partially embedded in mortar (Figure 6.8). The steel bar with the material parameters $E = 207$ GPa, $\nu = 0.3$, $\rho = 7894$ kg/m^3 of a 1 m length and 10 mm diameter. In the process of specimen preparation, the bar was inserted centrally in a PVC mould and filled by the fast setting cement-based mortar. The mould was 50 cm long, its outer diameter was 5 cm and a wall thickness equal 2.5 mm. The following material parameters were taken: $E = 23.68$ GPa; $\nu = 0.2$; $\rho = 1978.13$ kg/m^3 (mortar), $E = 1.5$ GPa; $\nu = 0{,}4$; $\rho = 900$ kg/m^3 (PVC). Prior to experimental tests the partially embedded bars were left to cure at room temperature for 14 days.

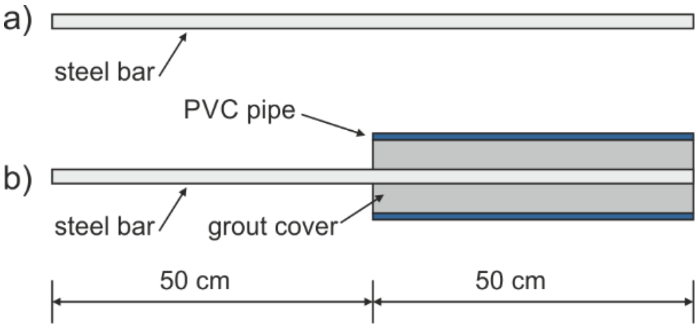

Figure 6.8 Geometry of test specimens: a) free bar; b) partially embedded bar

6.3.1.1 Preparation of test specimens with crack-type damage

A crack-type damage was introduced into the bar by making a notch with a depth of 5 mm and a width of 1 mm. The defect was situated at a distance of 76 cm from the bar left end (Figure 6.9). After ultrasonic tests conducted on the free bar, the bar was covered by mortar to make a partially embedded specimen.

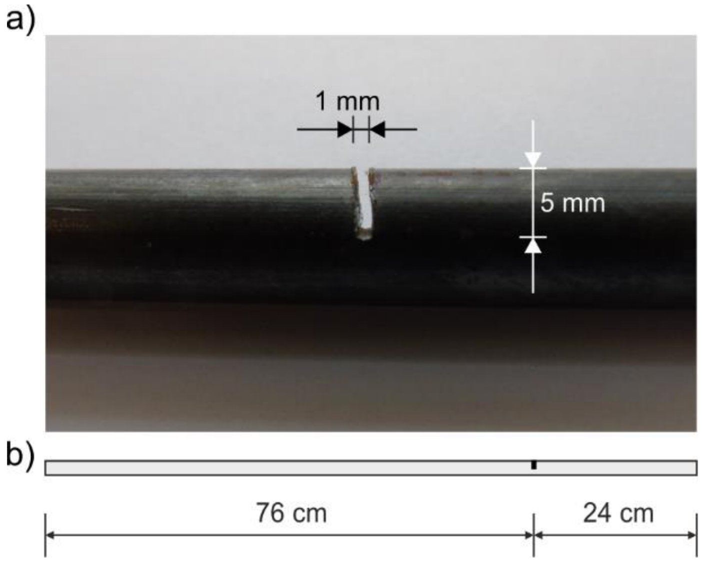

Figure 6.9. Bar with crack-like damage: a) defect geometry, b) defect localization

6.3.1.2 Preparation of test specimens with corrosion damage

Corrosion damage was triggered by an accelerated corrosion test (e.g. [62],[177]). The specimens were immersed in 5% sodium chloride solution and a direct electric current (DC) was impressed to increase the rate of corrosion. The steel bar was an anode and another metal bar acted as cathode. Firstly, the free bar was subjected to corrosion. The corrosion process was conducted in six stages. At each stage, the bar was immersed in the solution for one hour. Before the beginning of the next stage, the solution of NaCl was changed so that the electrolyte concentration was the same at the beginning of the each stage of the experiment. After each stage of the corrosion process, the uniformly corroded bar was left to dry, subjected to nondestructive testing and subjected to electrolysis again.

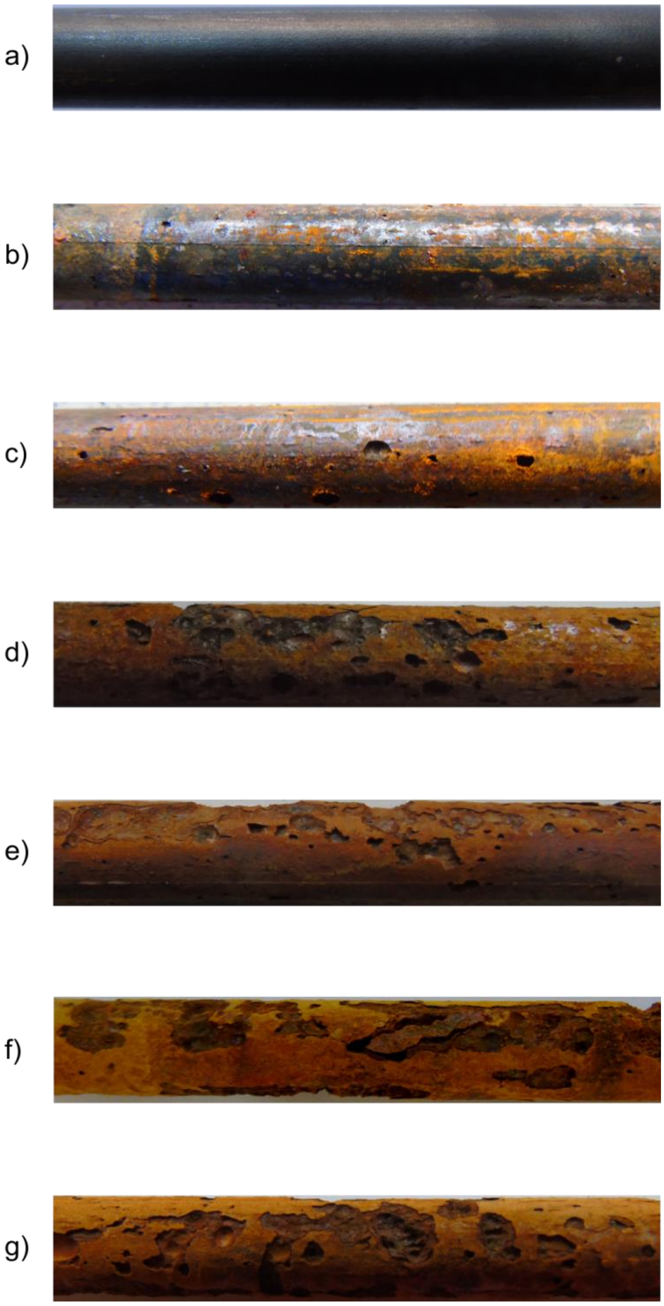

Figure 6.10. Corrosion progress in a steel bar: a) healthy bar and bar after b) 1 hour, c) 2 hours, d) 3 hours, e) 4 hours, f) 5 hours, g) 6 hours of corrosion test

Figure 6.10 illustrates corrosion progress in a free bar. It can be seen that the size and the number of pits significantly increased and the bar surface was degraded considerably. Moreover, the difference in diameter of the corroded bar was observable. The mass loss was estimated after each hour as:

$$\Delta m = M - m \tag{6.5}$$

where M denotes the initial mass of the bar and m is the mass after the considered corrosion stage. The obtained relationship between the mass loss and the corrosion time (Figure 6.11) stays with agreement with the Faraday's law of electrolysis.

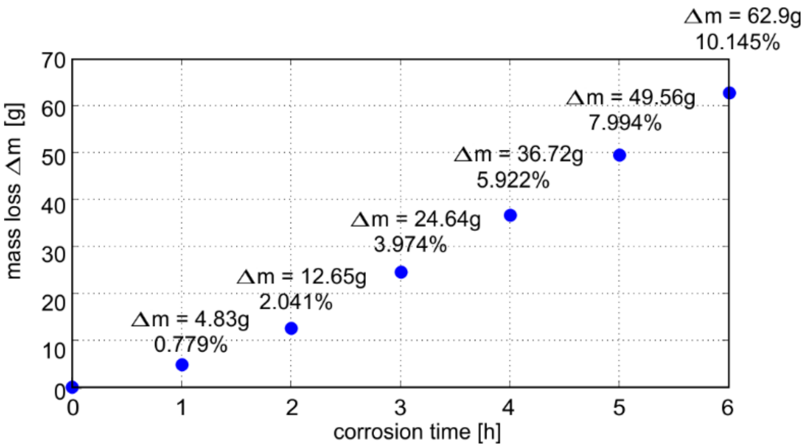

Figure 6.11. Mass loss of the free bar with respect to time of induced corrosion

Next, a partially embedded specimen was prepared with the use of the intact steel bars. The specimen was corroded only at the length embedded in mortar so the free part of the bar was pristine (Figure 6.12). Five four-hour corrosion stages were carried out. The corrosion process was much longer than in the free bar case because the mortar cover and PVC pipe ensured a significant anti-corrosion protection. After each stage of the corrosion process the specimen was left to dry, subjected to nondestructive testing and subjected to electrolysis again.

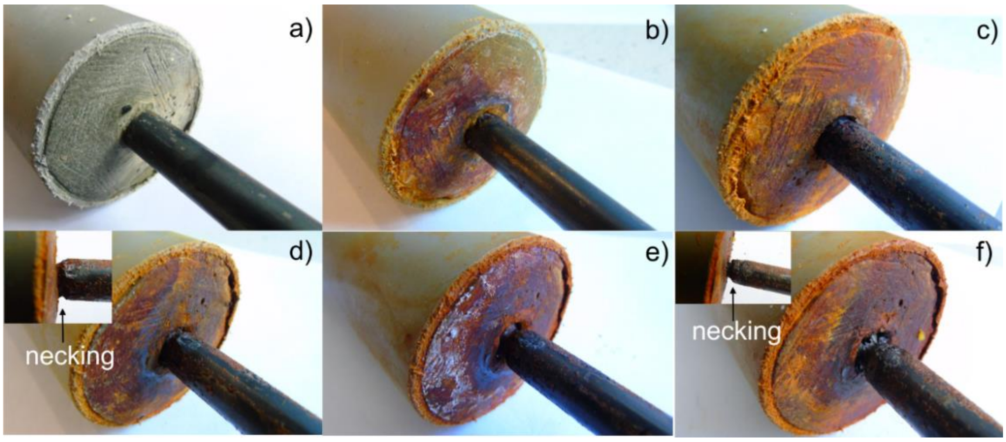

Figure 6.12. Corrosion progress in a steel bar embedded in mortar: a) healthy bar and bar after b) 4 hours, c) 8 hours, d) 12 hours, e) 16 hours and f) 20 hours of corrosion test

6.3.2 Experimental procedure

Ultrasonic waves were generated in two ways. In the first case, waves were excited by ultrasonic transducers (sending transducer ST) with the use of ultrasonic testing box OPBOX-01/100. The pulse width was equal to 3 microseconds. This broad-band excitation makes it possible to induce wave propagation with a frequency range up to 500 kHz. In the case of a free bar, the pulse-echo approach was applied with the use of a single sending/receiving (ST/RT) transducer attached to the left end of the bar. The ultrasonic test for a partially embedded bar was conducted in a pitch-catch mode. The signal was sent from a sending transducer (ST) at the free end of the specimen and received by a receiving transducer (RT) attached to the opposite side, at the embedded end of the specimen (Figure 6.13a). The change in configuration of both sending and receiving transducers with respect to experimental tests of the free bar was caused by the fact that in the case of pusler-receiver located at the one end, reflection from the anchorage could be registered, to possibly disrupt the results in the form of spectrograms presented in the further part of the Chapter.

In the second case, ultrasonic waves were excited by means of a plate piezo actuator mounted at the left end of the free bar (Figure 6.13b). The excitation signal was a wave packet consisting of a ten-cycle sine function modulated by the Hanning window. A carrier frequency of the signal was chosen on the basis of a tunning test and it was equal to 60 kHz for the free bar and 70 kHz for the multilayered bar. The propagating waves were sensed at selected points of the specimen by piezo actuators Noliac NAC2011 acting as sensors (S1, S2 and S3).

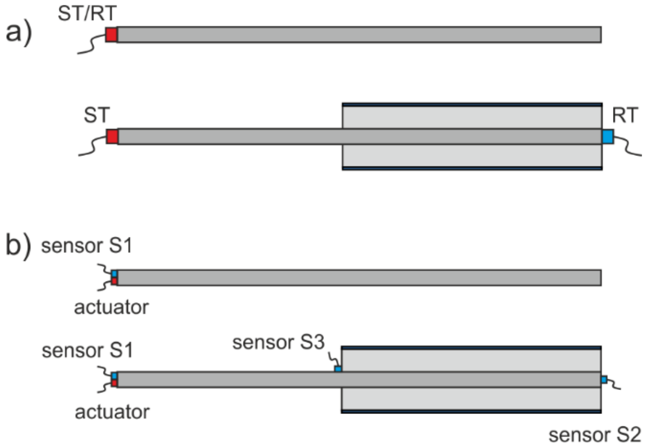

Figure 6.13. Localization of transducers during test with the use of: a) pulse excitation, b) wave packet excitation

6.4 Results and discussion

6.4.1 Time-frequency representation of wave propagation signals

Any time signal can be represented in a time-frequency domain to visualize its variable spectrum in time. In previous studies the time-frequency representation of wave propagation signals proved an effective tool in corrosion detection (e.g. [177], [60]). Such representation can be achieved using Short Time Fourier Transform (STFT). According to the STFT idea the signal is divided into a series of overlapping pieces which are then windowed and transformed by Fourier transform [37]. The STFT of a time-domain signal $s(t)$ is defined as [37]:

$$S_1(\omega,t)=\frac{1}{2\pi}\int_{-\infty}^{\infty}e^{-i\omega\tau}s(\tau)h(\tau-t)d\tau \tag{6.6}$$

where $h(\tau-t)$ is a window function centered at time t and with length equal to τ. The energy density of the STFT spectrum is given by [37]:

$$E_1(\omega,t)=\left|S_1(\omega,t)\right|^2 \tag{6.7}$$

and it is called a spectrogram of a transformed signal.

An analytical time-frequency representation of a wave propagation signal can be calculated on the basis of a known wave velocity and the length of the specimen. In general, the wave excitation with frequency *f* results in propagation of *n* modes in the free bar. Velocities of modes in the free bar are equal to c_{g_i}, while *i* varies from 1 to *n*. Then, the time to travel the double length 2*L* of the specimen for mode *i* can be calculated as:

$$t_{oF}^{bar}=\frac{2L}{c_{g_i}^{bar}} \tag{6.8}$$

While point damage occurs at the distance L_D from the excitation point, each of *n* modes is reflected from this point and registered after a time equal:

$$t_{oF}^{D}=\frac{2L_D}{c_{g_i}^{bar}} \tag{6.9}$$

Figure 6.14a presents spectrograms obtained for the intact free bar on the basis of the Pochhammer equation solution and Eq. (6.8). The spectrogram was performed assuming that the waves are generated and registered at the same end of the bar (compare Figure 6.13a). The spectrogram for the bar with a point damage is shown in Figure 6.14b. Additional curves, indicated by dashed lines, arise as a result of reflections from damage while the time-of-flight was calculated on the basis of Eq. (6.9).

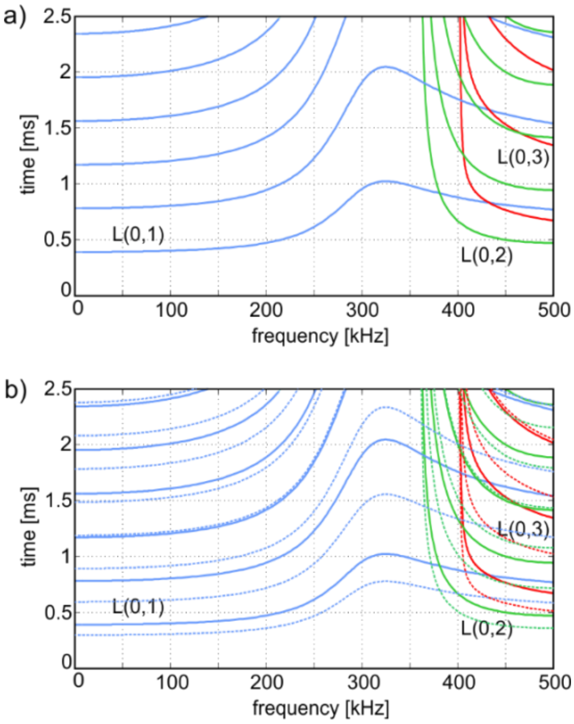

Figure 6.14. Analytical time-frequency representation for the free bar with wave excitation and signal registration at the same end: a) healthly bar; b) bar with point damage located 76 cm away from excitation point

Obtaining the analytical time-frequency representation for a partially embedded bar is more complicated because of various velocities of waves propagating along free and embedded parts as well as larger number of modes which are converted at the anchorage. Let's consider a general case of a partially embedded bar. Waves are excited at the free end and registered at the embedded end of the specimen (cf. Figure 6.13). The wave excitation with frequency f results in propagation of n modes in the free part and each of n modes can be converted into m modes in the multilayered part. Velocities of modes in the free part and the multilayered part are equal to c_{g_j} and c_{g_i}, respectively and i varies from 1 to n while j varies from 1 to m. It means that the time required to travel the length L of the specimen for mode i converted into mode j can be calculated as:

$$t_{oF}^{L} = \frac{L_F}{c_{g_i}^{bar}} + \frac{L_B}{c_{g_j}} \tag{6.10}$$

On the basis of Eq. (6.10), analytical results in the form of a graph presenting the wave velocity for any frequency can be performed. Figure 6.15a presents the time-frequency relation for the analysed specimen (L_F = 0.5 m and L_B = 0.5 m) on the basis of dispersion curves for the free and multilayered parts. An analytical spectrogram seems to be illegible, but it should be mentioned that in the considered frequency range three longitudinal modes in the free bar can be converted into seventeen modes in the multilayered part, thus the spectrogram contains $i \times j = 17 \times 3 = 51$ curves. When a point damage occurs along the embedded part, the wave reflects from the end of specimen, so the reflection from damage can be registered in a signal. A spectrogram in Figure 6.15b presents a time-frequency representation for a partially embedded bar taking into account a single reflection from damage located 76 cm away from excitation point. However in general, wave propagation phenomena may be much more complicated due to mode conversions and multiple reflections from damage and the anchorage.

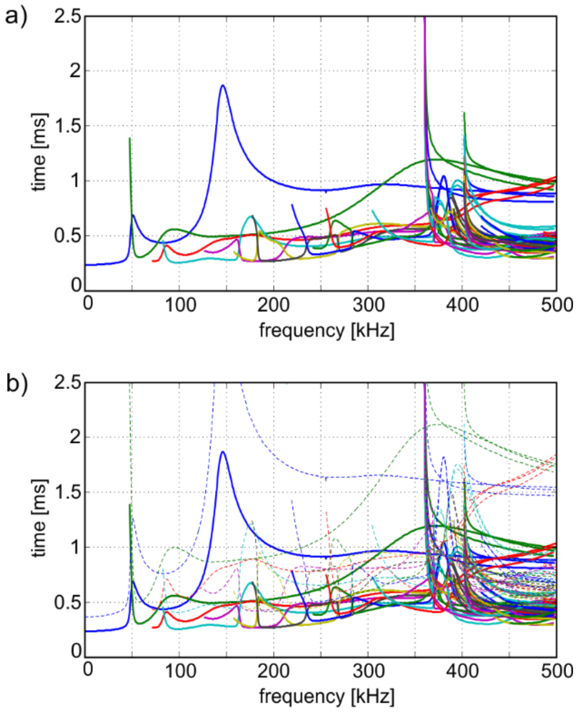

Figure 6.15. Analytical time-frequency representation for partially embedded bar with wave excitation and signal registration at opposite ends: a) healthy bar, c) bar with point damage located 76 cm away from excitation point

6.4.2 Crack type damage

Figure 6.16 shows time-frequency representation of experimental signals obtained by the ultrasonic sending/receiving (ST/RT) transducer attached to the left end of the intact bar and the bar with the crack. In experimental results for the intact bar (Figure 6.16a), the first three modes $L(0,1)$, $L(0,2)$ and $L(0,3)$ can be identified (cf. Figure 6.14a). For $L(0,1)$ mode several curves corresponding to consecutive reflections from the bar end are clearly visible. The spectrogram obtained for a bar with the notch (Figure 6.16b) is much less readable than the spectrograms for the intact bar (Figure 6.16a), however additional curves of $L(0,1)$ mode can be observed indicating reflection form the crack (cf. Figure 6.14b).

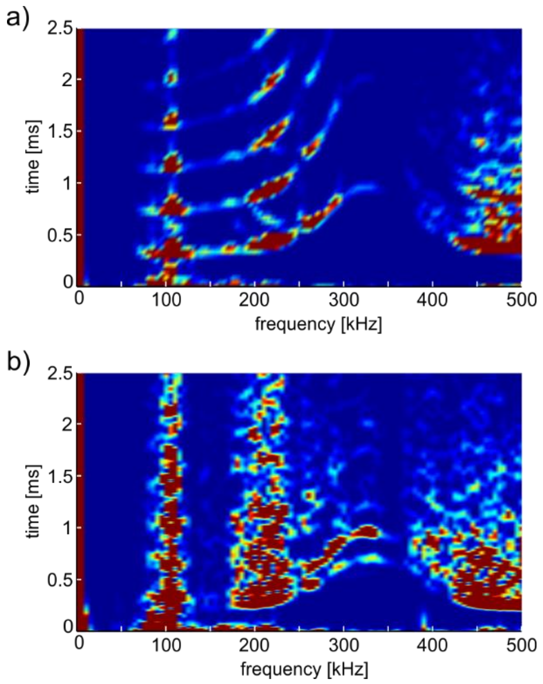

Figure 6.16. Spectrogram of ultrasonic signals registered in the free bar: a) intact bar, b) bar with crack

The spectrograms for multilayered bars with and without point defects are given in Figure 6.17. For the bar with the crack, the density of energy is lower, especially for higher frequencies, to probably result from energy dissipation caused by damage existence. Despite the fact that there are some differences between the obtained results for healthy and damaged rod, any spectrogram resembles results obtained analytically (compare Figure 6.15). On the basis of a spectrogram in Figure 6.17b the damage presence cannot be stated, thus the notch cannot be localized.

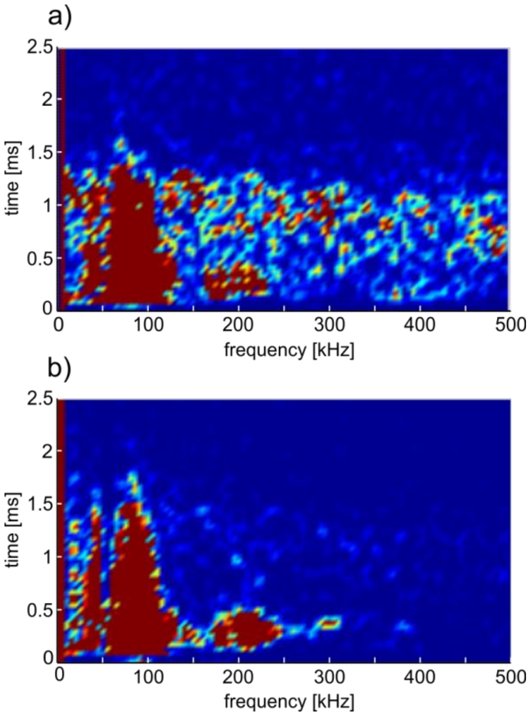

Figure 6.17. Spectrogram of ultrasonic signals registered in the partially embedded bar: a) specimen with intact bar, b) specimen with bar with crack

Figure 6.18 shows guided wave propagation signals excited by the piezo actuator. The signals were registered at the left end of the bar. The amplitude of the signals was normalized to 1. The characteristic reflections were identified and indicated. In the signal registered for the bar with the crack, additional reflection from damage is visible with the time-of-flight equal 0.3056 ms. For the excited wave with a frequency of 60 kHz, the analytical group velocity value was equal to 5071.9 m/s (Figure 6.2) and the experimental value determined on the basis of the signal registered for the intact bar was equal to 4950.5 m/s. The defect position was calculated using Eq. (6.1) and its value was equal to 0.775 m (for the analytical group velocity value) and 0.756 m (for the experimental group velocity value). The difference between the actual position and the position identified by guided waves was 1.97% (for analytical group velocity value) and 0.53% (for experimental group velocity value).

The wave propagation signals registered for the partially embedded specimen are presented in Figure 6.19. Additionally, the signal envelopes for a free bar with the crack and the partially embedded bar with the intact bar were plotted to compare the differences in signals between a free and a multilayered bar. One can see that the amplitude values for multilayered specimens are relatively lower than for the free bar as a result of wave energy leakage into the mortar cover. Comparing the results for damaged free and embedded specimens, it may be noticed that there is some shifting (denoted by Δt_{oF}^{D}) between registration times of reflections from damages. In the free bar case the reflection from defect is registered earlier, because the group velocity in the multilayered bar is lower than in the free bar case. Damage location can be estimated using the time-of-flight of reflection from damage (0.37 ms). The wave velocity in the multilayered part determined theoretically was equal to 2407.16 m/s and experimentally 2380.95 m/s. The position of damage was identified using Eq. (6.4) its values were 0.792 m and 0.80 m, respectively. The difference between the actual position and the position identified by guided waves was 4.21% (analytical group velocity value) and 5.26% (for experimental group velocity value).

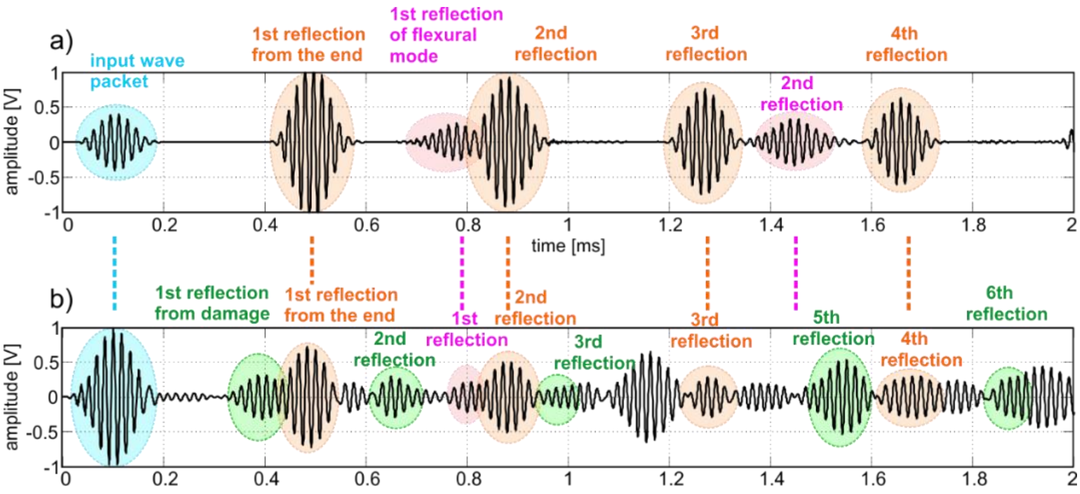

Figure 6.18. Experimental wave propagation signals registered for the free bar: a) intact bar, b) bar with crack

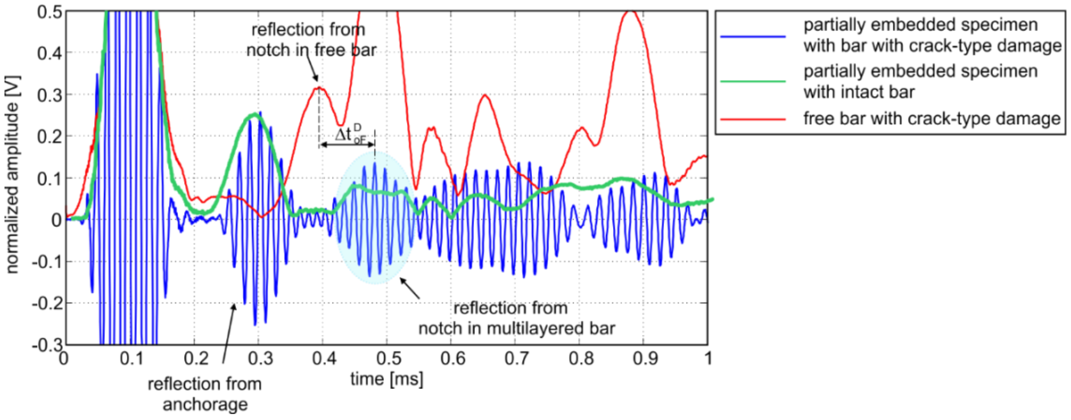

Figure 6.19. Experimental wave propagation signals registered for partially embedded bar: a) specimen with intact bar; b) specimen with bar with crack

6.4.3 Corrosion damage

Figure 6.20 shows time-frequency representation of experimental signals obtained by the ultrasonic pulser-receiver for a uniformly corroded bar. The shape of curves for the bar after 1 and hours of corrosion (Figure 6.20a and b) is similar to the curves for the intact bar (Figure 6.16a). For a longer duration of corrosion process the dispersion curves seem to disappear, however at spectrograms received after 3, 4 and 5 hours short segments of the dispersion curves of $L(0,1)$ mode are visible. After 6 hours of corrosion and the mass loss equal to 10.145%, in the spectrogram (Figure 6.16a) any curve was left, what indicates high sensitivity of this method to mass loss detection.

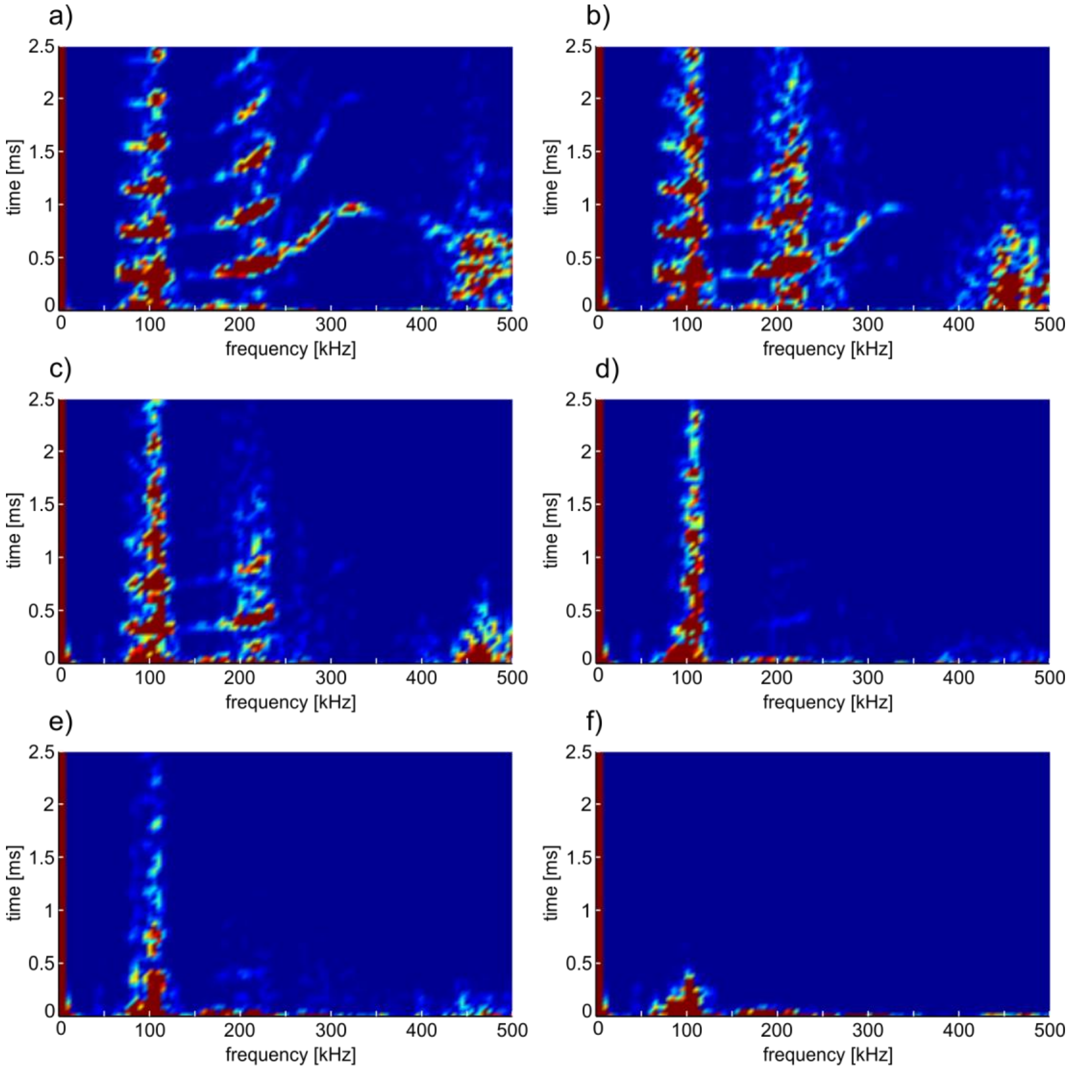

Figure 6.20. Spectrogram of ultrasonic signals registered in the free bar after a) 1 hour, b) 2 hours, c) 3 hours, d) 4 hours, e) 5 hours, 6) 6 hours of induced corrosion process

Figure 6.21 shows time-frequency representation of experimental signals obtained by the ultrasonic pulser-receiver for the corroded multilayered bar. One can see that the spectrograms obtained experimentally differ from the results obtained theoretically and the dispersion curves cannot be clearly indicated, but the energy density of the STFT spectrum is much lower for bars corroded for a longer time. It is clearly visible that especially higher frequencies vanish for a longer time duration of a corrosion process.

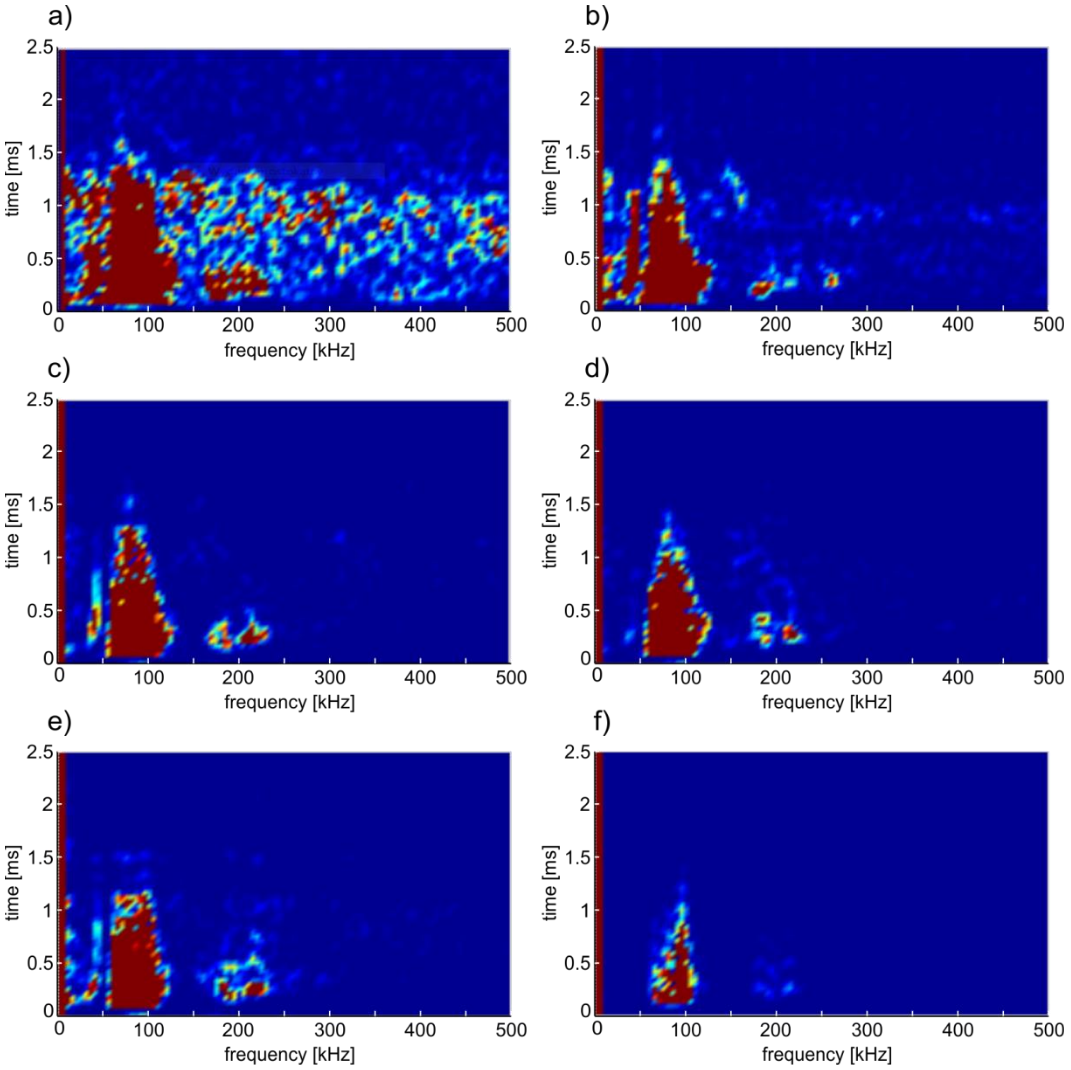

Figure 6.21. Spectrogram of ultrasonic signals registered in the partially embedded bar after a) 0 hour, b) 4 hours, c) 8 hours, d) 12 hours, e) 16 hours, f) 20 hours of induced corrosion process

Figure 6.22 presents envelopes of wave propagation signals for the free bar with a variable level of corrosion. Two effects of corrosion development can be observed. One can see that the amplitude of particular reflections of $L(0,1)$ mode from the end of the bar decreases with the increase of the damage level. The wave attenuation is a result of intense wave damping caused by the occurrence of corrosion pitting at the bar surface. The decrease of the amplitude value also applies to the additional converted flexural mode registered after 0.7 ms. However, the amplitude of the flexural mode does not decrease proportionally to the corrosion level like in the longitudinal mode case. For example in the presented case amplitude of $F(0,1)$ mode in a bar corroded for 6 hours was higher than in a bar corroded for 3 and 5 hours. The second effect related with corrosion damage concerns the wave propagation velocity. The more bar was destroyed, the shorter time-of-flight of reflections from the end was obtained. This observation agrees with theoretical considerations well. Dispersion curves determined for various diameter of steel bar indicate that with the decrease of bar diameter, the velocity of the first longitudinal mode increases (Figure 6.6).

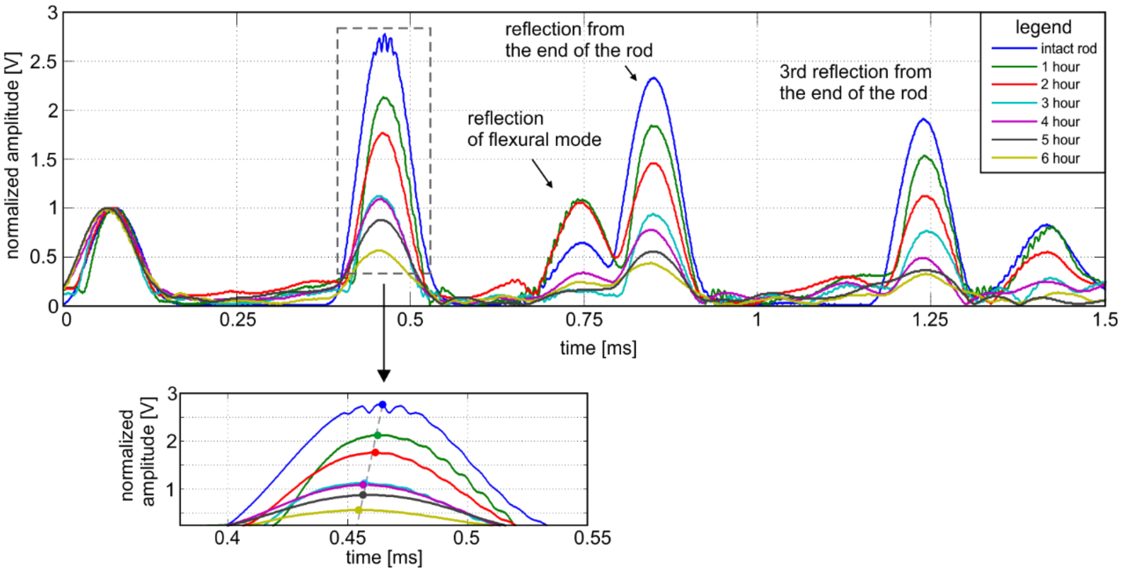

Figure 6.22. Envelopes of experimental wave propagation signals registered for free bar at different stages of corrosion

On the basis of experimental signals, the wave propagation velocity c_g^{bar} was determined for each stage of the corrosion process. Next, the diameter D_c of the corroded bar was calculated by means of the Pochhammer equation (Eq. (2.122)). The obtained results were compared with the diameter D_m calculated involving the mass loss according to the following formula:

$$D_m = \sqrt{\frac{4m}{\pi L \rho}} \tag{6.11}$$

The comparison of diameter values is given in Table 6.1. The differences in percentage mass loss obtained experimentally and theoretically are significant, however, in both cases the trend is downward. The results suggest that estimating the level of damage caused by corrosion on the basis of wave velocity is not effective and it gives the results that deviate significantly from the real ones. In the case of a bar corroded for 6 hours the percentage mass loss determined experimentally was equal to 10.145% while the theoretical analysis indicates the mass loss equal to 63.15%. Thus wave velocity may be an indicative parameter, whose variations indicate corrosion occurrence, but do not allow for accurate estimation of the mass loss. The first reason for large discrepancies of experimental and theoretical results was the choice of excitation frequency. A carrier frequency of 60 kHz used in experiment, chosen on the basis of tunning test, was insensitive to changes of bar diameter, because the significant changes in bar diameter were bound to trigger negligible changes in wave velocity (cf. Figure 6.6b). For this reason even small errors in wave velocity estimation may result in significant bar diameter variations. A second factor, to act upon diameter determination was an applied bar theory. Due to corrosion the bar was covered with a layer of oxides with a tendency to expand. Volumetric density of corrosion products is lower than steel density. For this reason a corroded bar became a multilayered bar with an external layer characterized by much worse material parameters than steel. In the case of multilayered bars Pochhammer theory is not valid, thus its use may bring inaccurate diameter estimation. The results for a partially embedded bar subjected to corrosion are given in Figure 6.23. Single-frequency wave propagation signals were registered at both ends of the specimen.

Table 6.1. Results of experimental and theoretical mass determining

	Experiment				**Theory**		
time of corrosion test [h]	**wave velocity [m/s]**	**bar mass [g]**	**bar diameter D_m [mm]**	**percentage mass loss [%]**	**Bar diameter D_c [mm]**	**bar mass [g]**	**percentage mass loss [%]**
0	4950.5	620	10	0	17.79	1964.41	-
1	4975.12	615.2	9.961	0.779	16.6	1708.47	13.03
2	5000	607.3	9.897	2.041	15.26	1443.78	26.5
3	5025.13	595.4	9.799	3.974	13.724	1167.76	40.55
4	5037.78	583.3	9.699	5.922	12.85	1023.76	47.88
5	5050.51	570.4	9.592	7.994	11.882	875.33	55.44
6	5063.29	557.1	9.479	10.145	10.806	723.97	63.15

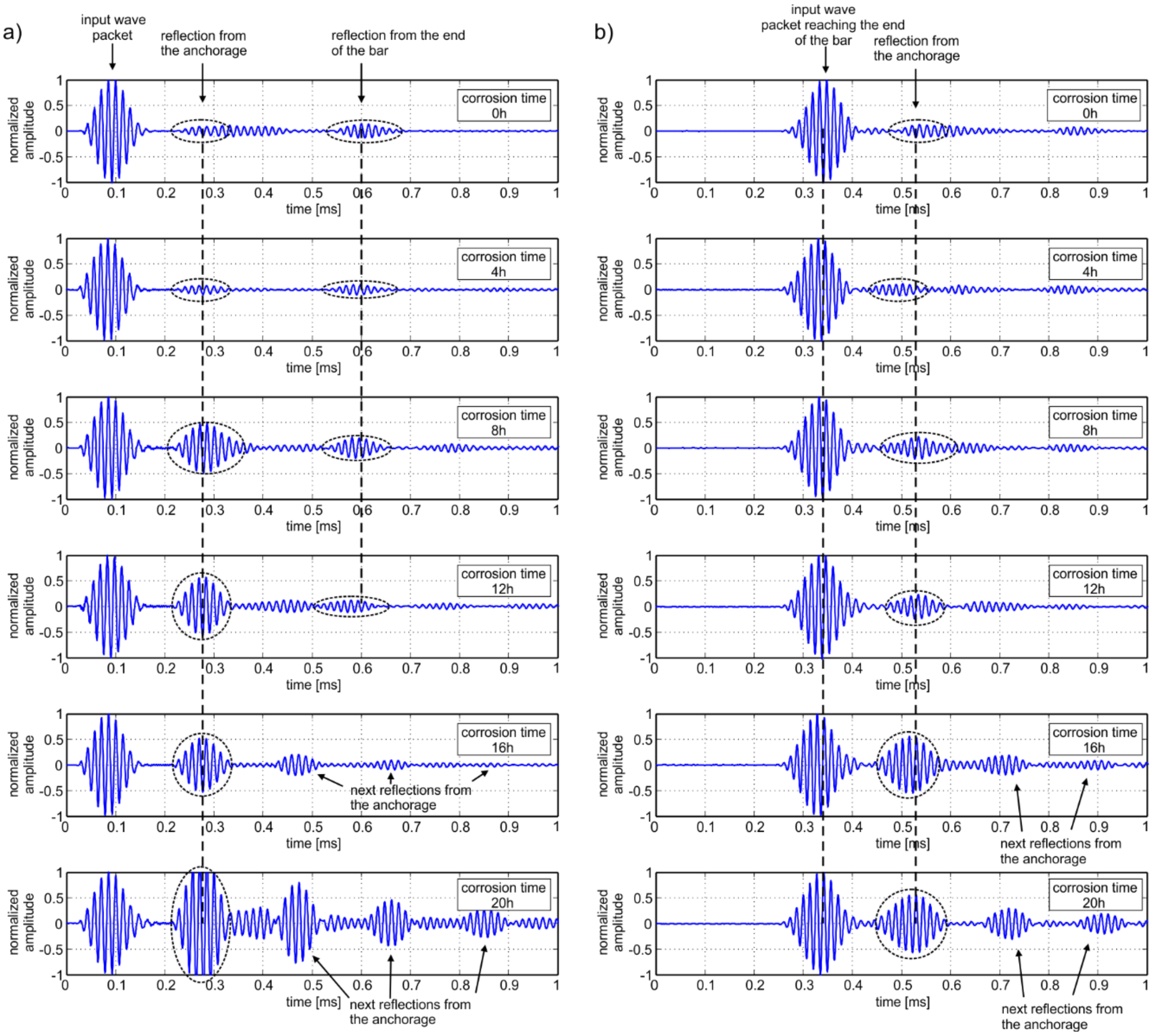

Figure 6.23. Signals registered for multilayered bar with variable level of level of corrosion level: a) signals registered at the free end of the bar and b) signals registered at the embedded end of bar

The amplitudes were normalized to make the peak value of the input wave is equal to 1. The input wave travelled along the free part of the bar. Next, after diffraction at the anchorage, part of the wave energy travelled back and was registered at the free end. The remaining part of the energy travelled along the embedded part and was registered at the embedded end. Each signal registered at the free end of the bar (Figure 6.23a) contained reflection from the anchorage and reflection from the end of the specimen. The amplitude of the reflection form the anchorage was strongly sensitive to the damage level of the anchor. It can be seen that for a longer time of the corrosion process the reflection from the anchorage is more visible. It is caused by corrosion pit occurring at the media boundary (Figure 6.12d-f). The narrower necking, the more energy was reflected, so that the amplitude of the reflections from the anchorage increased.

Moreover, in the signals registered after 20 hours of corrosion process multiple reflections from the anchorage at the same time intervals were clearly visible. Differences in the cross-section between the free bar and the bar embedded in mortar also caused the increase of the amplitude of reflection from the anchorage (indicated by straight dashed line in Figure 6.23b). In the signals registered at the free end reflections from the end of the bar are also indicated. The amplitudes of these reflections became smaller until finally, after 16 hours of the corrosion process reflection is not visible. An amplitude decrease is caused by energy dissipation at irregularities present on the bar surface. It is worth mentioning, that corrosion damage did not act on wave velocity in the presented case.

6.5 Conclusions

In this Chapter theoretical and experimental investigations were carried out on guided wave propagation in free steel bars and bars partially embedded in grout with pre-existing damage. Two groups of damage have been taken into consideration: point damage and surface damage in the form of uniform corrosion. The considered point damage was visible in the form of the notch. In order to investigate the influence of corrosion occurrence on wave propagation, both free and covered bars with variable level of corrosion damage were analysed. The results were presented as time-domain propagation signals, registered by piezo transducers as well as spectrograms performed by Short Time Fourier Transform for signals registered by pulser-receiver. Point defects and variable level of corrosion damage in free or embedded bars investigated additionally in two different ways allow to denote both advantages and drawbacks of various approaches of wave excitations and manners o presenting results. Several conclusions can be drawn:

- Damage detection by the use of time-domain signals is very effective. Single frequency used in experiment chosen on the basis of tunning test result in signals that are legible and easy to interpret. Damage location was successfully determined on the basis of time-of-flight and wave propagation velocity. Despite the fact that analytical and experimental velocities differ (the difference was equal to over 100 m/s) there were no significant results between the outcomes.

- Time-frequency representations performed with the use of Short Time Fourier Transform stay with very good agreement with analytical time-frequency representation for a healthy bar. Additionally, the STFT spectrograms allow to determine the presence of point damage.
- Surface damage of a bar caused by corrosion was successfully detected by guided wave propagation method. Time-domain signals were characterized by decreasing amplitude values resulting from higher wave energy damping in bars with multiple corrosion pits. The diameter decrease of the corroded bar caused the increase of wave velocity, confirmed by theoretical considerations. However, the wave velocity cannot be used as an indicator parameter to estimate diameter variations. Diameters of bar estimated experimentally on the basis of mass of the corroded bar and theoretically by the use of wave velocity and Pochhammer dispersion curves differ significantly. Significant divergence may result from the insensitivity of chosen frequency to diameter changes. In the case of insensitive frequency significant changes in bar diameter results in negligible changes in wave velocity, leading to significant error is diameter decrease estimation. The second factor, to probably act upon on inaccurate diameter estimation is the applied bar theory. The result of corrosion process is a layer of oxides covering the bar and expanding. Volumetric density of corrosion products is lower than steel density. For this reason the corroded bar act as a multilayered bar with an external layer characterized by much worse material parameters compared to steel. In the case of multilayered bars Pochhammer theory cannot be applied and diameter estimation on its basis may be inaccurate. As mentioned above wave propagation velocity cannot be used to accurately estimate the diameter of a corroded bar, but it may be an indicative parameter, whose changes indicate corrosion occurrence.
- The STFT spectrograms proved to be very efficient tool for corrosion detection of free steel bars. Significant changes in distinctiveness of dispersion curves were observed even for small changes in mass of corroded bars. Considerable sensitivity of spectrograms results in a complete lack of dispersion curves in spectrogram for relatively low mass loss equal to 10.145%.
- Point damages can be easily detected and localized in multilayered bars on the basis of time-domain propagation signals. However, in order to appropriately estimate

defect locations it is necessary to determine correctly the wave group velocities in particular parts of an embedded bar.

- For a vast range of excitation frequencies reflection from damage in free bar is registered earlier than in the covered bar. However, there exists a range of frequencies to show reflection for free bar registered later than for covered bar.
- The STFT spectrograms can be successfully used in the assessment of corrosion damage of embedded bars. Dispersion curves cannot be clearly indicated, but the energy density of the STFT spectrum is much lower for bars corroded for a longer time. It is clearly visible that especially higher frequencies vanish for longer time duration of corrosion process.
- Corrosion damage acts upon amplitude values of time-domain signals registered at both ends of the bar. The amplitude of reflection from the end of the bar registered at the free end of the bar decreases because of surface irregularities of a corroded rod. At the same time amplitudes of reflections from the anchorage registered at both ends of the rod increase with the increase of time duration of a corrosion process. The amplitude increase is caused by necking forming at the border between both free and multilayered parts.

CHAPTER 7

Experimental investigation of ground anchor system

7.1 Introduction

In the majority of the literature cases and in the previous Chapters of the thesis the tendon of the anchor is considered as a prismatic steel bar with a constant cross-sectional shape and without any connections throughout the length. However, tendons of ground anchors and soil nails are often fabricated with the use of self-drilling hollow bars [249]. Those bars are characterized by left-hand thread for standard percussive drilling so the cross-section varies through the bar length (Figure 7.1).

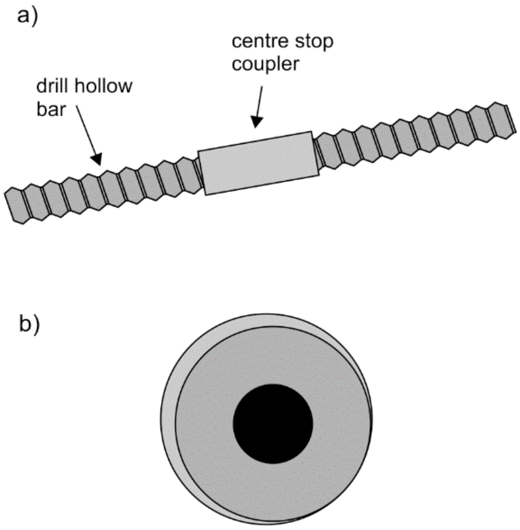

Figure 7.1 Scheme of self-drilling systems of ground anchors: a) two drill hollow bars connected by the centre stop coupler, b) cross-section of the bar

The hollow cross-section allows for simultaneous drilling and grouting. Moreover, in the case of long anchors, the tendon often made of debonded bars with partially bonded couplers (Figure 7.2). The tendon length can be easily adjusted to design assumptions by connecting appropriate number of bars. The guided wave propagation becomes more complicated in drill hollow bars than in simple prismatic bars. The major factors influencing the phenomena of wave propagation concern complex cross-section of the drill bar and the application of couplers.

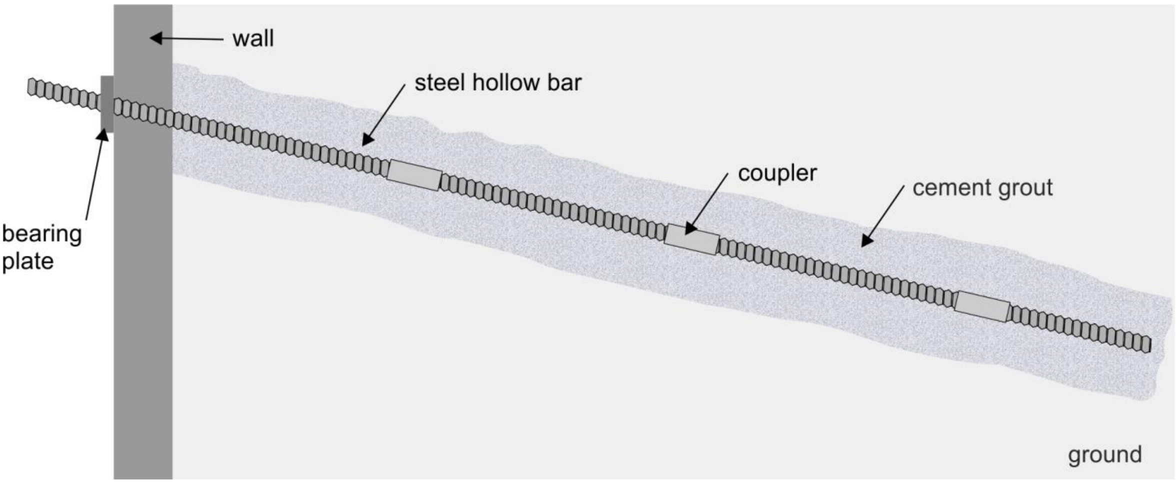

Figure 7.2 Scheme of ground anchor performed with the use of self-drilling systems

This chapter extends the investigations conducted on idealized, laboratory models of ground anchors into the ground anchor system DYWI® Drill Hollow Bar System [249]. The research contains four stages (Figure 7.3). At the first stage a single section of the bar (Figure 7.3a) and two sections connected by the coupler are investigated (Figure 7.3b). The main aim of the first study part is to analyse the wave attenuation due to discontinuities in the form of mounting connections occurring over the bar length. The differences in wave propagation signals registered at a single bar and the system of two bars were indicated and discussed. The presence of bonded couplers and their influence on wave attenuation has been analysed. Results of this investigation are presented in [240].

The next stage of the research involves investigation of wave propagation in a small-scale model of anchor performed in the ground (Figure 7.3c). Firstly, monitoring is conducted of a hardening process of the inject forming the anchor body.

When the mortar achieved its full strength the ground anchor was excavated and tested in laboratory (Figure 7.3d).

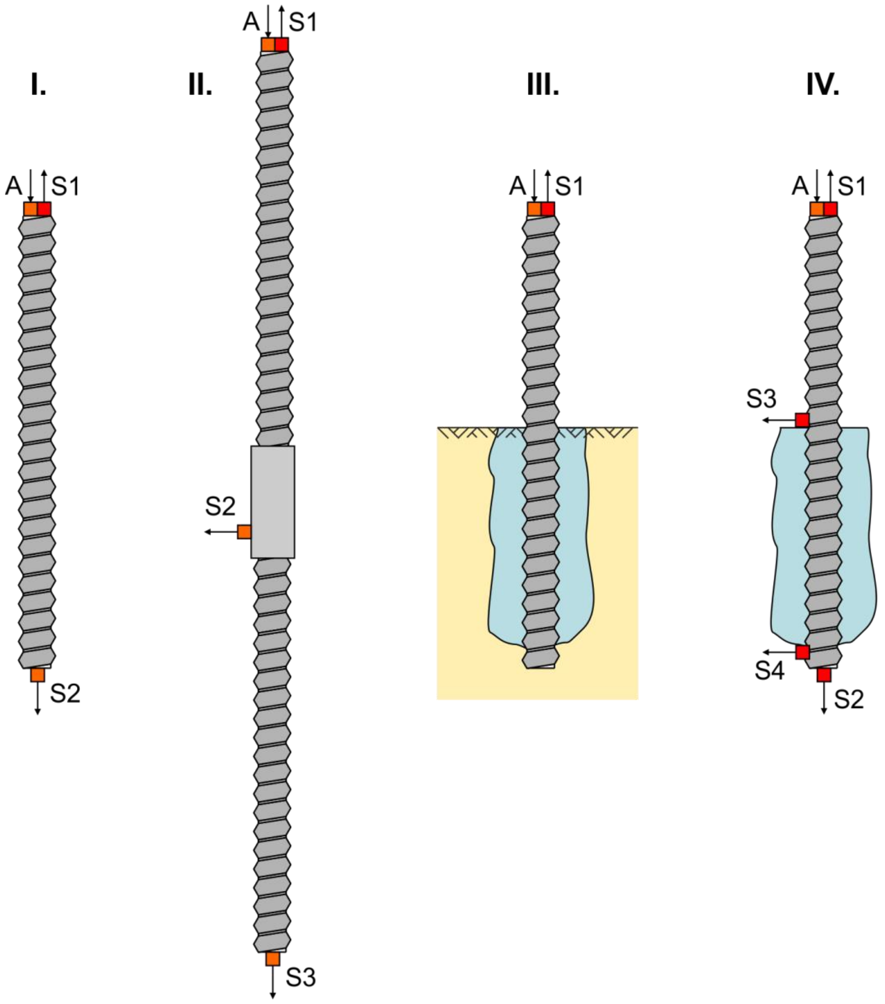

Figure 7.3 Stages of investigation

7.2 Investigation of drill-hollow bar system

7.2.1 Dispersion curves for hollow bar

Aimed at obtaining dispersion curves for a tendon of the anchor made with the use of self-drilling system, dispersive relations for the hollow bar are investigated. The group velocity dispersion curves for longitudinal modes obtained by PCDISP programme and results obtained experimentally are presented in Figure 7.4. Since the self-drilling bar has a non-uniform cross-section, the dispersion equation has been solved for the case of a hollow bar with regular, smooth internal and external surfaces. The drill bar was considered a pipe with the internal diameter equal to the diameter of the bar, while the external diameter was equal to the nominal diameter of the drill bar. For this reason, the curves presented in Figure 7.4 can be regarded an approximate solution only, producing a coarse information about the number of wave modes and their velocities.

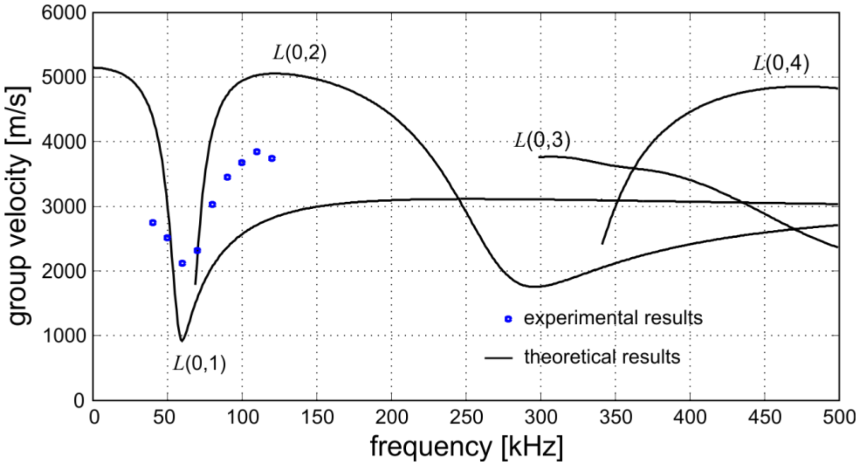

Figure 7.4 Dispersion curves for steel hollow bar (E = 210 GPa, ν = 0.3, ρ = 7938.54 kg/m^3) with external diameter of 38 mm and internal diameter of 19 mm

7.2.2 Experimental model

The investigations presented in this Chapter were conducted on DYWI® Drill Hollow Bar System [249]. The first specimen was a single-section self-drilling hollow bar R38-550, 1 m long. The technical data for the bar are taken from the manufacturer [249]. The nominal thread diameter was equal to 38 mm, the effective external diameter was equal to 36.4 mm and the internal diameter equal 19 mm. The density of steel was assumed 7938.54 kg/m^3. The photographs of the drill hollow bar and its cross-section are presented in Figure 7.5.

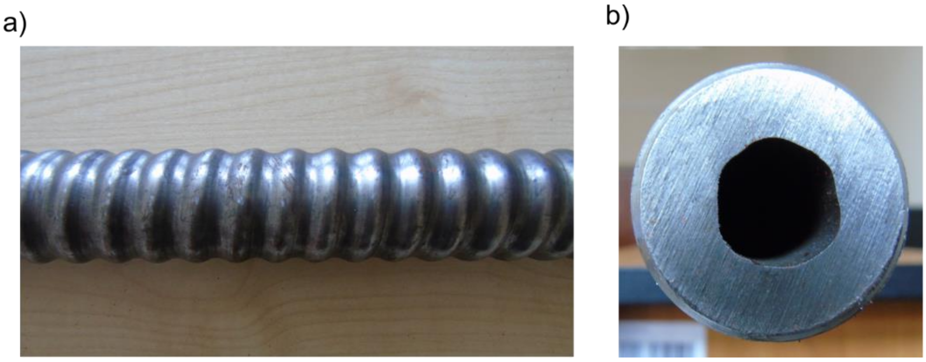

Figure 7.5 Photograph of a) single self-drilling hollow bar and b) its cross-section

The second experimental model was a self-drilling system containing two R38-550 equal length bars connected by a centre stop coupler (Figure 7.6). The total length of the specimen was 2 m.

Figure 7.6 Self-drilling hollow bar system connected by the centre stop coupler

The guided waves were excited and sensed by PZT plate transducers Noliac NAC2024. An excitation signal was a ten-cycle sine function modulated by the Hanning window. Guided wave propagation tests were conducted for wide range of frequencies, however results are presented for the carrier frequency of 60 kHz, producing the most legible output signals.

The configuration of measurement points is given in Figure 7.7 and Figure 7.8, for the single bar and the bar system, respectively. In both cases, the waves were excited in longitudinal direction by the actuator attached to the left end of the specimen. In the case of a single self-drilling hollow bar, vibrations were registered by two PZT sensors, attached to both ends of the bar (Figure 7.7).

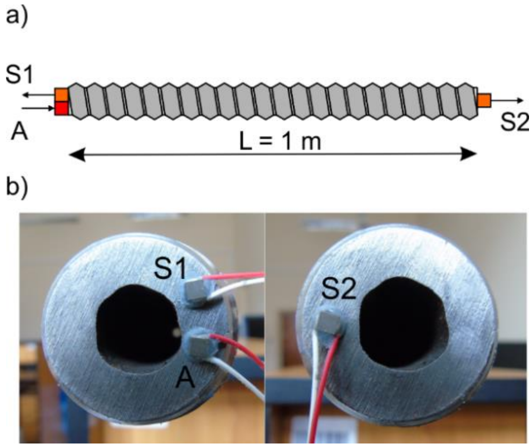

Figure 7.7 PZT transducers at the single self-drilling hollow bar: a) configuration of actuator and sensors; b) detail showing actuator and sensors at the beginning and the end of the bar

In the case of a self-drilling hollow bar system three PZT sensors were used. Two sensors were attached at both ends of the coupled bar to measure longitudinal waves, the third additional sensor was attached to the surface of the coupler between the bars to register vibrations perpendicular to the axis of the bar (Figure 7.8).

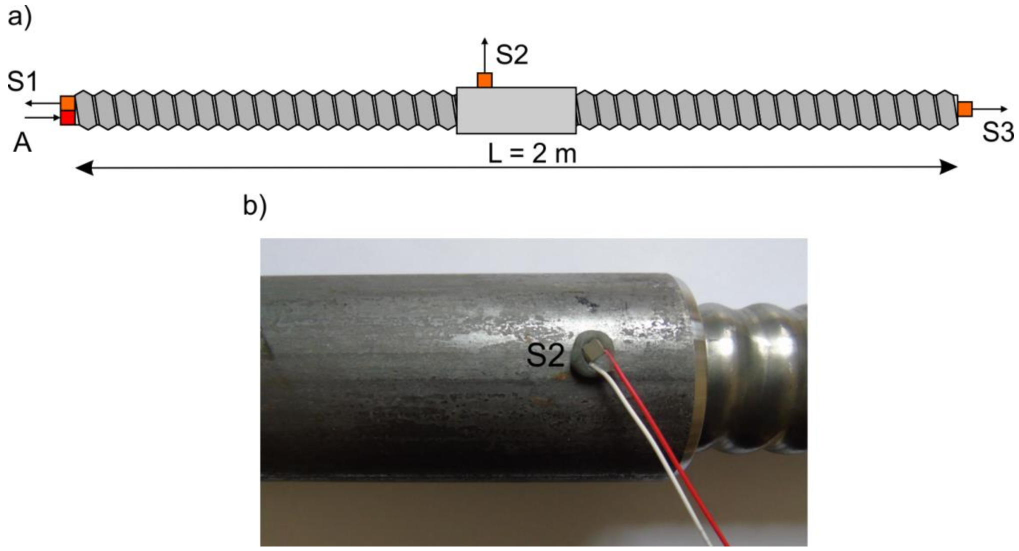

Figure 7.8 PZT transducers at the self-drilling hollow bar system: a) configuration of actuator and sensors; b) detail showing sensor attached to the coupler

7.2.3 Results

The wave propagation signals registered for a single self-drilling hollow bar are presented in Figure 7.9. The first signal (Figure 7.9a) was registered at the end the wave was excited (sensor S1), while the signal in Figure 7.9b was registered at the opposite end (sensor S2).

In both signals, the input wave packet and wave packets corresponding to consecutive reflections from the ends of the bar can be identified. Particular reflections from the bar ends occurred at the same regular time intervals Δt and they are characterized by a relatively higher value of the amplitude than other waveforms that can be observed in signals. These numerous additional low-amplitude peaks may be the outcome for the case of a specific cross-section of the bar varying throughout its length. They may also result from wave diffraction at the irregularities of the surface. Moreover, the actuator was not attached centrally. Imperfect, eccentric actuator location may result in excitation not only longitudinal, but also flexural modes. For the chosen carrier frequency equal 60 kHz, two additional flexural modes could be excited (compare Figure 7.4b).

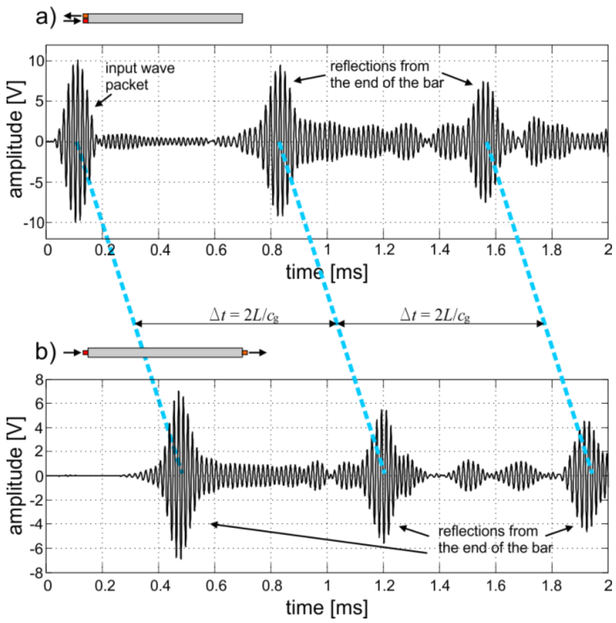

Figure 7.9 Wave propagation signals registered at the single self-drilling hollow bar: a) signal registered at the beginning and b) at the end of the bar

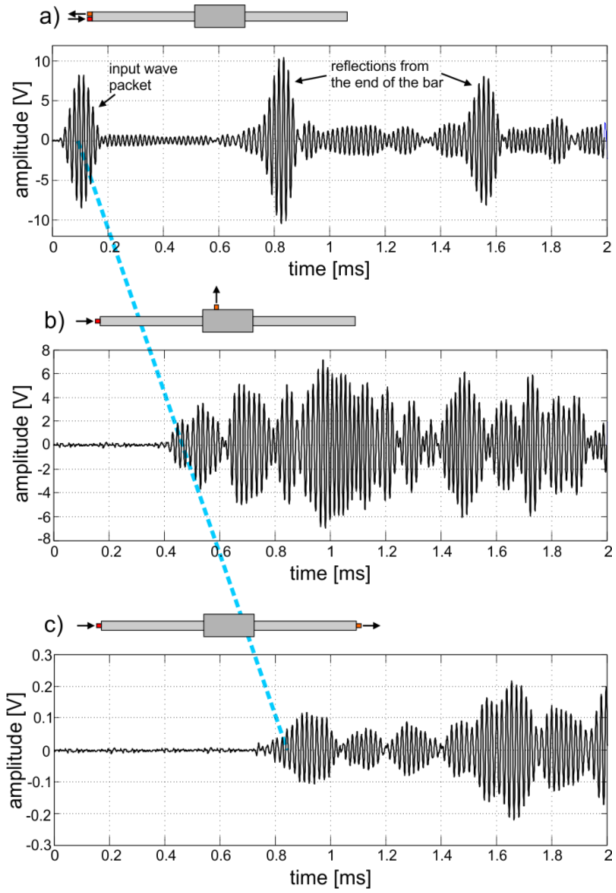

Figure 7.10 Wave propagation signals registered at the self-drilling hollow bar system: a) signal registered at the beginning, b) at the coupler in the middle and c) at end of the bar

The experimentally determined group velocity of the longitudinal wave calculated on the basis of time-of-flight (2116.4 m/s) differs considerably from the results based on dispersion curves for a uniform hollow bar (1029 m/s). This discrepancy confirms that the dispersion curves calculated for a smooth hollow cylinder with dimensions corresponding to the dimensions of the considered self-drilling hollow bar do not accurately reflect the shape of curves for the real bar with a thread.

The results for the self-drilling hollow bar system are illustrated in Figure 7.10. Three signals were registered at the beginning of the bar (sensor S1), in the middle at the coupler (sensor S2) and at the other end (sensor S3). The straight line is drawn through the first registered wave packets. It can be seen that their registration time is proportional to the distance between the sensor and the actuator. The angles of inclination of the lines for the single bar and the system of two bars do not significantly differ so one can conclude that the presence of a mounting connection does not act on the wave propagation velocity.

The character of the signals differs considerably with the propagation distance. Only in the case of the first signal, particular peaks corresponding to reflections from the bar ends can be easily identified. In two other cases the interpretation of signals is much more difficult and the signals are characterized by numerous wave packets with comparable amplitude values. Moreover, it can be seen that the amplitude values differ significantly between particular signals. The highest amplitude registered by sensor S1 was equal to 10 V, while in the case of vibrations registered at the coupler (sensor S2) the amplitude did not exceed 8 V. The lowest amplitude characterized the signal registered at the end of the coupled bar system (sensor S3). The highest amplitude registered in this signal was about 0.2 V, 50 times lower than for in signal registered by sensor S1. Therefore, it can be observed that the wave was strongly attenuated while passing through the mounting connection of two bars, despite the fact that bars were highly tightened without any gap in between. The internal thread of the coupler was the same as the threads of the bars, so the amplitude decrease was not caused by a connection defect. The same effect was observed for different frequencies.

Finally, comparison of signals registered by sensor S1 in both specimens is illustrated in Figure 7.11. The signal for a single self-drilling hollow bar is plotted by a black line while for the self-drilling hollow bar system the signal envelope is plotted by blue line. It can be seen that there are no significant differences between signals, even in extended time range up to 3 ms. The registration times of reflections from the end of the bar are similar and their amplitudes agree well. A high degree of similarity of these two signals registered for two different specimen lengths means that a vast majority of wave energy is reflected from the end of the first bar and it is not transferred from the coupler connection.

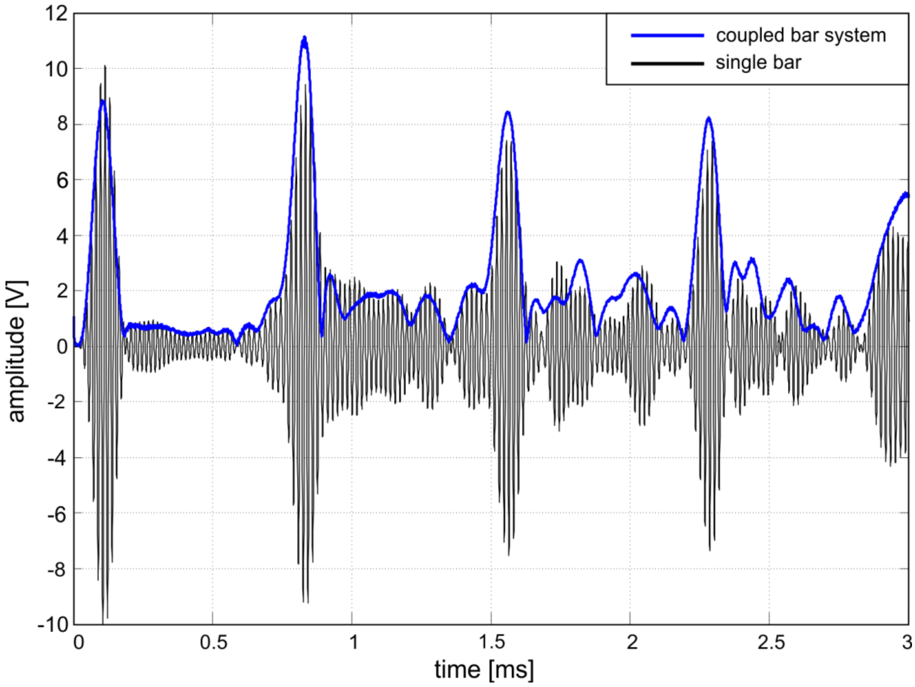

Figure 7.11 Comparison of wave propagation signals registered by sensor S1 for the single self-drilling hollow bar and the self-drilling hollow bar system

7.3 Monitoring of the ground anchor performed in the ground

7.3.1 Investigated object

A single self-drilling 1 m long hollow bar was located in the hole in the ground which was filled by liquid mortar (Figure 7.12). The diameter of the hole was about 10 cm and the length of the embedded part was about 50 cm. The actuator and sensor were located at the free end of the bar. During the first hour of the hardening process the signals were registered every 5 minutes. During the next three hours the signals were registered every 10 minutes. Wave measurement was also conducted after 24 hours and 72 hours. After one month (30 days) the anchor has been excavated and investigated in laboratory. The investigations carried out for underground and excavated anchor cases allow to observe the influence of the soil surrounding the ground anchor on wave propagation.

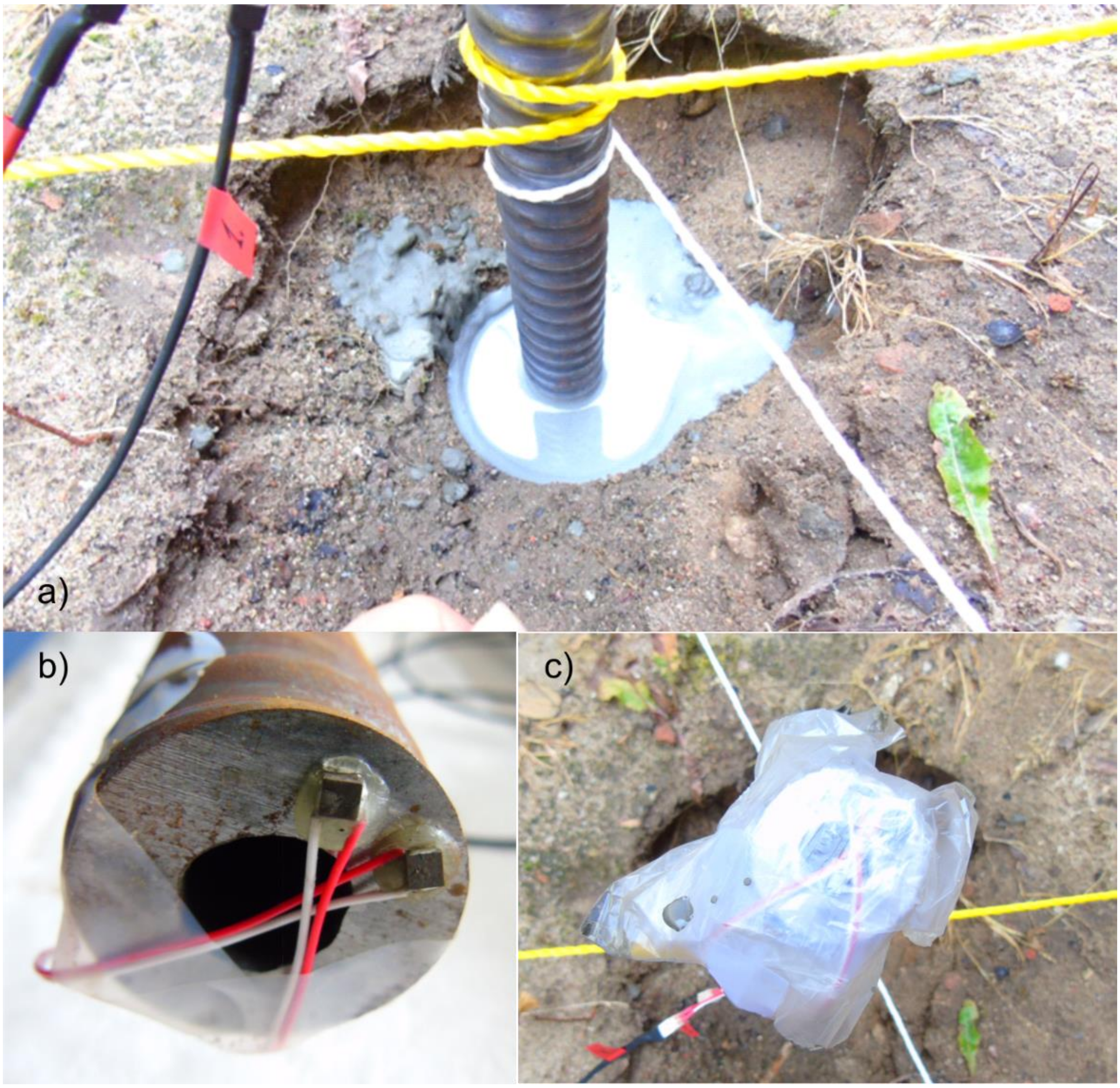

Figure 7.12 Small-scale anchor model performed in the ground: a) self-drilling bar placed in liquid mortar, b) sensor and actuator located at the end of the bar before placing in the ground and c) transducers protected against unfavorable environmental conditions

7.3.2 Monitoring of the hardening process of the mortar

Figures 7.13 to 7.17 present envelopes of time-domain signals during hardening process monitoring for a variable excitation frequency. The carrier frequency varies from 60 kHz to 100 kHz while the number of sine cycles was constant and was equal to 10. It can be clearly seen that the legibility of signals changes considerably for various frequencies. In each case mortar hardening makes the amplitude values change. In order to observe amplitude changes for each set of signals one wave packet has been marked and presented in a different scale. In case of each frequency it was possible to indicate wave packets whose amplitudes vary with the time duration of a setting process what can be applied in monitoring the process of mortar cover hardening.

For each frequency an analysis of amplitude values was performed. Figures 7.18 to 7.22 present graphs of reflection ratio defined as follows:

$$r = \frac{A_1}{A} \tag{7.1}$$

where A is the amplitude of the input wave packet, after normalization is equal 1, and is the amplitude of a chosen wave packet. Despite a relatively short length of the investigated specimen only for two cases (90 and 100 kHz) the reflection from the anchor end can be unambiguously indicated and their amplitudes are taken into account in further analysis. In the frequency cases of 60, 70 and 80 kHz wave packets have been selected characterized by a relatively high amplitude in the first registered signal (duration of a hardening process equal to 0 min), but it was difficult to determine whether it was a reflection from the end of the rod.

The presented results indicate that mortar hardening triggers decrease of the signal amplitude. The amplitude decrease is clearly visible especially while signals are registered during the first hour when mortar strength increases rapidly. After an hour differences in signals are not visible. The manufacturer declaration says that the pot life of the mortar is equal to approximately 40 minutes. In the investigation more water was used that specified in the recommendations what could slightly prolong the hardening time. Fast mortar setting explains fast decrease of the amplitude during the initial stage of the setting process.

The amplitude decrease may be caused by more intense wave energy leakage into an anchor body. At the first stage when mortar is a dense liquid the wave does not leak into a surrounding medium, thus is reflected from the end of specimen. In the course of mortar hardening, its physical parameters rise and the acoustic impedance of mortar also increases. As mentioned in paragraph 4.4.2 the relationship between the values of acoustic impedance of adjacent media determines the intensity of wave reflection and transmission phenomena. While the value of acoustic impedance of mortar approaches to the value of acoustic impedance of steel core wave energy leakage becomes intense and the signal amplitude at the free end decreases.

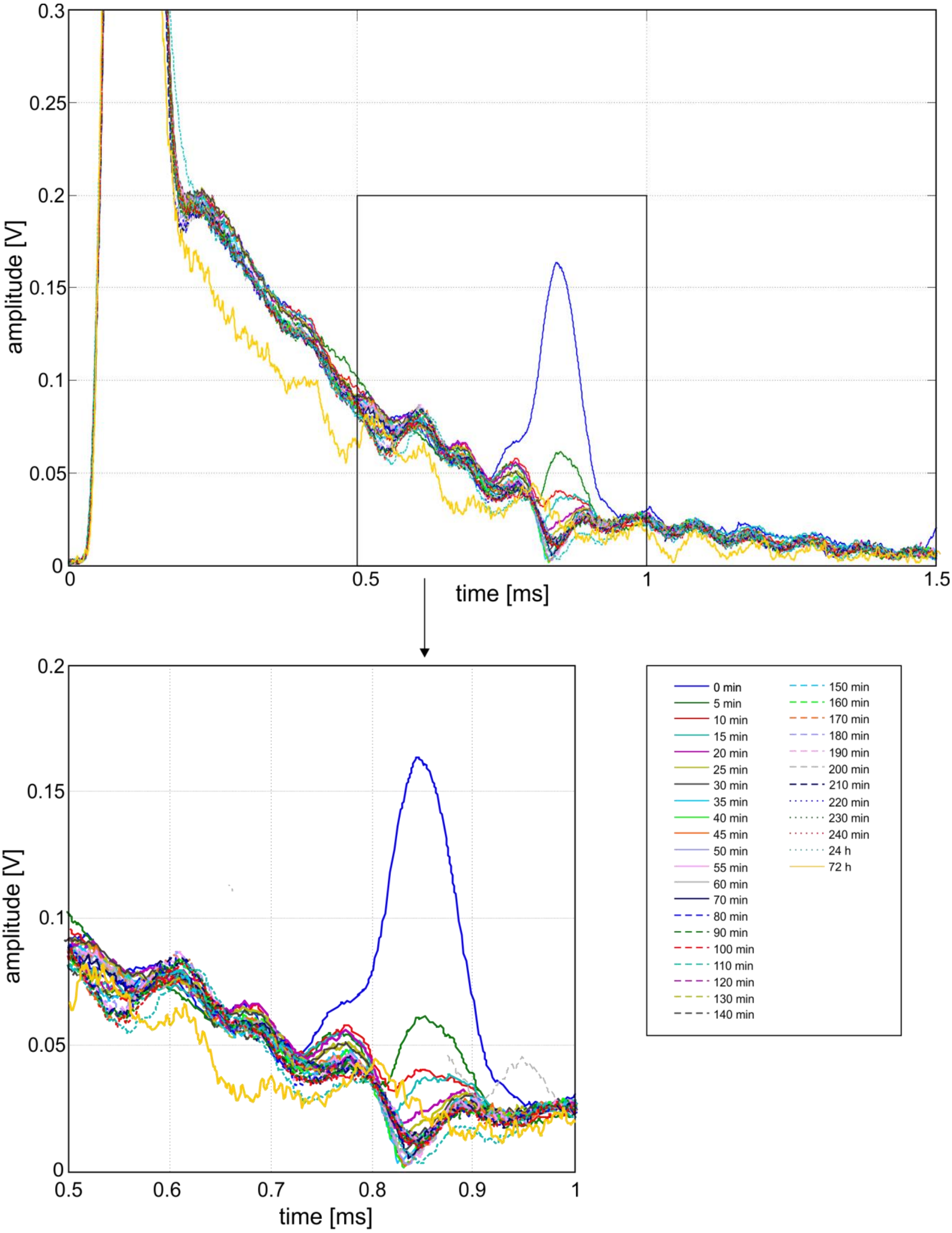

Figure 7.13 Envelopes of signals registered at the end of the anchor performed in the ground during hardening process (excitation frequency: 60 kHz)

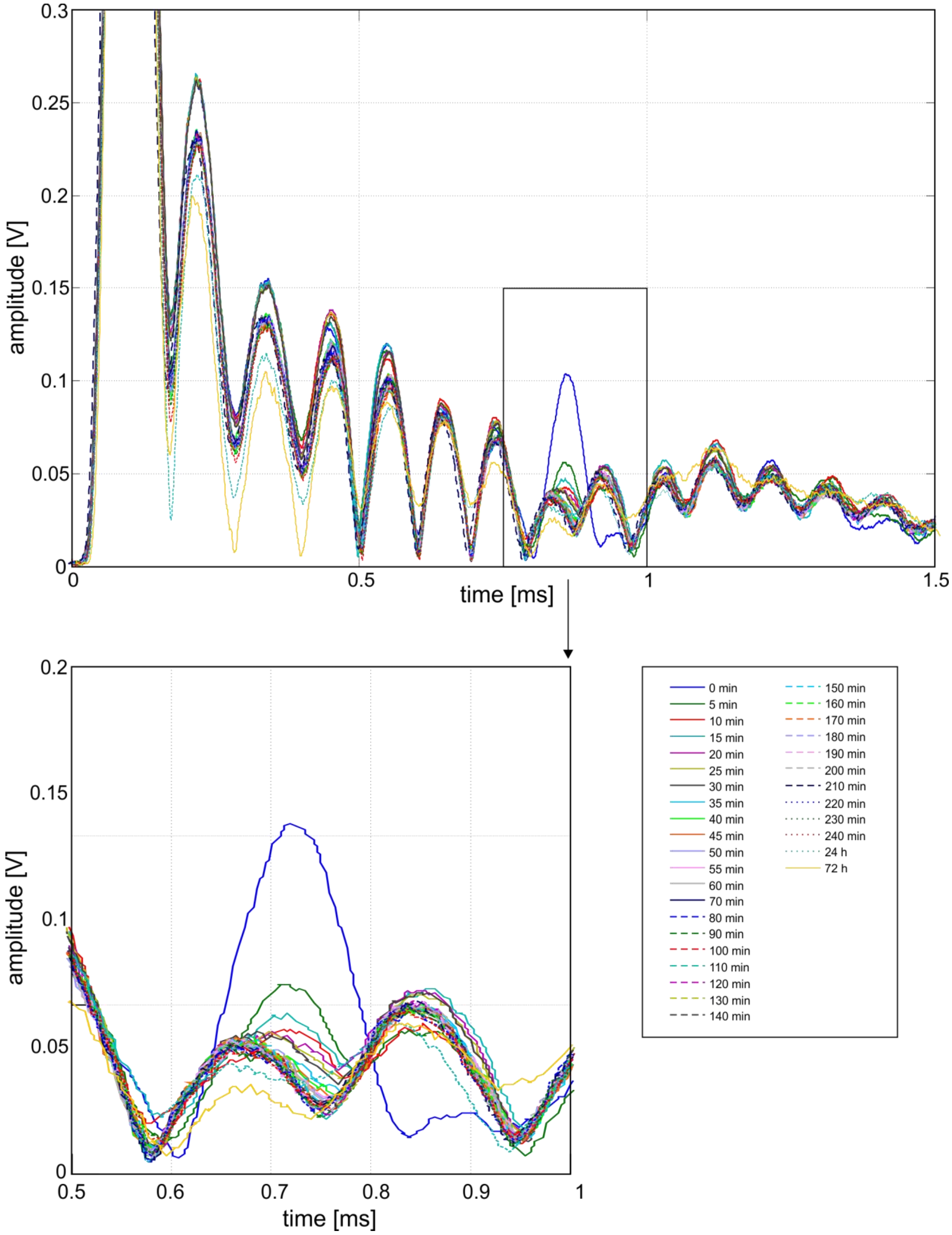

Figure 7.14 Envelopes of signals registered at the end of the anchor performed in the ground during hardening process (excitation frequency: 70 kHz)

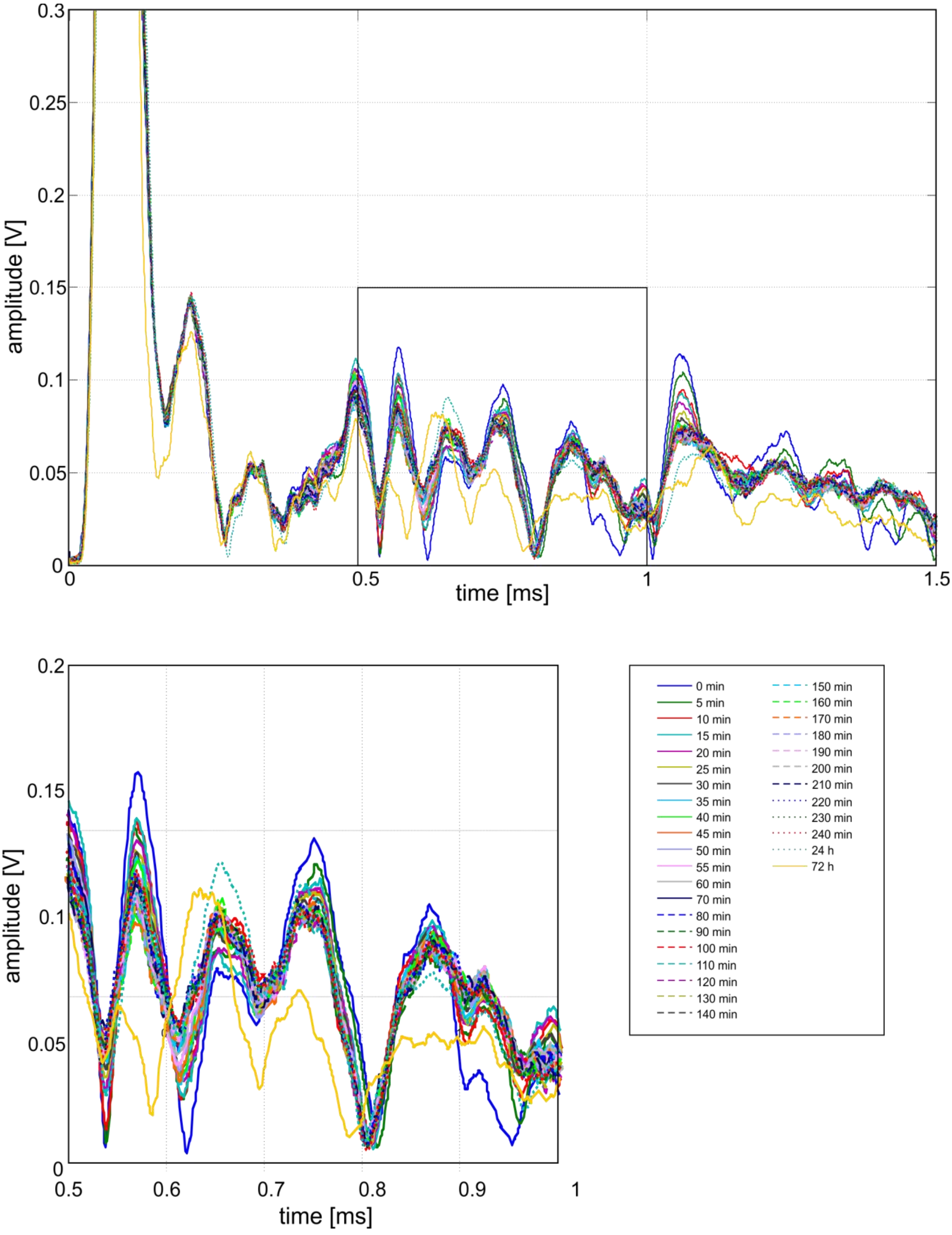

Figure 7.15 Envelopes of signals registered at the end of the anchor performed in the ground during hardening process (excitation frequency: 80 kHz)

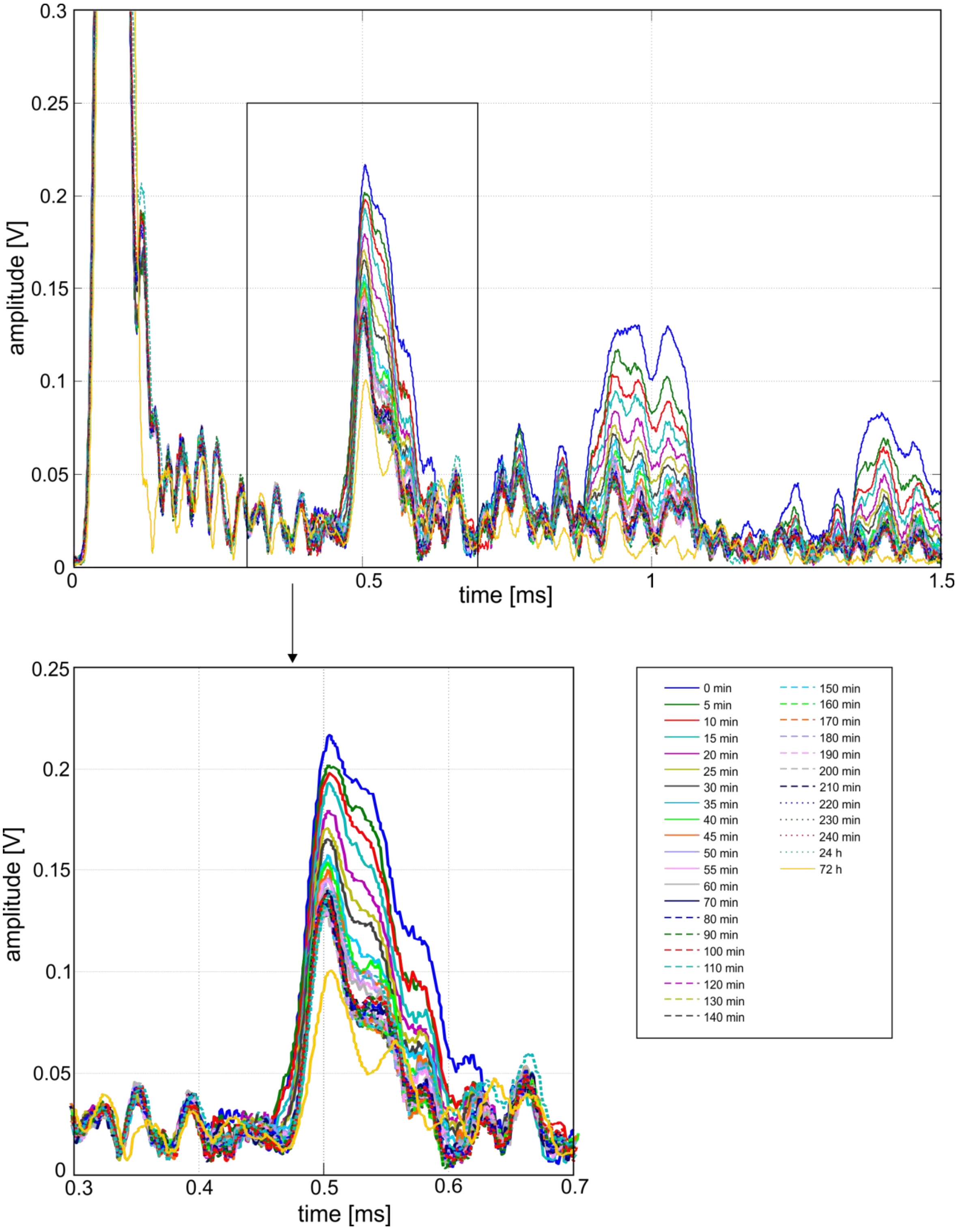

Figure 7.16 Envelopes of signals registered at the end of the anchor performed in the ground during hardening process (excitation frequency: 90 kHz)

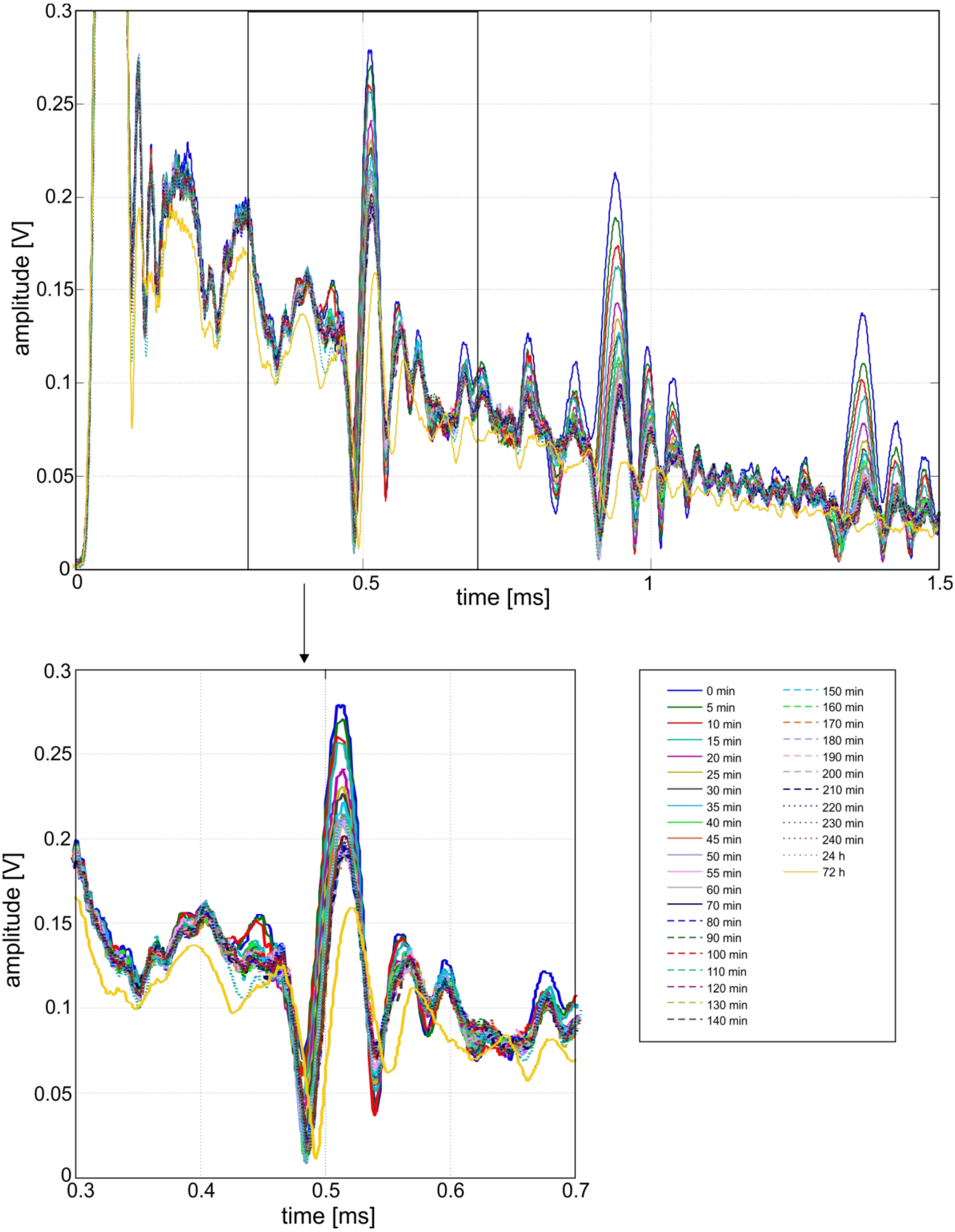

Figure 7.17 Envelopes of signals registered at the end of the anchor performed in the ground during hardening process (excitation frequency: 100 kHz)

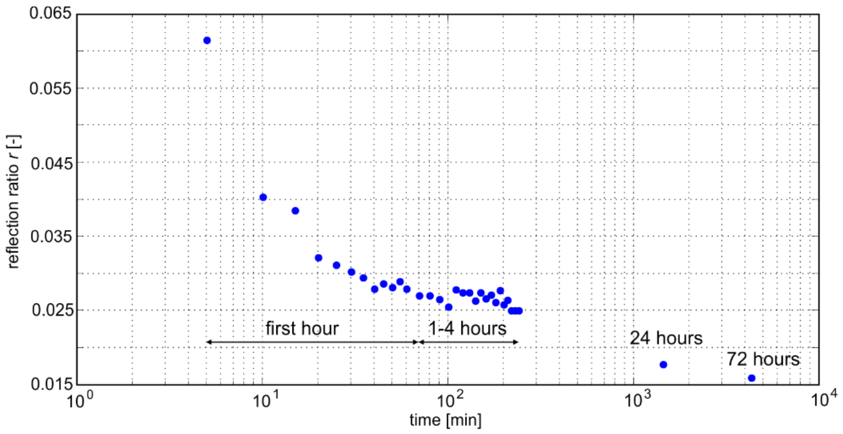

Figure 7.18 Reflection ratio calculated for reflection registered during hardening process indicated in Figure 7.13 for excitation frequency of 60 kHz

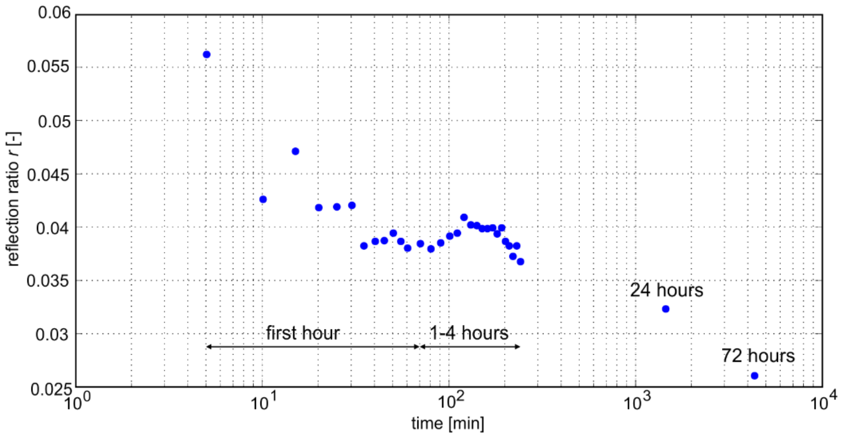

Figure 7.19 Reflection ratio calculated for reflection registered during hardening process indicated in Figure 7.14 for excitation frequency of 70 kHz

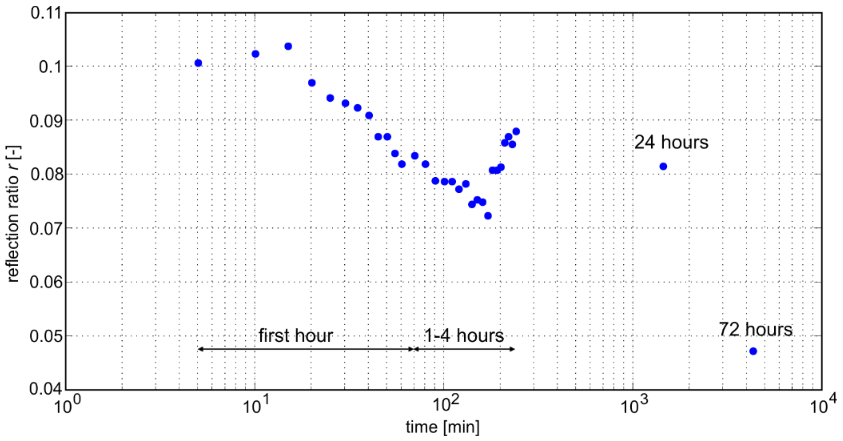

Figure 7.20 Reflection ratio calculated for reflection registered during hardening process indicated in Figure 7.15 for excitation frequency of 80 kHz

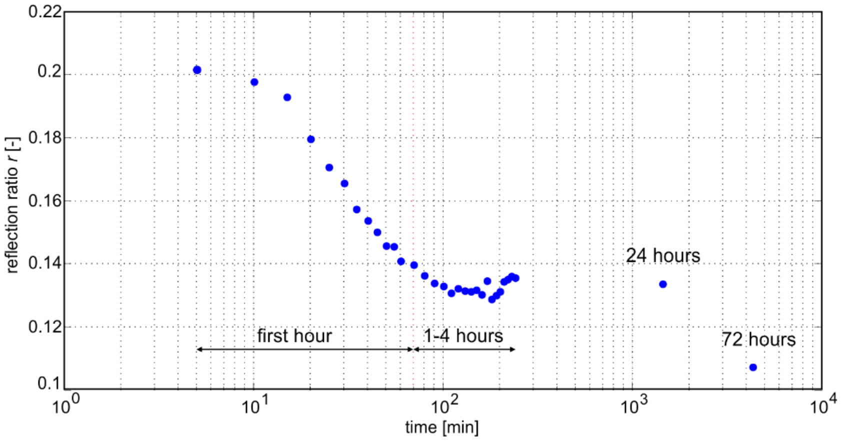

Figure 7.21 Reflection ratio calculated for reflection from the anchorage during hardening process indicated in Figure 7.16 for excitation frequency of 90 kHz

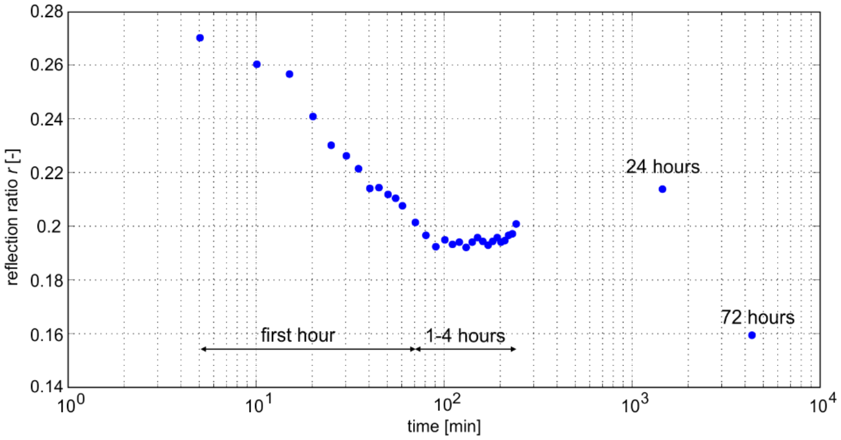

Figure 7.22 Reflection ratio calculated for reflection from the anchorage during hardening process indicated in Figure 7.17 for excitation frequency of 100 kHz

7.3.3 Laboratory tests of excavated anchor

After a period of one month ground anchor was excavated and tested in laboratory (Figure 7.23). The waves were excited at the free end of the bar and signals were registered by four sensors (Figure 7.23b): two located at the both ends of the steel bar (S1 and S4) and two located at the both ends of the anchor body (S2 and S3).

Figures 7.24 to 7.28 present the investigation results for excitation frequency range of 60-100 kHz. Despite a relatively short length of the anchor, the wave amplitude decreases rapidly due to spiral shape of a steel rod and irregularities of an anchor body. For this reason it was necessary to apply higher voltage to induce waves characterized by higher energy. The use of higher voltage results in the so-called avalanche breakdown. It manifests itself as an additional wave package registered at the signal beginning.

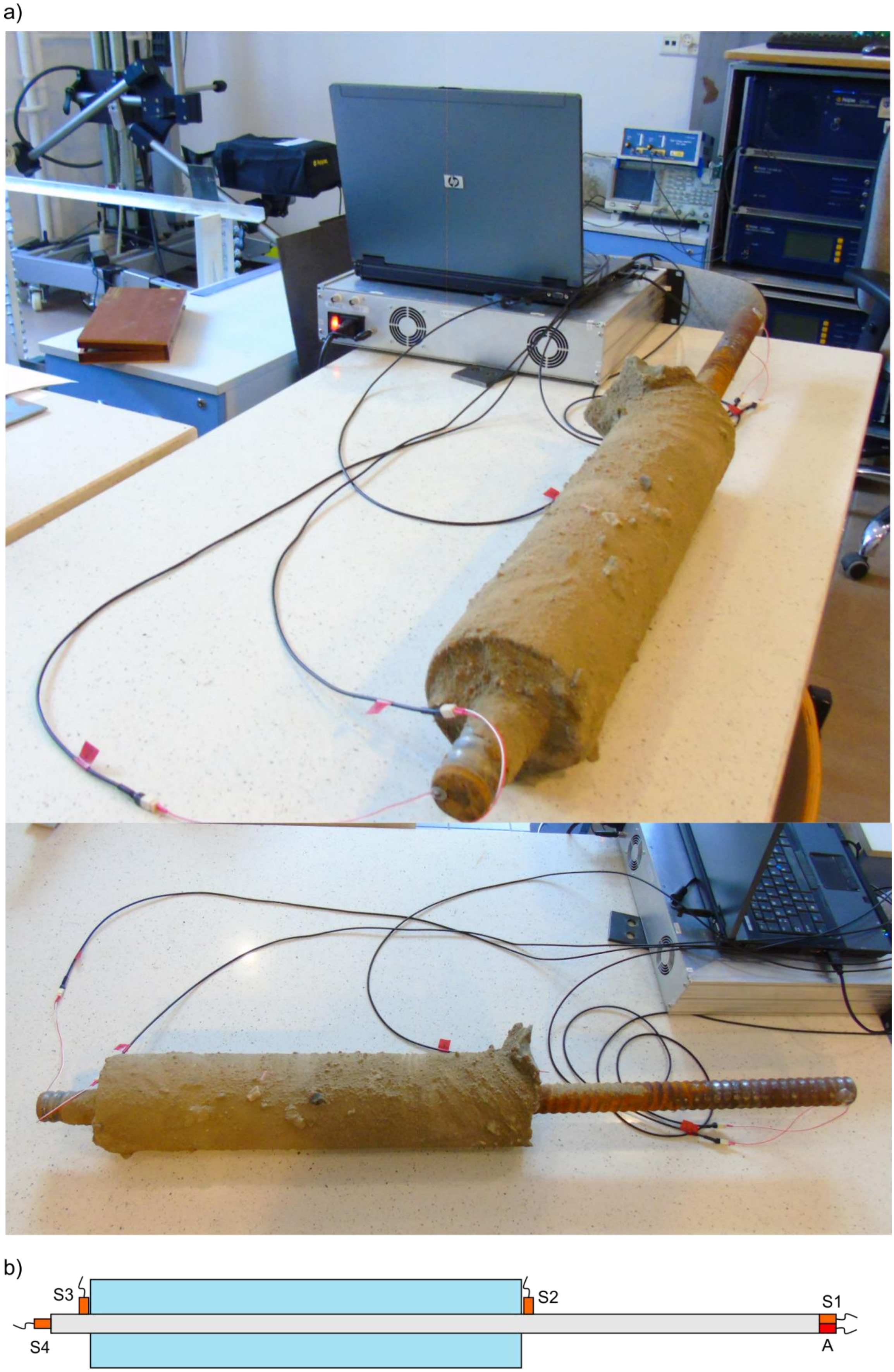

Figure 7.23 a) laboratory tests of excavated ground anchor, b) sensors location

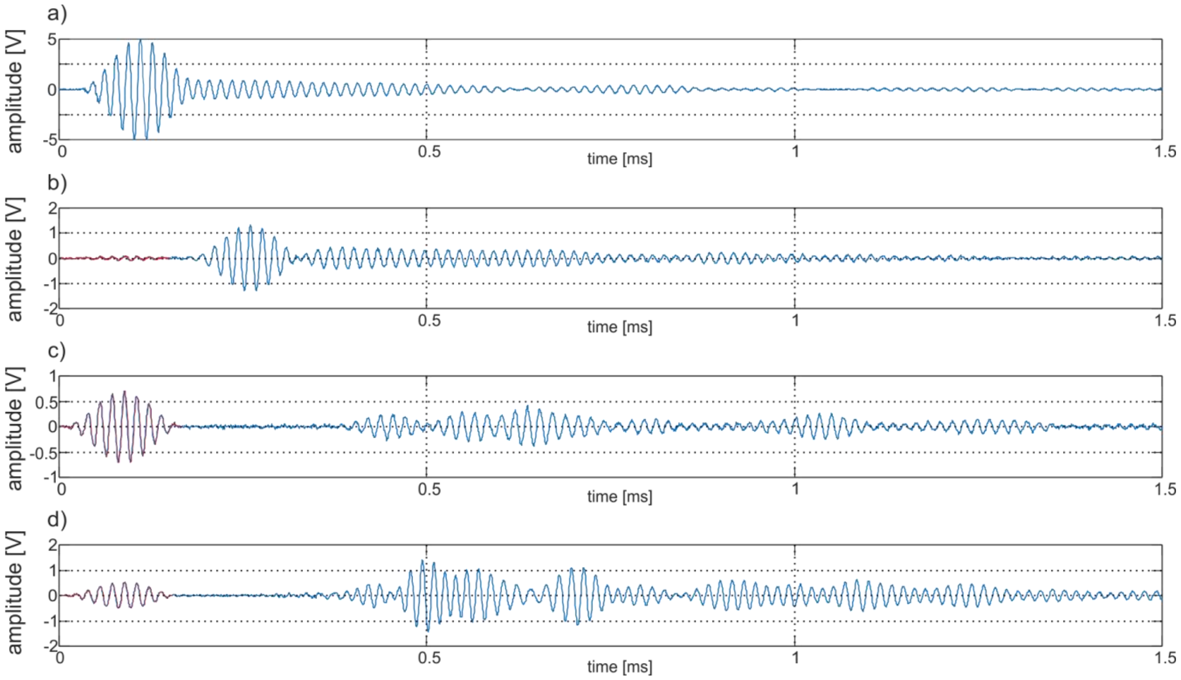

Figure 7.24 Signals registered for excavated anchor and carrier frequency of 60 kHz by sensor: a) S1, b) S2, c) S3 and d) signal S4.

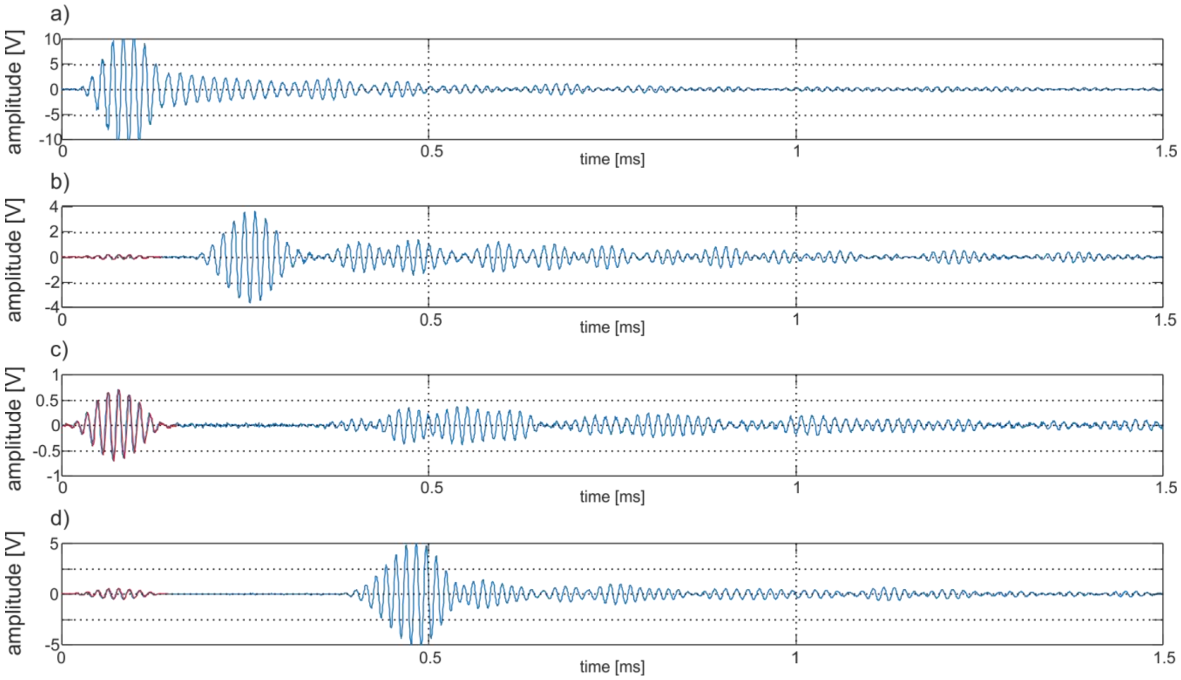

Figure 7.25 Signals registered for excavated anchor and carrier frequency of 70 kHz by sensor: a) S1, b) S2, c) S3 and d) signal S4.

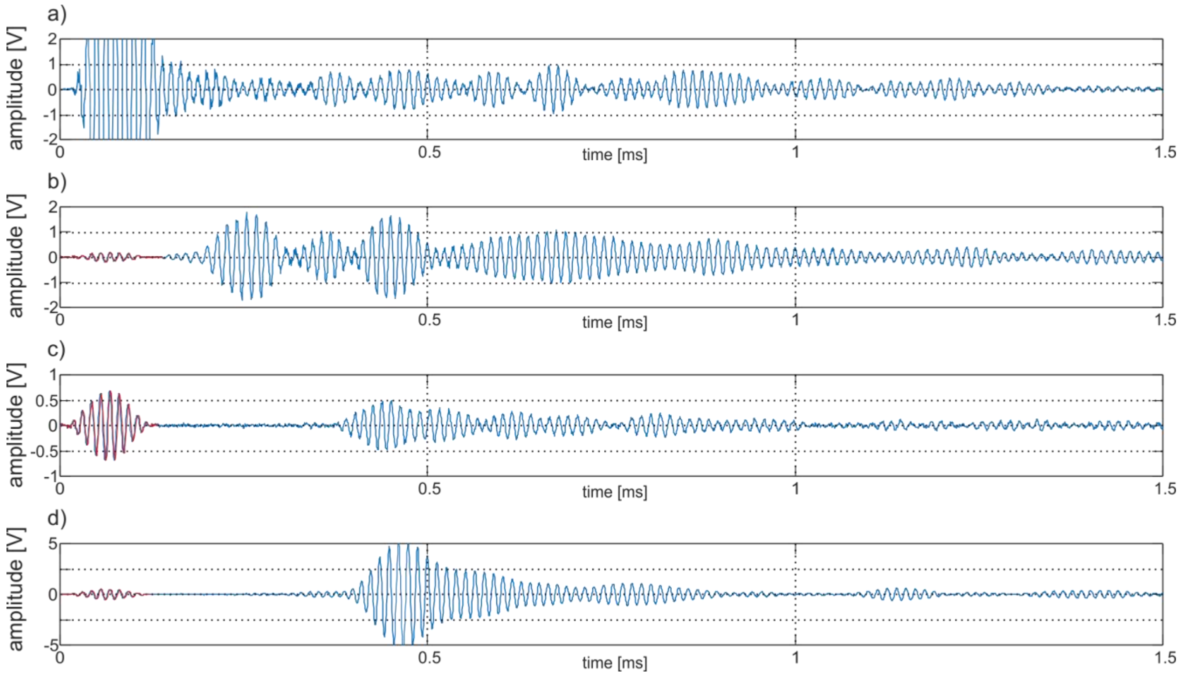

Figure 7.26 Signals registered for excavated anchor and carrier frequency of 80 kHz by sensor: a) S1, b) S2, c) S3 and d) signal S4.

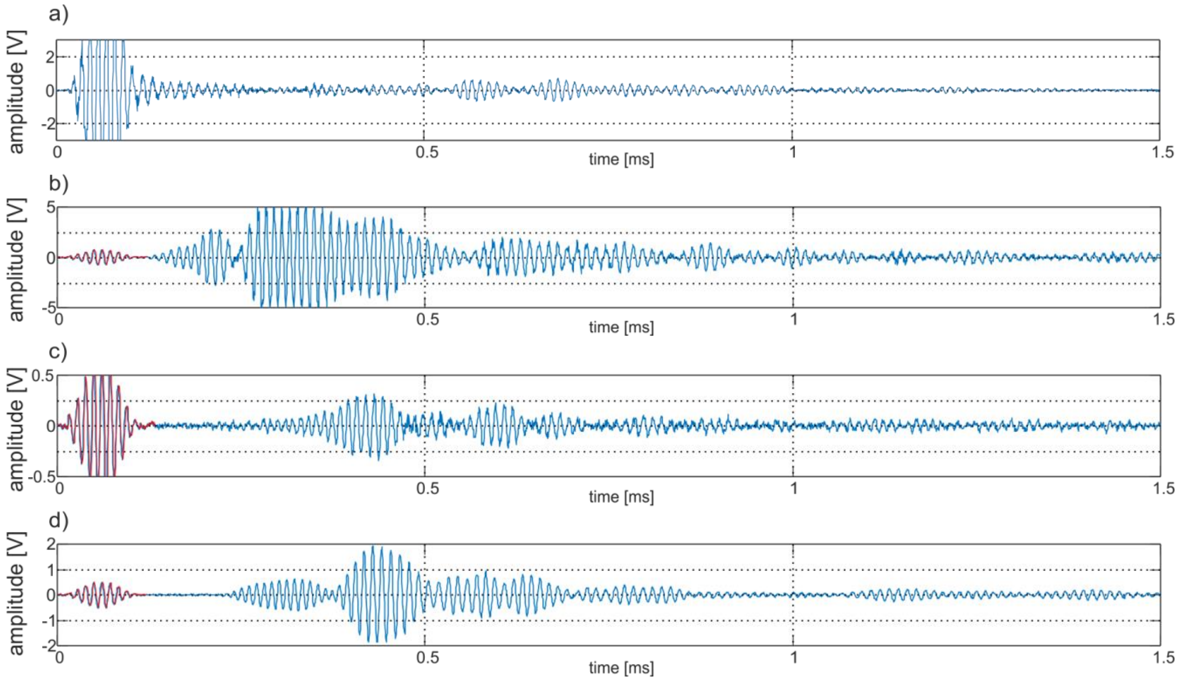

Figure 7.27 Signals registered for excavated anchor and carrier frequency of 90 kHz by sensor: a) S1, b) S2, c) S3 and d) signal S4.

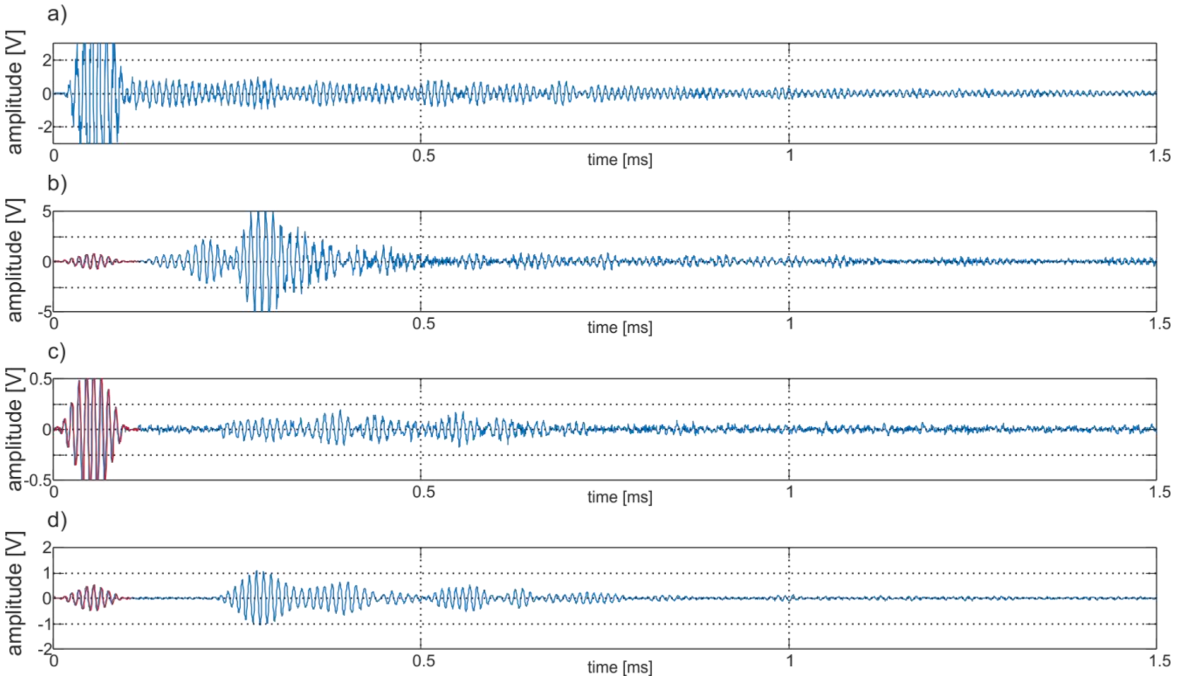

Figure 7.28 Signals registered for excavated anchor and carrier frequency of 100 kHz by sensor: a) S1, b) S2, c) S3 and d) signal S4.

These additional wave packets caused by avalanche breakdown were marked in the figures in red and they should be omitted in the signal analysis process. Despite using various, more or less sensitive frequencies, any signal does not contain clear reflection from the anchorage. Moreover, it is also hard to identify the reflection from the end of a specimen. Each signal registered at the free end of the anchor (Figure 7.24a-Figure 7.28a) contains additional wave packets which make the signal illegible unable to identify reflections important from the diagnostic point of view. In addition, signals registered by sensor S3 (at the end of the anchor body - Figure 7.23b), which measured perpendicular vibrations detect relatively small amplitudes. It is worth mentioning that even signals registered by sensor S4, located further from the actuator are characterized by a higher amplitude because propagating disturbance is dominated by longitudinal displacement.

Despite difficult interpretation, the results allow to draw important conclusions. The investigated drill hollow bar, commonly used as a component of real ground anchors is characterized by a spiral shape and non-uniform cross-section. As mentioned in paragraph 7.2.3 the presence of crests and troughs imply wave diffractions not observable while the anchor tendon is made of a smooth steel bar. Additional wave packets visible in signals, possibly caused by wave diffraction, make it impossible to indicate probably low-amplitude reflections from the anchorage and from the end of a specimen. Moreover, as a consequence of additional diffractions the wave damped faster than in the anchors analysed experimentally during the previous investigations (e.g. presented in Chapters 5 and 6). For some frequencies (90 and 100 kHz) the signal registered by sensor S3 is characterized by an amplitude comparable to a noise amplitude (compare Figure 7.27c and Figure 7.28c).

The second factor mentioned before, (paragraph 7.2.3) acting on signals is actuator location. In the previous cases of prismatic rods with smooth surfaces it was possible to locate it centrally. The hole in a drill bar forced the actuator attachment in the middle of rod wall. After the excitation a wave travels along the and also around bar circumference. The off-center actuator location excludes the possibility of inducing longitudinal modes only.

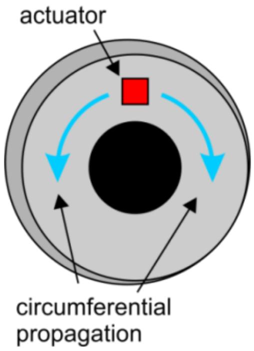

Figure 7.29 Circumferential propagation

The results presented in Figures 7.24 to 7.28 suggest that the application of guided waves in ground anchors diagnostics would be difficult, thus the proposed methods require a significant improvement. The wave in a real ground anchor is damped much faster than in the case of anchor models with simpler geometry considered in the previous Chapters, thus in order to inspect significant longer specimens or with complex geometry, a high-energy excitation must be applied.

At the second step the signals registered at the free end of the excavated anchor were compared with the results registered for an anchor in the ground after 24 and 72 hours of a hardening process. The envelopes of particular signals in the analysed frequency range (60-100 kHz) are plotted in Figure 7.30. All the compared signals have similar shapes and amplitudes regardless of carrier frequency. The similarity of the shape and amplitudes of signals collected before and after excavation indicates a negligible influence of surrounding ground on wave propagation. For this reason it is justified to neglect the additional external layer of soil in considerations.

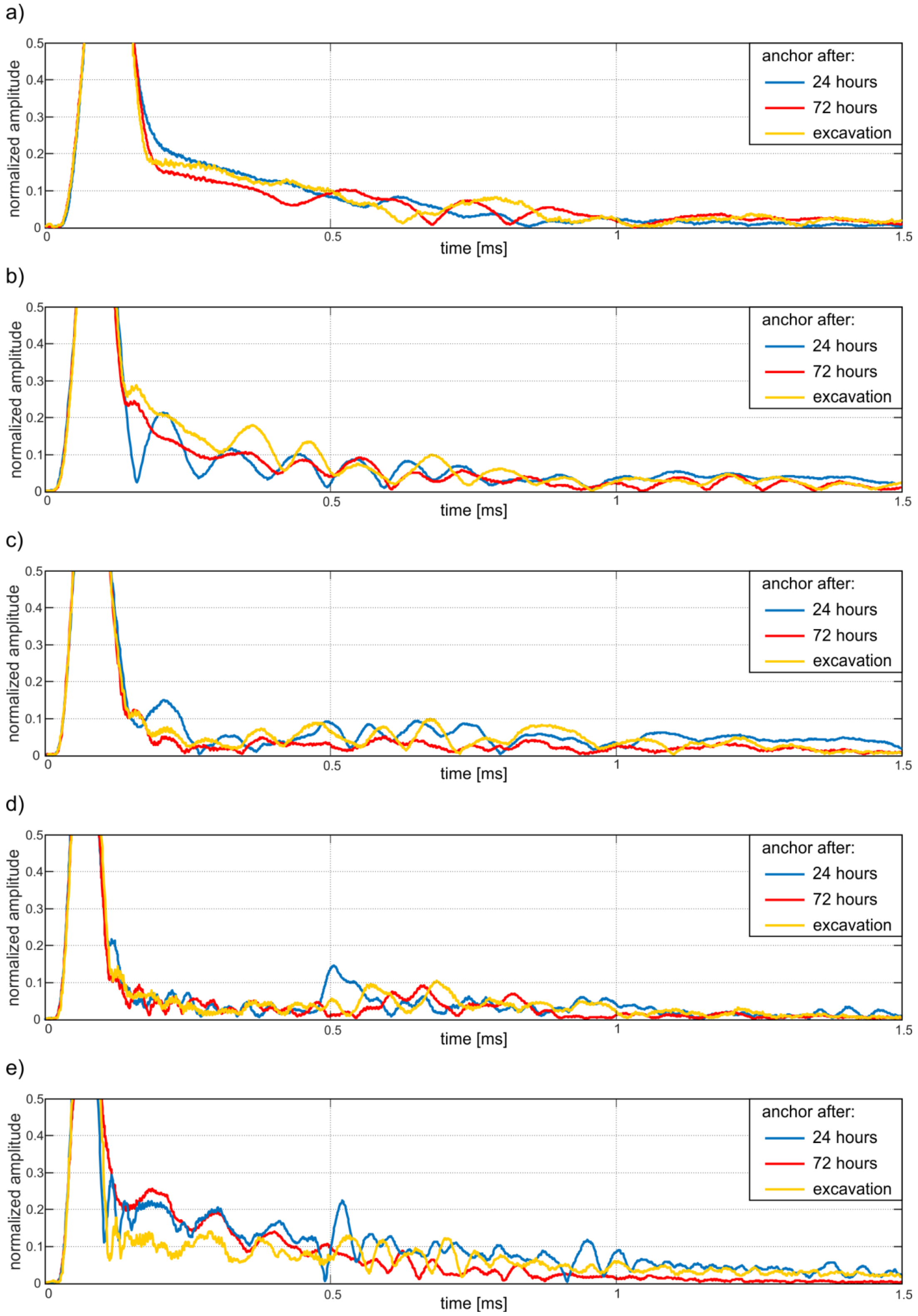

Figure 7.30 Comparison of signals collected for anchor after 24 and 72 hours of hardening process in the ground with signals registered for excavated anchor: a) 60 kHz, b) 70 kHz, c) 80 kHz, d) 90 kHz, e) 100 kHz

Despite the fact that signals collected after excavation do not include reflection from the anchorage and from the end of the anchor, they can be compared with signals registered during the hardening process when reflections from the end of specimen are visible. Signal registered at the beginning of a hardening process (for example for a 0 minute time of a hardening process) can be regarded as reference signals. On the basis of comparative analysis interesting reflections can be just ‘tracked’. This approach facilitates the interpretation of signals, however, its main drawback is the need for reference tests.

The lack of reflection from the anchorage indicates poor quality of bonding connection between steel and grout. If the hardening process proceeded correctly and the quality of anchorage is sufficient, the reflection from the anchorage should be visible in signals collected in Figures 7.13 to 7.17. In the process course, the amplitude value should increase. Meanwhile, this reflection was not registered during the hardening process, after 24 hours, 72 hours and even after anchor excavation. Lack of reflection from anchorage, which in previous cases was usually very easy to indicate and was considered crucial in determining geometric parameters, forced the need to verify the anchor workmanship quality. For this purpose, the anchor body was destroyed and the anchorage quality has been assessed. The photo of destroyed specimen is given in Figure 7.31. One can see a large-size gap between the bar and the mortar cover. Presence of this defect explains why wave was not diffracted at the anchorage and consequently is not register in signal. Paradoxically, in this case lack of reflection from anchorage does not indicate a limitation of ultrasonic method but confirms the possibility of using waves in assessing the quality of specimen.

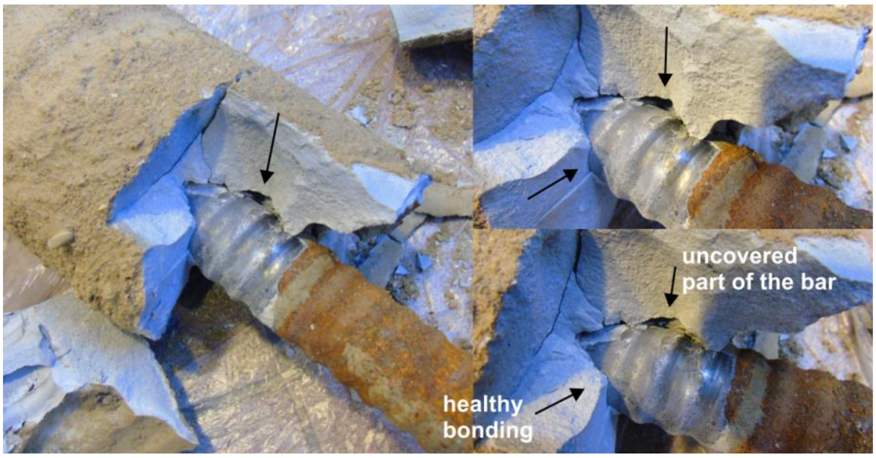

Figure 7.31 Damaged anchor: uncovered part of the bar and healthy connection at the anchorage place

7.4 Summary and conclusions

This Chapter was aimed at possible applications of guided waves in small-scale anchor performed in the ground. The proposed inspection method cannot be considered as complete solution to the ground anchor monitoring problems, however it can provide valuable information on the condition of an investigated object. Nevertheless, the research allowed to reveal disadvantages and difficulties associated with the diagnosis of real engineering objects.

The first section presents experimental research of guided wave propagation in the self-drilling hollow bar system. Two types of specimens were investigated. Firstly, longitudinal waves were excited in a single hollow bar and then, in the two-bar system connected by a centre stop coupler. The obtained results indicated that there was a discrepancy between the experimentally determined group velocity of the wave propagating in real hollow bar with thread and the group velocity determined based on dispersion curves for the pipe with external diameter equal to the nominal thread diameter. Therefore, such dispersion curves can be considered only as approximate solution in the assessment of wave velocity in thread bars.

The comparison of wave propagation signals and the time-of-flights of particular reflections in both specimens brought a conclusion that the mounting connection between the bars did not influence the wave propagation velocity. However, the connection highly affected the character of the signals. Signals registered at both ends of a single bar appeared easy to interpret. Particular reflections showed relatively high amplitudes and they could be clearly indicated. In contrast, signals registered at the coupler and at the end of the coupled bar system were characterized by numerous low-amplitude packets with comparable amplitudes.

The most important conclusion concerns the wave attenuation caused by the discontinuity in the form of the mounting connection. The signal registered at the end of the bar system showed an amplitude over 50 times lower than the signal registered near the actuator. Despite the fact that bars were highly tightened showing no gap between, the wave was strongly attenuated while passing through the connection of two bars. The comparison of two signals registered by a sensor attached at the beginning of the bar for the single bar and the system of coupled bars confirmed that a large majority of the wave energy was reflected from the end of the first bar and it was not transferred from the coupler connection.

The presented results indicated that strong wave dissipation at the bar connection has to be taken into account in the design of structural health monitoring systems dedicated for real geotechnical facilities, like ground anchors or soil nails, constructed with the use of the self-drilling hollow bar systems.

The second part of the study concerns nondestructive testing on a small-scale model. Firstly, hardening process of the underground specimen has been performed. It can be concluded that choosing a right frequency allows to effectively observe the hardening process of the outer cover. The decrease of reflection amplitude from the end of the anchor indicates intensified wave energy leakage into outer grout cover, its impedance value approaches to impedance of steel bar. Ultrasonic testing repeated after excavation of the anchor and comparison of signals registered for underground and excavated anchor showed negligible influence of surrounding ground medium on wave propagation.

Page intentionally left blank

CHAPTER 8

Conclusions and future plans

8.1 General conclusions

The presented thesis is focused on the guided wave propagation method and its application in nondestructive diagnostics of embedded circular waveguides. Significant part of the work is focused on theoretical description and recognition of the phenomenon - a crucial aspect in proper and effective implementation of the guided wave propagation method.

The first part of the study concerns wave propagation in free and multilayered rodlike structures. Several theories for rods with circular cross-sections were described and the relevant dispersion equations have been derived. Solutions of particular dispersion equations have been presented in the form of dispersion curves. The engineering applications, usually dealing with rods of significant diameters direct the exact analytical Pochhammer equation as the only tool to obtain the number and velocity of possible wave modes.

The essential part of the work concerns wave propagation in laboratory models of healthy and damaged ground anchors. Special emphasis was placed on a detailed description and explanation of wave propagation phenomena in ground anchors.

The analysis of wave propagation in undamaged anchors allows to describe methods to determine major geometrical parameters of the ground anchor: free length, bonding length and diameter of the anchor body. Despite the fact that results given in the Chapter 4 proved that guided waves can be effective tool in in the assessment of object geometry, it turned out that there are some important limitations of the used ultrasonic method.

One of the major obstacles concerns determining the diameter of the anchor body. The presented results indicate that determination of the anchor body size is not possible in every case. First of all, for relatively small diameters the wave diffracted at the anchorage and the wave reflected from the outer surface of the anchor body interfere with each other, significantly hindering the signal interpretation and extracting a desired information. Moreover, interference of these reflections also leads to distortion of the calculated free length. One can conclude that interference of relatively wide wave packets can be eliminated by a shift to higher frequencies. However, high excitation frequencies are inevitably associated with a larger number of wave modes. The second limitation of the diameter determination method based on Rayleigh wave velocity is the assumption that the diameter does not vary in thickness through its length. For this reason it is only possible to determine the diameter in the beginning of the anchor body located near the anchorage.

The influence of debonding length and its position along the anchor body was considered in further part of the thesis. It was proved that the debonding length can be assessed on the basis of the average wave velocity of the reflections from the specimen end, however, dispersion curves for the free core and for separate cladding must be prior known. Moreover, the effectiveness of the assessment of the debonding length is determined by selection of an appropriate excitation frequency. The change of average wave velocity which can be considered as indicator parameter in debonding length assessment is affected by the difference between the fastest mode propagating in the free bar and the fastest mode in the coated bar. The conducted research also indicated that waves are sensitive to even the smallest extend of damage. The debonding thickness modelled experimentally, equal approximately 60 micrometers was successfully detected by a proposed technique. Destructive tests confirmed that wave propagation makes it possible to detect anchor damage much faster before it is completely destroyed.

Other analysed damage types and their influence on wave propagation were point and surface damage in the form of uniform corrosion damage of steel part of the anchor. The results for partially embedded and free bars were presented in the form of time-domain propagation signals registered by piezo transducers as well as spectrograms performed using Short Time Fourier Transform for signals registered by pulser-receiver. Two different approaches of wave excitation and signal processing allow to assess advantages and drawbacks of various result presentation forms. However, it has been clearly demonstrated that both damage types can be detected by guided waves. Experimental time-frequency representations performed for a healthy bar and a bar with point damage with the use of Short Time Fourier Transform agreed well with analytical time-frequency representations. In the case of uniform corrosion damage, the STFT spectrograms allowed to determine the level of state deterioration.

The last investigation stage concerned wave propagation in self-drilling hollow bars commonly used in real engineering ground anchors or soil nails. The extension of the investigations conducted on idealized, laboratory models of ground anchors into the ground anchor system brought some additional difficulties. Firstly, a single bar R38-550 and a self-drilling system containing two bars of equal lengths connected by the centre stop coupler have been tested. The most important conclusion formulated on the basis of conducted research concerns the wave attenuation caused by discontinuity the mounting connection form. The wave was strongly attenuated while passing throughout the connection of two bars despite the fact that bars were highly tightened, detecting no gap in between. This observation led to the conclusion that the wave registration in the case of nondestructive tests of real objects, which is usually of significantly larger length may be significantly impeded. Moreover, the registration of reflections important from the point of view of diagnostics was hindered not only because of discontinuities in the form of mounting connections, but also due to more intense wave energy damping due to spiral shape of a bar cross-section. Crests and troughs may imply wave diffraction which led to registering additional wave packets in signals. As a consequence, the wave in a spiral hollow rod was damped faster, thus the signal was more difficult to interpret. For this reason, prior to applying the guided wave propagation method in situ in diagnostics of real engineering objects some technical difficulties need to be resolved related with short-range of wave energy generated by piezoelectric transducers.

Drill hollow bars were also used to perform in the ground small scale models of anchors. Monitoring of the hardening process was carried out. The decrease of amplitude of reflection from the end of the anchor indicated that wave energy leakage into outer grout cover became more intense due to increasing similarities between the acoustic impedances. The wave propagation method seems to be an effective tool to monitor the process of injecting and hardening of the outer cover. After one month laboratory tests were performed on an excavated anchor. The comparison of signals registered for underground and excavated anchors showed negligible influence of surrounding ground on wave propagation and justified skipping additional external layer in the previous considerations.

8.2 Future plans

Despite the fact that in many analyzed cases guided waves proved to be an effective tool in potential diagnostics of ground anchors, the major disadvantages of the proposed method have also been exposed at work.

First of all, the tested anchor model was significantly simpler than the real one. The model did not include selected elements, which are integral parts of anchoring systems. The Figure 8.1 presents real ground anchor head. Except the end of the anchor drill bar one can see the steel nut and plate locking the anchor in the embankment wall after compressing. Preliminary studies indicated that due to contact stress between steel plate and nut the wave excited in the steel rod is also transmitted into the steel bearing plate. A small size of bearing plate triggers multiple reflections from its edges visible in signal registered at the free end of the bar. As a consequence, the signal is illegible and difficult to interpret. Moreover, the majority of energy is transmitted into the bearing plate and only a small energy amount travels along the hollow bar. For this reason, there is a need to include additional hindering factors, e.g. the presence of additional elements in further studies.

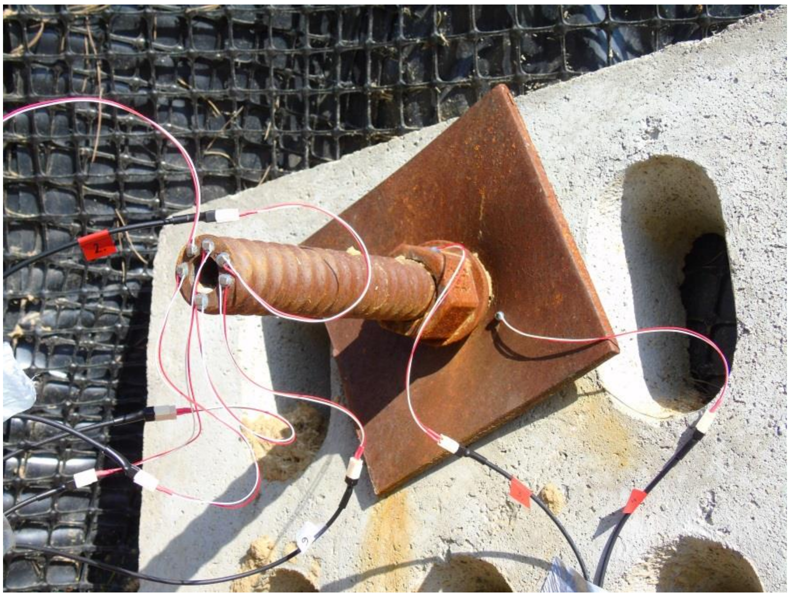

Figure 8.1 Anchor head

Acknowledgments

I would like to thank my supervisor Prof. Magdalena Rucka for guidance in this thesis process. My thanks extend to my friends, Rafał and Jacek, for their extraordinary support during last years. I would also like to thank Marek Skowronek for invaluable help in preparing this work. Due to my deepest belief everything we plan for the other people to give is bound for us to take it back ☺

The research work was partially supported by the project No. 2015/19/B/ST8/00779, financed by the National Science Centre, Poland and Young Scientist grants (editions 2014/2015 and 2015/2016) obtained from the Faculty of Civil and Environmental Engineering at Gdańsk University of Technology. Abaqus computations were carried out at the Academic Computer Centre in Gdańsk.

Page intentionally left blank

References

[1] Abaqus Analysis User's Guide (6.12), www.simulia.com.
[2] Achenbach J.D. Torsional oscillations of an encased hollow cylinder of finite length, Journal of Spacecraft and Rockets 3(11), 1637–1643, 1966.
[3] Achenbach J.D. Wave Propagation in Elastic Solids. North–Holland Publishing Company, 1975.
[4] Adem J. On axially–symmetric steady wave propagation in elastic circular rods, Quarterly of Applied Mathematics 12(3), 261–275, 1954.
[5] Akbarov S.D., Guliev M.S. The influence of the finite initial strains on the axisymmetric wave dispersion in a circular cylinder embedded in a compressible elastic medium, International Journal of Mechanical Sciences, 52(1), 89–95, 2010.
[6] Akisanya A.R., Ivanović A. Debonding along the fixed anchor length of a ground anchorage, Engineering Structures, 74, 23–31, 2014.
[7] Alani A.M., Aboutalebi M., Kilic G. Applications of ground penetrating radar (GPR) in bridge deck monitoring and assessment, Journal of Applied Geophysics, 97, 45–54, 2013.
[8] Alleyne D.N. The non–destructive testing of plates using ultrasonic Lamb waves, PhD thesis, Imperial College of Science Technology and Medicine, London, 1991.
[9] Alleyne D.N., Cawley P. The interaction of lamb waves with defects, IEEE Transactions on Ultrasonics, Ferroelectrics and Frequency Control, 39(3), 381–397, 1992.
[10] Alleyne D.N., Cawley P. The effect of discontinuities of the long–range propagation of Lamb waves in pipes, Proceedings of the Institution of Mechanical Engineers, Part E: Journal of Process Mechanical Engineering, 210(3), 217–226, 1996.
[11] Ambroziński Ł., Stępiński T., Paćko P., Uhl T. Self–focusing Lamb waves based on the decomposition of the time–reversal operator using time–frequency representation, mechanical Systems and Signal Processing, 27, 337–349, 2012.
[12] Amerini F., Meo M. Structural health monitoring of bolted joints using linear and nonlinear acoustic/ultrasound methods. Structural Health Monitoring – An International Journal, 10(6), 659–672, 2011.
[13] Anderson S.P. Higher–order rod approximations for the propagation of longitudinal stress waves in elastic bars, Journal of Sound and Vibration, 290(1–2), 290–308, 2006.
[14] Armenàkas A.E. Propagation of harmonic waves in composite circular–cylindrical shells. I: Theoretical investigation, AIAA Journal, 5(4), 740–744, 1967.
[15] Armenàkas A.E. Propagation of harmonic waves in composite circular–cylindrical rods, The Journal of the Acoustical Society of America, 47, 822–837, 1970.
[16] Auld B.A. Acoustic Fields and Waves in Solids 1990, Krieger.
[17] Baltrukonis J.H., Chi M., Gottenberg W.G. Free transverse vibrations in an infinitely–long, layered elastic cylinder, The Catholic University of America, Washington, D.C, Technical Report no. 3 to NASA, 1962.
[18] Baltrukonis J.H., Gottenberg W.G., Schreiner R.N. Axial–shear vibrations of an infinitely–long composite circular cylinder, The Journal of Acoustical Society of America, 33(11), 1447–1457, 1961.
[19] Bancroft D. The velocity of longitudinal waves in cylindrical bars, Physical Review, 59(7), 588–593, 1941.
[20] Barshinger J.N., Rose J.L. Guided wave propagation in an elastic hollow cylinder coated with a viscoelastic material, IEEE Transactions on Ultrasonics, Ferroelectrics and Frequency Control, 51(11) 1547–1556, 2004.
[21] Bathe K.J. Finite element procedures in engineering analysis, Prentice–Hall, Inc., Englewood Cliffs, New Jersey, 1982.
[22] Beard M.D. Guided wave inspection of embedded cylindrical structures. Ph.D. Thesis, Department of Mechanical Engineering, Imperial Collage, London, 2002.
[23] Beard M.D., Lowe M.J.S., Cawley P. Ultrasonic Guided Waves for Inspection of Grouted Tendons and Bolts, Journal of Materials in Civil Engineering, 15(3), 212–218, 2003.
[24] Beard M.D, Lowe M.J.S. Non–destructive testing of rock bolts using guided ultrasonic waves, International Journal of Rock Mechanics and Mining Sciences, 40(4), 527–536, 2003.
[25] Belytschko T., Hughes T.J.R. (eds) Computational methods for transient analysis. Vol 1 in computational methods in mechanics, North–Holland Publishing, Amsterdam–New York, 1983.
[26] Benmokrane B., Chekired M., Xu H. Monitoring behavior of grouted anchors using vibrating–wire gauges, Journal of Geotechnical Engineering 121(6), 466–475, 1995.
[27] Bird J.F., Hart R.W., McClure F.T. Vibrations of thick–walled hollow cylinders: exact numerical solutions, The Journal of Acoustical Society of America, 32(11), 1404–1412, 1960.

[28] Bird J.F. Vibrations of thick–walled hollow cylinders: approximate theory, The Journal of Acoustical Society of America, 32(11), 1413–1419, 1960.

[29] Bishop R.E.D. Longitudinal waves in beams, The Aeronautical Journal, 3(4), 280–293, 1952.

[30] Boller C., Chang F–K., Fijino Y. Encyclopedia of Structural Health Monitoring. John Wiley & Sons, Ltd., 2009.

[31] Chaki S., Bourse G. Guided ultrasonic waves for non–destructive monitoring of the stress levels in prestressed steel strands, Ultrasonics, 49(2), 162–171, 2009.

[32] Cheung Y.K. Finite Strip Elements in Structural Analysis. Pergamon Press, Oxford, 1976.

[33] Cho Y., Rose J.L. A boundary element solution for a mode conversion study on the edge reflection of Lamb waves, The Journal of Acoustical Society of America, 99(4), 2097–2109, 1996.

[34] Chree C. Longitudinal vibrations of a circular bar, The quarterly journal of pure and applied mathematics, 21, 287–288, 1886.

[35] Chree C. The equations of an isotropic elastic solid in polar and cylindrical coordinates, their solutions and applications, Transactions of the Cambridge Philosophical Society, 14, 250–369, 1889.

[36] Chróścielewski J. Rucka M., Wilde K., Witkowski W. Formulation of spectral truss element for guided waves damage detection in spatial steel trusses, Archives of Civil Engineering, 55(1), 43–63, 2009.

[37] Cohen L. Time Frequency Analysis. Prentice–Hall, 1995.

[38] Courant R., Friedrichs K., Lewy H. Über die partiellen Differenzengleichungen der mathematischen Physik, Mathematische Annalen, 100(1), 32–74, 1928.

[39] Cui Y, Zou D.H, Numerical simulation of attenuation and group velocity of guided ultrasonic wave in grouted rock bolts, Journal of Applied Geophysics, 59(4), 337–344, 2006.

[40] Cui Y, Zou D.H. Assessing the effect of insufficient rebar and missing grout in grouted rock bolts using guided ultrasonic waves, Journal of Applied Geophysics, 79, 64–70, 2012.

[41] Czarnecki L., Garbacz A., Krystosiak M. On the ultrasonic assessment of adhesion between polymer coating and concrete substrate, Cement and Concrete Composites, 28(4), 360–369, 2006.

[42] Dalton R.P., Cawley P., Lowe M.J.S. The potential of guided waves for monitoring large areas of metallic aircraft structures, Journal of Nondestructive Evaluation, 20(1), 29–46, 2001.

[43] Datta S.K., Shah A.H., Bratton R.L, Chakraborty T. Wave propagation in laminated composite plates, The Journal of Acoustical Society of America, 83(6), 2020–2026, 1988.

[44] Davies R.M. A critical study of the Hopkinson pressure bar, Philosophical Transactions of the Royal Society A, 240(821), 375–457, 1948.

[45] Degala S., Rizzo P., Ramanathan K., Harries K.A. Acoustic emission monitoring of CFRP reinforced concrete slabs, Construction & Building Materials, 23(5), 2016–2026, 2009.

[46] Delsanto P.P., Whitcombe T., Chaskelis H.H., Mignogna R.B. Connection machine simulation of ultrasonic wave propagation in materials I: one–dimensional case, Wave Motion, 16(1), 65–80, 1992.

[47] Delsanto P.P., Schechter R.S., Chaskelis H.H., Mignogna R.B., Klein R. Connection machine simulation of ultrasonic wave propagation in materials II: two–dimensional case, Wave Motion, 20(4), 295–314, 1994.

[48] Delsanto P.P., Schechter R.S., Mignogna R.B. Connection machine simulation of ultrasonic wave propagation in materials III: three–dimensional case, Wave Motion, 26(4), 329–339, 1997.

[49] Delsanto P.P., Chaskelis H.H., Whitcombe T., Mignogna R.B., Klein R. Connection machine simulation of boundary effects in ultrasonic NDE, Nondestructive Characterization of Materials IV, Plenum Press, 1991.

[50] Delsanto P.P., Scalerandi M. A spring model for the simulation of the propagation of the ultrasonic pulses through imperfect contact interfaces, The Journal of Acoustical Society of America, 104(5), 2584–2591, 1998.

[51] Doyle J.F.: Wave propagation in Structures: An FFT–Based Spectral Analysis Methodology, New York, Springer–Verlag, 1989.

[52] Doyle J.F.: Wave propagation in Structures: Spectral Analysis Using Fast Discrete Fourier Transforms, New York, Springer–Verlag, 1997.

[53] Drecher–Krasicka E., Simmons J.A. Leaky axisymmetric modes in infinite clad rods. I, The Journal of the Acoustical Society of America, 92(2), 1061–1090, 1992.

[54] Drecher–Krasicka E., Simmons J.A. Leaky axisymmetric modes in infinite clad rods. II, The Journal of the Acoustical Society of America, 92(2), 1091–1105, 1992.

[55] Drobiec Ł., Jasiński R., Piekarczyk A. Diagnostyka konstrukcji żelbetowych, badania laboratoryjne betonu i stali, Wydawnictwo Naukowe PWN, 2010.

[56] Drozdz M.B. Efficient finite element modelling of ultrasound waves in elastic media, PhD Thesis, Imperial College of Science Technology and Medicine, University of London, 2008.

[57] Dunkin J.W. Computation of modal solutions in layered elastic media at high frequencies, Bulletin of Seismological Society of America, 55(2), 335–358, 1965.

[58] Dziendzikowski M., Dragan K., Katunin A. Localizing impact damage of composite structures with modified RAPID algorithm and non–circular PZT arrays, Archives of Civil and Mechanical Engineering, 17, 178–187, 2017.
[59] Epp T., Cha Y–J. Air–coupled impact–echo damage detection in reinforced concrete using wavelet transforms, Smart Materials and Structures, 26(2), 15 pages, 2017.
[60] Ervin B.L., Reis H. Longitudinal guided waves for monitoring corrosion in reinforced mortar, Measurement Science and Technology, 19(5), 1–19, 2008.
[61] Ervin B.L., Kuchma D.A., Bernhard J.T., Reis H. Monitoring corrosion of rebar embedded in mortar using high–frequency guided ultrasonic waves, Journal of Engineering Mechanics 135(1), 9–19, 2009.
[62] Farhidzadeh A., Salamone S. Reference–free corrosion damage diagnosis in steel strands using guided ultrasonic waves, Ultrasonics, 57, 198–208, 2015.
[63] Firestone F.A., Ling D.S Jr. Method and means for generating and utilizing vibrational waves in plates, US Patent 2,536,126, 1951.
[64] Fritzen C.–P., Kraemer P., Buethe I. Vibration–based damage detection under changing environmental and operational conditions, Advances in Science and Technology, 83, 95–104, 2013.
[65] Gamboa E, Atrens A. Environmental influence on the stress corrosion cracking of rock bolts, Engineering Failure Analysis, 10(5), 521–558, 2003.
[66] Garbacz A., Piotrowski T., Courard L., Kwaśniewski L. On the evaluation of interface quality in concreto repair system by means of impact–echo signal analysis, Construction and Building Materials, 134, 311–323, 2017.
[67] Gazis D.C. Three dimensional investigation of the propagation of waves in hollow circular cylinders. I. Analytical foundation, The Journal of the Acoustical Society of America, 31(5), 568–573, 1959.
[68] Gazis D.C. Three dimensional investigation of the propagation of waves in hollow circular cylinders. II. Numerical results, Journal of the Acoustical Society of America, 31(5), 573–578, 1959.
[69] Giurgiutiu V. Structural Health Monitoring of Aerospace Composites, Academic Press, 2005.
[70] Giurgiutiu V., Yu L., Kendall J.R., Jenkins C. In situ imaging of crack growth with piezoelectric–wafer active sensors, AIAA Journal, 45(11), 2758–2769, 2007.
[71] Giurgiutiu V. Structural Health Monitoring with Piezoelectric Wafer Active Sensors, Academic Press, 2008.
[72] Gosh J. Longitudinal vibrations of a hollow cylinder, Bulletin of the Calcutta Mathematical Society, 14(1), 31–40, 1923.
[73] Goszczyńska B., Świt G., Trąmpczyński W., Krampikowska A., Tworzewska J., Tworzewski P. Experimental validation of concrete crack identification and location with acoustic emission method, Archives of Civil and Mechanical Engineering, 12(1), 23–28, 2012.
[74] Goszczyńska B., Świt G., Trąmpczyński W. Analysis of the microcracking process with the Acoustic Emission method with respect to the service life of reinforced concrete structures with the example of the RC beams, Bulletin of the Polish Academy of Sciences Technical Sciences, 63(1), 2015.
[75] Graff K. F. Wave Motion in Elastic Solids, Oxford, Clarendon Press, 1975.
[76] Green W.A. Dispersion relations for elastic waves in bars, Progress in Solid Mechanics, Vol. I Edited by I.N. Sneddon dn R. Hill, Chapter 5, North Holland Publishing Co., Amsterdam.
[77] Greenspon J.E. Flexural vibrations of a thick–walled circular cylinder according to the exact theory of elasticity, Journal of Aerospace Sciences, 27(1), 37–40, 1960.
[78] Greenspon J.E. Vibrations of thick cylindrical shells, The Journal of Acoustical Society of America, 32(5), 612–613, 1960.
[79] Greenspon J.E. Vibrations of a thick–walled cylindrical shell – comparison of the exact theory with approximate theories, The Journal of Acoustical Society of America, 32(5), 571–578, 1960.
[80] Habib P. An Outline of Soil and Rock Mechanics, Cambridge University Press, 1983.
[81] Han S.–I., Lee I.–M., Lee Y.–J., Lee J.–S. Evaluation of rock bolt integrity using guided ultrasonic waves, Geotechnical Testing Journal, 32(1), 31–38, 2009.
[82] Haskell N.A. Dispersion of surface waves on multi–layered media, Bulletin of Seismological Society of America, 43(1), 17–34, 1953.
[83] Henneke E.G., Reifsnider K.L. Stinchcomb W.W. Thermography – NDI method for damage detection, Journal of Metals, 31(9), 11–15, 1979.
[84] Herrmann G. Forced motions of elastic rods, Journal of Applied Mechanics, 21, 221–224, 1954.
[85] Herrmann G., Mirsky I. Three–dimensional and shell–theory analysis of axially symmetric motions of cylinders, Journal of Applied Mechanics, 23(4), 563–568, 1956.
[86] Hobst L, Zajíc J. Anchoring in Rock and Soil. Elsevier Science Publishing Company; 1983.
[87] Holden A.N. Longitudinal modes of elastic waves in isotropic cylinders and slabs, Bell Labs Technical Journal, 30(4), 956–969, 1951.

[88] Hoła J., Schabowicz K. State–of–the–art non–destructive methods for diagnostic testing of building structures – anticipated development trends, Archives of Civil and Mechanical Engineering, 10(3), 5–18, 2010.

[89] Hoła J., Sadowski Ł., Schabowicz K. Nondestructive identification of delaminations in concrete floor toppings with acoustic methods, Automation in Construction, 20(7), 799–807, 2011.

[90] Hou J., Jankowski Ł., Ou J. An online substructure identification method for local structural health monitoring, Smart Materials and Structures, 22(9), 20 pages, 2013.

[91] Hua J., Rose J.L. Guided wave inspection penetration power in viscoelastic coated pipes, Insight – Non–Destructive Testing and Condition Monitoring, 52(4), 195–205, 2010.

[92] Hudson G.E. Dispersion of elastic waves in solid circular cylinders, Physical Review, 63(1–2), 46–51, 1943

[93] Ihn J–B., Chang F–K. Detection and monitoring of hidden fatigue crack growth using a built–in piezoelectric sensor/actuator network: I. Diagnostics, Smart Materials and Structures, 13(3), 609–620, 2004.

[94] Ihn J–B., Chang F–K. Pitch catch active sensing methods in structural health monitoring for aircraft structures, Structural Health Monitoring, An International Journal, 7(1), 5–19, 2008.

[95] Ivanović A., Neilson R.D. Modelling of debonding along the fixed anchor length, International Journal of Rock Mechanics and Mining Sciences, 46(4), 699–707, 2009.

[96] Ivanović A, Neilson R.D. Non–destructive testing of rock bolts for estimating total bolt length. International Journal of Rock Mechanics and Mining Sciences, 64, 36–43, 2013.

[97] Jeng C–J., Chen Y–C. Investigation the performance of ground anchors through the failure slope disaster in Taiwan, Seventh International Conference on Case Histories in Geotechnical Engineering, 29 April–4 May, 2013, Chicago.

[98] Jiang S–H, Li D–Q, Zhang L–M, Zhou C–B. Time–dependent system reliability of anchored rock slopes considering rock bolt corrosion effect, Engineering Geology, 175, 1–8, 2014.

[99] Kelkar V.S. Vibrations of a hollow elastic cylinder bonded to a thin casting of a different material, NASA TN D–4221, 1967.

[100] Kędra R., Rucka M. Research on assessment of bolted joint state using elastic wave propagation, Journal of Physics: Conference Series, 628(1), 8 pages, 2015.

[101] Kirby R., Zlatev Z., Munge P. On the scattering of torsional elastic waves from axisymmetric defects in coated pipes, Journal of Sound and Vibration, 331(17), 3989–4004, 2012.

[102] Kausel E. Wave propagation in anisotropic layered media, International Journal for Numerical Methods in Engineering, 23(8), 1567–1578, 1986.

[103] Knopoff L. A matrix method for elastic wave problems, Bulletin of Seisomological Society of America, 54(1), 431–438, 1964.

[104] Kolman R., Cho S.S., Park K.C. Accurate explicit finite element method for wave propagation and dynamic contact problems, 11th World Congress on Computational Mechanics WCCM XI, 5th European Conference on Computational Mechanics ECCM V, 6th European Conference on Computational Fluid Dynamics ECCFD VI, Barcelona, Spain, 20–25 July 2014.

[105] Korzeniowski M., Piwowarczyk T., Maev R.G. Application of ultrasonic method for quality evaluation of adhesive layers, Archives of Civil and Mechanical Engineering, 14(4), 661–670, 2014.

[106] Koshiba M., Karakida S., Suzuki M. Finite element analysis of lamb waves scattering in an elastic waveguide, IEEE Transactions on Sonics and Ultrasonics, 31(1), 18–24, 1984.

[107] Krawczuk M., Grabowska J., Palacz M. Longitudinal wave propagation. Part I – Comparison of rod theories, Journal of Sound and Vibration, 295(3–5), 461–478, 2006.

[108] Kudela P., Krawczuk M., Ostachowicz W. Wave propagation modelling in 1D structures using spectral finite elements, Journal of Sound and Vibration, 300(1–2), 88–100, 2007.

[109] Kudela P., Żak A., Krawczuk M., Ostachowicz W. Modelling of wave propagation in composite plates using the time domain spectral element method, Journal of Sound and Vibration, 302(4–5), 728–745, 2007.

[110] Kudela P., Ostachowicz W., Żak A., Damage detection in composite plates with embedded PZT transducers, Mechanical Systems and Signal Processing, 22(6), 1327–1335, 2008.

[111] Lachowicz J., Rucka M. 3–D finite–difference time–domain modelling of ground penetrating radar for identification of rebars in complex reinforced concrete structures, Archives of Civil and Mechanical Engineering, 2018.

[112] Lai J–L. Propagation of harmonic waves in a composite elastic cylinder, Journal of Acoustical Society of America, 49(1), 220–228, 1971.

[113] Lai W.W.L., Derobert X., Annan P. A review of Ground Penetrating Radar application in civil engineering: A 30–year journey from Locating and Testing to Imaging and Diagnosis, NDT&E International, 2017 (in press).

[114] Lamb H. On waves in an elastic plate, Proceedings of Royal Society A, 93(648), 114–128, 1917.

[115] Lanza di Scalea F., Rizzo P., Seible F. Stress measurement and defect detection in steel strands by guided stress waves, Journal of Materials in Civil Engineering, 15(3), 291–227, 2003.

[116] Lee B.C., Staszewski W.J. Lamb wave propagation modelling for damage detection: I. Two–dimensional analysis, Smart Materials and Structures, 16(2), 249–259, 2007.

[117] Lee B.C., Staszewski W.J. Lamb wave propagation modelling for damage detection: II. Damage monitoring strategy, Smart Materials and Structures, 16(2), 260–274, 2007.

[118] Lee I–M, Han S–I, Kim H–J, Yu J–D, Min B–K., Lee J–S. Evaluation of rock bolt integrity using Fourier and wavelet transforms, Tunnelling and Underground Space Technology, 28, 304–314, 2012.

[119] Lee Y.S., Rose J.L., Cho Y. A guided wave approach to defect detection under shelling in rail, NDT&E International, 42(3), 174–180, 2009.

[120] Lestari W., Qiao P. Application of wave propagation analysis for damage identification in composite laminated beams, Journal of Composite Materials, 39(22), 1967–1984, 2005.

[121] Li D., Zhang S., Yang W., Zhang W. Corrosion Monitoring and Evaluation of Reinforce Concrete Structures Utilizing the Ultrasonic Guided Wave Technique, International Journal of Distributed Sensor Networks, 2014, 1–9, 2014.

[122] Liang M–T., Su P–J. Detection of the corrosion damage of rebar in concrete using impact–echo method, Cement and Concrete Research, 31(10), 1427–1436, 2001.

[123] Liang T., Ren W., Tian G–Y., Elradi M., Gao Y. Low energy impact damage detection in CFRP using eddy current pulsed thermography, Composite Structures, 143, 352–361, 2016.

[124] Liu G.R., Achenbach J.D. Strip element method to analyse wave scattering by cracks in anisotropic laminated plates, Journal of Applied Mechanics, 62(3), 607–613, 1995.

[125] Lord Rayleigh, On waves propagating along the plane surface of an elastic solid, Proceedings of the London Mathematical Society, 17(1), 4–11, 1885.

[126] Lord Rayleigh. Theory of Sound. Dover Publications, New York, 1945.

[127] Love A.E.H. The mathematical Theory of Elasticity, Cambrigde University Press, 1927.

[128] Love A.E.H. Some problems of Geodynamics, London Cambridge University Press, 1911.

[129] Lowe M.J.S. Matrix Techniques for Modeling Ultrasonic Waves in Multilayered Media, IEEE Transactions on Ultrasonics, Ferroelectrics and Frequency Control, 42(4), 525–542, 1995.

[130] Lowe M.J.S. Alleyne D.N., Cawley P. Defect detection in pipes using guided waves, Ultrasonics, 36, 147–154, 1998.

[131] Lu Y., Li J., Ye L., Wang D. Guided waves for damage detection in rebar–reinforced concrete beams, Construction and Building Materials, 47, 370–378, 2013.

[132] Lucena R.L., Dos Santos J.M.C. Structural health monitoring using time reversal and cracked rod spectral element, Mechanical Systems and Signal Processing, 79, 86–98, 2016.

[133] Lyons R.G. Understanding digital signal processing, 3rd edition, Prentice Hall, 2011.

[134] Ma S., Nemcik J., Aziz N. An analytical model of fully grouted rock bolts subjected to tensile load, Construction and Building Materials, 49, 519–526, 2013.

[135] Madenga, V., Zou, D.H., Zhang, C. Effects of curing time and frequency on ultrasonic wave velocity in grouted rock bolts, Journal of Applied Geophysics, 59(1), 79–87, 2006.

[136] Mariani S., Nguyen T., Phillips RR., Kijanka P., Lanza di Scalea F., Staszewski WJ., Fateh M., Carr G. Noncontact ultrasonic guided wave inspection of rails, Structural Health Monitoring, 12(5–6), 539–548, 2013.

[137] Marzani A., Viola E., Bartoli I., Lanza di Scalea F., Rizzo P. A semi–analytical finite element formulation for modeling stress wave propagation in axisymmetric damped waveguides, Journal of Sound and Vibration, 318(3), 488–505, 2008.

[138] Malinowski P., Wandowski T., Ostachowicz W. Damage detection potential of a triangular piezoelectric configuration, Mechanical Systems and Signal Processing 25(7), 2722–2732, 2011.

[139] McFadden J.A. Radial vibrations of thick walled hollow cylinders, The Journal of the Acoustical Society of America, 26(5), 714–715, 1954.

[140] McNiven H.D., McCoy J.J. Vibrations and Wave Propagation in Rods, M.D, Mindlin and Applied Mechanics, Edited by G. Herrmann, Chapter 6, Pergamon Press Inc., 1974.

[141] McNiven H.D., SackMan J.L., Shah A.H. Dispersion of axially symmetric waves in composite, elastic rods, The Journal of the Acoustical Society of America, 35, 1602–1690, 1963.

[142] Mendrok K., Uhl T. Experimental verification of the damage localization procedure based on modal filtering, Structural Health Monitoring, 10(2), 157–171, 2011.

[143] Mindlin R.D., Herrmann G. A one–dimensional theory of compressional waves in an elastic rod, Proceedings of First U.S. National Congress of Applied Mechanics, American Society for Mechanical Engineers, 187–191, 1951.

[144] Mindlin R.D., McNiven H.D. Axially symmetric waves in elastic rods, Journal of Applied Mechanics, 27(1), 145–151, 1960.

[145] Miklowitz J. Travelling compressional waves in an elastic rod according to the more exact one–dimensional theory. Proceedings of the Second U.S. National Congress of Applied Mechanics, American Society for Mechanical Engineers, 179–186, 1955.

[146] Miklowitz J. The propagation of compressional waves in a dispersive elastic rod, Journal of Applied Mechanics, 24, 231–239, 1957.

[147] Miklowitz J. The Theory of Elastic Waves and Wave Guides, Amsterdam, North–Holland, 1978.

[148] Min J., Park S., Yun C–B., Lee C–G., Lee C. Impedance–based structural health monitoring incorporating neural network technique for identification of damage type and severity, Engineering Structures, 39, 210–220, 2012.

[149] Mirsky I., Herrmann G. Nonaxially symmetric motions of cylindrical shells, The Journal of Acoustical Society of America, 29(10), 1116–1123, 1957.

[150] Mirsky I., Herrmann G. Axially symmetric motions of thick cylindrical shells, The Journal of Applied Mechanics, 25, 97–102, 1958.

[151] Miśkiewicz M., Pyrzowski Ł., Wilde K., Mitrosz O. Technical Monitoring System for a New Part of Gdańsk Deepwater Container Terminal, Polish Maritime Research, 24(s1), 149–155, 2017.

[152] Miśkiewicz M., Mitrosz O., Brzozowski T. Preliminary field tests and long–term monitoring as a method of design risk mitigation: a case study of Gdańsk Deepwater Container Terminal, Polish Maritime Research, 24(3), 106–114, 2017.

[153] Mitra M., Gopalakrishnan S. Guided wave based structural health monitoring: A review, Smart Materials and Structures, 25(5), 27 pages, 2016.

[154] Monnier T. Lamb–Waves based Impact Damage Monitoring of a Stiffened Aircraft Panel using Piezoelectric Transducers, Journal of Intelligent Material Systems and Structures, 17(5), 411–421, 2006.

[155] Moser F., Jacobs L.J., Qu J. Modeling elastic wave propagation in waveguides with the finite element method, NDT&E International, 32(4), 225–234, 1999.

[156] Moustafa A., Dehghan–Niri E., Farhidzadeh A., Salamone S. Corrosion monitoring of post–tensioned concrete structures using fractal analysis of guided ultrasonic waves, Structural Control and Health Monitoring, 21(3), 438–448, 2014.

[157] Moustapha S., Lu Y., Li J., Ye L. Damage detection in rebar–reinforced concrete beams based on time reversal of guided waves, Structural Health Monitoring, 13(4), 347–358, 2014.

[158] Na W.–B., Kundu T., Ehsani M.R. Ultrasonic guided waves for steel bar concrete interface testing, Materials Evaluation, 60(3), 437–444, 2002.

[159] Na W.–B., Kundu T., Ehsani M.R. Lamb waves for detecting delamination between steel bars and concrete, Computer–Aided Civil and Infrastructure Engineering, 18(1), 58–63, 2003.

[160] Nazarko P., Ziemiański L. Damage detection in aluminum and composite elements using neural networks for Lamb waves signal processing, Engineering Failure Analysis, 69, 97–107, 2016.

[161] Neilson RD, Ivanović A, Starkey A.J, Rodger A.A. Design and dynamic analysis of a pneumatic impulse generating device for the non–destructive testing of ground anchorages, Mechanical Systems and Signal Processing, 21(6), 2523–2545, 2007.

[162] Onoe M. Tables of modified quotients of Bessel functions, Columbia University Press, New York, 1958.

[163] Onoe M., McNiven H.D., Mindlin R.D. Dispersion of axially symmetric waves in elastic rods, Journal of Applied Mechanics, 29(4), 729–734, 1962.

[164] Ostachowicz W., Kudela P., Krawczuk M., Żak A. Guided waves in structures for SHM. The Time–domain Spectral Element Method, John Wiley & Sons Ltd., 2012.

[165] Palacz M., Krawczuk M., Ostachowicz W. Detection of additional mass in rods: Experimental and numerical investigation, Archives of Applied Mechanics, 74(11–12), 820–826, 2005.

[166] Park K.C. Practical aspect of numerical time integration, Computers & Structures, 7(3), 343–353, 1977.

[167] Patera A.T. A spectral element method for fluid dynamics: laminar flow in a channel expansion, Journal of Computational Physics, 54(3), 468–488, 1984.

[168] Pao Y.H., Mindlin R.D. Dispersion of flexural waves in an elastic, circular cylinder, Journal of Applied Mechanics, 27(3), 513–520, 1960.

[169] Pau A., Capecchi D., Vestroni F. Reciprocity principle for scattered fields from discontinuities in waveguides, Ultrasonics 55, 85–91, 2015.

[170] Pavlakovic B.N., Lowe M.J.S., Cawley P., Alleyne D. Disperse: A general purpose program for creating dispersion curves, Review of Progress in Quantitative Nondestructive Evaluation, 16, 185–192, 1997.

[171] Pavlakovic B.N. Leaky guided ultrasonic waves in NDT, (1998) PhD thesis, Imperial College of Science, Technology and Medicine.

[172] Peng H., Meng G., Li F. Modeling of wave propagation in plate structures using three–dimensional spectral element method for damage detection, Journal of Sound and Vibration, 320(4–5), 942–954, 2009.

[173] Plass H.J., Steyer C.C. Studies in longitudinal and bending waves in long elastic rods. The University of Texas, Defense Research Laboratory, Report DRL–376, CM–860, 1956.

[174] Pochhammer L. Ueber die Fortpflanzungsgeschwindigkeiten kleiner Schwingungen in einem unbegrenzten isotropen Kreiscylinder. Journal fur die reine und angewandte Mathematik, 81, 324–336, 1876.

[175] Randall M.J. Fast programs for layered half–spaced problems, Bulletin of Seismological Society of America, 57(6), 1299–1316, 1967.

[176] Reuter R.C. Dispersion of flexural waves in a circular biomaterial cylinders – theoretical treatment, The Journal of the Acoustical Society of America, 46(3), 643–648, 1969.

[177] Reis H., Ervin B.L., Kuchma D.A., Bernhard J.T. Estimation of corrosion damage in steel reinforced mortar using guided waves, Journal of Pressure Vessel Technology, 127(3), 255–261, 2005.

[178] Rokhlin S.I., Wang L. Stable recursive algorithm for elastic wave propagation in layered anisotropic media: Stiffness matrix method, The Journal of the Acoustic Society of America, 112(3), 822–834, 2002.

[179] Rokhlin S.I., Wang L. Ultrasonic waves in layered anisotropic media: characterization of multidirectional composites, International Journal of Solids & Structures, 39(16), 4133–4149, 2002.

[180] Rose J.L. Ultrasonic Waves in Solid Media. Cambridge University Press; 1999.

[181] Rucka M. Experimental and numerical studies of guided wave damage detection in bars with structural discontinuities, Archive of Applied Mechanics, 80(12), 1371–1390, 2010.

[182] Rucka M. Modelling of in–plane wave propagation in a plate using spectral element method and Kane–Mindlin theory with application to damage detection, Archive of Applied Mechanics, 81(12), 1877–1888, 2011.

[183] Rucka M. Wave Propagation in Structures. Modelling, Experimental Studies and Application to Damage Detection, Wydawnictwo Politechniki Gdańskiej, 2011.

[184] Rucka M., Wilde K. Application of continuous wavelet transform in vibration based damage detection method for beam and plates, Journal of Sound and Vibration, 297(3–5), 536–550, 2006.

[185] Rucka M., Wilde K. Non–destructive diagnostics of concrete cantilever beam and slab by impact echo method, Diagnostyka, 3(55), 63–68, 2010.

[186] Rucka M., Wilde K. Experimental study on ultrasonic monitoring of splitting failure in reinforced concrete, Journal of Nondestructive Evaluation, 32(4), 372–383, 2013.

[187] Rucka M., Witkowski W., Chróścielewski J., Burzyński S., Wilde K. A novel formulation of 3D spectral element for wave propagation in reinforced concrete, Bulletin of the Polish Academy of Sciences Technical Sciences, 65(6), 805–813, 2017.

[188] Sabatini P.J., Pass D.G., Bachus R.C. Geotechnical engineering circular no. 4. Ground anchors and anchored systems, Report No. FHWA–IF–99–015, 1999.

[189] Sanderson R.M., Hutchins D.A., Billson D.R., Mudge P.J. The investigation of guided wave propagation around a pipe bend using an analytical modelling approach, The Journal Acoustical Society of America, 133(3), 1404–1414, 2013.

[190] Schabowicz K., Modern acoustic techniques for testing concrete structures accessible from one side only, Archives of Civil and Mechanical Engineering, 15(4), 1149–1159, 2015.

[191] Schabowicz K., Ranachowski Z., Jóźwiak–Niedźwicka D., Radzik Ł., Kudela S., Dvorak T. Application of X–ray microtomography to quality assessment of fibre cement boards, Construction and Building Materials, 110, 182–188, 2016.

[192] Seco F, Jimenez AR. Modelling the Generation and Propagation of Ultrasonic Signals in Cylindrical Waveguides. Ultrasonic Waves, Dr Santos (Ed.), ISBN: 978–953–51–0201–4, 1–28, 2012.

[193] Senyurek V.Y., Detection of cuts and impact damage at the aircraft wing slat by using Lamb wave method, Measurement, 67, 10–23, 2015.

[194] Sharma S., Mukherjee A. Longitudinal guided waves for monitoring chloride corrosion in reinforcing bars in concrete, Structural Health Monitoring, 9(4), 555–567, 2010.

[195] Siemińska–Lewandowska A. Głębokie wykopy. Projektowanie i wykonawstwo, Wydawnictwa Komunikacji i Łączności WKŁ, 2013.

[196] Silk M., Bainton K. The propagation in metal tubing of ultrasonic wave modes equivalent to Lamb waves, Ultrasonics, 17(1), 11–19, 1979.

[197] Simmons J.A., Drescher–Krasicka E., Wadley H.N.G. Leaky axisymmetric modes in infinite clad rods. I., The Journal of the Acoustical Society of America, 92(2), 1061–1090, 1992.

[198] Stępiński T., Uhl T., Staszewski W. Advanced Structural Damage Detection: From Theory to Engineering Applications, Wiley, 2013.

[199] Strickwerda J.C. Finite difference schemes and partial differential equations. Wadsworth–Brooks, Belmont, 1989.

[200] Stoneley R. Elastic waves at the surface of separation of two solids, Proceedings of Royal Society A, 106, 416–428, 1924.

[201] Sun Z.Z., Wu X. A fully discrete difference scheme for a diffusion–wave system, Applied Numerical Mathematics, 56(2), 193–209, 2006.

[202] Świt G., Krampikowska A., Chinh L–M. A prototype system for acoustic emission–based structural health monitoring of My Thuan bridge, Prognostics and System Health Management Conference (PHM–Chengdu), 2016.

[203] Thomson W.T. Transmission of elastic waves through a stratified solid medium, Journal of Applied Physics, 21(2), 89–93, 1950.

[204] Thurston R.N. Elastic waves in rods and clad rod, The Journal of the Acoustical Society of America 64(1), 1–37, 1978.

[205] Tomaszewska A., Szymczak C. Identification of the Vistula Mounting tower model using measured modal data, Engineering Structures, 42, 342–348, 2012.

[206] Tse P., Wang X. Semi–quantitative analysis of defect in pipelines through the use of technique of ultrasonic guided waves, Key Engineering Materials, 413–414, 109–116, 2009.

[207] Vogt T., Lowe M.J.S., Cawley P. The scattering of guided waves in partly embedded cylindrical structures, The Journal of the Acoustical Society of America, 113(2), 1258–1272, 2003.

[208] Volterra E.G. A one–dimensional theory of wave propagation in elastic rods based on assumption of constrained elasticity. Office of Naval Research Project NOR R (591)05, Rensselaer Poly, Inst. Progress Rept. Nr(2), 1956.

[209] Wandowski T., Malinowski P., Ostachowicz W. Damage detection with concentrated configurations of piezoelectric transducers, Smart Materials and Structures, 20(2), 14 pages, 2011.

[210] Wang C., He W., Ning J., Zhang C. Propagation properties of guided wave in the anchorage structure of rock bolts, Journal of Applied Geophysics, 69(3–4), 131–139, 2009.

[211] Wang L., Rokhlin S.I. Stable reformulation of transfer matrix method for wave propagation in layered anisotropic media, Ultrasonics, 39(6), 413–424, 2001.

[212] Wang T., Song G., Wang Z., Li Y. Proof–of–concept study of monitoring bolt connection status using a piezoelectric based active sensing method, Smart Materials and Structures, 22(8), 5 pages, 2013.

[213] Whittier J.S., Jones J.P. Axially symmetric wave propagation in a two–layered cylinder, International Journal of Solids and Structures, 3(4), 657–675, 1967.

[214] Wilde K., Modal diagnostics of civil engineering structures, Wydawnictwo Politechniki Gdańskiej, 2008.

[215] Witkowski W., Rucka M., Chróścielewski J., Wilde K. On some properties of 2D spectral finite elements in problems of wave propagation, Finite Elements in Analysis and Design, 55, 31–41, 2012.

[216] Worlton D.C. Ultrasonic testing with Lamb waves, Nondestructive Testing, 15, 218–222, 1957.

[217] Worlton D.C. Experimental confirmation of Lamb waves at megacycles frequencies, Journal of Applied Physics, 32(6), 967–971, 1961.

[218] Worlton D.C. Method of applying Lamb waves in ultrasonic testing, US Patent 3,165,922, 1965.

[219] Wu F., Chang F.–K. Debond detection using embedded piezoelectric elements in reinforced concrete structures – part I: experiment, Structural Health Monitoring, 5(1), 5–15, 2006.

[220] Wu F., Chang F.–K., Debond detection using embedded piezoelectric elements in reinforced concrete structures – part II: analysis and algorithm, Structural Health Monitoring, 5(1), 17–28, 2006.

[221] Wu R, Xu J, Li C, Zhou B, Ma Q, Wang Z. Stress wave propagation in supporting bolts: A test for bolt support quality, International Journal of Mining Science and Technology, 22(4), 567–571, 2012.

[222] Xanthakos P.P. Ground anchors and anchored structures, John Wiley & Sons, 1991.

[223] Yan G. A Bayesian approach for damage localization in plate–like structures using Lamb waves, Smart Materials and Structures, 22(3), 17 pages, 2013.

[224] Yim H., Sohn Y. Numerical simulation and visualisation of elastic waves using mass–spring lattice model, IEEE Transactions on Ultrasonics, Ferroelectrics and Frequency Control, 47(3), 549–558, 2000.

[225] Yu J.–D., Bae M.–H., Lee I.–M., Lee J.–S. Nongrouted ratio evaluation of rock bolts by reflection of guided ultrasonic waves, Journal of Geotechnical and Geoenvironmental Engineering, 139(2), 298–307, 2013.

[226] Zalameda J.N., Winfree W.P., Seebo J.P., Johnston P.H. Thermography inspection for detection and tracking of composite cylinder damage during load testing, AIP Conference Proceedings 1335(1), 450–457, 2011.

[227] Zembaty Z., Kokot S., Bobra P. Application of rotation rate sensors in an experiment of stiffness 'reconstruction', Smart Materials and Structures, 22(7), 1–6, 2013.

[228] Zemanek J. An experimental and theoretical investigation of elastic wave propagation in a cylinder, The Journal of the Acoustical Society of America, 51(1B), 265–283, 1972.

[229] Zhang C.S, Zou D.H., Madenga V. Numerical simulation of wave propagation in grouted rock bolts and the effects of mesh density and wave frequency, International Journal of Rock Mechanics and Mining Sciences, 43(4), 634–639, 2006.

[230] Zhang J., Ma H., Yan W., Li Z. Defect detection and location in switch rails by acoustic emission and Lamb wave analysis: A feasibility study, Applied Acoustic, 105, 67–74, 2016.

[231] Zhao X., Rose J.L. Boundary element modelling for defect characterization potential in a wave guide, International Journal of Solids and Structures, 40(11), 2645–2658, 2003.

[232] Ziaja A., Cheng L., Su Z., Staszewski W.J., Uhl T., Paćko P. On the coupling of guided waves in thick–walled structures, 7th European Workszhop on Structural Health Monitoring, July 8–11, France 2014.

[233] Ziaja A., Cheng L., Su Z., Paćko P., Pieczonka Ł., Uhl T., Staszewski W.J. Thick hollow cylindrical waveguides: A theoretical, numerical and experimental study, Journal of Sound and Vibration, 350, 73–90, 2015.

[234] Zienkiewicz O.C. The Finite Element Method, 4th Edition, New York: McGraw–Hill, 1989.

[235] Zima B., Rucka M. Analiza możliwości oceny stanu technicznego kotew gruntowych za pomocą propagacji fal prowadzonych, Inżynieria i Budownictwo, 11, 614–617, 2015.

[236] Zima B., Rucka M. Wave propagation in damage assessment of ground anchors. Journal of Physics: Conference Series 628, 8 pages, 2015.

[237] Zima B., Rucka M. Detection of debonding in steel bars embedded in concrete using guided wave propagation, Diagnostyka, 17(3), 27–34, 2016.

[238] Zima B., Rucka M. Guided waves for monitoring of plate structures with linear cracks of variable length, Archives of Civil and Mechanical Engineering, 16(3), 387–396, 2016.

[239] Zima B., Rucka M. Non–destructive inspection of ground anchors using guided wave propagation, International Journal of Rock Mechanics and Mining Sciences, 94, 90–102, 2017.

[240] Zima B., Rucka M. Elastic wave propagation in diagnostics of self–drilling system of grouted anchors, Diagnostyka, 18(2), 31–36, 2017.

[241] Zima B., Rucka M. Guided ultrasonic waves for detection of debonding in bars partially embedded in grout, Construction and Building Materials, 168, 124–142, 2018.

[242] Zou D.H, Cui Y, Madenga V, Zhang C. Effects of frequency and grouted length on the behaviour of guided ultrasonic waves in rock bolts, International Journal of Rock Mechanics and Mining Sciences, 44(6), 813–819, 2007.

[243] Zou D.H, Cheng J, Yue R, Sun X. Grout quality and its impact on guided ultrasonic waves in grouted rock bolts, Journal of Applied Geophysics, 72(2), 102–106, 2010.

[244] Zou D.H, Cui Y. A new approach for field instrumentation in grouted rock bolt monitoring using guided ultrasonic waves, Journal of Applied Geophysics, 75(3), 506–512, 2011.

[245] Zumpano G., Meo M. A new damage detection technique based on wave propagation for rails, International Journal of Solids and Structures, 43(5), 1023–1046, 2006.

[246] Żak A., Krawczuk M., Ostachowicz W. Propagation of in–plane waves in an isotropic panel with a crack, Finite Element in Analysis and Design, 42(11), 929–941, 2006.

[247] Żak A., Krawczuk M. Assessment of rod behaviour theories used in spectral finite element modelling, Journal of Sound and Vibration, 329, 2099–2113, 2010.

[248] Żak A., Krawczuk M., Skarbek Ł., Palacz M. Numerical analysis of elastic wave propagation in unbounded structures, Finite Element in Analysis and Design, 90, 1–10, 2014.

[249] Dywi Drill system: https://www.dywidag.co.uk/products/geotechnical–systems/dywi–drill–system/system–description.html